

TEKST NR 345

1998

**Modeling the Arterial System with
Reference to an Anesthesia Simulator**

Ph.D. Thesis

by

Mette Sofie Olufsen

TEKSTER fra

IMFUFA

ROSKILDE UNIVERSITETSCENTER
INSTITUT FOR STUDIET AF MATEMATIK OG FYSIK SAMT DERES
FUNKTIONER I UNDERVISNING, FORSKNING OG ANVENDELSER

IMFUFA, Roskilde Universitetscenter,
Postbox 260, 4000 Roskilde

Modeling the Arterial System with
Reference to an Anesthesia Simulator

Ph.D. Thesis (2nd ed)
by
Mette Sofie Olufsen.

IMFUFA tekst nr. 345/98, RUC. 193 sider. ISSN 0106-6242

Abstract

Modeling blood flow and especially the propagation of the pulse wave in the systemic arteries is a topic which is interesting to the medical society since the shapes of the pressure profiles have diagnostic significance.

We set up a mathematical model for the blood flow in the larger arteries and propose a physiologically based boundary condition representing the smaller arteries and arterioles as a structured tree in which a simplified version of the model is solved. Because the structured tree models wave propagation effects we claim that it is able to capture more of the dynamics in blood flow than traditional approaches. Numerical simulations and comparisons with existing models as well as empirical data supports this claim.

Preface

A central problem when modeling blood flow and pressure in the larger systemic arteries is to determine a physiologically based boundary condition such that the arterial tree can be truncated a few generations distally from the aorta, iliac, and femoral arteries. In this dissertation we have developed a one-dimensional fluid dynamical model, based on Navier-Stokes equations for an incompressible Newtonian fluid, predicting flow and pressure in the systemic arteries. The boundary condition, representing the smaller arteries, is modeled by calculating the root impedance of a structured tree which is attached to each terminal branch of the larger arteries. The root impedance for each of the structured trees is determined using a semi-analytical approach based on linearization of the viscous axisymmetric Navier-Stokes equations for an incompressible Newtonian fluid. This provides a dynamical boundary condition that reflects the actual phase-lag between flow and pressure and also accommodates wave propagation effects for all of the systemic arteries. The result is a model which is physiologically adequate as well as computationally feasible.

This Ph.D. study has been accomplished at the Department of Mathematics, Roskilde University, at Math-Tech (a private company engaged in commercial mathematical modeling), and at the Department of Anesthesia, Herlev University Hospital. The study has been organized as an industrial Ph.D. and apart from the three institutions mentioned above, it has been supported by the Danish Academy of Technical Sciences. In addition to this dissertation these results are (or will be) published in (Olufsen, Nielsen, Jensen and Pedersen, 1994; Olufsen and Ottesen, 1995a; Olufsen and Ottesen, 1995b; Olufsen, 1997a; Olufsen, 1997b; Olufsen, 1998).

I want to thank the following people without whom I would never have been able to accomplish this study. These are my advisors J. Larsen, Ph.D., Math-Tech, Professor S.A. Pedersen, Roskilde University, and M.D. P.F. Jensen, Ph.D., Department of Anesthesia, Herlev University Hospital. In addition I want to thank Professor C.S. Peskin, Courant Institute of Mathematical Sciences, New York University, USA, Professor T.J. Pedley, Department of Applied Mathematics and Theoretical Physics, Cambridge University, UK, J. Ottesen, Ph.D., Department of Mathematics, Roskilde University, Professor V.A. Barker and O.M. Nielsen, Department of Mathematical Modelling, Technical University of Denmark, H. Larsen, Math-Tech, the Biomath group at Roskilde University, the mechanics group at the department of Mathematics, Australian Defense Force Academy, Canberra, my colleagues at Math-Tech, and finally, but not least importantly, my family and friends.

Mette S. Olufsen
Roskilde, 14th May 1998

Contents

1	Introduction	1
2	Historical review	3
3	Background, the physiology of blood flow	15
3.1	The circulatory system	15
3.2	Systemic arteries	17
4	Model of flow and pressure in the systemic arteries	29
5	Structure of the larger arteries	33
5.1	Geometrical properties of the larger arteries	33
5.2	Structural properties of the vessel walls	37
6	Structure of the smaller arteries	39
6.1	Radius and asymmetry relations	42
6.2	Order of the structured tree	44
6.3	Length of the segments	44
6.4	Wall thickness and Young's modulus	45
6.5	Conclusion – Parameter choices	49
7	Fluid dynamical model of a large artery	51
7.1	Momentum and continuity equations	51
7.2	State equation	58
7.3	Coupling the state equation to the fluid dynamic equations	63
7.4	Characteristic equations	65
8	Flow and pressure in the tree of larger arteries	69
8.1	Boundary conditions	69
8.2	Non-dimensional formulation	74
9	Numerical methods for the larger arteries	77
9.1	Numerical method of characteristics	77
9.2	The Lax-Wendroff method	83
9.3	Convergence of the two methods	89

10 Fluid dynamical model of a small artery	93
10.1 Model assumptions and basic equations	94
10.2 Motion of the fluid	94
10.3 Motion of the vessel walls	94
10.4 Elasticity Relations	103
10.5 Balancing fluid and wall motions	103
10.6 Linearization	104
10.7 Solution of the linearized equations	107
10.8 Momentum equation	115
10.9 Continuity equation	116
10.10 Solutions of the linear model	117
11 Flow and pressure in the tree of smaller arteries	119
11.1 Bifurcation condition	119
11.2 Outflow boundary condition	119
11.3 Root impedance of the structured tree	120
12 Results	125
12.1 Results from the model problem	126
12.2 Comparison of the structured tree, the Windkessel, the pure resistance models, and measured data	126
12.3 Parameter variation	144
13 Conclusion	159
13.1 Perspectives	161
13.2 Pathological situations	163
13.3 Comparison with measured data	163
13.4 Arterial modeling and anesthesia simulation	163
A Derivation of non-linear equations for the Lax-Wendroff method	165
A.1 Outflow boundary condition	165
A.2 Bifurcation conditions	167
B Gas dynamics analogy	173
C The self-similar tree	175
C.1 Case 1: Unscaled bifurcations, ($\alpha = \beta = 1$)	177
C.2 Case 2: Symmetric bifurcations, ($\alpha = \beta$)	180
C.3 Case 3: Asymmetric bifurcations, ($\alpha \neq \beta$)	180
D English summary	183
E Resume på dansk	185
Bibliography	187

Chapter 1

Introduction

Modeling of blood flow and pressure in the systemic arteries has been a topic of interest both to theoretical and clinical investigators. Thus, research in this field has a strong interdisciplinary aspect. The aim of this research has been to obtain a thorough theoretical as well as clinical understanding of physiological systems in order to be able to treat cardiovascular diseases better. This is important since the majority of deaths in developed countries result from cardiovascular diseases, most of which are associated with abnormal flow in the arteries (Ku, 1997).

The inspiration for this project arises from previous and present efforts to develop an anesthesia simulator based on mathematical models. An important aspect of such a simulator is having a good model of the cardiovascular system. During surgery monitoring of invasive arterial and venous pressures at certain locations are important means for observing the state of a patient. Pressure and flow profiles are often affected by various pathological conditions but these relations are not always fully interpreted. In order to understand the changed or manipulated hemodynamic conditions occurring under diseases or during anesthesia it is important to understand blood flow under normal physiological conditions. It is exactly these normal situations which will be analyzed in the dissertation.

Our model constitutes a one-dimensional fluid dynamical model of the systemic arteries predicting blood flow and pressure at all times in one spatial dimension. The blood is viewed as an incompressible Newtonian fluid and the vessels as elastic. The model is split in two parts: The first comprises the larger arteries (ranging not more than two generations from the aorta, iliac, and femoral arteries) and the second the smaller arteries. For these we set up a structured tree in which the geometry of all daughter vessels are determined from the parent vessel. For the larger arteries we solve the non-linear Navier-Stokes equations and for the smaller arteries we solve, analytically, a linearized system of equations. The purpose of the smaller arteries is to provide an outflow boundary condition which can be applied at the terminals of the larger arteries, this is done by determining the impedance at the root of the structured tree. There are two reasons for choosing to make a one-dimensional model. The first is that it is not possible to make a computationally feasible model of the entire arterial system in any higher dimension and the second is that measured flow- and pressure profiles during surgery are one-dimensional.

Outline for the dissertation

Chapter 1: Introduction. This introduction.

Chapter 2: Historical review. Gives a short review of the development of arterial modeling from ancient times till today and places our model in the context of anesthesia simulation.

Chapter 3: Background, the physiology of blood flow. Gives an overview of the physiological properties of blood and arteries.

Chapter 4: Model of flow and pressure in the systemic arteries. States the hypothesis for the dissertation.

Chapter 5: Structure of the larger arteries. Describes the geometry and elastic properties of the larger arteries.

Chapter 6: Structure of the smaller arteries. Describes the geometry and elastic properties of the smaller arteries. It focuses on how the smaller arteries can be combined into a structured model.

Chapter 7: Fluid dynamical model of a large artery. Derives the fluid dynamic equations for blood flow and pressure in the larger arteries.

Chapter 8: Flow and pressure in the tree of larger arteries. Extends the fluid dynamic model of a single vessel to apply for the tree of systemic arteries and gives the equations in non-dimensional form.

Chapter 9: Numerical methods for the larger arteries. Shows how to solve the fluid dynamic equations numerically. Two approaches, both explicit, are presented: the method of characteristics and Richtmeyer's two step version of the Lax-Wendroff method.

Chapter 10: Fluid dynamical model of a small artery. Presents a linear fluid dynamic model predicting blood flow and pressure in the smaller arteries. These are combined to give the impedance at the root of any vessel in the structured tree of smaller arteries.

Chapter 11: Flow and pressure in the tree of smaller arteries. Derives the impedance at the root of the tree comprising the smaller arteries. The impedance is used as outflow boundary conditions for the larger arteries and thus provides coupling to the model of the larger arteries discussed in Chapter 8. Since the root impedance is found using a simple numerical approach the algorithm is described in this chapter rather than in a separate chapter.

Chapter 12: Results. Gives results from simulations with the combined model including a comparison with both data and other models.

Chapter 13: Conclusion.

Appendix A: Derivation of non-linear equations for the Lax-Wendroff method. Derives the residual equations and the Jacobian matrix used when solving the fluid dynamic equations for the combined model.

Appendix B: Gas dynamics analogy. Presents an analogy between the fluid dynamic equations, treating the blood as incompressible and the vessels as distensible, and the gas-dynamics equations, in which a compressible gas moves in a rigid tube.

Appendix C: The self-similar tree. Presents a self-similar solution for an inviscid version of the linearized fluid dynamic equations used when predicting the root impedance of the structured tree of smaller arteries.

Appendix D: English summary.

Appendix E: Dansk resume. Summary in Danish.

Chapter 2

Historical review

The history of the arterial pulse is the history of medicine – of its art and of its science. Scientific understanding of the pulse and its application to medicine has at all times been dependent on the knowledge of theory and of physiological mechanisms, and on the availability of methods for its measurements.

This is the first sentence in the first chapter of "The Arterial Pulse" by O'Rourke, Kelly and Avolio (1992) and it reflects the importance of the arterial pulse. Indeed, the pulse has always been one of the first clinical signs examined by any physician. What we find interesting about the story of the arterial pulse are the following two points. First, the fact that examination and knowledge about the characteristics of the arterial pulse dates much further back than the scientific understanding of the circulatory system, and second, that throughout time the most important persons contributing to the understanding of the arterial pulse often had interdisciplinary backgrounds in both medicine, mathematics, and physics.

Since ancient times detection of the arterial pulse by sensations appreciated by the physicians fingers (palpation) was an essential part in diagnosing diseases. Chinese, Indian, and Greek medicine used it often. It was believed that a good physician could diagnose diseases and their severity, detect pregnancy, the sex of an unborn child among other things solely from palpation of the pulse. Especially in Indian and Chinese medicine these examinations often took the form of a mystic rite, where the physician offered diagnosis and prognosis without any other examination at all. An example is the Hindu physician Susruta who is depicted in Figure 2.1. The story tells that he took advantage of the situation and gained a huge wealth from his predictions.

In contrast to these ritual predictions ancient Greek physicians had a more practical and clinical approach. In the fourth century B.C. the Greeks recognized and named various features of the pulse, e.g. the dicrotic and arcrotic waves, names still in use today. However, they did not make any connection to the beating of the heart and believed that arteries were filled with air. In fact, it is from this belief that arteries got their name. The word artery is composed of the two Greek words "aer" and "trachea", which literally means air duct. The reason for this was that when a dead person was cut open there were no longer blood in the arteries but air. Furthermore, they attributed the pulsatile sensations to an active dilation of the arteries and believed that they were drawing vital spirits from the airways. After Hippocrates, Herophilus noted that there



Figure 2.1: Consultation with the Hindu physician Susruta where he is practicing his examination of a patient by palpation of the pulse. From O'Rourke et al. (1992).

must be some communication between the arteries and the heart. He also was the first to describe the four basic qualities of the pulse, namely

- size,
- force,
- contour, and
- frequency.

He compared them to a musical note and the cadence of a verse. All of these qualities were found by palpations without any instrumental measurements. By simultaneously sensing the pressure at several places on the human body Erasistratos later noted a delay in the travel of the pulse from central to peripheral arteries.

These early investigators drew the right conclusions even though they based them on a false notion of the physics of the pulse. Because of the belief that arteries contained air the pulse was regarded as a wave traveling through an air-duct. At that time the circulation was assumed to consist of two fundamental elements: blood, the source of matter, which nourished all constituents of the body with natural spirit that it carried and pneuma, in its two forms – vital and animal spirit – which was the source of energy animating matter. Blood and pneuma were distributed in two separate systems: (1) Blood was manufactured in the liver and transported, through the veins, toward all organs. As a result only a small fraction reached the right ventricle. From here it was unable to return to the vena cava because of the tricuspid valve. Instead it flowed through the “artery-like vein” (the pulmonary artery) towards the lungs for their nourishment. (2) Pneuma inspired into the lungs flowed through the “vein-like artery” (the pulmonary vein) to the cavity of the left ventricle, where it became vital spirit, and was then distributed to the body through the aorta and the arteries. Furthermore, it was assumed that the part of the vital spirit that reached the brain was transformed into animal spirit, which was then accumulated in the cerebral ventricles, and transported through the hollow nerves to the entire body. In this scheme, motion of blood and pneuma was furnished by the diastolic activity of the heart, and reflux from or to the ventricles of both blood and pneuma was prevented by the valves. The unidirectional motion of blood to the lungs and of air to the left ventricle was, for the first time explicitly recognized. Erasistratos also emphasized that veins, arteries, and nerves were distributed over all parts of the body and that the finest divisions of the veins and arteries intercommunicated.

This was the predominant view until Galen (129–199 A.D.) late in the Greek era corrected some of these false understandings. He was probably the most influential man at his time, and it was his results which founded the medical practice for the next 1000 years. Galen noted a relation between the heart, arteries, and veins and pointed out that arteries during life contained blood – not air. However, he still did not relate the dilation of the arteries to the beating of the heart. He claimed that the arteries were dilating actively and by this action generated the pulse. Furthermore, he did not recognize that blood circulated.

Inspired by Erasistratos he considered the venous, the arterial and the nervous systems, with the liver, the heart, and the brain as the respective but separate centers which each distributed one of the three spirits; the natural, the vital, and the animal, through

the body. As Erasistratos he believed that blood was created in the liver and from here transported to all organs through the veins such that only a small fraction of it reached the right ventricle. It was this wrong conception which made him believe that arterial blood came from a direct transport from the right and into the left ventricle. This transport was assumed to occur through invisible pores located in the interventricular septum. Once in the cavity of the left ventricle, and only there, were blood and air elaborated into vital spirit. Through their own pulsating activity the aorta and the arteries drew the spirits from the blood in the left ventricle and distributed it throughout the body. This is seen in Figure 2.2.

It was not until the beginning of the seventeenth century that these false interpretations were corrected. The full scientific knowledge that arteries are part of a circulatory system in which the heart is pumping blood around was not known until Harvey in 1628 published his book "*De Motu Cordis et Sanguinis in Animalibus*" or the English translation "*Movement of the Heart and Blood in Animals, an anatomical essay*" (Fishman and Richards, 1964).

His studies established, for the first time, that the arterial pulse is a consequence of cardiac contraction which causes arterial dilation when blood is flowing through the aortic valve into the ascending aorta and further into the sophisticated network of vessels. Two facts convinced him that there must be a circulation, the first was the discovery of valves in the veins. Their function is a passive fluid mechanical process and he saw that these could be effective only if the blood in the veins flowed towards the heart not away from it as proposed by Galen. The other important point was his estimation of the magnitude of the cardiac output, even though it was still underestimated (he estimated it to approximately 1 liter per minute) this was much more than previously thought and it was much more than could be created in the liver as believed since the time of Galen. Furthermore, another old concept was abandoned namely that blood passed through the wall which separates the two sides of the heart. Based on these facts he concluded (and managed to convince most of his skeptics) that blood was circulating. There was a missing link in Harvey's studies namely the capillaries. They were discovered soon after by Malpighi in 1661 who used a microscope, something Harvey did not have at his disposal. Harvey also realized that changes of the pulse in a diseased body is a consequence of abnormalities in the function of the heart and blood vessels. Another important point was that he established the effect of the wave reflection of the arterial pulse.

One can say that with Harvey the modern view of physiology started and the scene was set for improvements of the basic physiological knowledge. The time of Harvey is the time of many great scientists. The most important was probably Galileo (1564–1642) who was a professor of mathematics while Harvey was still a medical student. He was important because it was probably his teaching which inspired Harvey. Galileo, who was also an astronomer, was instrumental in changing the perception of the natural science from a philosophy into the modern science as it is known today.

The understanding of blood flow as a fluid dynamical system, in which the blood is treated as a viscous fluid pulsating along a system of elastic tubes could not have been established without the studies by Newton (1642–1727), who was both a mathematician and a physicist. His contribution was to establish the concept of viscosity which is presented in an addended proposition in his book "*Principia Mathematica*". Furthermore, he was as a president for the Royal society responsible for the publica-

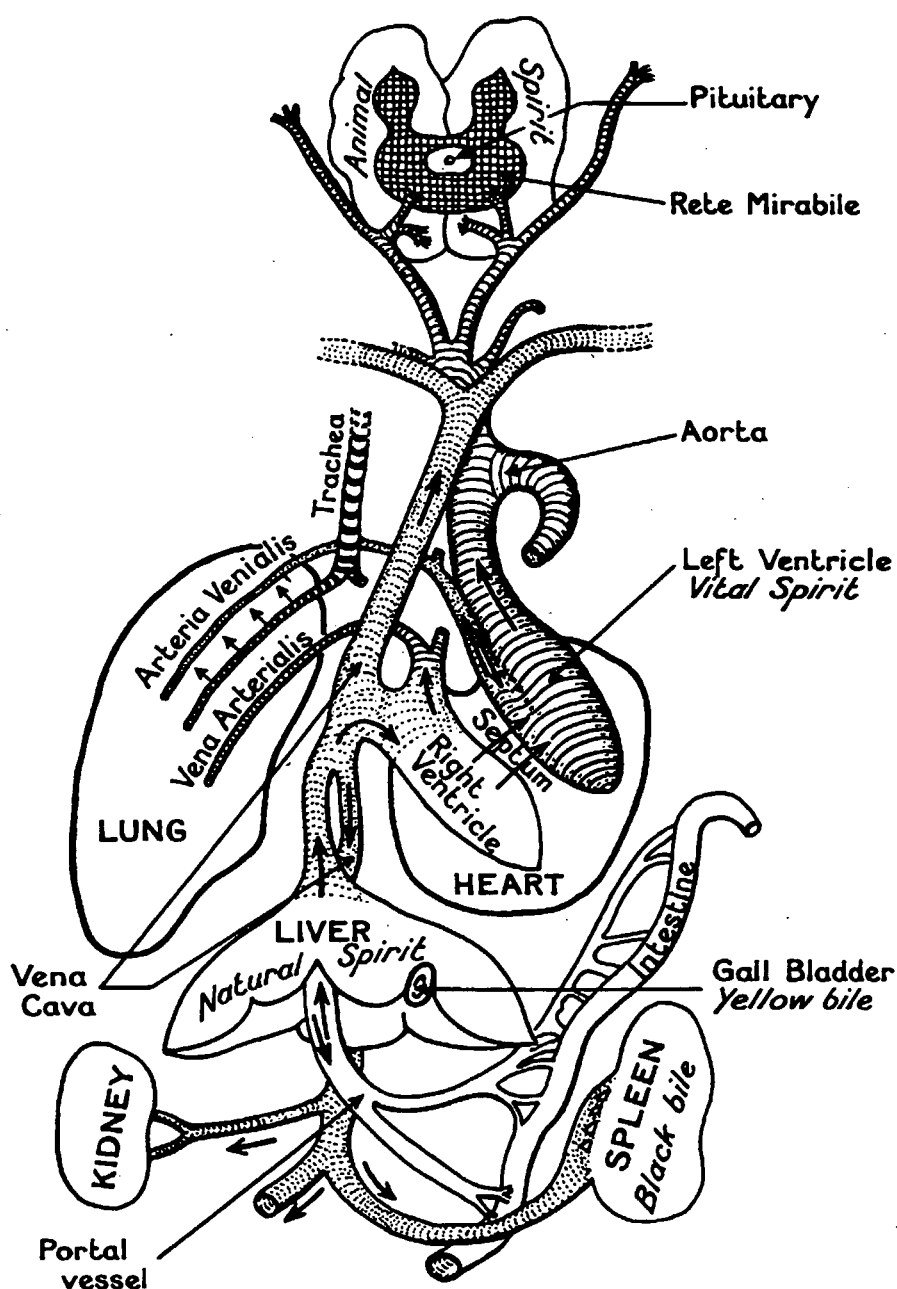


Figure 2.2: Galen's system of physiology. Blood is created in the liver and circulated to all organs through the veins. Some of this reaches the right ventricle and from here it diffuses through the septum to the left ventricle. At this point vital spirits are added and the blood is distributed through the arteries to the organs. From Crombie (1961).

tion of the book "Hemostatics" by Hales in 1733. Hales (1677–1761) was the first to measure arterial pressure, to document the response of arterial pressure to blood loss, to formulate the concept of peripheral resistance, and to show in an elegantly simple experiment that the greatest resistance to blood flow resides in the tiny blood vessels that are invisible to the naked eye. But probably the most famous of his results is his comparison of arteries to a fire engine compression chamber, called a Windkessel in the German translation of his book, a terminology which is widely used today. The comparison came from observing the similarity between the arterial system and the inverted air-filled dome of an contemporary fire engine. The purpose of the dome was to smooth oscillations, which was a result of intermittent pumping, so that flow of water through the fire hose nozzle would be almost constant. The comparison was that he saw the larger arteries as the cushion, the arterioles as the resistance to the intermittent pumping of the heart, and finally he compared the almost constant flow through the tissues to the nozzle of the fire hose.

Other people who influenced the development were the founders of the theory for fluid mechanics. Euler (1707–1783) established the general equations of fluid motion and he was the first to apply them to blood flow in arteries. He was a multi talented person, perhaps the greatest mathematician who ever lived, yet he also studied theology, medicine, astronomy, physics and oriental languages. He was a close friend of D. Bernoulli (1700–1782), who was also both a medical doctor as well as a great mathematician. Bernoulli used his interdisciplinary competence when he was formulating what is today known as Bernoulli's equation. A consequence of this equation is that pressure can be converted to kinetic and potential energy, or vice versa, provided that the flow is steady (Fung, 1996). The more general fluid equations known as Navier-Stokes equations were, however, not derived until 1845 where Stokes presented a derivation similar to the one used today. Before that, in 1827, the equations were set up by Navier who found them from model studies.

There are many other important contributions from the nineteenth century. For example Poiseuille (1799–1869) started his research in cardiovascular physiology while he was still a medical student. His primary training was as a physician but he had a great interest and some training in physics as well. His major contribution was to establish the relationship between flow, the pressure gradient, and the dimensions of a capillary tube. He showed experimentally that flow was related to the fourth power of the tubes internal diameter and this is what is expressed in the well known Poiseuille equation. However, it was not Poiseuille who established the theoretical basis of the law, this was derived by Hagenbach in 1860. Another important contribution by Hagenbach was to confirm Hales statement, that the most significant part of the peripheral resistance should be found in the smaller arteries. Young (1773–1829), who is mainly known for his research in optics and human vision, contributed with important achievements within the area of elasticity. This study was based on his interest in the relationship between the elastic properties of the arteries and the propagation velocity of the arterial pulse. His studies led to the concept of the elastic modulus which today is known as Young's modulus. Finally, we will mention the studies by Moens and Korteweg. In 1878 they established a relationship between the propagation velocity of the arterial pulse and Young's modulus of the arterial wall.

It would take us too far to include all the important contributions of this century. Therefore, we stop this selective description and start focusing on the one thing which

all of the early researchers have in common; their variety of interests and commitment to multi-disciplinary fields all involving the understanding of hemodynamics together with the basic science of mathematics and physics. The contributions mentioned here are selected such that the founding for the basic elements used later in this report are all covered. For more details and for a more elaborate discussion of the important developments in nineteenth and twentieth century we refer to O'Rourke et al. (1992), Nichols and O'Rourke (1998), Pedley (1980), and Boyer (1989).

Even though today's knowledge has brought the art and the science of the arterial pulse much closer together, there are still many problems that remain to be investigated. Today it is important to bring closer together the facts that can be obtained from measurements and the theoretical knowledge that can be obtained using modeling and simulations. This is important in our continuous effort to be able to manipulate and repair the body. We want to have the same control as the plumber fixing our pipes. The biological system is, however, much more complex so more sophisticated tools are necessary. Perhaps simulations can help to gain more insight into human physiology and in particular into the nature of the arterial pulse. Simulations in biology require close cooperation between two different scientific traditions. In the more technical sciences, e.g. development of flight simulators, there are mathematicians, engineers, and physicists working together all people with a similar background, but when we talk about biology, medicine, and technology the interdisciplinary span increases and that requires more from the people involved. Looking back this is exactly what characterized the men working in this area from the ancient Greek era until today. The traditions of doing interdisciplinary studies in this area is long, but the history of simulations in medicine is short, especially compared with the more technical sciences, e.g. it is commonly accepted today that pilots should have simulator training before flying with passengers. Today, however, there are many initiatives using interdisciplinary activities in the development of simulators for the medical sector.

The original idea of this project was not to study the arterial pulse as such but an interest in cognitive studies of the performance of anesthesiologists in the operating theater. They work in a typical high-stress environment, similar to pilots. There are long periods where practically nothing happens and then suddenly they have to act very fast in order to deal with potentially hazardous situations. In these environments there are often a large number of human errors, which can be reduced e.g. by simulator training. In Jensen (1997) anesthesia related mortality and morbidity rates are discussed, and it is concluded that morbidity is low but that a substantial part of the fatalities are a result of sub-standard care, and that some of these incidents could have been avoided with better training. The latter is concluded from a study performed in the United Kingdom where the number of deaths from anesthesia since 1982 was recorded. It was found that only 1 out of 10000 deaths were totally attributed to anesthesia. However, there is a long list of critical incidents occurring during anesthesia that does not necessarily imply death of the patient, and it would improve patient safety substantially if these incidents could be avoided. It is likely that this could be accomplished with more education in a simulator environment where, in addition to practical skills, tasks such as teamwork and leadership can be trained. This has been proven successful in aviation and the study by Jensen (1997) has tried to port a methodology for studying and identifying critical incidents from aviation to anesthesia.

This cognitive project started in 1991; originally the idea was to study anesthesiologists during their work, and record the studies on video. However, since critical incidents happens with very long intervals there is much wasted time. Therefore, the idea of developing a cognitive laboratory based on studies of anesthesiologists working in a simulator environment was born. Soon after it became clear that a simulator also would be ideal for training purposes, since some of the critical incidents, e.g. malignant hyperthermia, are very rare. At that time there were only a few other simulators available and they were very expensive and were only running on some special purpose equipment, e.g. the simulator developed by Gaba and DeAnda (1988). The idea was to be able to use the simulator in familiar surroundings, i.e. with standard monitoring equipment. Such a simulator was not available and hence a new project started with the aim of developing an anesthesia simulator. The requirements were that it should run in real time, that it should run on an inexpensive personal computer, and that it should be possible to connect it to the monitoring equipment and anesthesia machines common in most operating theaters. Furthermore, in order to predict the output in a physiological sound way it was decided that the simulator should be based on mathematical models. This project was initiated in 1992 as an interdisciplinary research project by Professor S.A. Pedersen, Department of Mathematics, Roskilde University, M.D. H. Ørding, Ph.D. and M.D. P.F. Jensen, Ph.D. Department of Anaesthesiology, Herlev University Hospital, and F. Jensen, Cognitive Systems Group, Risø National Laboratory.

Developing an anesthesia simulator requires deep knowledge not only of how the various parts of human physiology work but also of how they interact. Since the aim was to build an anesthesia simulator that can run in real time the mathematical models on which it should be based must be simple. However, it requires a thorough physiological understanding to make the right simplifications to these models. Therefore, the study was split in two projects, a commercial project SIMA, in which the main objective was to build a real time anesthesia simulator based on simple mathematical models, and a research project where the aim was to gain more insight and study more detailed models of the various parts, but keeping in mind that they should be able to be used when evaluating the models used by the SIMA project. The SIMA project is lead by Math-Tech in cooperation with Artema Monitoring and Emergency Care, The Department of Anaesthesiology, Herlev University Hospital, the Biomath Group, Department of Mathematics, Roskilde University, and CRS4 Center for Advanced Studies, Research, and Development, Cagliari, Italy.

Since the human physiological system is very complex it is not a trivial process to identify the areas which need to be modeled. The strategy used when choosing the models was to examine the information shown on a standard anesthesia monitor, i.e. pressure, ECG, oxygen and carbon dioxide profiles, heart rate, cardiac output, temperature, and systolic and diastolic pressures. From this information the following models were identified:

- A cardiovascular model providing
 - heart rate,
 - cardiac output
 - systolic and diastolic pressures,

- a number of pressures both arterial and venous, both in the systemic and pulmonary circuits.
- A pharmacokinetic model providing information about the concentration of drugs and inhalation anesthetics in blood, tissue, and each of the major organs.
- A pharmacodynamic model converting these concentrations into effects regulating parameters of the cardiovascular model, i.e. heart rate, compliance, and peripheral resistance.
- A baroreceptor model relating changes in pressure to physiological regulations of the parameters in the cardiovascular model.
- A respiratory model simulating transport of oxygen and carbon dioxide.
- A metabolic model controlling carbon dioxide and heat production.
- A fluid and electrolyte balance model accounting for the body volumes of plasma, protein, and electrolytes as well as the distribution of the body fluids.
- An ECG model providing profiles for the various ECG derivatives.

It is not easy to establish which of these models is most important, but one could say that the cardiovascular model in some sense is the driving force of the system and therefore fundamental to the simulator. Therefore, it is the main subject of this dissertation. Several of the other models have been studied in detail at the Department of Mathematics at Roskilde University.

During surgery several arterial blood pressures can be measured both non-invasively and invasively; for instance the aortic pressure, the radial pressure, the brachial pressure, or the femoral pressure. The resulting waveforms as well as the systolic and diastolic pressure levels are shown on the monitors. These are of diagnostic importance to the anesthesiologists. For example, in some patients suffering from diabetes or atherosclerosis, or in elderly people the dicrotic wave is often diminished. Furthermore, since the dicrotic wave is present as a result of reflections, abnormal dicrotic waves, or maybe even comparison of pressure profiles at different sites, could be used when diagnosing stenosis in the larger arteries. Generally, it can be said that if the shape of the pressure wave "looks" wrong it affects the anesthesiologists and he or she may interpret it to understand what is wrong.

It is difficult to make satisfactory and simple mathematical models of the cardiovascular system. As a result the simulator often uses curves generated from drawings of a number of characteristic situations. In order to give a better descriptive and technical characterization of the various physiological conditions in the future, we have found it important to study more detailed mathematical models of the systemic arteries. This dissertation is one of the results from this study. Our first approach was to study the characteristics of the arterial pulse. These are listed below:

- The leading edge of the pressure pulse of the larger arteries undergoes an increase in amplitude and steepness of the wave front.
- The mean pressure of the larger arteries drops slowly towards the periphery.

- A second “reflected” wave (the dicrotic wave) forms after the leading wave and they both propagate along the arteries. The dicrotic wave, however, propagates faster than the leading pulse wave.
- Far from the heart (towards the capillaries) one can observe an approximate proportionality between flow and pressure, but close to the heart proportionality is absent.

Since the studies by Galen, investigation of the arterial pulse has been continued and today there is a large number of studies both based on mathematical models and measurements of the characteristics of the arterial pulse. The study of the shape of the arterial pulse using mathematical models has over the years been done using quite different approaches ranging from electrical analog models to advanced three dimensional models based on fluid mechanics. The cardiovascular model in the SIMA project is based on an electrical analog model, see Figure 2.3, where only a small number of pressures labelled $PA[1-3]$ (systemic arterial pressures), $PV[1-2]$ (systemic venous pressures), $PP[1-3]$ (pulmonary arterial pressures), $PL[1-2]$ (pulmonary venous pressures), $P[L, R]V$ (left/right atrial pressures), and $P[L, R]V$ (left/right ventricular pressures). While such a model can be used when determining the systolic and diastolic pressures correctly it is not adequate in describing the phenomena listed above. Therefore, we have chosen to derive a one-dimensional model that, as closely as possible, follows physiological principles.

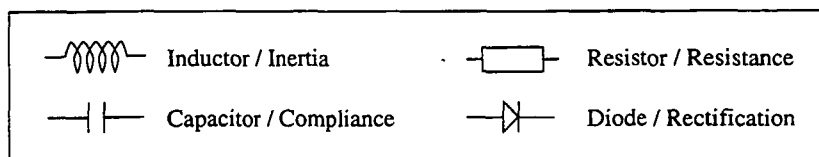
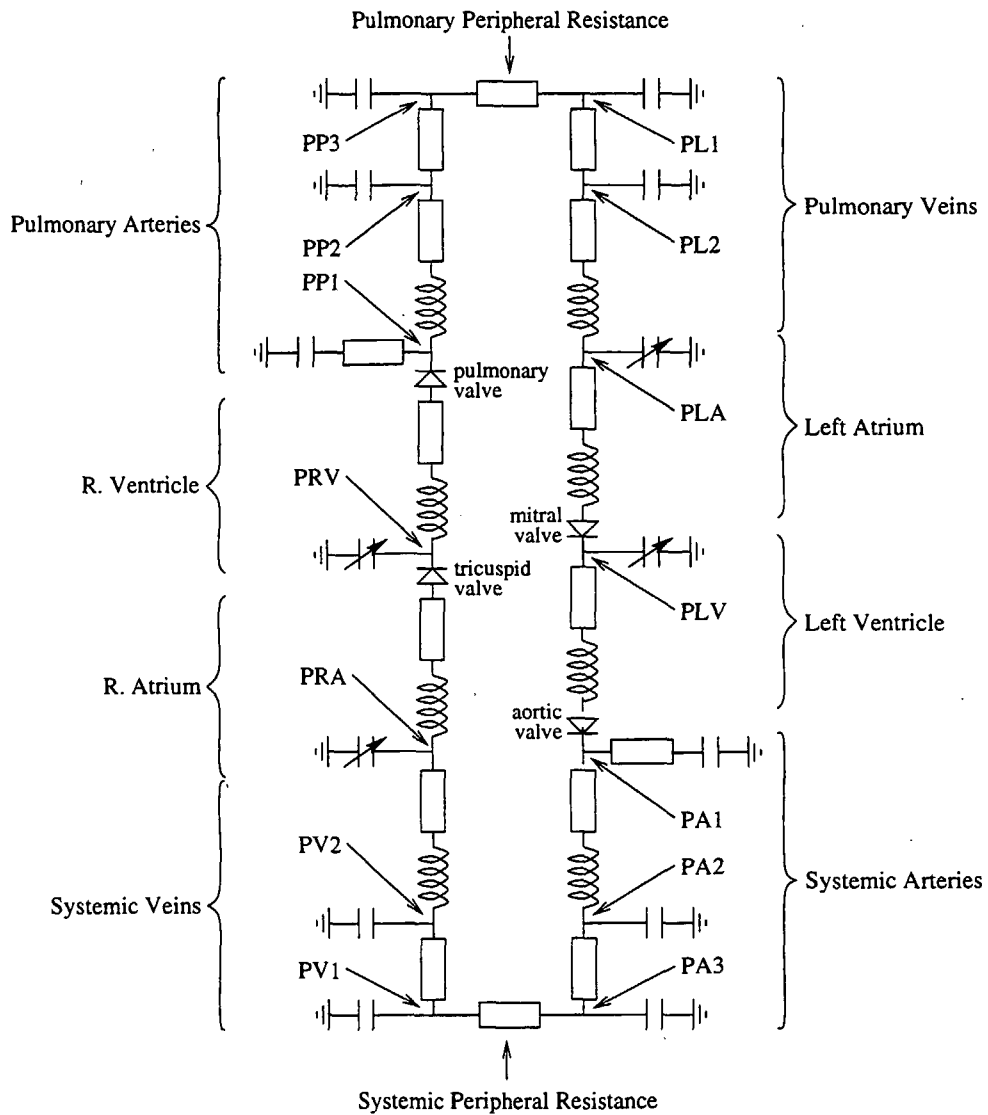


Figure 2.3: The cardiovascular model from the SIMA anesthesia simulator.

Chapter 3

Background, the physiology of blood flow

The function of the circulation is to service the needs of the tissues – to transport nutrients to the tissues, to transport waste products away, to conduct hormones from one part of the body to another, and in general to maintain an appropriate environment in all the tissue fluids for optimal survival and function of the cells.

The above quotation is taken from “Textbook of Medical Physiology” by Guyton (1991). It states that the purpose of the circulatory system is to be our pickup and delivery system servicing all cells in our body. In this chapter we will give an overview of the physical characteristics of the circulatory system together with some specific details about the systemic arteries.

3.1 The circulatory system

The cardiovascular circulatory system is divided into two parts each connected to the heart, see Figure 3.1. These are the systemic circulation which emanates at the left ventricle and ends at the right atrium, and the pulmonary circulation which emanates at the right ventricle and ends at the left atrium. The purpose of the systemic circulation is to transport oxygenated blood to all tissues, where part of the oxygen is exchanged with carbon dioxide, and then to transport the partly deoxygenated blood back from these tissues to the heart. The purpose of the pulmonary circulation is to transport the partly deoxygenated blood to the lung tissues, where the carbon dioxide is removed and the blood becomes fully oxygenated again, and then to transport the oxygenated blood back from the lungs to the heart. The basic organization of the two systems is similar. They are each composed of two parts; an arterial part, which transports blood from the heart to the tissues, and a venous part, which transports blood from the tissues towards the heart. The transport in the arteries is conducted under high pressure and high velocities, hence the arteries have strong vascular walls, while the transport in the veins is conducted under low pressure and low velocities, hence the venous walls are generally thin. In addition to transporting blood back to the heart the veins serve as a

major reservoir of blood. Both veins and arteries are often classified according to their size in the following four groups:

- Larger arteries and veins.
- Smaller arteries and veins.
- Arterioles and venules.
- Capillaries.

The circulation is driven by the heart: Cardiac contraction forces the mitral valve to close preventing flow back into the left atrium. This implies that the pressure of the left ventricle increases. When the pressure level has increased above the aortic pressure the aortic valve opens and a surge of blood is ejected into the ascending aorta. This is called the systolic phase. When pressure in the ventricle has fallen below the aortic pressure the valve closes and remains so until the beginning of the next cardiac cycle. During this period there is no flow into the aorta. This is called the diastolic phase. These two alternating phases define the heart cycle and they are repeated periodically. The period of the heart cycle for a normal adult at rest is approximately 0.8 s. It is the periodic repetition of a high outflow and no outflow which in turn leads to flow and pressure pulsations in the arteries. From the ascending aorta blood is pumped through the arteries and arterioles into the capillary network. The arterioles act as control valves through which blood is released into the capillaries. The arterioles have a strong muscular wall capable of both closing the arterioles completely or dilating them severalfold. The purpose is to alter the blood flow into the capillaries in response to the needs of the tissues. The function of the capillaries is to exchange fluid, oxygen, carbon dioxide, nutrients, electrolytes, hormones, and other substances between the blood and the interstitial fluid of the cells or alveolus in case of the pulmonary circuit. This diffusion is achieved through a slow and steady flow through the vast network that the capillaries cover in all organs, muscles and tissues; and it takes place because the capillary walls are permeable to small molecular substances. Since flow through the capillaries has to be steady and slow, another important role of the arteries is to cushion the flow fluctuations resulting from the pulsating ejection from the heart.

Blood is collected from the capillaries by the venules and transported via progressively larger veins into the right atrium and then into the right ventricle. Generally, none of the arterial pulsations are transmitted into the veins. However, it is possible to observe pulsations here as well, but these are either due to heart generated waves passing retrograde towards the periphery or to respiratory fluctuations (O'Rourke et al., 1992). From the right ventricle blood is pumped into the pulmonary circuit where it is oxygenated prior to its return to the left atrium. This part of the circulation works similarly to the systemic circulation. However, there are some differences. The most obvious difference is that the oxygenated blood is found in the veins and the deoxygenated blood in the arteries.

Furthermore, the pressure level in the pulmonary circuit is much lower than in the systemic circuit, see Figure 3.2. The high pressure in the systemic arteries ranges from 80–120 mmHg under normal rest conditions, while pressure in the pulmonary arteries ranges from only 8–25 mmHg. This is opposite in capillaries and veins: In the

	Diameter (cm)	Wall Thickness (mm)	Cross-Sectional Area (cm ²)	Percentage of Blood Volume Contained
Aorta	2.5	2	4.5	2
Arteries	0.4	1	20	8
Arterioles	0.003	0.2	400	1
Capillaries	0.0005	0.01	4500	5
Venules	0.002	0.02	4000	54
Veins	0.5	0.5	40	
Vena Cava	3	1.5	18	

Table 3.1: Lumen diameter, wall thickness, approximate total cross-sectional area, and percentage of blood contained in the given group of arteries. The total volume of blood is not 100% since the table does not account for 12% blood in the heart and 18% in the pulmonary circulation. From Gregg (1966).

pulmonary capillaries and veins pressure drops to 7 mmHg, whereas pressure in the systemic capillaries and veins drops to as little as 0 mmHg.

The blood ejected from the left ventricle into the ascending aorta is called the cardiac output which in an adult at rest is approximately 5 l/min. The blood ejected from the right ventricle into the pulmonary artery is slightly smaller (1–2%) because the oxygenated blood needed to supply the lung tissues is not returned to the right atrium but continues through the lung into the pulmonary veins. However, this blood continues into pulmonary vein and enters the left atrium rather than passing back through the systemic veins into the right atrium.

3.2 Systemic arteries

The systemic arteries consist as described above of the larger arteries, the smaller arteries, and the arterioles, see Figure 3.4. Together, they form a vast network of branching vessels. As seen in Table 3.1 the cross-sectional area increases from 4.5 cm² at the root of the aorta to approximately 400 cm² at the entrance to the arterioles. These numbers should be seen as orders of magnitude because it is impossible to measure the arterioles precisely. Consequently, there is a considerable variation in the tabulated values given in different textbooks of physiology (Guyton, 1991; Gregg, 1966; Caro, Pedley, Schroter and Seed, 1978).

The diameters of blood vessels range over several orders of magnitude. This may be a problem for modeling purposes, but it can be overcome by dividing the arteries into two groups: the larger arteries and the arterioles. This distinction is somewhat arbitrary, because the properties of the vessels change gradually as they become smaller.

Seen from a mechanical point of view the distinction makes sense because blood flow in the arteries and the arterioles are significantly different. This can be explained in terms of the fluid mechanical characterization of the flow: If the flow has a Reynolds number significantly larger than one it is dominated by inertia and if it is much smaller

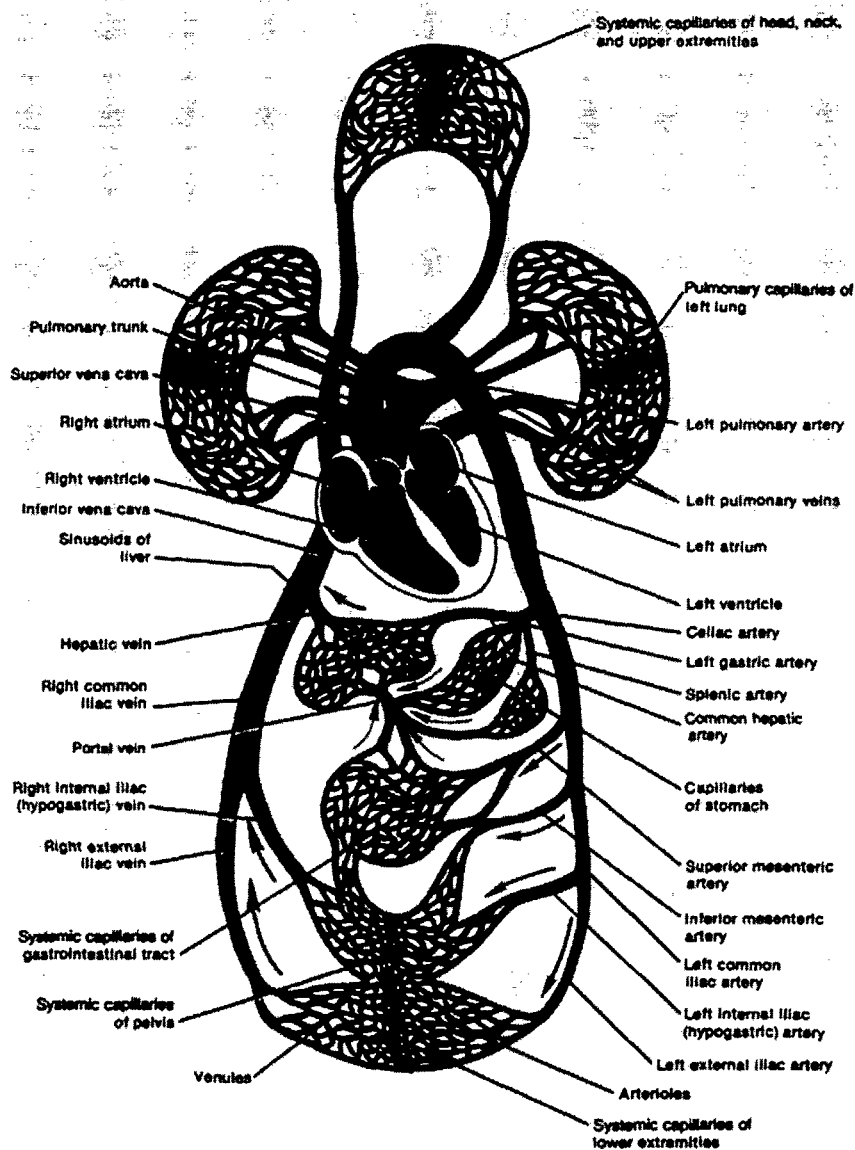


Figure 3.1: The circulatory system. From Tortora and Anagnostakos (1990).

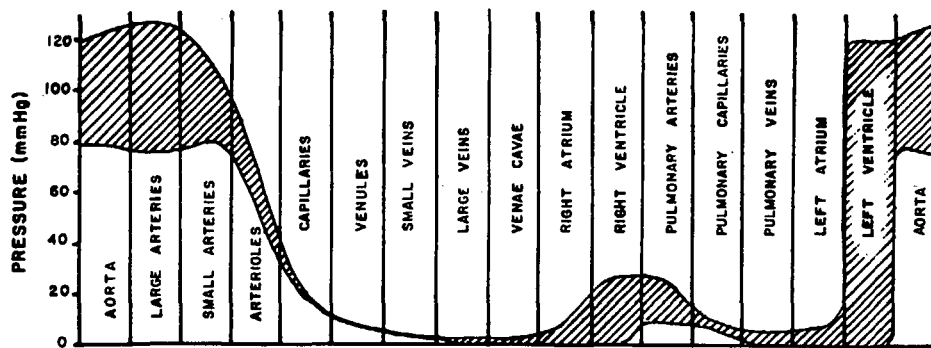


Figure 3.2: Pressure levels in the cardiovascular circulation. From Noordergraaf (1978).

than one it is dominated by viscosity. In case of blood flow the Reynolds number drops below one when the vessels diameter becomes less than $100\ \mu\text{m}$ (Caro et al., 1978). This corresponds to the diameter of the larger arterioles they have a diameter of $50\text{--}100\ \mu\text{m}$. The diameter of the arterioles decreases by progressive bifurcations until at the level of the origin of the met-arterioles where the diameter is approximately $30\ \mu\text{m}$. This is the diameter shown in Table 3.1. Furthermore, there is a functional difference between the two types of arteries. The purpose of the larger arteries is to distribute blood to the different organs and tissues, while the role of the smaller arteries and arterioles is to distribute blood (and, in the case of the arterioles, to control its distribution) within those organs and tissues.

The arteries and larger arterioles can all be modeled as sophisticated bifurcating trees. We will henceforth refer to this as the arterial tree. However, the smaller arterioles (sometimes called the met-arterioles (Caro et al., 1978)) do not have a bifurcating tree structure since multiple branches and loops often occur.

The order of the arterial tree is large. Assume an arteriolar diameter of $30\ \mu\text{m}$ and a total cross-sectional area of $400\ \text{cm}^2$, as shown in Table 3.1. If we then construct a binary tree consisting of the aorta, the arteries, and the larger arterioles it will have 26 generations. Even if we do not take the arterioles into account and only consider the larger and smaller arteries, i.e. those with a diameter larger than $100\ \mu\text{m}$ (corresponding to $40\ \text{cm}^2$) then the tree will have as much as 19 generations. Such a tree cannot be depicted but the tree shown in Figure 3.3, where only the larger and a few of the smaller arteries are shown, is still rather complex.

So far we have discussed the geometrical properties of the vessels, but in order to find out how to model flow in the systemic arteries we also need to investigate the composition of the blood and the arterial walls.

3.2.1 The arterial wall

The arterial wall is composed of variable amounts of elastic fibers and smooth muscles enabling it to dilate when the pulse wave propagates along an artery. It is not purely elastic but exhibits some viscoelastic behavior. To a first approximation arteries are circular vessels tapering along their length. Arteries can be subdivided into the following three groups according to their elastic behavior:

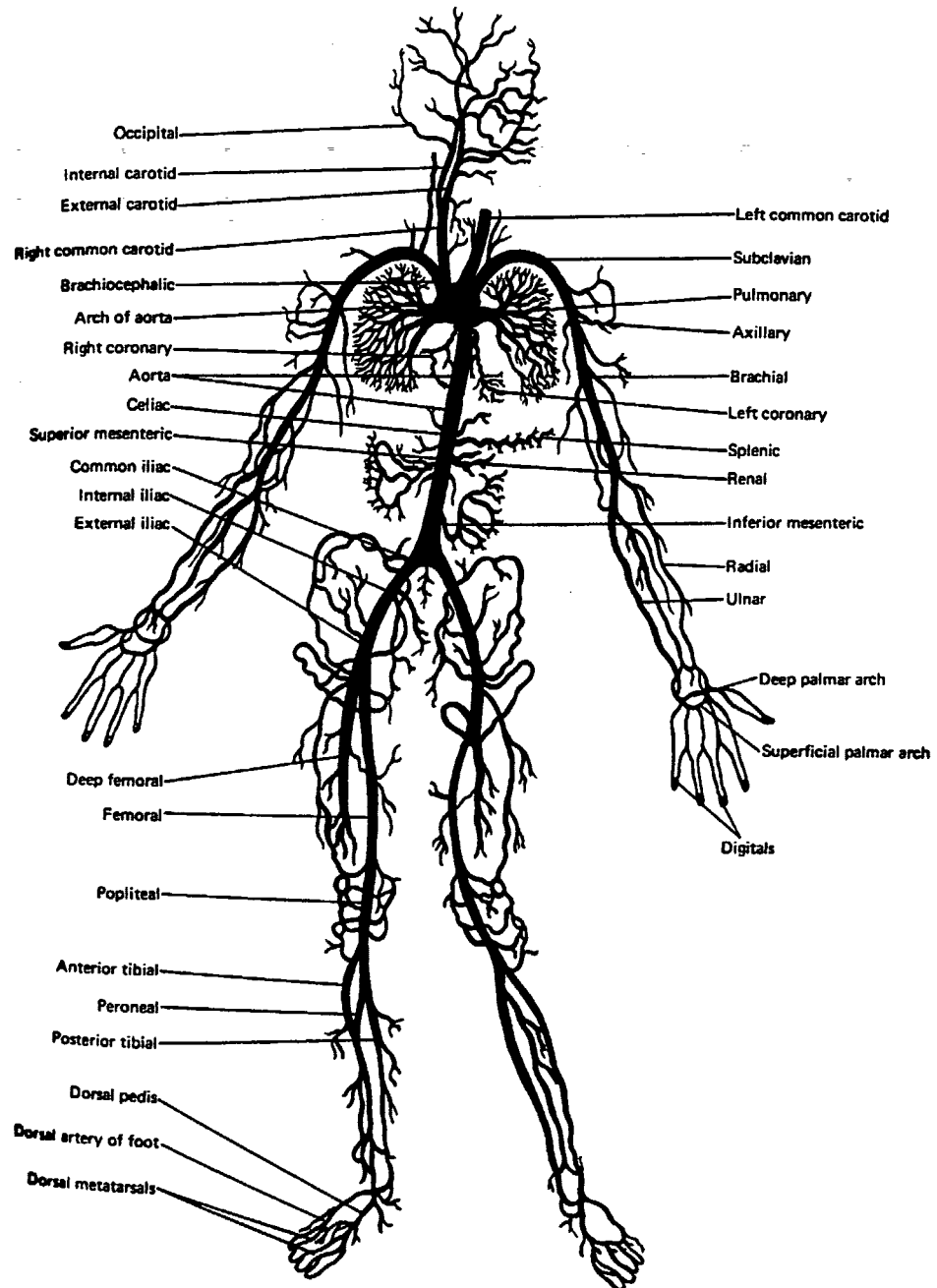


Figure 3.3: The arterial tree. From Solomon, Smidt and Adragna (1990).

- Elastic arteries which comprise the major distribution vessels, such as the aorta, the common carotid arteries, or the subclavian arteries.
- Muscular arteries (see Figure 3.5) comprise the main distributing branches of the arterial tree, such as the radial or femoral arteries.
- Arterioles (see Figure 3.6).

The transition in structure and function between the three arterial types is gradual. Generally, the amount of elastic tissue decreases as the vessels become smaller and at the same time smooth muscle component becomes more prominent (Wheater, Burkitt and Daniels, 1979). Hence, the arteries become markedly stiffer with increased distance from the heart. The parameters characterizing the elastic properties are Young's modulus, which increases away from the heart, and the relative wall thickness which is constant for the larger arteries, but increases for the smaller arteries and arterioles. The arterial wall is composed of three layers characterized by their predominant structure and cell types.

- The internal layer, the tunica intima, is composed of an endothelial layer and an outer elastic laminar layer.

The endothelial layer comprises an inner layer consisting of a single layer of endothelial cells and an outer sub-endothelial layer. The single cell endothelial layer is present as a border to all surfaces that come in contact with the blood. It is rather fragile and is easily damaged e.g. by excessive shear rates, however, it also easily regenerates. The sub-endothelial layer contains a few collagen generating cells and collagen fibers.

The elastic laminar layer consists of branching elastic fibers. It is particularly well defined in the smaller arteries where it forms a clear boundary to the middle layer.

- The middle layer, the tunica media, is the thickest layer in the wall. It is also the layer which has the greatest variation in structure and properties in the different regions of the circulation, and it is the transitions in the structure of this layer which has given rise to the partition above in elastic and muscular arteries.

The tunica media of the elastic arteries is made of multiple concentric layers of elastic tissue separated by thin layers of connective tissue, collagen fibers and sparse smooth muscle cells organized in a longitudinal way forming cross-links to the successive elastic layers. For more details see Caro et al. (1978). In the corresponding layer of the muscular arteries, elastic tissue is reduced and the smooth muscle cells are dominant and oriented circumferentially in spiral structures.

- The external layer, the tunica adventitia, can in some places be as thick or even thicker than the tunica media, however, it is less prominent microscopically. It is composed of loose connective tissues and relative sparse elastin and collagen fibers running in a predominantly longitudinal direction. The boundary with the surrounding tissue is often not well defined.

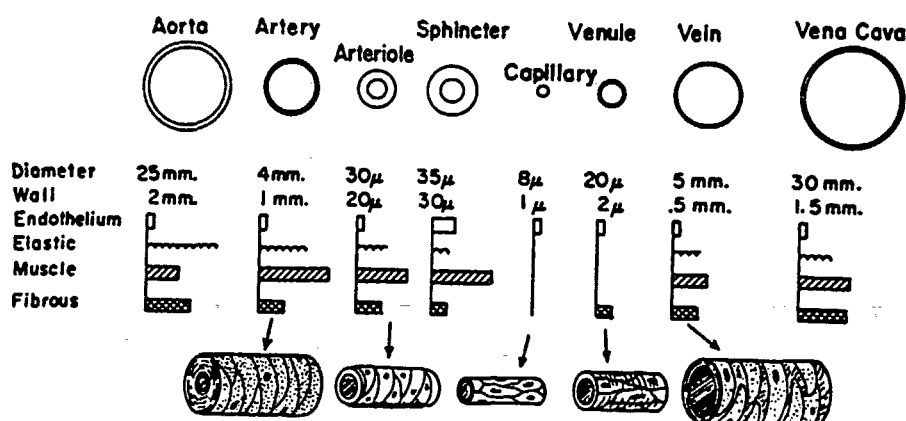


Figure 3.4: A cross-section of an artery and the relative contents of the various layers of tissue in the circulatory system. From Li (1987).

In Figure 3.4 the various layers of the arteries are shown including the order of magnitude of the various vessels. The walls of arteries larger than about one mm in diameter have their own nutrient blood vessels, the vasa vasorum. They originate either from the parent artery or from a neighboring one and break up into capillary networks, which supply the tunica adventitia and part of the tunica media. The tunica intima and the innermost layers of the tunica media are primarily supplied by transport of materials from the arterial lumen. Due to the complex composition of the arterial walls the distensibility or elastic properties of the arteries are non-linear and therefore not easily described by a mathematical model.

In order to investigate the mechanical properties of blood flow an important input parameter is the thickness of the arterial wall. It is hard to describe the wall thickness precisely. The arteries are not loose vessels inserted in the body but attached to the surrounding tissue, and the outer layer of the arterial wall, the tunica adventitia, usually merges gradually into the surrounding tissue. We will, however, attempt to do it anyway. Generally, the thickness of the arterial wall varies considerably throughout the circulation, as can be seen in Tables 3.1 and 3.2. Instead, one often studies the thickness of the wall relative to the diameter of the vessel. For the larger arteries the ratio is approximately constant. For the smaller arteries this is no longer true. Even though the wall thickness decreases, the wall thickness to radius ratio increases. The increase continues until the bottom of the arterioles where the external diameter are almost twice that of the lumen even when the smooth muscle is relaxed. Finally, thickness of the vessel wall in the capillaries is very similar in all mammalian species. This is due to the fact that the wall has to be thin and permeable in order for diffusion of molecules to occur. These have a fixed size independent on the species in question and require a certain structure of the wall.

In the dissertation we concentrate on modeling a normal young adult at rest. However, it should be mentioned that the wall thickness of the arteries changes significantly with age along with the change of the elastic properties of the vessels. Aging causes elastic elements in the wall to degenerate. The vessels may become calcified and the collagen fibers increase in number, both replacing muscle-cells and proliferating in

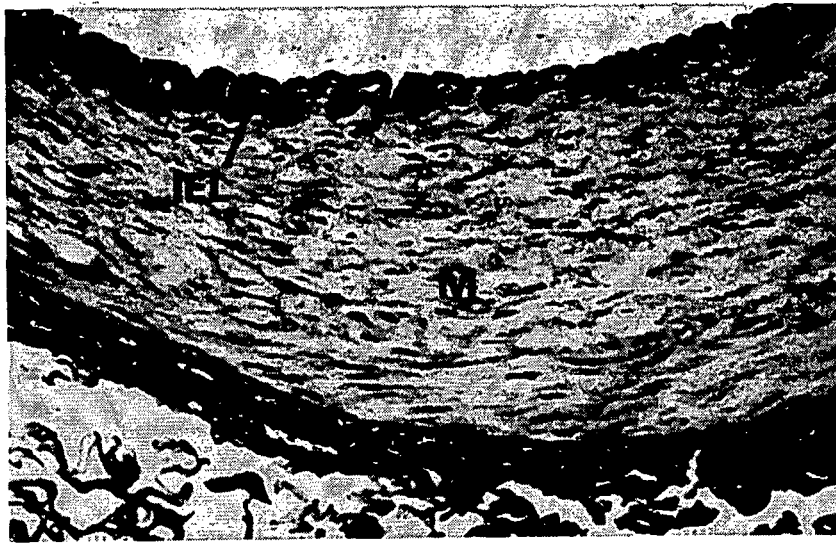


Figure 3.5: The wall of a muscular artery. The internal layer mainly consist of a thin elastic sheet (stained black), it is marked with IEL. The middle layer, the tunica media (marked with an M) is composed mainly of smooth muscle (stained white). The outermost layer, the tunica adventitia is composed of a diffusive external elastic lamina. Note finally that collagen fibers (stained gray) are scattered throughout the vessel wall. From Wheater et al. (1979).

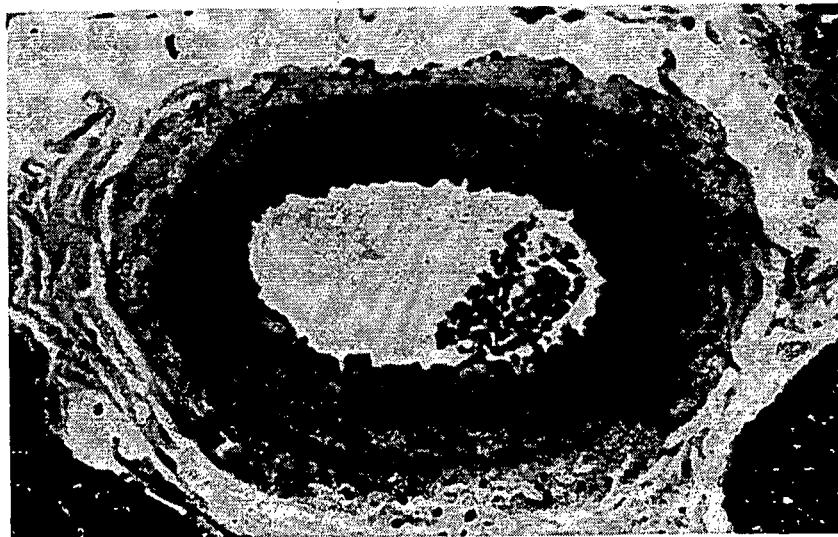


Figure 3.6: A large arteriole. The arterioles have a very thin internal layer which comprises a endothelial lining, little collagenous connective tissue and a thin but distinct, internal elastic lamina. The middle layer is almost entirely composed of smooth muscle cells organized in concentric circles. The outermost layer the tunica adventitia is very thick and merges with the surrounding connective tissue. From Wheater et al. (1979).

other parts of the wall. The overall effect is that the diameter of the vessel increases, and the wall becomes thick and much less distensible.

In Table 3.2, taken from Caro et al. (1978), typical values for the various physiological parameters are presented. These are based on measurements from dogs but most of them apply approximately to humans as well.

3.2.2 Blood

Blood consists of plasma with red (erythrocytes) and white (leucocytes) blood cells, and platelets (thrombocytes) in suspension. The primary function of erythrocytes is to transport oxygen and carbon dioxide. Leucocytes constitute an important part of the defense and immune systems of the body. Thrombocytes are a vital component of the blood clotting mechanism. Erythrocytes comprise approximately 40–45% of the blood in the larger arteries, this percentage is called the hematocrit. Normally erythrocytes are biconcave discs with a mean diameter of 6–8 μm and a maximal thickness of 1.9 μm . The average volume of an erythrocyte cell is approximately $83 (\mu\text{m})^3$ and the number of erythrocytes per mm^3 is approximately $4\text{--}6 \times 10^6$. Leucocytes, which are roughly spherical, are usually larger than the red blood cells ranging from 6–17 μm , however, their number is small, approximately $4\text{--}11 \times 10^3$ per mm^3 in a normal adult. Thrombocytes are, however, much smaller than both erythrocytes and leucocytes. They are rounded or oval and have a mean diameter of approximately 2–3 μm , so even though there are approximately $2.5\text{--}5 \times 10^5$ per mm^3 , their total volume is small. Together leucocytes and thrombocytes have a volume concentration of only approximately one percent. Furthermore, it should be noticed that these cells are all very deformable, with the erythrocytes being the most deformable of them all. Significant deformations occur when the cells are passing through the capillaries. However, the cell membranes do not rupture because the cells have a cytoskeleton that supports their shape.

Therefore, the mechanical properties of blood should be studied by analyzing a liquid with a suspension of flexible particles. By definition, a liquid is said to be Newtonian if the coefficient of viscosity is constant at all rates of shear. This applies to most homogeneous liquids including blood plasma, but in the case of a liquid with a suspension of particles the mechanical behavior can deviate such that the liquid becomes non-Newtonian. These deviations become particularly significant when the particle size becomes appreciably large in comparison with the dimension of the channel in which the fluid is flowing. This is the case of the vessels in the micro-circulation.

Consider a suspension where the suspending fluid has a Newtonian behavior. Then if the suspended particles are spherical and non-settling, that is, if they have the same density as the suspending fluid, then in any motion the shear stress will be proportional to the rate of shear and the suspension will behave as a Newtonian fluid. This applies as long as the concentration of spheres is low, less than 30 percent. This is a result of experiments performed under steady-state conditions with suspensions of rigid spheres (Caro et al., 1978). These experiments showed that the viscosity of the suspension, defined as the viscosity when measured in a particular viscometer under particular conditions, was independent of the shear-rate for volume concentrations of suspended spheres as high as 30 percent. However, if the suspended particles are not spherical or are deformable in any way, then the shear stress is not proportional to the shear-rate

Normal values for canine cardiovascular parameters. An approximate average value, and then the range, is given where possible.

Site	Ascending aorta	Descending aorta	Abdominal aorta	Femoral artery	Carotid artery	Arteriole	Capillary	Venule	Inferior vena cava	Main pulmonary artery
Internal diameter d_i	cm 1.5 1.0-2.4	1.3 0.8-1.8	0.9 0.5-1.2	0.4 0.2-0.8	0.5 0.2-0.8	0.005 0.001-0.008	0.0006 0.0004-0.0008	0.004 0.001-0.0075	1.0 0.6-1.5	1.7 1.0-2.0
Wall thickness h	cm 0.065 0.05-0.08	0.065 0.05-0.08	0.05 0.04-0.06	0.04 0.02-0.06	0.03 0.02-0.04	0.002 0.001-0.003	0.0001 0.0001-0.0002	0.0002 0.0001-0.0002	0.015 0.01-0.02	0.02 0.01-0.03
h/d_i	0.07 0.055-0.084	0.07 0.055-0.084	0.06 0.04-0.09	0.07 0.055-0.11	0.08 0.053-0.095	0.4 0.15-0.2	0.17 0.06-0.1	0.05 0.01-0.2	0.015 0.01-0.02	0.01 0.01-0.03
Length	cm 5	20	15	10	15	0.15 0.1-0.2	0.06 0.02-0.1	0.15 0.1-0.2	30 20-40	3.5 3-4
Approximate cross-sectional area	cm ² 2	1.3	0.6	0.2	0.2	2 × 10 ⁻³	3 × 10 ⁻⁷	2 × 10 ⁻⁵	0.8	2.3
Total vascular cross-sectional area at each level	cm ² 2	2	2	3	3	125	600	570	3.0	2.3
Peak blood velocity	cm s ⁻¹ 120	105	55	100	100	0.75 0.5-1.0	0.07 0.02-0.17	0.35 0.2-0.5	25 15-40	70
Mean blood velocity	cm s ⁻¹ 40-290	25-250	50-60	100-120	100-120					
Reynolds number (peak)	cm s ⁻¹ 20	20	15	10	10					
α (heart rate 2 Hz)	10-40	10-40	8-20	10-15	10-15					
	4500	3400	1250	1000	1000					
	13.2	11.5	8	3.5	4.4					
Calculated wave-speed c_0	cm s ⁻¹ 580	770	770	840	850					
Measured wave-speed c	cm s ⁻¹ 500	700	700	900	800					
	400-600	600-750	800-1030	800-1100	600-1100					
Young's modulus E	Nm ⁻² × 10 ⁵ 3-6	4.8	10	10	9					
		3-6	9-11	9-12	7-11					

(From C. G. Caro, T. J. Pedley, and W. A. Seed (1974). 'Mechanics of the circulation', Chapter 1 of *Cardiovascular physiology* (ed. A. C. Guyton). Medical and Technical Publishers, London.)

Table 3.2: Physiological data for the various parameters in the circulatory system. From Caro et al. (1978).

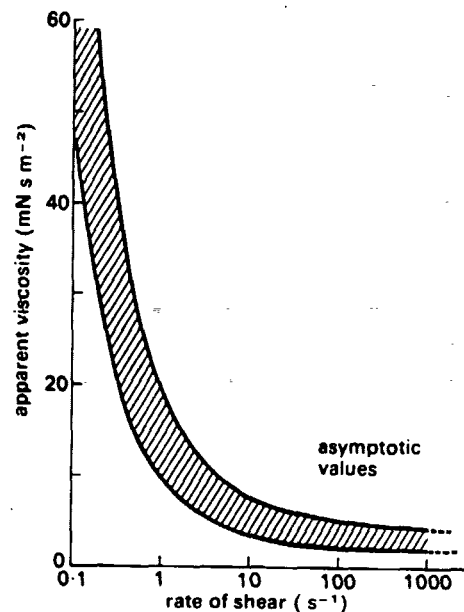


Figure 3.7: The apparent viscosity as a function of the shear rate in human blood. When the shear rate is about 1000 s^{-1} the non-Newtonian behaviour becomes insignificant, and the apparent viscosity approaches an asymptotic value ranging from $0.03\text{--}0.04 \text{ g}/(\text{cm s})$ ($\approx 3\text{--}4 \text{ mN s m}^{-2}$). From Caro et al. (1978).

unless the concentration is much less than 30 percent.

Blood does not consist of rigid spheres and the volume fraction of erythrocytes is about 40 percent. Thus it should be expected that the behavior of blood is non-Newtonian. It has been shown that human blood is Newtonian at all rates of shear for hematocrit up to about 12 percent, although blood has a higher viscosity than plasma (Caro et al., 1978). However, as the hematocrit is raised, not only does the viscosity of the suspension increase, but non-Newtonian behavior is observed, detectable first at very low rates of shear.

Since the hematocrit in arteries usually is higher than 12 percent, blood might be expected to have a non-Newtonian behavior. Results based on several studies with human blood, however, show that viscosity is independent of shear rate when the shear rate is high. With a reduction of shear-rate the apparent viscosity increases slowly, until at a shear-rate less than 1 s^{-1} where it rises extremely steeply, see Figure 3.7 (Caro et al., 1978). The shear stresses can be divided into two groups according to the effect of the shear rate:

- At low shear rates, the apparent viscosity increases markedly. The reason is that a tangled network of aggregated cell structures (Rouleaux) can be formed. If blood is subjected to shear stress below a critical value, then aggregated structures form without the blood flowing, and as a result they exhibit a yield stress. This is, however, only present if the hematocrit is high. If the hematocrit falls below a critical value there are not enough cells to produce the aggregated structures and no yield stresses will be found.

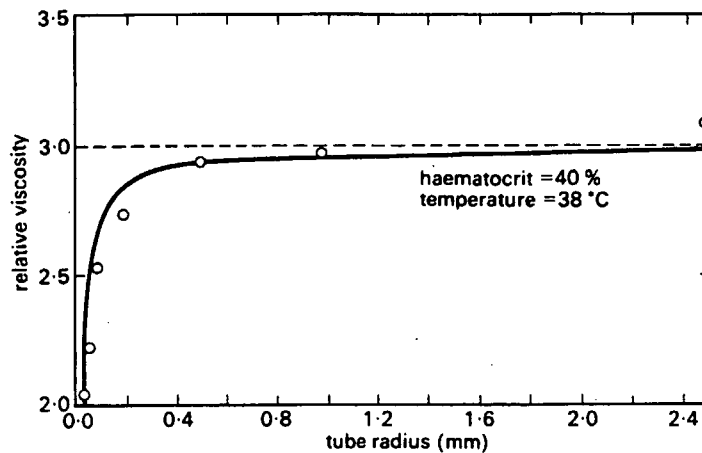


Figure 3.8: The relationship between the apparent viscosity of blood relative to the plasma viscosity and the diameter of the tube in which the blood is flowing. The tube is assumed to be cylindrical. From Caro et al. (1978).

- At high shear rates, the apparent viscosity in small vessels is lower than it is in the larger vessels. The progressive diminution with the size of the vessels becomes detectable when the internal diameter of the vessels becomes less than one mm and becomes marked in tubes with a diameter of 100–200 μm . This is known as the Fåhræus and Lindqvist effect (Caro et al., 1978). Experiments were performed at high enough shear rates for the erythrocytes not to aggregate. It was found that the viscosity was approximately constant in vessels larger than 0.1 cm, but when the radius dropped below that, there was a substantial decrease in viscosity. This is shown in Figure 3.8

In the large vessels it is a reasonable assumption to regard the blood viscosity as constant, both because the vessel diameters are large compared with the individual cell diameters, and because shear rates are high enough for viscosity to be independent of them (Caro et al., 1978). Hence, the non-Newtonian behavior becomes insignificant and blood can be considered as a Newtonian fluid. Measurements of the apparent viscosity show that it ranges from 0.03–0.04 g/(cm s).

In the micro-circulation, it is no longer possible to think of the blood as a homogeneous fluid; it is essential to treat it as a suspension of red cells in plasma. The reason being that even the largest vessels of the micro-circulation are only approximately 15 cells in diameters. Also, as discussed earlier in this chapter, viscosity starts dominating leading to very low Reynolds numbers; typical Reynolds numbers in 100 μm arteries are about 0.5.

Summing up we can conclude that blood is generally a non-Newtonian fluid, but it is reasonable to regard it as a Newtonian fluid when modeling arteries with a diameter larger than 100 μm . For the very small vessels it is not easy to make any conclusions because some of the effects here tend to decrease the viscosity the Fåhræus-Lindqvist effect, and others tend to increase the viscosity. The latter is due to a small flow which increase the viscosity significantly as well as the fact that cells often become stuck at constrictions in small vessels, this happens, however, most often in the capillaries.

However, the result is that it is reasonable to assume that the overall viscous effects in the small vessels are approximately equivalent to those that occur in the larger vessels (Guyton, 1991).

Chapter 4

Model of flow and pressure in the systemic arteries

Modeling of blood flow and pressure has been studied intensively over the years, and as discussed in the previous chapters the shape of pressure and flow profiles can have diagnostic significance.

Good examples are the old studies by Lax, Feinberg and Cohen (1956), Lax and Feinberg (1959), and Dawber, Thomas and McNamara (1973). They suggest that changes of shape of the dicrotic wave are results of changes in the elasticity of the vascular walls and the peripheral resistance. This conclusion stems from observations showing that the dicrotic wave is either diminished or totally absent in patients with diabetes, hypertension, atherosclerosis, or in elderly people. Furthermore, observations by Jensen (1994–1998) have shown that a proximal stenosis, e.g. at the iliac bifurcation, can lead to amplification of the dicrotic wave simply because the partly or fully occluded artery behaves as a high peripheral resistance giving an early and more prominent reflection of the pulse wave. Hence, these studies suggest that regular observations of the changes in the shape of the pulse wave can be used for early detection of some vascular diseases.

Consequently, the purpose of this study is to investigate the shape of the arterial pulse from mathematical models based on physiological principles such that it becomes possible to reproduce the true physiological behavior of the arteries. If one wants a precise model it is necessary to set up a three dimensional model including: the exact geometrical structure of all vessels, the compliance of the walls, and the non-Newtonian fluid equations. This is not computationally feasible. The other extreme would be to derive a model of the entire circulation based on a lumped element model. While such a model is adequate when studying relations between cardiac output and the peripheral load it can not imitate the wave propagation effects unless a large number of elements are used. Finally, the relatively small number of elements also have the disadvantage that the high frequency behavior of the system can not be captured well (Raines, Jaffrin and Shapiro, 1974). The lumped models can, however, be expanded by including a large number of elements, see e.g. Karlson (1995), but they approximate a true one-dimensional model, and then it would be better to develop an explicit one-dimensional model. The advantage of the one-dimensional model is the ability to capture the wave propagation effects, see e.g. Anliker, Rockwell and Ogden (1971), Raines et al. (1974), Stettler, Niederer and Anliker (1981), Stergiopoulos, Young and

Rogge (1992), or Olufsen and Ottesen (1995a). However, a one-dimensional model of the entire systemic arterial tree, as shown in Figure 3.3, is too large for computational purposes. It is not feasible to construct a model that comprises everything ranging from the aorta to the capillaries. Therefore, the tree has to be truncated in some way and this truncation is the main topic for the dissertation. Besides the computational difficulties in making such a large model there is also another problem: Not enough detailed data are available for the smaller arteries (Raines et al., 1974). It is possible to measure the dimensions of the smaller arteries from casts, but because of their large number it would be practically impossible to measure all of them. Based on the material presented in this chapter we state the following hypothesis:

Hypothesis:

We put forward a mathematical model based entirely on fundamental physiological principles, which predicts blood flow and pressure at any site along the systemic arteries. It is suggested that the model can be divided into two parts: one comprising the larger arteries and one comprising the smaller arteries, linked together through an outflow boundary condition at the terminals of the larger arteries.

- *Blood flow and pressure in the larger arteries are predicted from a non-linear one-dimensional model, based on the incompressible Navier-Stokes equations for a Newtonian fluid in an elastic tube.*
- *The inflow boundary condition is modeled using a function matching the outflow from the left ventricle into the aorta, while the outflow boundary condition is predicted from a dynamic impedance applied at all terminals of the larger arteries. This impedance will be found from a separate model of the smaller arteries.*
- *Blood flow and pressure in the smaller arteries are predicted from a linear one-dimensional viscous model (a wave-equation) which is derived from linearization of the incompressible axisymmetric Navier-Stokes equations for Newtonian fluid in a tube.*

We claim that such a model is adequate for prediction of blood flow and pressure in human systemic arteries.

The model will be validated by comparison with both human data and other existing models using other (and simpler) boundary conditions, a pure resistor boundary condition (Anliker et al., 1971) or a three-element Windkessel boundary condition (Raines et al., 1974; Stergiopoulos et al., 1992). Furthermore, we will investigate the feasibility of this model as a reference model for the lumped cardiovascular model which is part of the SIMA anesthesia simulator and described in Olufsen et al. (1994). We will investigate this problem by:

- Setting up geometrical models of the larger and the smaller arteries, respectively.
- Deriving and solving numerically the fluid dynamic equations for the larger and the smaller arteries, coupled together.

- Comparing the results with other models and measured data, and analyzing the model response to changes, within physiological range of the involved parameters.

Chapter 5

Structure of the larger arteries

The purpose of the systemic arteries is to supply all organs, tissues, and muscles of the body with oxygenated blood and nutrients. The arteries are organized in a sophisticated network that covers the entire organism. This is denoted the arterial tree and it is characterized by:

- Geometrical properties of the individual vessels; their diameter and lengths.
- Structural properties of the vessels; the wall thickness and Young's modulus.

5.1 Geometrical properties of the larger arteries

The larger systemic arteries are organized in a bifurcating tree in which the individual vessels are tapering along their length. At each bifurcation, the cross-sectional area at the top of each of the daughter vessel is smaller than that of the bottom of the parent vessel. However, the combined cross-sectional area of the daughter arteries is larger than that of the parent artery.

Several papers describe the geometry of the larger arteries, many of them date back to the study by Westerhof, Bosman, DeVries and Noordergraaf (1969) which presents data for a standard man. Examples are the studies by Stergiopoulos et al. (1992) and Segers, Dubois, DeWachter and Verdonck (1997). The first presents data to be used in a mathematical model while the second presents data to be used in a physical latex tube model. In addition to these, data are also presented in Anliker, Stettler, Niederer and Holenstein (1978), Stettler et al. (1981), McDonald (1974), Li (1987), and Schaaf and Abbrecht (1972). Most of these data are estimated for use in mathematical models of the human systemic arteries, but the data in McDonald (1974) and Li (1987) are from dogs. Generally, the dimensions presented in the papers above vary significantly across individuals. This reflects the large variations found in humans where it is not unusual to see deviations of more than 50 percent from the mean values (Jensen, 1994–1998). The radius, r , of the tapering arteries follow an exponential curve of the form

$$r(x) = r_{top} \exp(-kx) \quad (5.1)$$

where r_{top} is the mean proximal radius, k is the tapering factor, and x is the location along the artery, see e.g. Anliker et al. (1971), Cafilisch, Majda, Peskin and Strumolo

Artery	k (cm ⁻¹)
Abdominal aorta	0.027 ± 0.007
Iliac artery	0.021 ± 0.005
Femoral artery	0.018 ± 0.007
Carotid artery	0.008 ± 0.004

Table 5.1: The exponential tapering factors for a number of arteries. From Li (1987).

(1980), Werff (1974), or Li (1987). In Li (1987) tapering factors for a number of arteries are listed, see Table 5.1. These data are from dogs so we cannot assume that the tapering factors for humans are the same. Therefore, we have chosen to model the tapering according to (5.1) and with the tapering factor $k = \log(r_{bot}/r_{top})/L$ found from measured geometrical values for each vessel. Hence, the radius is given by

$$r(x) = r_{top} \exp \left(\log \left(\frac{r_{bot}}{r_{top}} \right) \frac{x}{L} \right) = r_{top} \left(\frac{r_{bot}}{r_{top}} \right)^{x/L} \quad (5.2)$$

where r_{top} , r_{bot} are the top and bottom radii, and L is the length of the vessel. For the aorta $L = 55.75$ cm, $r_{top} = 1.530$ cm, $r_{bot} = 0.540$ cm, giving a tapering factor $k = 0.019$ cm⁻¹. This corresponds well to the data in Table 5.1. Thus, in order to describe the full geometry for the tree of larger arteries, we need data for the proximal and distal radius for each vessel as well as the length of each vessel segment.

The physical latex tube model in Segers et al. (1997) is based on data by Stergiopulos et al. (1992) but with some modifications. We have chosen to base our simulations on these data because they are new and similar to numerous older studies. Hence, we define the larger arteries as those shown in Figure 5.1 with the dimensions presented in Table 5.2. We have rounded all segment lengths to units of 0.25 cm and assumed that:

- The aorta, iliac and femoral, subclavian and brachial arteries taper continuously with a constant exponential rate. This is a contradiction to the data presented in Segers et al. (1997), but we find it more physiological to have these vessels taper gradually.
- The body is symmetric, in the sense that those vessels existing in both the left and the right side of the body have the same dimensions. Some examples are the arm, from the subclavian artery and down, the renal arteries, and the iliac and femoral arteries. The latter example has a computational advantage because the bifurcation is symmetric, i.e. the inflow into the daughter arteries is identical, $q_p = 2q_d$, where q_p is the flow in the parent vessel and q_d is the flow in the daughter vessels. Hence, we only need to calculate flow and pressure for one leg. A similar approach can not be used for the subclavian and renal arteries because, even though their dimensions are the same, they do not have the same inflow. Hence, both the right and left parts must be computed separately.
- The coronary arteries each with cross-sectional area A_1 and length L can be lumped into one branch with length L and cross-sectional area $A_2 = \sqrt{2}A_1$.

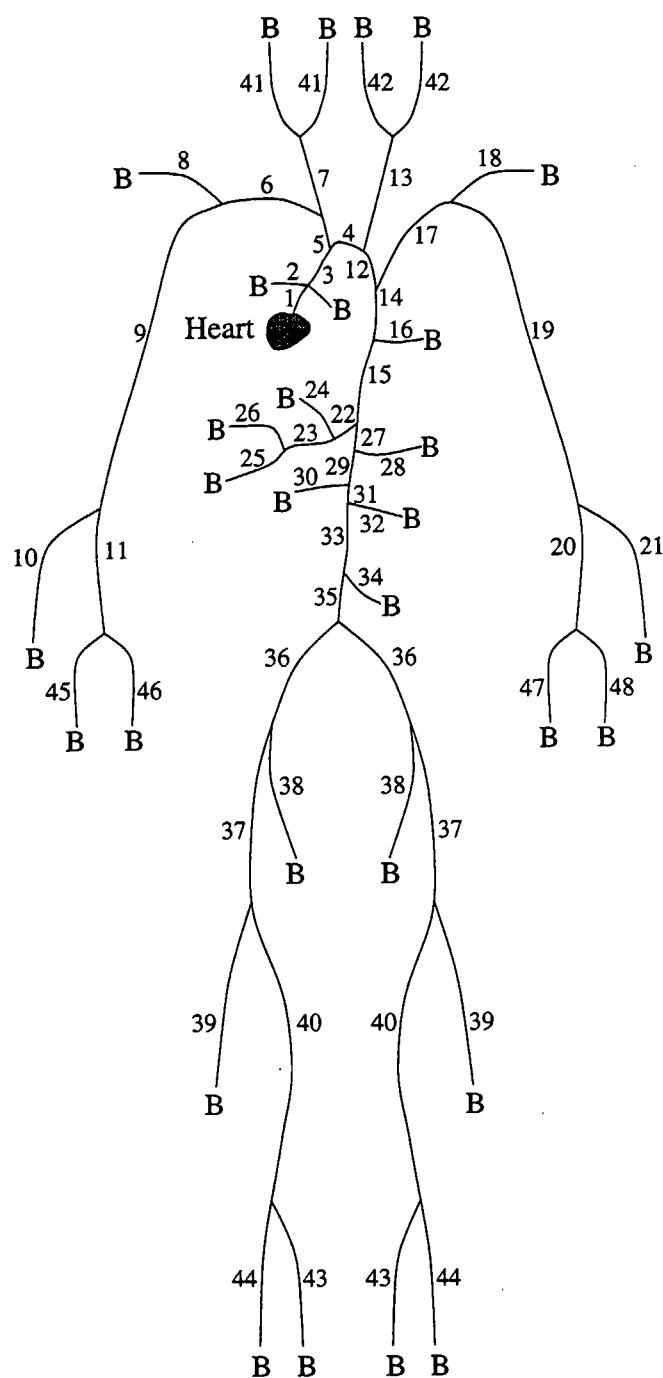


Figure 5.1: The larger systemic arteries. The numbers on the figure refer to Table 5.2. Branches marked by the same numbers are identical and thus only modeled once. The letters mark the terminals of the arteries, i.e. the blood flows into the arteries at the vessel marked with an **A**, and it flows out at the vessels marked with **B**.

#	Artery	L (cm)	r_{top} (cm)	r_{bot} (cm)
1	Ascending aorta	1.00	1.525	1.502
3	Ascending aorta	3.00	1.502	1.420
4	Aortic arch	3.00	1.420	1.342
12	Aortic arch	4.00	1.342	1.246
14	Thoracic aorta	5.50	1.246	1.124
15	Thoracic aorta	10.50	1.124	0.924
27	Abdominal aorta	5.25	0.924	0.838
29	Abdominal aorta	1.50	0.838	0.814
31	Abdominal aorta	1.50	0.814	0.792
33	Abdominal aorta	12.50	0.792	0.627
35	Abdominal aorta	8.00	0.627	0.550
36	External iliac	5.75	0.400	0.370
37	Femoral	14.50	0.370	0.314
40	Femoral	44.25	0.314	0.200
38	Internal iliac	4.50	0.200	0.200
39	Deep femoral	11.25	0.200	0.200
43, 44	Post. + ant. tibial	32.00	0.125	0.125
2	Coronaries	10.00	0.350	0.300
5	Brachiocephalic	3.50	0.950	0.700
6, 17	R. + L. Subclavian	3.50	0.425	0.407
9, 19	R. + L. Brachial	39.75	0.407	0.250
10, 21	R. + L. Radial	22.00	0.175	0.175
11, 20	R. + L. Ulnar	22.25	0.175	0.175
46, 47	R. + L. Ulnar	17.00	0.200	0.200
45, 48	R. + L. Interosseus	7.00	0.100	0.100
8, 18	R. + L. Vertebral	13.50	0.200	0.200
7	R. com. carotid	16.75	0.525	0.400
13	L. com. carotid	19.25	0.525	0.400
41, 42	Ext. + int. carotid	15.75	0.275	0.200
16	Intercostals	7.25	0.630	0.500
28	Superior mesenteric	5.00	0.400	0.350
22	Celiac axis	2.00	0.350	0.300
23	Hepatic	2.00	0.300	0.250
24	Hepatic	6.50	0.275	0.250
25	Gastric	5.75	0.175	0.150
26	Splenic	5.50	0.200	0.200
30, 32	R. + L. Renal	3.00	0.275	0.275
34	Inferior mesenteric	3.75	0.200	0.175

Table 5.2: Data for the length, top and bottom radii for the larger arteries. The numbering in the left column refer to the numbers shown in Figure 5.1.

This relation is found by letting the flow in the lumped branch be twice the flow in each of the coronary arteries, i.e. by letting $q_2 = 2q_1$, and assuming Poisseuille flow. The reason for this is that the coronary arteries branch off the ascending aorta very close to each other, and hence it is inconvenient to insert a separate piece of artery between the two branches. The same approach is applied to the intercostal arteries. However, in this case it is not because they are close to each other but because it reduces the number of arterial segments. There are approximately 10–15 intercostal arteries which are all very small, and modeling each of them separately would increase the computational time considerably. However, it could easily be done if necessary. An alternative approach for modeling the intercostal arteries could be to include a continuous outflow function along the thoracic aorta, see e.g. Anliker et al. (1971) or Stettler et al. (1981). In fact our derivation in Chapter 7 of the fluid dynamical equations allows for this possibility.

- The renal arteries are modeled as two separate branches. They could be lumped together using the same approach as for the coronary arteries because they are also situated very close to each other. However, we have modeled them separately because of the magnitude of their outflow. In order for the numerical computations to converge and for the flow to be fully developed, we have increased the distance between these arteries, even though it is somewhat larger than in the natural life.
- The tibial and interosseous arteries have been neglected in most of our computations. We did this for computational reasons, but it can be justified because the order of magnitude of the flow in these vessels are smaller than that of the other arteries.

5.2 Structural properties of the vessel walls

The arterial wall is composed of several layers consisting of different materials as described in Chapter 3. Mathematically the arterial wall can be described by the volume compliance or the elasticity of the vessels. The volume compliance C can be approximated by

$$C = \frac{dV}{dP} \approx \frac{3A_0 L}{2} \frac{r_0}{Eh} \quad (5.3)$$

where V is the volume of the given segment, P is the pressure, r_0 is the radius, $A_0 = \pi r_0^2$ is the cross-sectional area, L is the length of the artery, E is Young's modulus, and h is the wall thickness. Thus, the elastic properties of the vessels can either be found from the compliance or from Young's modulus. This relation is estimated from (7.17).

In this study we have chosen to describe the elasticity from estimates of Young's modulus, the radius, and the wall thickness. In fact, it is possible to show that there is a connection between Young's modulus, the wall thickness and the vessel radius. This is seen in Figure 5.2 where Eh/r_0 is plotted as a function of r_0 . The data for the

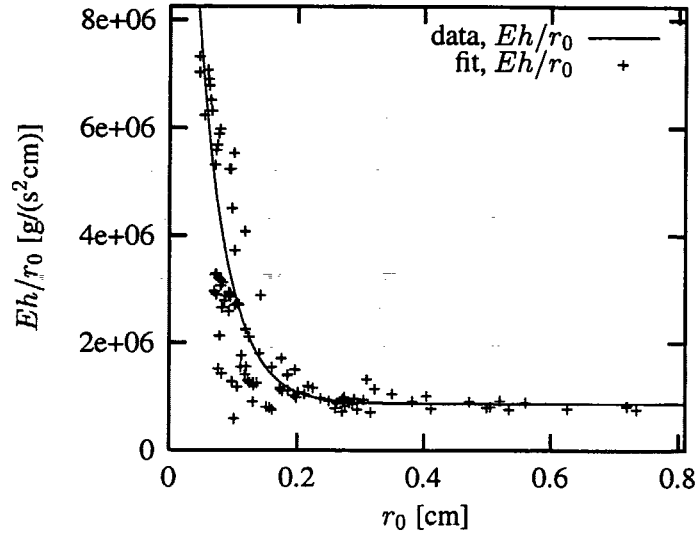


Figure 5.2: Fit to data for Eh/r_0 , where E is Young's modulus, h is the wall thickness and r_0 is the radius. The fitted function has the form $k_1 \exp(k_2 r) + k_3$, where $k_1 = 2.00 \times 10^7 \text{ g/(s}^2\text{cm)}$, $k_2 = -22.53 \text{ cm}^{-1}$, and $k_3 = 8.65 \times 10^5 \text{ g/(s}^2\text{cm)}$. This fit was made using the "fit" function in gnuplot.

figure are as given in Stergiopoulos et al. (1992). However, Stergiopoulos' data gives the volume compliance and are therefore converted to Young's modulus using (5.3). The data for Eh/r_0 are marked with +. Through these points we have empirically fitted a curve of the form

$$\frac{Eh}{r_0} = k_1 \exp(k_2 r_0) + k_3 \quad (5.4)$$

where $k_1 = 2.00 \times 10^7 \text{ g/(s}^2\text{cm)}$, $k_2 = -22.53 \text{ cm}^{-1}$, and $k_3 = 8.65 \times 10^5 \text{ g/(s}^2\text{cm)}$. The discrepancies between the observations and the fitted curve are due to compliance variations throughout the body. This means that two arteries with the same radius may have different compliance, and hence different values for Eh/r_0 , if they belong to different organs.

Chapter 6

Structure of the smaller arteries

The role of the smaller arteries and arterioles is to provide the capillaries of all organs, tissue, and muscles with a sufficient blood supply. The total cross-sectional area of the smaller arterioles in a normal human adult is approximately 400 cm^2 . This should be compared with the total cross-sectional area of the larger arteries which is approximately 20 cm^2 , or with that of the aorta which is approximately 4.5 cm^2 , see Table 3.1. Since the smaller arterioles have a diameter of approximately 0.003 cm the arterial tree, ranging from the aorta to the arterioles, will have approximately 26 generations if we assume that it is binary.

The larger arteries can be modeled as the tree shown in Figure 5.1. According to this, the smaller arteries generally originate 2–3 generations from the aorta, iliac, and femoral arteries, e.g. at the end of the tibial arteries, the internal or external carotids, or the radial arteries. Hence, they have approximately 24 generations. Dealing with such large trees is practically infeasible unless they are structured in some way. However, there is evidence that the smaller arteries are distributed in a structured and optimal way, see e.g. Zamir (1978), Bassingthwaite, Liebovitch and West (1994), or Schreiner and Buxbaum (1993).

These studies mostly comprise two-dimensional models of local areas such as the coronary arteries, but Bassingthwaite et al. (1994) suggest that such models could be generalized to cover any area of small arteries. We have used some of these results to construct a one-dimensional asymmetric structured tree model of the smaller arteries where the radii of the daughter vessels are scaled linearly relative to their parent vessel by factors α and β , i.e.

$$\begin{aligned} r_{d_1} &= \alpha r_p \\ r_{d_2} &= \beta r_p \end{aligned}$$

the subscript p refer to the parent vessel and the subscripts d_1 and d_2 refer to the two daughter vessels, respectively. This is seen in Figure 6.1.

The aim is to construct a tree representing the smaller arteries that can be applied at each of the terminals of the larger arteries, i.e. at the **B**'s in Figure 5.1. The combined model including both larger and smaller arteries looks as shown in Figure 6.2. We have assumed that the arterial tree is binary. Hence, it is only necessary to consider one type of junctions, the bifurcations. While this is not true in general, the majority of

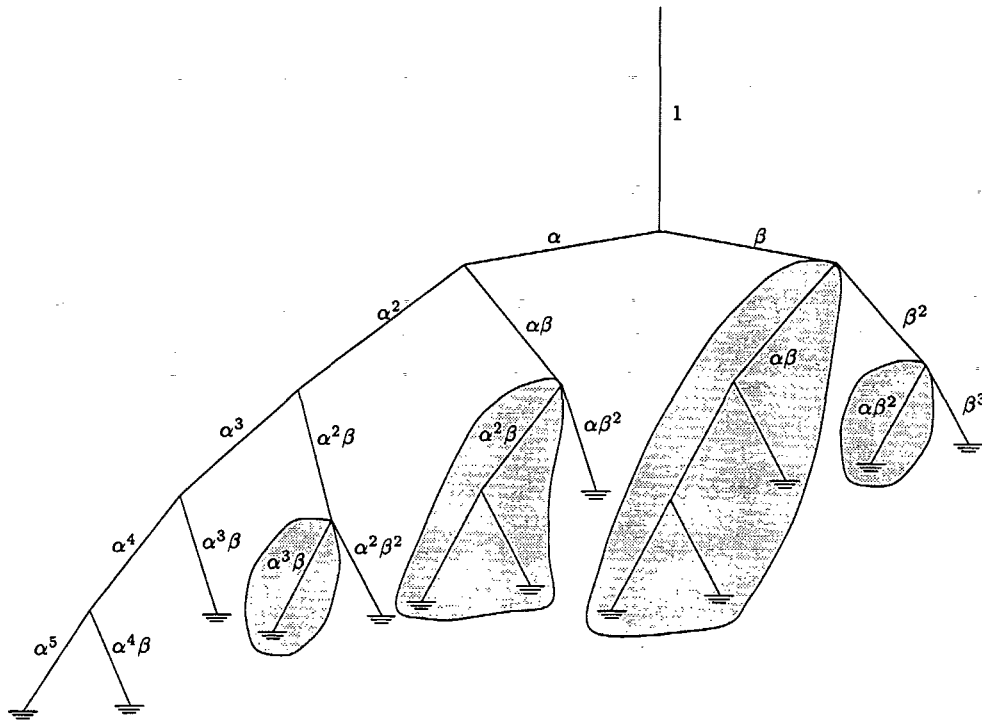


Figure 6.1: A structured tree, at each bifurcation the radii of the daughter vessels are scaled by a factor α and β , respectively. Because each branch is terminated when the radius is less than some given minimum radius the tree does not have a fixed number of generations.

the junctions in the systemic arteries are bifurcations (Caro et al., 1978). Furthermore, we assume that the tree is asymmetric and structured in such a way that the radii of the daughter vessels are scaled with factors $\alpha < 1$ and $\beta < 1$, respectively. In order to determine α and β we need a relation determining how the geometry (radius or cross-sectional area) changes over a bifurcation, as well as an area and asymmetry ratio between the cross-sectional area of the parent and its two daughter vessels. As for the larger arteries we also need to describe the length L and the compliance

$$C = dA/dp \approx 3A_0 r_0 / (2Eh)$$

for each vessel. The compliance here differs from the one defined for the larger arteries, in (5.3), since it is not the volume compliance but the area compliance, i.e. it is defined per unit length of the vessels. However, this is the definition we will use in the remainder of this chapter.

It is not practically possible to determine these parameters individually for all the vessels in the structured tree. So we will investigate the possibilities of determining these parameters as functions of the vessel radius. Thus, to construct an asymmetric structured binary tree we need the following relations:

- A radius relation over the bifurcations.
- Area and asymmetry ratios.

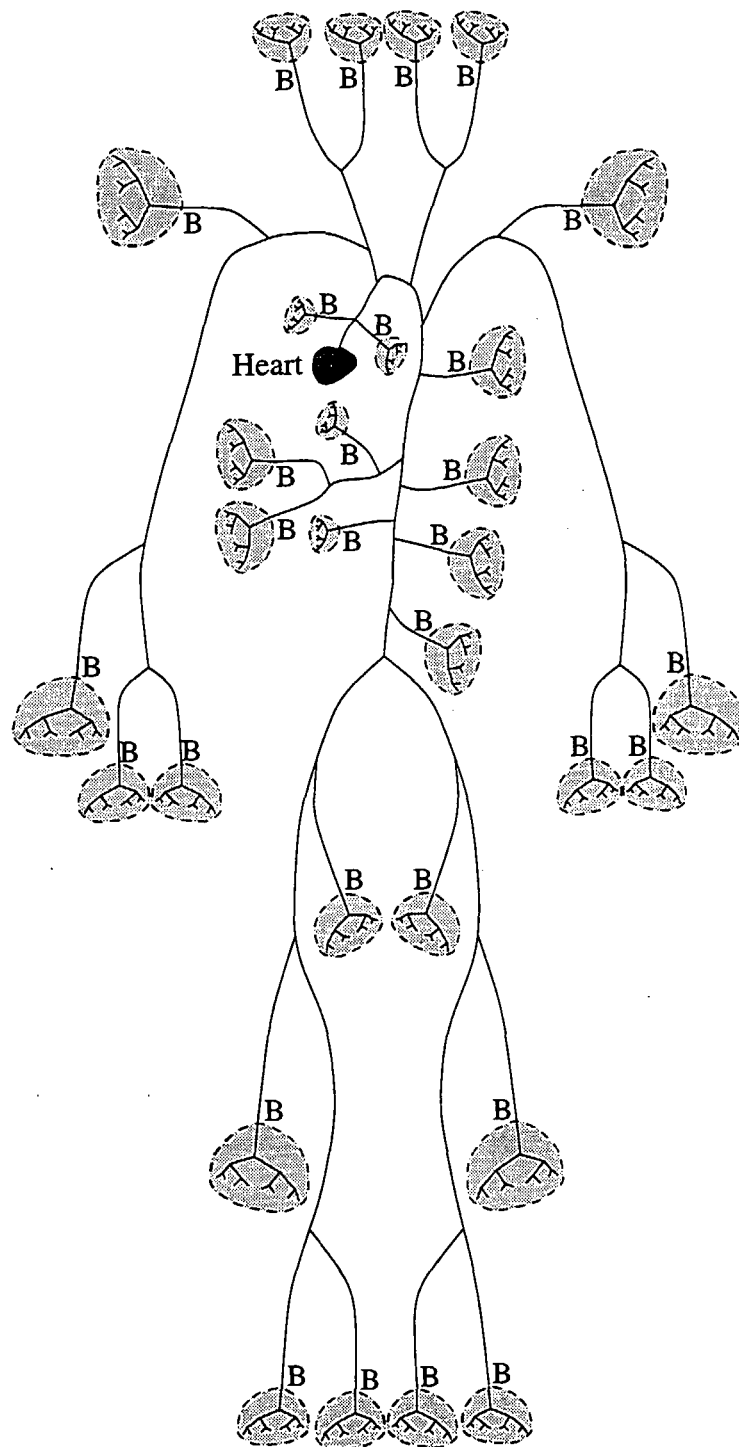


Figure 6.2: The systemic arterial tree. The tree consisting of the larger arteries, in which the non-linear equations are solved, originates at the heart (marked with an A) and terminates at the points marked with B. The structured trees representing the smaller arteries originate at these terminals and provide the main tree with outflow boundary conditions.

- Estimates of the order of each sub-trees.
- The length of the arteries, preferably as a function of the vessel radius.
- Wall thickness and Young's modulus, preferably as functions of the vessel radius.

Because of the repetitive scaling of the daughter arteries with factors α and β together with the definitions of the other geometrical parameters as functions of the vessel radius, the tree is geometrically self-similar.

6.1 Radius and asymmetry relations

The first relation determining how the radius changes over an arterial bifurcation was suggested by Murray in (1926a; 1926b). It is derived from the principle of minimum work and is given by

$$r_p^3 = r_{d_1}^3 + r_{d_2}^3$$

This relation is based on the assumption of laminar flow in a cylindrical vessel. Uylings (1977) derived a more general power law (still based on the principle of minimum work) which is valid for a range of flows; from turbulent to laminar.

$$r_p^\xi = r_{d_1}^\xi + r_{d_2}^\xi \quad (6.1)$$

$\xi = 3.0$ corresponds to laminar flow (this corresponds to the relation suggested by Murray) and $\xi = 2.33$ corresponds to turbulent flow.

Constructing an asymmetric tree requires some information about the area and asymmetry-ratio, i.e. an area ratio relating the cross-sectional areas of the two daughter vessels to their parent vessel and a ratio relating the areas of the two daughter vessels. In Zamir (1978) the following definitions are made, the area-ratio is given by

$$\eta = \frac{r_{d_1}^2 + r_{d_2}^2}{r_p^2} \quad (6.2)$$

and the asymmetry-ratio is given by

$$\gamma = (r_{d_2}/r_{d_1})^2 \quad (6.3)$$

Now we have three conditions, (6.1), (6.2), and (6.3), that characterizes the structure of the tree. However, the parameters ξ , η , and γ can not be determined independently of each other. They are related by

$$\eta = \frac{1 + \gamma}{(1 + \gamma^{\xi/2})^{2/\xi}}$$

This means that if we know the asymmetry-ratio γ and the exponent ξ we can calculate the area-ratio η , but it is not trivial to invert the relation. This is necessary since we have data for the area-ratio and not the asymmetry-ratio.

Reference	Value	Comment
Uylings (1977) •	$\eta = 1.04$	Measurements by Thoma (1922): Abdominal aorta \rightarrow comm. iliac art.
•	$\eta = 1.11$	Measurements by Newman et al. (1971): Across symm. aortic \rightarrow iliac bifurcation.
•	$\eta = 1.15$	Calc. from zero reflection Karreman (1952): Symm. bifurcation (arbitrary).
•	$\eta = 1.15 - 1.20$	Womersley (1958): Ext. of above + viscous eff. Min. refl. abdominal aorta of dog or man.
•	$\eta = 1.35$	McDonald (1960): Min. reflection in symm. art. bifurcation.
•	$\eta = 1.0 - 1.25$	Hunt (1969): Study of opt. energy transfer: Symm. aortic bif. in man.
Horsfield et al. (1981)	$\xi = 2.6 - 3.00$ $\xi = 2.885$ $\xi = 2.1 - 2.8$	Bronchial tree (method 1). ¹ Mean value. Bronchial tree (method 2). ²
Roy et al. (1982) Δ	$\xi = 0.8 - 10.0$ $\xi = 3.0$	Exp. in arteries suff. var. deg. of atherosclerosis: Average value by Hutchins et al. (1976).
Δ	$\xi = 2.2 - 3.1$ $\xi = 2.885$	13 regions from pulm. arteries: Mean value.
Kamiya et al. (1988) Δ Δ	$\xi = 2.6$ $\xi = 2.7$ $\xi = 3.2$	Average for systemic art. tree Groat (1948). Av. renal, mesen. and other art. Suwa et al. (1971). Left main coronary art. Hutchins et al. (1976).
Griffith et al. (1990) Δ	$\xi = 3.0$	Exp. rabbit ear art. ³
Pollanen (1992) Δ Δ Δ	$\xi = 2.5$ $\xi = 2.58$ $\xi = 3.20$	Av. aorta + main branches, Altman et al. (1972). Av. aorta + main branches, Griffith (1989). Av. art. generations 2 and 3, Griffith (1989).
Schreiner et al. (1995)	$\xi = 2.55$ $\xi = 3.0$	Simulation of coronary arteries: Min. wave reflection, Arts et al. (1979). Min. shear stress + exp., Zamir et al. (1987, 1988).
Schreiner et al. (1994)	$\xi = 3.0$	Exp. coronary art., Smaje et al. (1980). Min. shear stress, Robard (1975).
Rossitti et al. (1993) • Δ	$\eta = 1.2 \pm 0.4$ $\xi = 2.9 \pm 0.7$	Exp. carotid, anterior and mid. cerebral art.: Mean value and std. deviation. Mean value and std. deviation.
Kassab et al. (1995) Δ	$\xi = 2.73$ $\xi = 2.7$	Coronary arteriolar bifurcations: Min. work fct. and close to exp. val. Exp. casts var. human org., Suwa et al. (1973).
Horsfield et al. (1989) Δ •	$\xi = 2.3 \pm 0.1$ $\eta = 1.09$	Arithmetic mean exp. data pulm. arteries: Regression from exp. data.
Papageorgiou et al. (1990) • • •	$\eta = 1.179$ $\eta = 0.848$ $\eta = 1.14$ $\eta = 1.259$	Mean val. exp. for coronary bif. Mean val. exp. for aortoiliac bif. Overall mean area-ratio. ⁴ Min. work in small art., Murray (1926).

Table 6.1: Area-ratios and exponents for the radii relation. Rough approximations show an average for the area-ratio (those marked by •) of 1.16 and for the exponent (those marked by Δ) of 2.76.

However, there is a one-to-one relationship between η and γ for any given ξ . Hence, it is possible to determine the inverse function numerically using binary search. Several suggestions for the exponent ξ and the area-ratio has been analyzed over the years. These results are shown in Table 6.1.

From the relations discussed above it is then possible to determine the scaling parameters α and β . According to the radius relation (6.1) and the asymmetry ratio (6.3) one finds that

$$\alpha = \left(1 + \gamma^{\xi/2}\right)^{-1/\xi} \quad \beta = \alpha\sqrt{\gamma} \quad (6.4)$$

6.2 Order of the structured tree

As mentioned earlier the smaller arteries and arterioles comprise a tree with approximately 24 generations. However, because the structured tree is asymmetric a fixed number of generations will yield significant variations in the diameter of the terminal branches. This is not physiologically correct, because for a given organ or tissue the arterioles will have approximately the same diameter in order to ensure an even blood supply. Therefore, we have chosen to terminate the structured tree when the radius of the terminal vessels becomes less than some given minimum radius. However, the peripheral resistance, which is regulated by the smaller arterioles varies among the organs. For example, the peripheral resistance of the renal arteries is very low while the resistance of the femoral arteries is high. This can be modeled by allowing a variable minimal radius determined to match the peripheral resistance of the organ in question.

6.3 Length of the segments

A number of the papers offer suggestions to estimate the physical lengths of the various arterial segments, e.g. Kamiya and Togawa (1972), Zamir (1976), or Schreiner (1993). In these papers the length of the segments and bifurcation points are found from geometrical principles based on minimization (e.g. of the volume) of a two-dimensional distribution of the vessels, i.e. the length of the vessels were determined from the location of the origin and angles between the vessels.

Alternatively, disregarding small side branches (compared to the main vessel), Iberall (1967) suggests expressing the vessel length as a function of its diameter. The conclusion is that

$$L/d \approx 25 \pm 5 \quad (6.5)$$

where L is the length and d is the diameter of the vessel. This relation is extrapolated from measurements by Suwa (1963) who found that L/d tends to be constant for

¹Good results are achieved for the pulmonary arteries. Data for other species than humans are also given but will not be repeated here.

²Best for monopodially branching trees, intervals found from median values instead of mean values as is the case in method 1.

³The effect of EDRF (endothelium-derived relaxation factor) was studied and except for one case ξ were close to 3.

⁴A list of various measurements is listed in the paper, a total of 444 measurements were made.

$d \in [20; 4000] \mu\text{m}$ and Patel (1963) who, for $d \in [2; 20] \text{ mm}$, suggested a 20 to 1 ratio of length to the entrance diameter. The constant length to diameter (or similar length radius) relation is also repeated in West, Bhargava and Goldberger (1986). However, this study is concerned with the airways in the mammalian bronchial tree. Finally, the paper by Kassab, Rider, Tang and Fung (1993) finds that the mean vessel length in the coronary arteries obeys Horton's law ($\log_{10} L_n = a + bn$), where a, b are constants, and n is the Strahler order within the tree. The Strahler order is defined such that the capillaries have order 0 and the smallest arteries have order 1, i.e. when two order 0 capillaries meet. Now if two daughter vessels of order 0 and 1 meet the parent vessel will be of order 1.

Generally, we have chosen the constant length to radius relation since this seems most well documented. However, even though the paper by Kassab et al. (1993) only involves the coronary arteries, it would be interesting to investigate this idea further as a possible basis for constructing a structured tree model.

6.4 Wall thickness and Young's modulus

If we can find expressions relating the wall thickness h and Young's modulus E to the radius r_0 of the blood vessel we can determine the compliance $C = 3A_0 r_0 / (2Eh)$ solely as a function of the radius r_0 .

This is exactly what has been done for the larger arteries, see Figure 5.2. However, the relation found here does not apply to the smaller arteries because we cannot extrapolate the interpolating function outside its domain. Furthermore, one has to be careful because the walls of the smaller arteries and arterioles have a different composition of layers than the larger arteries, see Figure 3.4. However, when trying to investigate these parameters we only found a few papers discussing the wall thickness and Young's modulus specifically for the smaller arteries. Therefore, we will in the following sections present a more general discussion of the wall thickness and Young's modulus, for both large and small arteries.

6.4.1 Wall thickness

Oka and Nakai (1987) propose the relation $h = A r_0^B$, where A and B are dimensionless constants, and r_0 is the vessel radius (cm). This relation is based on empirical measurements and they give data for small arteries with a radius less than 0.1 mm. In Kassab and Fung (1995) they refer to a study by Tomanek et al. (1986) where the thickness of the wall of various caliber coronary arteries in dogs were measured. They fitted their data using a least square method and found that $A = 1.06$ and $B = 0.457$.

McDonald (1974) refers to experiments for measuring the wall thickness in the larger arteries in a series of 8 dogs. He found that $h/(2r_0)$, where r_0 is the mean radius, remained remarkably constant in all larger arteries (ranging from the ascending aorta to the saphenous artery). He notes, however, that the ratio varies with the arterial pressure and that it is technically difficult to measure. For the same animal one must measure the dimensions of a large number of arteries at identical mean pressure and this requires extensive surgical dissection. On the other hand the stipulation of a constant ratio applies well to the physical properties: The mean pressure is approximately the same

Relation			Reference
$h = Ar_0^B, r_0 < 0.05 \text{ mm.}$	<i>A</i>	<i>B</i>	
Renal arteries	0.032	0.25	Oka et al. (1987).
Mesenteric arteries	0.055	0.46	do
Var. cal. coronary art.	1.06	0.457	Kassab et al. (1995). NB: $\xi = 2.73$.
$h/(2r_0) = c, r_0 > 0.05 \text{ mm.}$	$h \text{ (cm)}$	$h/(2r_0)$	
Asc. aorta – saphenous art.		0.08	• McDonald (1974).
Larger arteries		0.1	• Rodkiewicz (1983).
Arterioles $r_0 < 0.05 \text{ mm.}$		0.04	do
As ⁵ , descending aorta ⁵	0.065	0.07	• Caro et al. (1978).
do ⁶	0.05 – 0.08	0.055 – 0.084	do
Abdominal aorta ⁵	0.05	0.06	• do
do ⁶	0.04 – 0.06	0.04 – 0.09	do
Femoral artery ⁵	0.04	0.07	• do
do ⁶	0.02 – 0.06	0.055 – 0.11	do
Carotid artery ⁵	0.03	0.08	• do
do ⁶	0.02 – 0.04	0.53 – 0.095	do
Arteriole ⁵ $r_0 < 0.05 \text{ mm.}$	0.002	0.4	do
Capillary ⁵ $r_0 < 0.05 \text{ mm.}$	0.0001	0.17	do

Table 6.2: Wall thickness and wall thickness to diameter ratios. A rough average of the values for $r_0 > 0.05 \text{ mm}$ (marked with a •) is 0.077 mm.

throughout the larger arteries, and the wall tension, which in a cylinder is proportional to the pressure, decreases linearly with the radius. Furthermore, if we assume that the elastic properties of the wall are similar throughout the arterial tree it is to be expected that the arteries will only require a wall thickness that decreases linearly with the radius in order to maintain the wall tension. This was pointed out in Thompson (1988). This also indicates that the constant ratio only applies as long as the composite of the wall remains the same, such as the smooth muscle coats of the arterioles.

Rodkiewicz (1983) shows, for animals weighing more than 60 kg, that the vessel diameter changes proportionally to the wall thickness with a ratio of approximately 0.1. In the smaller peripheral arteries the wall becomes thinner, but the thickness to diameter ratio increases. Finally, he states that in the arterioles the ratio may be as big as 0.4. The same relation is presented in Caro et al. (1978). Furthermore, they add that in the smallest vessels of the micro-circulation, particularly for capillaries, the relation with body size disappears and the diameter to wall thickness ratio is similar in all species.

Another important point is that both wall thickness and diameter of the vessel changes with age in general, but again it seems that the wall thickness to diameter ratio is approximately constant for all ages. The values for the wall thickness h and the wall thickness diameter ratio $h/(2r_0)$ are shown in Table 6.2.

⁵Mean value.

⁶Range.

6.4.2 Young's modulus

Generally, an analysis of elastic behavior of the arterial wall should include viscoelastic, anisotropic, and inhomogeneous properties. The composition of blood vessel walls is not homogeneous and since the material is arranged in such a way that it is most unlikely to be isotropic, classical elasticity theory cannot be applied directly and a single Young's modulus cannot be defined. However, it is still possible to describe the deformation of the wall as a whole in response to known applied stresses, and to infer from these measurements the value which Young's modulus would have had if the material had been elastic, homogeneous, and isotropic. In this model all the different constituent parts of the wall are lumped together to obtain an effective Young's modulus, defined as a function of the vessel radius, see Figures 5.2 and 6.3.

Tissue	E, $10^6 \text{ g/(s}^2\text{cm)}$	Reference
Thoracic aorta, – static, 100 mmHg	4.4	McDonald (1974).
– dyn. 2.0 Hz, 100 mmHg	4.7	do
– dyn. 18.0 Hz, 100 mmHg	5.3	do
Abdominal aorta, – static, 100 mmHg	9.2	do
– dyn. 2.0 Hz, 100 mmHg	10.9	do
– dyn. 18.0 Hz, 100 mmHg	12.2	do
Femoral artery, – static, 40–200 mmHg	1.2–16.1	do
– static, 100 mmHg	9.0	do
– dyn. 2.0 Hz, 100 mmHg	12.0	do
– dyn. 18.0 Hz, 100 mmHg	10.6	do
Carotid, – static, 40–200 mmHg	1.0–12.8	do
– static, 100 mmHg	6.9	do
– dyn. 2.0 Hz, 100 mmHg	11.0	do
– dyn. 18.0 Hz, 100 mmHg	12.8	do
As-, descending aorta ⁷	4.8	Caro et al. (1978).
do ⁸	3–6	do
Abdominal aorta ⁷	10	do
do ⁸	9–11	do
Femoral artery ⁷	10	do
do ⁸	9–12	do
Carotid artery ⁷	9	do
do ⁸	7–11	do
Thoracic aorta ⁹	0.36–4.09	Langewouters et al. (1984).
Abdominal aorta	0.39–2.52	do
Thor. and Abd. aorta ¹⁰	1	do

Table 6.3: Young's modulus.

McDonald (1974) presents a comprehensive discussion of the elasticity of the arteries, but we will only mention the essentials here.

⁷Mean value.

⁸Range.

⁹Only one value goes up to 4.09 g/(s²cm). However, in general they stay below 2.85 g/(s²cm).

¹⁰A typical value.

In vivo the arteries are tethered in all directions. However, because of the structure of the tissue they are able to dilate in the radial direction, but are fixed in the longitudinal direction. Therefore, the stresses in the longitudinal direction can be neglected and Young's modulus can be described from the tangential stresses only. Even with this simplification it is difficult to estimate Young's modulus. For example in the thoracic aorta, which according to McDonald (1974) has the most linear behavior, the results vary with a factor of 10 over the physiological range of blood-pressures. In Table 6.3 some of these results are shown. The advantage of these measurements is that the vessels are kept in their in vivo length, tethered at both ends. In all these studies the wall is considered isotropic and incompressible, even though this is not entirely physiologically correct. McDonald presents extensive data from in vivo measurements of blood vessels in dogs, but we have only quoted those for pressures of approximately 100 mmHg, since they compare well with the mean blood-pressure in the human arteries. However, we have included values for a range of frequencies. The frequency dependent modulus shows a significant rise between 0–2 Hz. Thereafter the modulus is no longer frequency dependent (up to 18 Hz). Generally, all of these measurements (both the static and dynamic modulus) show that the arteries become stiffer, i.e. that Young's modulus increases, towards the periphery.

Also Caro et al. (1978) gives a range of Young's modulus for different sizes of arteries, see Table 6.3. In these all of the elastic properties are lumped into one coefficient. As for the data in McDonald (1974) only the tangential stress component of the modulus is measured. The data are measured in vivo for a variety of blood vessels in dogs. These data also show that E increases peripherally.

Finally, Langewouters, Wesseling and Goedhard (1984) gives measurements of the static elastic properties of 45 human thoracic and 20 abdominal aortas in vitro. The results are significantly scattered but show a strong dependency on pressure and age of the person examined. In the thoracic aorta the values vary from $0.36 \times 10^6 \text{ g/(s}^2\text{cm)}$ to $4.09 \times 10^6 \text{ g/(s}^2\text{cm)}$. However, only one value is as high as this. In general they stay below $2.85 \times 10^6 \text{ g/(s}^2\text{cm)}$. The lowest value is obtained for the youngest person examined (30 years). In the abdominal aorta the values vary from $0.39 \times 10^6 \text{ g/(s}^2\text{cm)}$ to $2.52 \times 10^6 \text{ g/(s}^2\text{cm)}$.

In Figure 6.3 we have plotted Young's modulus as it appears in Stergiopulos et al. (1992), which are the same data presented in Figure 5.2 and measured values presented in Table 6.3. However, only the static modulus from McDonald (1974) and the data from Caro et al. (1978) are included. Thus, we have left out both the dynamic moduli from McDonald and the data from Langewouters et al. (1984). From the figure it becomes clear that the relation between Young's modulus and the vessel radius is not nearly as obvious as when the wall thickness is also taken into account which was the case in Figure 5.2. Moreover, the comparison with measured data shows that they are generally higher than the converted compliance data. This is especially pronounced for the abdominal and carotid arteries whereas data for the ascending and thoracic aorta as well as the femoral arteries are fairly close to the estimates by Stergiopulos. Keeping in mind that McDonald mentions that measurements easily vary with a factor of ten we find the converted data by Stergiopulos et al. (1992) acceptable.

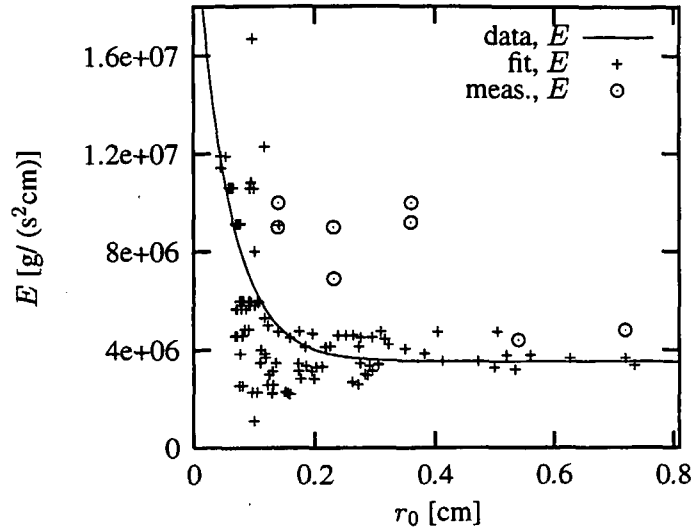


Figure 6.3: Fit to data for Young's modulus. The points marked with circles corresponds to measured values, see Table 6.3, the points marked with a + corresponds are converted from measured compliance data, see Stergiopoulos et al. (1992), and the line is fitted through all points marked with a +. The the fitted function has the form $k_1 \exp(k_2 r) + k_3$, where $k_1 = 1.89 \times 10^7 \text{ g/(s}^2\text{cm)}$, $k_2 = -18.34 \text{ cm}^{-1}$, and $k_3 = 3.53 \times 10^6 \text{ g/(s}^2\text{cm)}$. This fit is made using the "fit" function in gnuplot.

6.5 Conclusion – Parameter choices

In the previous sections we have discussed some of the problems and suggestions made in the literature regarding the parameter choices for characterizing some of the physiological features. In general, many of the parameters vary significantly and since the measurements reviewed are not taken from the same environments, it is quite complicated to extract anything general using simple statistical methods. We are interested in modeling a structured tree based on a representative physiological behavior, so we have tried to estimate these parameters, regardless. In the following we have listed our parameter choices.

- **Radius relation:** The exponent ξ discussed in Section 6.1 varies from 2.33 to 3, at least if the aorta and its side-branches are excluded. We have chosen a value of 2.76, but it is not quite clear if this is the correct choice. In fact, from Table 6.1 we see that the exponent increases slightly as we descend down the tree.
- **Area- and asymmetry-ratios:** Again there are large variations and it is not at all clear whether this parameter can be kept constant for all sub-trees and even throughout each of these. But from the mean values it seems appropriate to choose an area ratio of $\eta = 1.16$ giving an asymmetry ratio of $\gamma = 0.41$.
- **Scaling ratios:** The relations in (6.4) and the estimates above give the scaling ratios $\alpha = 0.9$ and $\beta = 0.6$.

- **Number of generations:** We have chosen to terminate the structured trees when the radius becomes smaller than some given minimum radius. The minimum radius determines the overall resistance of the structured tree, so it should be chosen to simulate the resistance of the tissue or organ in question.
- **Length of the segments:** According to Iberall (1967) the ratio between the vessel length and diameter (L/d) is constant. For the smaller arteries we have chosen $L/d = 25$.
- **Young's Modulus and wall thickness to radius ratio:** None of our investigations have indicated that the functional dependence in Figure 5.2 cannot be continued for smaller radii. Hence, we have chosen to use the extrapolated function for the smaller arteries. It should be noted that we do not need Young's Modulus and the wall thickness separately, only the combination Eh/r_0 is significant.

Chapter 7

Fluid dynamical model of a large artery

In this and the following chapters we derive and solve the model of blood flow and pressure in the larger systemic arteries. As discussed earlier the aim is to derive a one-dimensional model based on Navier-Stokes equations for fluid flow in a network of vessels. The larger arteries can be thought of as a binary tree of compliant and tapering vessels containing an inviscid, incompressible, and Newtonian fluid.

There exist numerous one-dimensional models predicting blood flow and pressure in the larger arteries. While all of these models are based on Navier-Stokes equations they differ in the way they treat the shear stresses of the fluid, the relation between pressure and cross-sectional area, and the boundary conditions. The derivation presented here will primarily be based on Barnard, Hunt, Timlake and Varley (1966) and Peskin (1976) but we will discuss some of the other approaches where the models differ.

In this chapter the model is derived for one compliant vessel with a continuous outflow along it and in Chapter 8 this derivation is extended to include more vessels organized in a binary tree structure. In Chapter 9 we discuss two numerical methods for solving the equations. Finally, in Appendix B an analogy to gas-dynamics is presented: We show that the blood flow in arteries either can be modeled using compliant vessels containing an incompressible fluid, as we are doing, or as rigid vessels containing a compressible gas. Most of these chapters were used as lecture notes for a graduate course in fluid mechanics taught by the author at Roskilde University.

7.1 Momentum and continuity equations

A blood vessel can be regarded as a rotation symmetric tubular surface S , with end-surfaces in the planes $x = 0$ and $x = L$ see Figure 7.1. Assume that:

- S moves with velocity $\mathbf{v} = (v_x, v_r, v_\theta)$ where x is the longitudinal coordinate and the polar coordinates are r and θ .
- S encloses a volume V which is filled with an incompressible fluid moving with velocity $\mathbf{u} = (u_x, u_r, u_\theta)$. Both u_i and v_i are functions of (x, r, θ, t) .

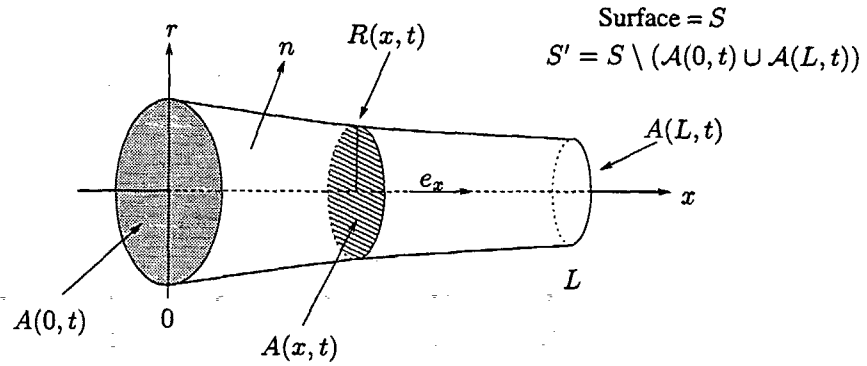


Figure 7.1: A typical vessel.

Furthermore, note that the surface S does not in general move with the same velocity as the fluid, i.e. \mathbf{u} and \mathbf{v} are generally different.

- The density ρ of the fluid is constant.
- The pressure in the fluid is denoted $p(x, r, \theta, t)$.
- $r_0(x)$ is the vessel radius at zero transmural pressure, i.e. when $p = p_0$. As discussed in Section 5.1 we assume that the arteries taper exponentially, hence

$$r_0(x) = r_{top} \left(\frac{r_{bot}}{r_{top}} \right)^{x/L} \quad (7.1)$$

where x is the position along a given artery with length L , and r_{top} , r_{bot} are the radii at the proximal and distal ends of the artery, respectively.

- $R(x, t)$ is the radius of the vessel.
- $A(x, t) = \pi R(x, t)^2$ is the cross-sectional area, i.e. the end-surfaces of S are $A(0, t)$ and $A(L, t)$, respectively.
- $\mathcal{A}(x, t) = \{(r, \theta) : 0 \leq r \leq R(x, t), 0 \leq \theta \leq 2\pi\}$ is the collection of points in the plane x at time t . The area of $\mathcal{A}(x, t)$ is $A(x, t)$.
- $S' = S \setminus (A(0, t) \cup A(L, t))$.
- $\mathbf{v} = \mathbf{0}$ on $A(0, t)$ and $A(L, t)$.
- \mathbf{n} is the outward unit normal to the surface S .
- $\mathbf{e}_x, \mathbf{e}_r, \mathbf{e}_\theta$ are the unit vectors in the x, r, θ -directions.

Using conservation laws (of volume and x -momentum) it is possible to derive the one-dimensional equations predicting blood flow and pressure in the larger arteries.

Conservation of Volume:

$$\begin{aligned}
& \frac{\partial}{\partial t} \iiint_V dV + \iint_S (\mathbf{u} - \mathbf{v}) \cdot \mathbf{n} dA = 0 \quad \Leftrightarrow \\
& \frac{\partial}{\partial t} \int_0^L \left(\iint_A dA \right) dx + \iint_{A(0) \cup A(L)} (\mathbf{u} - \mathbf{v}) \cdot \mathbf{n} dA + \iint_{S'} (\mathbf{u} - \mathbf{v}) \cdot \mathbf{n} dA = 0 \quad \Leftrightarrow \\
& \frac{\partial}{\partial t} \int_0^L A dx + \left[\iint_A u_x dA \right]_0^L + \iint_{S'} (\mathbf{u} - \mathbf{v}) \cdot \mathbf{n} dA = 0 \quad (7.2)
\end{aligned}$$

Conservation of x -Momentum:

$$\begin{aligned}
& \frac{\partial}{\partial t} \iiint_V \rho u_x dV + \iint_S \rho u_x (\mathbf{u} - \mathbf{v}) \cdot \mathbf{n} dA + \\
& \iint_S (p(\mathbf{n} \cdot \mathbf{e}_x) - (\mathbf{d}\mathbf{n}) \cdot \mathbf{e}_x) dA = 0 \quad \Leftrightarrow \\
& \frac{\partial}{\partial t} \int_0^L \left(\iint_A \rho u_x dA \right) dx + \left[\iint_A \rho u_x^2 dA \right]_0^L + \iint_{S'} \rho u_x (\mathbf{u} - \mathbf{v}) \cdot \mathbf{n} dA + \\
& \int_0^L \left(\iint_A \frac{\partial p}{\partial x} dA \right) dx - \int_0^L \left(\int_0^{2\pi} (\mathbf{d}\mathbf{n}) \cdot \mathbf{e}_x R d\theta \right) \sqrt{1 + \left(\frac{\partial R}{\partial x} \right)^2} dx = 0 \quad (7.3)
\end{aligned}$$

where \mathbf{d} is a tensor representing the shear stresses (also called the deviatoric stress tensor, see Ockendon and Ockendon (1995)). The last integral can be explained from Figure 7.2.

Generally, the surface stress tensor for incompressible flow is given by Ockendon and Ockendon (1995)

$$\sigma_{ij} = -p\delta_{ij} + d_{ij}$$

The tensor has two components; $-p\delta_{ij}$ which is the isotropic part, as would exist in an inviscid fluid, and d_{ij} which is the deviatoric part, which is due to the viscous forces in the fluid. The isotropic part of the tensor $-p\delta_{ij}$ is already incorporated in the fourth term of (7.3). Assuming that $u_\theta = 0$, i.e. that there is no swirl, then, according to Batchelor (1992), the deviatoric part of the surface stress tensor is given by

$$\mathbf{d} = 2\mu \begin{bmatrix} \frac{\partial u_x}{\partial x} & \frac{1}{2} \left(\frac{\partial u_r}{\partial x} + \frac{\partial u_x}{\partial r} \right) & 0 \\ \frac{1}{2} \left(\frac{\partial u_r}{\partial x} + \frac{\partial u_x}{\partial r} \right) & \frac{\partial u_r}{\partial r} & 0 \\ 0 & 0 & \frac{u_r}{r} \end{bmatrix}_R$$

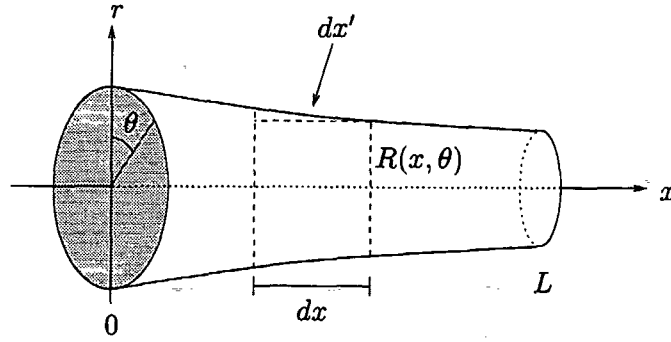


Figure 7.2: The surface integral in (7.5) can be split into two parts. The first integrates over the circumference with radius R for $\theta \in [0 : 2\pi]$. The second integrates over the length of the tube, $x \in [0 : L]$. Since the vessel is tapering each infinitesimal piece is given by $dx' = \sqrt{1 + (\partial R / \partial x)^2} dx$.

where μ is the viscosity. Hence,

$$\begin{aligned}
 (d\mathbf{n}) \cdot \mathbf{e}_x = & \\
 2\mu \left[\begin{array}{ccc} \frac{\partial u_x}{\partial x} & \frac{1}{2} \left(\frac{\partial u_r}{\partial x} + \frac{\partial u_x}{\partial r} \right) & 0 \\ \frac{1}{2} \left(\frac{\partial u_r}{\partial x} + \frac{\partial u_x}{\partial r} \right) & \frac{\partial u_r}{\partial r} & 0 \\ 0 & 0 & \frac{u_r}{r} \end{array} \right]_R \begin{pmatrix} 0 \\ 1 \\ 0 \end{pmatrix} \cdot \begin{pmatrix} 1 \\ 0 \\ 0 \end{pmatrix} = & \\
 \left[\mu \left(\frac{\partial u_r}{\partial x} + \frac{\partial u_x}{\partial r} \right) \right]_R & \quad (7.4)
 \end{aligned}$$

If the vessels were not tapering then $u_r = 0$ and hence $\partial u_r / \partial x = 0$. Assuming that the tapering is small this term can be neglected. Hence, the last integral in (7.3) can be written as

$$\begin{aligned}
 \iint_S (d\mathbf{n}) \cdot \mathbf{e}_x &= \int_0^L \left(\int_0^{2\pi} (d\mathbf{n}) \cdot \mathbf{e}_x R d\theta \right) \sqrt{1 + \left(\frac{\partial R}{\partial x} \right)^2} dx \\
 &= \int_0^L 2\pi \mu R \left[\frac{\partial u_x}{\partial r} \right]_R \sqrt{1 + \left(\frac{\partial R}{\partial x} \right)^2} dx \quad (7.5)
 \end{aligned}$$

The first equality is explained in Figure 7.2. The assumption of a small tapering factor also justifies neglect of $\partial R / \partial x$. Hence, the wall shear stress can be found from

$$\int_0^L 2\pi \mu R \left[\frac{\partial u_x}{\partial r} \right]_R dx \quad (7.6)$$

Let $\Psi(x)$ be the outflow of volume V and let $\Psi_P(x)$ be the outflow of momentum (both per unit length), i.e.

$$\int_0^L \Psi dx = \iint_{S'} (\mathbf{u} - \mathbf{v}) \cdot \mathbf{n} dA$$

$$\int_0^L \Psi_P dx = \iint_{S'} \rho u_x (\mathbf{u} - \mathbf{v}) \cdot \mathbf{n} dA$$

Note that both Ψ and Ψ_P vanish when the normal component of the surface velocity equals that of the fluid (when $(\mathbf{u} - \mathbf{v}) \cdot \mathbf{n} = 0$), i.e. all outflow from the system occurs through the end surfaces $A(0)$ and $A(L)$. Inserting (7.6) in (7.3) and differentiating (7.2) and (7.3) with respect to L , and replacing L by x throughout gives

$$\frac{\partial A}{\partial t} + \frac{\partial}{\partial x} \iint_A u_x dA + \Psi = 0 \quad (7.7)$$

$$\frac{\partial}{\partial t} \iint_A \rho u_x dA + \frac{\partial}{\partial x} \iint_A \rho u_x^2 dA + \iint_A \frac{\partial p}{\partial x} dA - 2\pi\mu R \left[\frac{\partial u_x}{\partial r} \right]_R + \Psi_P = 0 \quad (7.8)$$

These equations describe flow in the vessel shown in Figure 7.1. However, they do not constitute a one-dimensional theory since the velocity distribution over the cross-sectional area appears in the equations. Hence, a few more assumptions are needed.

First, it is assumed that p and thus $\partial p / \partial x$ are functions of x and t only, i.e. that pressure is constant over the entire cross-sectional area. Then the average velocity over the cross-sectional area is defined as

$$u = \frac{1}{A} \iint_A u_x dA$$

and

$$\chi = \frac{1}{Au^2} \iint_A u_x^2 dA$$

Using these definitions (7.7) and (7.8) can be written by

$$\Psi_P = \rho u \Psi$$

$$\frac{\partial A}{\partial t} + \frac{\partial(Au)}{\partial x} + \Psi = 0 \quad (7.9)$$

$$\rho \left(\frac{\partial(Au)}{\partial t} + \frac{\partial(\chi Au^2)}{\partial x} \right) + A \frac{\partial p}{\partial x} - 2\pi\mu R \left[\frac{\partial u_x}{\partial r} \right]_R + \Psi_P = 0 \quad (7.10)$$

Assuming that the velocity profile is parabolic, i.e.

$$u_x = 2u \left(1 - \frac{r^2}{R^2} \right)$$

then

$$2\pi\mu R \left[\frac{\partial u_x}{\partial r} \right]_R = -8\pi\mu u$$

and

$$\chi = \frac{1}{Au^2} \int_0^R 4u^2 \left(1 - \frac{r^2}{R^2} \right)^2 2\pi r dr = \frac{4}{3}$$

Many of the earlier models assumed a parabolic velocity profile, e.g. Streeter, Keitzer and Bohr (1963), Barnard et al. (1966), Anliker et al. (1971), Raines et al. (1974), Werff (1974), Anliker et al. (1978), Forbes (1981), or Reuderink, Hoogstraten, Sipkema, Hillen and Westerhof (1989). However, many of these papers note that the simple way of describing the wall-shear stress only applies for a steady and laminar flow. Generally, the system is much more dynamic and the velocity profile changes according to the flow conditions. In general for laminar flow in slightly tapering vessels the velocity profile is rather flat (McDonald, 1974; Pedersen, 1993). Therefore, a better approach is to assume that the velocity profile is flat but with a boundary layer of thickness δ , hence

$$u_x = \begin{cases} u, & \text{for } r \leq R - \delta \\ u(R - r)/\delta & \text{for } R - \delta < r \leq R \end{cases}$$

The thickness of the boundary layer can be estimated from $(\nu T)^{1/2} \approx 0.2$ cm for the aorta, where $\nu = \mu/\rho$ is the kinematic viscosity. This also corresponds to the results obtained by McDonald (1974) and Pedersen (1993). In this case

$$2\pi\mu R \left[\frac{\partial u_x}{\partial r} \right]_R = -\frac{2\pi\mu u R}{\delta} \quad (7.11)$$

and

$$\chi = \frac{1}{Au^2} \left(\int_0^{R-\delta} u 2\pi r dr + \int_{R-\delta}^R \frac{u(R-r)}{\delta} 2\pi r dr \right) = 1 - \frac{4\delta}{3R} + \frac{\delta^2}{2R^2} \approx 1$$

The last approximation only applies if the boundary layer is thin compared with the vessel radius.

Both of these conditions are derived from an approximation of steady flow, but blood flow in real arteries is not steady. Therefore, the wall shear stresses should be investigated in further detail. In fact there are papers accounting for the shear stress in a more detailed way, e.g. Olsen and Shapiro (1967), Wemple and Mockros (1972), Schaaf and Abbrecht (1972), or Stergiopoulos et al. (1992). In these, the shear stress is defined as a combination of two terms; one accounting for the steady part of the flow and one from the unsteady part. The first is found from assuming Poiseuille flow and the second from assuming a sinusoidally driven flow in a long straight rigid tube.

Inserting the conditions arising from the assumption of a flat velocity profile and dividing by ρ , the momentum equation becomes

$$\begin{aligned}\Psi_{\bar{p}} &= u\Psi \\ \frac{\partial A}{\partial t} + \frac{\partial(Au)}{\partial x} + \Psi &= 0 \\ \frac{\partial(Au)}{\partial t} + \frac{\partial(Au^2)}{\partial x} + \frac{A}{\rho} \frac{\partial p}{\partial x} + \frac{2\pi\nu u R}{\delta} + \Psi_{\bar{p}} &= 0\end{aligned}$$

Finally, the equations can be rewritten in terms of the flow $q = Au$, with $\Psi_{\bar{p}}$ replaced by $q/A\Psi$.

$$\frac{\partial A}{\partial t} + \frac{\partial q}{\partial x} + \Psi = 0 \quad (7.12)$$

$$\frac{\partial q}{\partial t} + \frac{\partial}{\partial x} \left(\frac{q^2}{A} \right) + \frac{A}{\rho} \frac{\partial p}{\partial x} + \frac{2\pi\nu q R}{\delta A} + \Psi \frac{q}{A} = 0 \quad (7.13)$$

These equations cannot be solved analytically and many numerical schemes require the system to be in conservation form. In order to rewrite the equations in conservation form we introduce the quantity B chosen to fulfill

$$B(r_0(x), p(x, t)) = \frac{1}{\rho} \int A dp \quad (7.14)$$

Hence,

$$\frac{\partial B}{\partial x} = \frac{A}{\rho} \frac{\partial p}{\partial x} + \frac{\partial B}{\partial r_0} \frac{dr_0}{dx}$$

Since the term $(\partial B / \partial r_0)(dr_0 / dx)$ does not contain any partial derivatives of p and hence of A and q , it can be evaluated directly and therefore may be added to both sides of (7.13). Thus, the momentum equation (7.13) can be rewritten as

$$\frac{\partial q}{\partial t} + \frac{\partial}{\partial x} \left(\frac{q^2}{A} + B \right) = -\frac{2\pi\nu q R}{\delta A} - \Psi \frac{q}{A} + \frac{\partial B}{\partial r_0} \frac{dr_0}{dx} \quad (7.15)$$

The momentum equation (7.15) and the continuity equation (7.12) can be rewritten in conservation form

$$\frac{\partial}{\partial t} \begin{pmatrix} A \\ q \end{pmatrix} + \frac{\partial}{\partial x} \begin{pmatrix} q \\ \frac{q^2}{A} + B \end{pmatrix} = \begin{pmatrix} -\Psi \\ C \frac{q}{A} + \frac{\partial B}{\partial r_0} \frac{dr_0}{dx} \end{pmatrix} \quad (7.16)$$

where $C = -2\pi\nu R / \delta - \Psi$. The equations above are the basic equations for the one-dimensional theory for the wave propagation of the arterial pulse. However, there are two equations and three dependent variables, namely p , q , and A . Therefore, we need a third relation, the so-called state equation. This is based on the compliance of the vessels and gives an equation for pressure as a function of cross-sectional area. Several approaches can be taken on how to model these "elastic" properties. We summarize some of these in the next section.

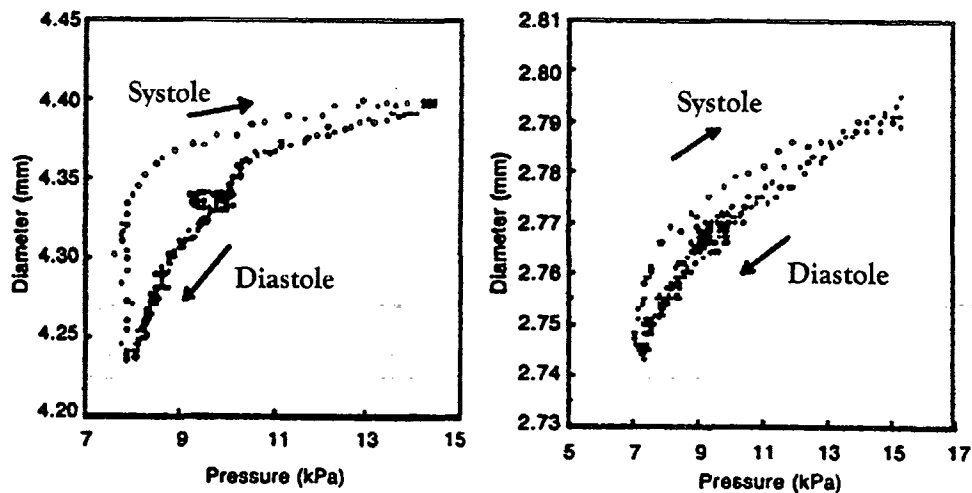


Figure 7.3: Pressure versus cross-sectional area in the brachial and radial artery, respectively. A clear hysteresis between the systolic and diastolic period is seen. From Tardy et al. (1991).

7.2 State equation

The arterial wall exhibits a viscoelastic behavior. This means that there is a delay from the time a given change in pressure takes place until it affects the corresponding cross-sectional area. Hence, the state equation should take this into account. For simplicity the theory for viscoelasticity is often left out in the original one-dimensional models. Generally it is assumed that cross-sectional area is related instantaneously to pressure for any given time and space, i.e. there is no phase lag. The simplest equations on this form are those derived from the theory of elasticity. However, in addition to not including the viscoelastic properties, these relations do not exhibit the right behavior. First of all they predict a decrease in the wave-speed with an increase in pressure, which should be opposite. Second, the cross-sectional area A becomes infinite at a finite transmural pressure, “blow-out”. This can, however, be avoided by having a non-linear Young’s modulus which increases with increasing strain.

Another approach is to fit measurements of the arterial compliance to some empirical function and in this way obtain a state equation which does not have the problems with decreasing wave-speed and “blow-out” as discussed above. However, these ad-hoc relations do not necessarily take the viscoelastic effects into account either.

When plotting experimental values for pressure versus cross-sectional area over one cardiac cycle, we get a picture as shown in Figure 7.3, where pressure is plotted as a function of cross-sectional area for a given x . The resulting curves show a hysteresis between the systolic and diastolic part of the cardiac cycle. According to Tardy et al. (1991) the hysteresis is a result of two independent factors: First, a phase lag due to a finite distance between the two sites of measurement of pressure and cross-sectional area, and second, because of viscoelasticity of the vessel walls as described above. In their paper they claim that the first factor is dominant. This hypothesis is supported by the fact that the separation between the pressure and diameter measurement sites is smaller for the radial artery than for the brachial artery and that the observed delay

and hysteresis are correspondingly smaller, see Figure 7.3. Furthermore, he supports the idea by setting up a method correcting for the finite difference between the measurement sites. In this way most of the hysteresis can be eliminated and a resulting curve, approximating the one obtained during the diastolic period, is obtained. However, since we have only one paper discussing the delay due to varying measurement sites the idea should be investigated further.

The larger arteries are viscoelastic, but the discussion above shows that it is the elastic properties that dominate, and hence it can be justified to study one of the simple models which do not account for viscoelasticity. However, for further details on viscoelastic models we refer to Horsten, Steenhoven and Dongen (1989), Rockwell, Anliker and Elsner (1974), Milnor (1982), Gerrad (1985), Steenhoven and Dongen (1986), Holenstein, Niederer and Anliker (1980), Holenstein, Nerem and Niederer (1984), Niederer (1985), and Bergel (1972). In the following we will summarize and discuss some of the different non-viscoelastic models.

7.2.1 Elastic models

One of the simplest models is the one discussed by Barnard et al. (1966). They assume that arteries are tapered thin-walled vessels with $r(x, t)$ being the radius of the moving boundary, and $r_0(x)$ being the radius at zero transmural pressure. The relation between pressure and cross-sectional area is then found from balancing the internal and external forces in the radial direction of a surface element of the vessel wall. This analysis is carried out in detail in Chapter 10. In that chapter equation (10.29) gives the linear stress-strain relation

$$\begin{aligned} \frac{T_\theta}{r_0} - p &= 0 \quad \Leftrightarrow \\ p &= \frac{4}{3} \frac{Eh}{r_0} \left(1 - \sqrt{\frac{A_0}{A}} \right) \approx \frac{4}{3} \frac{Eh}{r_0} \left(\frac{1}{2} \frac{\Delta A}{A_0} \right) \end{aligned} \quad (7.17)$$

since

$$\Delta A = A - A_0, \quad A_0 = \pi r_0^2$$

and

$$\frac{T_\theta}{r_0} = \frac{r - r_0}{r_0 r} \frac{Eh}{1 - \sigma_p^2} \quad (7.18)$$

T_θ/r_0 is the tangential strain and p is the corresponding external stress per unit radius. In the equation above we assumed that the Poisson ratio $\sigma_p = 1/2$.

A plot of p is shown in Figure 7.4. From the figure and from (7.17) it is seen that the relation between p and A is almost linear but with a slight curvature, however, opposite to what it is supposed to. For comparison see Figure 7.3. However, since the curvature is small the error is not significant. Furthermore, the wave-speed $c(x, t)$ decreases with an increased pressure.

$$c^2 = \frac{A}{\rho} \frac{dp}{dA} = c_0^2 - \frac{p}{2\rho}$$

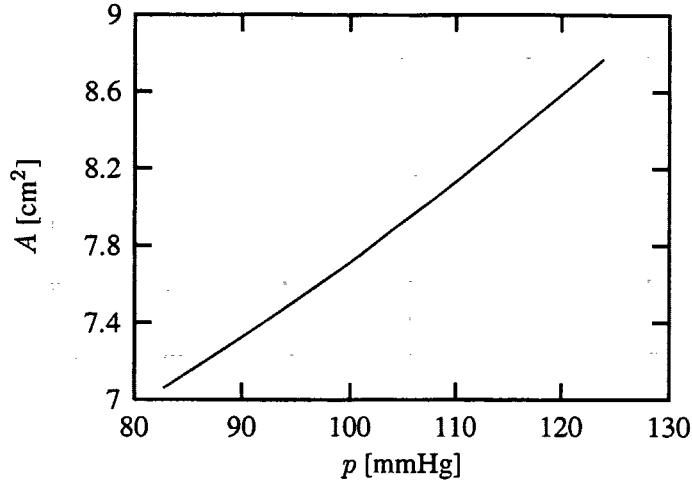


Figure 7.4: Pressure versus cross-sectional area using a simple model based on linear elasticity.

where $c_0 = \sqrt{2Eh/(3\rho r_0)}$ is the Moens-Korteweg wave-speed. This expression for the wave-speed is derived in Section 7.4.

This model has been used in many of the previous one-dimensional models of the larger arteries. They vary slightly but are all on the form

$$p = k \frac{Eh}{r_0} \left(1 - \frac{A_0^m}{A^m} \right) h_0$$

where k , m , and h_0 are non-dimensional constants. h_0 is a correction factor taking the thickness of the wall into account (Lambert, 1958; Streeter et al., 1963; Olsen and Shapiro, 1967; Wemple and Mockros, 1972; Schaaf and Abbrecht, 1972; Taylor and Gerrard, 1977; Gerrard, 1981; Mazumdar, 1989; Nichols and O'Rourke, 1998; Belardinelli and Cavalcanti, 1992). Finally, Lighthill (1989) imposed the condition

$$p = \frac{Eh}{r_0} \left(\sqrt{\frac{A}{A_0}} - 1 \right)$$

The reason why this expression differs from the equation above is that (7.18) between the tangential strain and p is approximated by

$$\frac{T_\theta}{r_0} = \frac{Eh}{r_0} \frac{r - r_0}{r_0}$$

In this case the Poisson ratio $\sigma_p = 0$ and the relative expansion of the radius is

$$\frac{r - r_0}{r} \approx \frac{r - r_0}{r_0}$$

However, the behavior of the wave-speed using Lighthill's expression is qualitatively correct; an increasing wave-speed with an increasing pressure.

$$c^2 = \frac{A}{\rho} \frac{dp}{dA} = c_0^2 + \frac{p}{2\rho}$$

where as before c_0 is the Moens-Korteweg wave-speed.

7.2.2 Ad-Hoc models

Pedley (1980), Anliker et al. (1978), Stettler et al. (1981), Jones (1973), and Forbes (1981), among others, derive a state equation from the following empirical function for the wave-speed.

$$c^2 = \frac{A}{\rho} \frac{dp}{dA} = (c_0 + c_1 p)^2 (1 + nx)^2 \quad (7.19)$$

where c_0 , c_1 , and n are constants estimated by fits to experimental measurements. It should be emphasized that the parameters as such do not have a physiological meaning. Integration of (7.19) gives

$$p = \rho c(p, x) c(p_0, x) \log \left(\frac{A}{A_0} \right) + p_0$$

By definition the wave-speed above has the right qualitative behavior, i.e. an increasing pressure leads to an increasing wave-speed.

Werff (1974) derives a state equation fitted from measurements of the static pressure versus volume for the aorta

$$p = \rho c_n^2 \tanh^{-1} \left(\frac{A}{A_0} - 1 \right) + p_0$$

where $c_n(x) = c_0 \exp\{kx/r_0\}$, k is the "wave-speed factor", A_0 is the mean cross-sectional area, p_0 is the mean pressure, c_0 is the mean wave-speed, and r_0 is the mean radius; all evaluated at $x = 0$. It should be noted that these definitions differs from our usual definitions where the quantities with subscript 0 refer to the state with zero transmural pressure. This model also has the right qualitative behavior; the wave-speed

$$c^2 = \frac{A}{\rho} \frac{\partial p}{\partial A} = \frac{c_n^2}{2 - A/A_0}$$

increases when the cross-sectional area (and hence pressure) is increased.

Finally, there are a number of models based on measurements of the arterial compliance. We will discuss two of these. They are based on the same idea, but yields results which have somewhat different characteristics.

The simpler of the two is given by Raines et al. (1974). They assume that the arterial compliance $C(x, t)$ is given by

$$C = \frac{\partial A}{\partial p} = \frac{b}{p} \quad (7.20)$$

where b is taken to be constant over a limited range of arteries. The paper emphasizes that the expression above is only valid for a normal physiological range of parameters i.e. pressures ranging from approximately 50–200 mmHg. Integration of (7.20) yields

$$p = p_0 \exp \left(\frac{A - A_0}{b} \right)$$

It is possible to determine b from measurements of the vessel distensibility, i.e. by estimating the change in cross-sectional area per 50 mmHg. This estimate is denoted

by a . From the equation above it is then possible to obtain a relation between a and b . For a pressure change from $p_l = 75$ mmHg, to $p_h = 125$ mmHg

$$a = p_m \frac{b}{A_0} \log \left(\frac{p_h}{p_l} \right) = \frac{p_1}{A_0} b$$

where p_m is the mean pressure and $p_1 = p_m \log(p_h/p_l)$.

In general a can be found in two ways either by direct measurements or by measuring the wave-speed which is given by

$$c^2 = \frac{A}{\rho} \frac{\partial p}{\partial A} = \frac{p}{\rho} \left(\frac{p_1}{a} + \log \left(\frac{p}{p_0} \right) \right)$$

In fact Raines et al. (1974) advocate the latter way for finding a because they have found that this is more precise. The state equation also shows the right qualitatively behavior; an increasing pressure with an increasing wave-speed.

Finally, we mention the model by Langewouters et al. (1984). It is also based on measurements of the arterial compliance. This model resembles much the one suggested by Werff (1974), however, it is based on compliance measurements instead of measurements for static pressure versus volume. It follows the same idea as Raines et al. (1974) but with a more sophisticated model assuming that

$$C = \frac{\partial A}{\partial p} = \frac{1}{a + bp + cp^2} \quad (7.21)$$

Let

$$\begin{aligned} a(r_0) &= \left(1 + \frac{p_0^2}{p_1^2} \right) / C_m \\ b(r_0) &= -\frac{2p_0}{p_1 C_m} \\ c(r_0) &= \frac{1}{p_1^2 C_m} \end{aligned}$$

where r_0 is the radius at zero transmural pressure and p_0 , p_1 , and C_m are parameters dependent on r_0 . Using these parameters (7.21) can be rewritten as

$$C = \frac{\partial A}{\partial p} = \frac{C_m}{1 + \left(\frac{p-p_0}{p_1} \right)^2} \quad (7.22)$$

Langewouters et al. (1984) derive the relation for a given artery and hence the parameters do not depend on r_0 . However, the model cannot be extended to comprise all of the larger arteries without taking this into account. By integration with respect to p equation (7.22) becomes

$$A = p_1 C_m \tan^{-1} \left(\frac{p-p_0}{p_1} \right) + A_2 \quad (7.23)$$

where $A_2(r_0)$ is the integration constant. Assuming that $\lim_{p \rightarrow -\infty} A = 0$ then $A_2(r_0) = \pi p_1 C_m / 2$. Thus, equation (7.23) can be written as

$$A = A_m \left(\frac{1}{2} + \frac{1}{\pi} \tan^{-1} \left(\frac{p-p_0}{p_1} \right) \right) \quad (7.24)$$

where $A_m(r_0) = \pi p_1 C_m$ represents the maximal cross-sectional area of the given artery at high pressures at a given site. This is referred to as the "max area". p_0 is the pressure at the inflection point of the pressure cross-sectional area curve for a given r_0 . $A = A_m/2$ for $p = p_0$, at this point the compliance is maximal and hence p_0 is called the "max-C-pressure". Finally, p_1 represents the steepness of rise of the compliance. When $p = p_0 \pm p_1$ the compliance is halved $C = C_m/2$ and hence p_1 is called the "half-width pressure". It is possible to estimate A_m , p_0 , and p_1 from data. However, in order to determine how these parameters depend on r_0 results from a number of vessels are needed and this is not easy to obtain (Wiinberg, 1996–1997). Now, p can be found by inverting equation (7.24). Hence,

$$p = p_0 + p_1 \tan \left(\pi \left(\frac{A}{A_m} - \frac{1}{2} \right) \right) \quad (7.25)$$

and the wave-speed is given by

$$c^2 = \frac{A}{\rho} \frac{\partial p}{\partial A} = \frac{\pi p_1 A}{\rho A_m \cos^2(\theta)}$$

where

$$\theta = \pi \left(\frac{A}{A_m} - \frac{1}{2} \right)$$

Also in this case the wave-speed increases with an increased pressure as it is supposed to, but, only for $p > p_0$. However, p_0 is usually small, of order 20–40 mmHg, depending on age, so within the physiological range of pressures the behavior of the model is correct.

There are a number of papers advocating this model, e.g. Gizdulich and Wesseling (1988), Tardy et al. (1991), Laurent, Hayoz, Trazzi, Boutouyrie, Waeber, Omboni, Brunner, Mancina and Safer (1993), or Wesseling, Jansen, Settels and Schreuder (1993). Tardy et al. (1991) compares a number of models and with their data the model is significantly better.

7.3 Coupling the state equation to the fluid dynamic equations

The state equation suggested by Langewouters et al. (1984) has proved to behave well for the thoracic and abdominal aorta. However, because of lack of data we were not able to estimate the parameters to apply it for all systemic arteries. Provided that data for all relevant arteries can be obtained, this is the model we recommend. However, because of the lack of data we have chosen to use the model by Barnard et al. (1966) but with an Young's modulus which depends on the vessel radius r_0 , i.e. the radius at zero transmural pressure. Specifically, we set

$$\frac{Eh}{r_0} = k_1 \exp(k_2 r_0) + k_3$$

as shown in (5.4), and then we use

$$p(r_0, A) = \frac{4}{3} \frac{Eh}{r_0} \left(1 - \sqrt{\frac{A_0}{A}} \right) \quad (7.26)$$

together with the fluid dynamic equations (7.12) and (7.13) or as stated on conservation form in (7.16). In order to couple the state equation to the fluid dynamic equations the following quantities should be determined

$$\begin{aligned} p(r_0, A) & \quad B(r_0, p) = \frac{1}{\rho} \int A \, dp \\ \frac{\partial p}{\partial A}(r_0, A) & \quad \frac{\partial B}{\partial A}(r_0, p) \\ \frac{\partial p}{\partial x}(r_0, A) & \quad \frac{\partial B}{\partial x}(r_0, p) \\ & \quad \frac{\partial^2 B}{\partial A \partial x}(r_0, p) \end{aligned}$$

Using (7.26) and the shorthand notation $f(r_0) = 4Eh/(3r_0)$ yields

$$\begin{aligned} \frac{\partial p}{\partial A} &= \frac{f}{2} \sqrt{\frac{A_0}{A^3}} \\ \frac{\partial p}{\partial r_0} \frac{dr_0}{dx} &= \left(\frac{df}{dr_0} \left(1 - \sqrt{\frac{A_0}{A}} \right) - f \sqrt{\frac{\pi}{A}} \right) \frac{dr_0}{dx} \\ B &= \frac{1}{\rho} \int A \, dp = \frac{f A_0}{\rho(1-p/f)} = \frac{f}{\rho} \sqrt{A_0 A} \\ \frac{\partial B}{\partial A} &= \frac{f}{2\rho} \sqrt{\frac{A_0}{A}} \\ \frac{\partial B}{\partial r_0} \frac{dr_0}{dx} &= \frac{1}{\rho} \left(\frac{2\pi r_0 f + A_0 \frac{df}{dr_0}}{1-p/f} + \frac{A_0 p}{f(1-p/f)^2} \frac{df}{dr_0} \right) \frac{dr_0}{dx} \\ &= \frac{1}{\rho} \left(2\sqrt{A} \left(\sqrt{\pi} f + \sqrt{A_0} \frac{df}{dr_0} \right) - A \frac{df}{dr_0} \right) \frac{dr_0}{dx} \\ \frac{\partial^2 B}{\partial r_0 \partial A} \frac{dr_0}{dx} &= \frac{1}{\rho} \left(\frac{f \sqrt{\pi} + \sqrt{A_0} \frac{df}{dr_0}}{\sqrt{A}} - \frac{df}{dr_0} \right) \frac{dr_0}{dx} \end{aligned}$$

Inserting these definitions in (7.16) gives the total system of equations

$$\begin{aligned} \frac{\partial}{\partial t} \begin{pmatrix} A \\ q \end{pmatrix} + \frac{\partial}{\partial x} \begin{pmatrix} q \\ \frac{q^2}{A} + \frac{f}{\rho} \sqrt{A_0 A} \end{pmatrix} &= \\ \begin{pmatrix} -\Psi \\ -\frac{2\pi\nu q R}{\delta A} - \Psi \frac{q}{A} + \frac{1}{\rho} \left(2\sqrt{A} \left(\sqrt{\pi} f + \sqrt{A_0} \frac{df}{dr_0} \right) - A \frac{df}{dr_0} \right) \frac{dr_0}{dx} \end{pmatrix} & \end{aligned} \quad (7.27)$$

7.4 Characteristic equations

Using (7.26) equations (7.12–7.13) can be rewritten as

$$\frac{\partial A}{\partial t} + \frac{\partial q}{\partial x} + \Psi = 0 \quad (7.28)$$

$$\frac{\partial q}{\partial t} + \frac{\partial}{\partial x} \left(\frac{q^2}{A} \right) + \frac{A}{\rho} \frac{\partial p}{\partial r_0} \frac{\partial r_0}{\partial x} + \frac{A}{\rho} \frac{\partial p}{\partial A} \frac{\partial A}{\partial x} + \frac{2\pi\nu q R}{\delta A} + \frac{q}{A} \Psi = 0 \quad (7.29)$$

or from (7.27) on conservation form: For appropriate choices of Ψ this form a system of hyperbolic quasi-linear first-order partial differential equations. In order to show that they are quasi-linear first-order partial differential equations they must have the form

$$\frac{\partial \mathbf{w}}{\partial t} + \mathbf{A} \frac{\partial \mathbf{w}}{\partial x} = \mathbf{B} \quad (7.30)$$

where $\mathbf{w} = (A, q)^T$, and \mathbf{A} and \mathbf{B} are functions of (x, t) , and \mathbf{w} . In order to show that they are hyperbolic the eigenvalues of \mathbf{A} must be real.

Assuming that there is no outflow, i.e. the walls move with the fluid $\Psi = \Psi_P = 0$. This applies for the larger arteries since they are almost impermeable. Hence, all outflow is localized to the top and bottom of the vessel. Thus, these equations can be applied to all branches of the larger arteries.

$$\frac{\partial A}{\partial t} + \frac{\partial q}{\partial x} = 0 \quad (7.31)$$

$$\frac{\partial q}{\partial t} + \frac{\partial}{\partial x} \left(\frac{q^2}{A} \right) + \frac{A}{\rho} \frac{\partial p}{\partial x} = -\frac{2\pi\nu q R}{\delta A} \quad (7.32)$$

Expanding the terms $\partial p/\partial x$ and $\partial(q^2/A)/\partial x$ gives

$$\begin{aligned} \frac{\partial A}{\partial t} + \frac{\partial q}{\partial x} &= 0 \\ \frac{\partial q}{\partial t} + \frac{2q}{A} \frac{\partial q}{\partial x} + \left(-\frac{q^2}{A^2} + \frac{A}{\rho} \frac{\partial p}{\partial A} \right) \frac{\partial A}{\partial x} &= -\frac{A}{\rho} \frac{\partial p}{\partial r_0} \frac{\partial r_0}{\partial x} - \frac{2\pi\nu q R}{\delta A} \end{aligned}$$

If \mathbf{w} , \mathbf{A} and \mathbf{B} is defined as below it is possible to obtain the desired form

$$\mathbf{w} = \begin{bmatrix} A \\ q \end{bmatrix} \quad (7.33)$$

and

$$\mathbf{A} = \begin{bmatrix} 0 & 1 \\ -\frac{q^2}{A^2} + \frac{A}{\rho} \frac{\partial p}{\partial A} & \frac{2q}{A} \end{bmatrix} \quad (7.34)$$

Using (7.26) for p gives

$$\frac{A}{\rho} \frac{\partial p}{\partial r_0} \frac{\partial r_0}{\partial x} = \frac{A}{\rho} \left(\frac{df}{dr_0} \left(1 - \sqrt{\frac{A_0}{A}} \right) - f \sqrt{\frac{\pi}{A}} \right) \frac{dr_0}{dx} \quad (7.35)$$

Inserting

$$f = \frac{4Eh}{3r_0} = \frac{4}{3}(k_1 \exp(k_2 r_0) + k_3) \quad \text{and} \quad \frac{df}{dr_0} = \frac{4}{3}k_1 k_2 \exp(k_2 r_0)$$

Equation (7.35) can be written as

$$\frac{A}{\rho} \frac{\partial p}{\partial r_0} \frac{\partial r_0}{\partial x} = \frac{C_1 A + C_2 \sqrt{A}}{\rho}$$

where

$$C_1 = \frac{df}{dr_0} \frac{dr_0}{dx}$$

$$C_2 = - \left(\frac{df}{dr_0} \sqrt{A_0} + f \sqrt{\pi} \right) \frac{dr_0}{dx}$$

Thus, the right hand side of (7.29) becomes

$$\mathbf{B} = \begin{bmatrix} 0 \\ -(C_1 A + C_2 \sqrt{A})/\rho - C_3/A \end{bmatrix} \quad (7.36)$$

where $C_3 = 2\pi\nu q R/\delta$.

Hyperbolic equations can be analyzed by studying their characteristics which are the curves $(x(s), t(s))$ in the (x, t) plane along which the system of partial differential equations reduces to a system of ordinary differential equations. Since the partial differential equations above are non-linear, the characteristics will not be determined from the partial differential equations alone but also from their solutions. This is caused by the fact that slopes of the characteristics (the velocity of the propagation of the solution, "the system sound velocity") depends on the values of q and A , respectively. Consider the curve $(x(s), t(s))$ parameterized by s , the total derivative of \mathbf{w} is then

$$\frac{d\mathbf{w}}{ds} = \frac{\partial \mathbf{w}}{\partial x} \frac{dx}{ds} + \frac{\partial \mathbf{w}}{\partial t} \frac{dt}{ds}$$

In order to match this to the partial differential equation (7.30) one takes $t = s$ and gets $dt/ds = 1$. Hence, the curve is given by $(x(t), t)$. Let

$$c = \frac{dx}{dt} \quad (7.37)$$

Along a curve satisfying this condition any differentiable function \mathbf{w} has the form

$$\frac{d\mathbf{w}}{dt} = \frac{\partial \mathbf{w}}{\partial t} + c \frac{\partial \mathbf{w}}{\partial x} \quad (7.38)$$

Using the definitions (7.33), (7.34), and (7.36) for \mathbf{w} , \mathbf{A} , and \mathbf{B} in (7.30) together with (7.38) we get

$$\begin{pmatrix} 1 & 0 & 0 & 1 \\ 0 & 1 & -\frac{q^2}{A^2} + \frac{A}{\rho} \frac{\partial p}{\partial A} & \frac{2q}{A} \\ 1 & 0 & c & 0 \\ 0 & 1 & 0 & c \end{pmatrix} \begin{pmatrix} \partial A / \partial t \\ \partial q / \partial t \\ \partial A / \partial x \\ \partial q / \partial x \end{pmatrix} = \begin{pmatrix} 0 \\ -(C_1 A + C_2 \sqrt{A})/\rho - C_3/A \\ dA/dt \\ dq/dt \end{pmatrix}$$

or on a more compact form

$$\begin{pmatrix} \mathbf{I} & \mathbf{A} \\ \mathbf{I} & c\mathbf{I} \end{pmatrix} \begin{pmatrix} \partial \mathbf{w} / \partial t \\ \partial \mathbf{w} / \partial x \end{pmatrix} = \begin{pmatrix} \mathbf{B} \\ d\mathbf{w} / dt \end{pmatrix} \Leftrightarrow$$

$$\begin{pmatrix} \mathbf{I} & \mathbf{A} \\ 0 & c\mathbf{I} - \mathbf{A} \end{pmatrix} \begin{pmatrix} \partial \mathbf{w} / \partial t \\ \partial \mathbf{w} / \partial x \end{pmatrix} = \begin{pmatrix} \mathbf{B} \\ d\mathbf{w} / dt - \mathbf{B} \end{pmatrix}$$

This has a solution if and only if the subproblem (of order 2×2)

$$(c\mathbf{I} - \mathbf{A}) \frac{\partial \mathbf{w}}{\partial x} = \frac{d\mathbf{w}}{dt} - \mathbf{B} \quad (7.39)$$

has a solution. We are only interested in solutions along the characteristics. Recall, that a characteristic is a curve along which the expression to be integrated is independent of partial derivatives in other directions.

If the determinant of $(c\mathbf{I} - \mathbf{A})$ is non-zero we can specify \mathbf{w} arbitrarily and extend \mathbf{w} as a solution of the partial differential equations over a strip in some neighborhood of the curve (7.37). In that case, we can choose \mathbf{w} on the curve and hence determine \mathbf{B} and $d\mathbf{w}/dt$. Then we can solve for $\partial \mathbf{w} / \partial t$ and $\partial \mathbf{w} / \partial x$ which can be used to expand \mathbf{w} off the curve; but this is not a reduction of the original problem. On the other hand, if the determinant is zero then

$$|c\mathbf{I} - \mathbf{A}| = 0 \Leftrightarrow$$

$$\begin{vmatrix} c & -1 \\ \frac{q^2}{A^2} - \frac{A}{\rho} \frac{\partial p}{\partial A} & c - \frac{2q}{A} \end{vmatrix} = 0$$

gives

$$c = \frac{q}{A} \pm \sqrt{\frac{A}{\rho} \frac{\partial p}{\partial A}} = \frac{q}{A} \pm c_0 \quad (7.40)$$

where c_0^2 is the wave-speed. Hence, the equations for the characteristics are

$$\frac{dx}{ds} = \frac{q}{A} \pm c_0 \quad (7.41)$$

$$\frac{dt}{ds} = 1 \quad (7.42)$$

Note that, since c (the eigenvalues of \mathbf{A}) are real, the system of partial differential equations is hyperbolic.

Furthermore, a zero determinant implies that $\partial \mathbf{w} / \partial x$ exists only if \mathbf{B} and $d\mathbf{w} / dt$ fulfill the condition given in (7.44). This is seen by multiplying (7.39) with $\gamma^T = (\gamma_1, \gamma_2)$ yielding

$$\gamma^T (c\mathbf{I} - \mathbf{A}) \frac{\partial \mathbf{w}}{\partial x} = \gamma^T \left(\frac{d\mathbf{w}}{dt} - \mathbf{B} \right)$$

If γ^T is chosen as the left eigenvectors to $(c\mathbf{I} - \mathbf{A})$ then

$$\gamma^T (c\mathbf{I} - \mathbf{A}) \frac{\partial \mathbf{w}}{\partial x} = 0 \quad (7.43)$$

and

$$\gamma^T \left(\frac{d\mathbf{w}}{dt} - \mathbf{B} \right) = 0 \quad (7.44)$$

This is a necessary condition for the existence of a solution. Using the definition for c (7.43) gives

$$(\gamma_1, \gamma_2) \begin{bmatrix} \frac{q}{A} \pm c_0 & -1 \\ \frac{q^2}{A^2} - c_0^2 & -\frac{q}{A} \pm c_0 \end{bmatrix} = 0$$

Let $\gamma_1 = 1$, then

$$\gamma_2 = \left(-\frac{q}{A} \pm c_0 \right)^{-1}$$

From (7.44) the following system of ordinary differential equations, which is valid along the characteristics in (7.38), can be obtained

$$\begin{aligned} \left(1, \left(-\frac{q}{A} \pm c_0 \right)^{-1} \right) \left[\frac{dA}{ds} + \sqrt{A} \left(\frac{C_1 A + C_2 \sqrt{A}}{\rho} + \frac{C_3}{A} \right) \right] &= 0 \quad \Leftrightarrow \\ \frac{dA}{ds} + \left(-\frac{q}{A} \pm c_0 \right)^{-1} \frac{dq}{ds} &= H^\pm \end{aligned} \quad (7.45)$$

where

$$H^\pm = - \left(-\frac{q}{A} \pm c_0 \right)^{-1} \left(\frac{C_1 A + C_2 \sqrt{A}}{\rho} + \frac{C_3}{A} \right)$$

The result is a system of ordinary differential equations which can not be solved analytically, except in some simple cases which we will not discuss further here. Instead, we will (in Chapter 9) set up a numerical scheme based on the characteristics.

Chapter 8

Flow and pressure in the tree of larger arteries

In this chapter we derive the boundary conditions needed to establish the complete system of equations for modeling flow and pressure in the arterial tree. In addition we make the equations non-dimensional, preparing them for the numerical method described in Chapter 9.

8.1 Boundary conditions

The model derived in the previous chapter predicts blood flow and pressure for a single vessel segment only. In order to extend the model to the arterial tree some appropriate boundary conditions must be established.

The arterial tree is, as seen in Figure 3.3, a very complex structure, even when the model is limited to the larger arteries, as shown in Figure 5.1. But simplifications are obtained from the fact that the tree is binary and the vessels are one-dimensional. Therefore, three types of boundaries can be identified; one at the inflow, one at the bifurcations, and one at the terminals.

The system of equations is hyperbolic with a positive wave propagation velocity much larger than the velocity of the blood. Thus, the characteristics will cross and have opposite directions. This means that one boundary conditions is needed at each end of the vessels. Consequently, the following boundary conditions for the arterial tree must be derived:

- One equation at the inlet to the arteries, i.e. at the aortic valve. This is marked with an **A** in Figure 5.1.
- Three equations at the bifurcations; an outflow condition from the parent artery and inflow conditions to both of the daughter arteries.
- One equation specifying the outflow from each of the terminal vessels of the arterial tree. These are marked with **B** in Figure 5.1.

Each of these should be specified by an equation for either flow, pressure, or a relation between them.

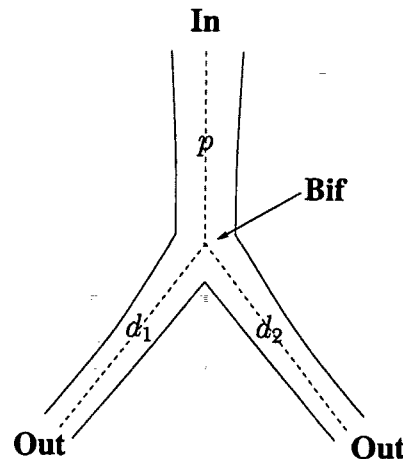


Figure 8.1: A single binary branch consisting of a parent and two daughters, even though they are depicted as symmetric they do not need to be so.

In order to describe these boundary conditions we will consider a tree with only three branches, see Figure 8.1. The inflow appears at **In** the outflows at **Out** and the bifurcation conditions are applied at **Bif**. In general, when modeling the arterial tree, the branches will be labeled as shown in Figure 5.1.

8.1.1 Inflow boundary condition

At the aortic valve practically all previous models specify the flow, i.e. $q(0, t)$, emanating from the aortic valve. This is done either directly from measurements or by deriving a function based on a simple model. Since we are interested in the qualitative behavior we have chosen the latter. Such a function can be the following periodic function based on parameters for the total cardiac output and the length of the cardiac period.

$$\begin{aligned} q(0, t) &= \bar{q}_0 t / \tau^2 \exp(-t^2 / (2\tau^2)), & 0 \leq t < T \\ q(0, t + jT) &= q(0, t), & j = 1, 2, 3, \dots \end{aligned} \quad (8.1)$$

\bar{q}_0 is the cardiac output, τ is the time at which the maximal cardiac output is reached, and T is the length of the cardiac period. The function has a jump at $t = T$, but it is of order 10^{-18} and can hence be neglected. Furthermore, it should be noted that the back-flow into the left ventricle is not included. Figure 8.2 shows $q(0, t)$ for the first three periods.

8.1.2 Bifurcation conditions

Assuming that the bifurcation takes place at a point (at **Bif**) the three conditions needed to close the system of equations should be evaluated at this point. Assuming that there is no leakage of blood at the bifurcations the in- and outflows must be balanced. Hence,

$$q_p = q_{d_1} + q_{d_2} \quad (8.2)$$

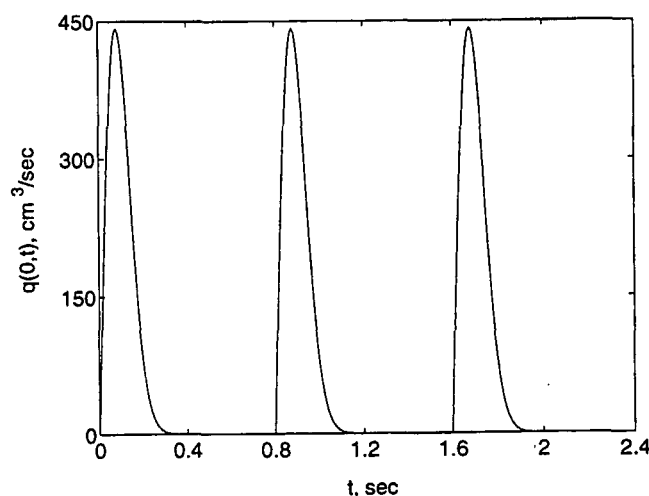


Figure 8.2: The inflow as a function of time over three periods of length 0.8 s.

The remaining conditions are found from assuming that pressure is continuous over the bifurcation, i.e. that

$$p_p = p_{d_1} = p_{d_2} \quad (8.3)$$

However, these conditions pose some questions because of the Bernoulli law that may or may not apply depending on the details of the flow pattern at the junction. At a boundary where the total cross-sectional area decreases proceeding downstream, one would, according to the Bernoulli law, expect a drop in pressure associated with the increase in velocity. In the arterial system, however, the total cross-sectional area typically increases at junctions (again, proceeding downstream towards the periphery) and hence an decrease in pressure would be expected. On the other hand, because the change in area at the junction is discontinuous, flow separation and vortex formation is expected just downstream from the bifurcation and the Bernoulli law does not apply. In these circumstances, which invoke dissipation of kinetic energy, it seems more appropriate to use pressure continuity. Alternative models of the bifurcations are discussed in Anliker et al. (1971), Stettler et al. (1981), Lighthill (1989), and Olufsen and Ottesen (1995a).

8.1.3 Outflow boundary conditions

The outflow boundary condition can be determined in several ways. We will discuss three of these approaches, a pure resistance model, a Windkessel model, and our structured tree model.

The simplest reasonable approach is to let the outflow be proportional to pressure, i.e. to let the boundary condition be determined by a pure resistive load. This is commonly used in previous studies (Olsen and Shapiro, 1967; Schaaf and Abbrecht, 1972; Anliker et al., 1971; Streeter et al., 1963; Forbes, 1981; Stettler et al., 1981). However, it is not obvious how to choose the correct value for the peripheral resistance at the points where the larger arteries are terminated. Furthermore, if we assume a constant

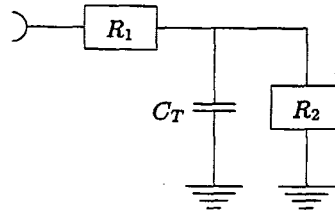


Figure 8.3: The Windkessel element model used for predicting the impedance at the terminals of the larger arteries. The resistances R_1 and R_2 and the capacitance C_T must be estimated for each of the terminal vessels.

relation between flow and pressure at the downstream boundary flow and pressure are forced to be in phase, which is generally not physiologically valid in these relatively large arteries. This is also pointed out in e.g. Anliker et al. (1978) where it is noted that the pure resistance boundary condition only applies if the arteries are sufficiently small. The problem can be seen from the hysteresis curves appearing when plotting p versus q parametrized by t and for a fixed x , see Figure 12.6 in Chapter 12. The forced in-phase condition propagates back through the vessel changing the overall slope as well as narrowing the width of the hysteresis which means that the phase is disturbed throughout the vessel. Since we are looking for some reflections in the system (just enough to produce the dicrotic wave) a small change in the hysteresis curves is expected, but not as drastic as the one appearing with this boundary condition. In order to avoid these problems, the boundary condition should incorporate a phase-shift between p and q .

Another approach is to set up a model based on the basic properties for the impedance. This has been accomplished by Wemple and Mockros (1972), Raines et al. (1974), and Stergiopoulos et al. (1992) among others. They derive an outflow condition by attaching a three-element Windkessel model at the boundary. Such a model represents the resistance and elasticity of the vessels by an electrical analog model consisting of a resistance in series with a parallel combination of a resistance and a capacitor, the resistances $R_1 + R_2$ simulates the total resistance and the capacitor C_T simulates the compliance of the vascular bed. This circuit is shown in Figure 8.3. The frequency dependent impedance of the Windkessel model is given by

$$Z(0, \omega) = \frac{R_1 + R_2 + i\omega C_T R_1 R_2}{1 + i\omega C_T R_2} \quad (8.4)$$

where the parameters C_T , R_1 , and R_2 are the volume compliance and resistances as shown in Figure 8.3. Transforming this to the time domain gives the following differential equation.

$$\frac{\partial p}{\partial t} = R_1 \frac{\partial q}{\partial t} - \frac{p}{R_2 C_T} + \frac{q(R_1 + R_2)}{R_2 C_T} \quad (8.5)$$

In order to apply the boundary condition three parameters must be specified. That could be the total peripheral resistance $R_T = R_1 + R_2$, the fraction R_1/R_T , and the total compliance C_T . The total peripheral resistances for each of the terminals can be found in Schaaf and Abbrecht (1972) and Stergiopoulos et al. (1992). They are found

from estimates of the total arterial peripheral resistance and the distribution of flow to the various branches. The ratio R_1/R_T was taken to be approximately 0.2. This has been estimated in Raines et al. (1974) by fit to data. Finally, the arterial compliance C_{T_i} for each segment was estimated from the total volume compliance (Westerhof et al., 1969). These parameters are listed in Table 12.1.

Such a model can not include the wave propagation effects in the part of the arterial system that it models and it should also be shown whether it is able to capture the phase-lag between p and q adequately. Therefore, we have investigated how the physical domain extends beyond the boundary of the larger arteries. As discussed in Chapter 6 the smaller arteries comprise a large asymmetric tree with a varying number of generations, ranging to approximately 24 generations before the arteriolar level is reached. At this point, however, all vessels have approximately the same diameter. Beyond this point loops are formed and the structure becomes too complex to easily describe the geometry. In Chapter 6 we showed that the smaller arteries can be modeled as an asymmetric structured binary tree.

It would be too comprehensive to compute the full non-linear model of such a tree. Therefore, a more appropriate strategy is to describe flow and pressure in these smaller arteries using a simpler model that can be solved analytically, e.g. a linear model. From these sub-trees for the smaller arteries it is possible to obtain a boundary condition for the system of non-linear equations as a time dependent relation between flow and pressure. These sub-trees of smaller arteries are treated as a structured tree of straight vessels in which the corresponding linear equations are solved, this was described in detail in Chapter 6. From these solutions it is possible, using Fourier analysis, to determine a dynamic impedance, which can be used to get a relation between flow and pressure.

The three boundary conditions discussed here, the pure resistance model, the Windkessel model, and the structured tree model will be compared in Section 12.2.

For any Fourier mode, the frequency dependent impedance $Z(x, \omega)$ (e.g. obtained by the structured tree model, see Chapters 10 and 11) can be related to pressure and flow by

$$P(x, \omega) = Z(x, \omega)Q(x, \omega) \quad (8.6)$$

where we have used the terminology of electrical networks, with P playing the role of voltage and Q the role of current.

Because the inflow boundary condition is periodic we assume that flow and pressure can be expressed using complex periodic Fourier series. Then any feature of the system response can be determined separately for each term. Let

$$p(x, t) = \sum_{k=-\infty}^{\infty} P(x, \omega_k) e^{i\omega_k t} \quad (8.7)$$

$$q(x, t) = \sum_{k=-\infty}^{\infty} Q(x, \omega_k) e^{i\omega_k t} \quad (8.8)$$

where $\omega_k = 2\pi k/T$ is the angular frequency and

$$P(x, \omega_k) = \frac{1}{T} \int_{-T/2}^{T/2} p(x, t) e^{-i\omega_k t} dt \quad (8.9)$$

$$Q(x, \omega_k) = \frac{1}{T} \int_{-T/2}^{T/2} q(x, t) e^{-i\omega_k t} dt \quad (8.10)$$

By inverse Fourier transform the results for $Z(x, \omega)$ can then be transformed to obtain $z(x, t)$. By the convolution theorem it is then possible to arrive at an analytic relation between p and q :

$$p(x, t) = \int_{t-T}^t q(x, \tau) z(x, t - \tau) d\tau \quad (8.11)$$

This is our new outflow boundary condition for the larger arteries which should be evaluated at each of the terminals, marked by B in Figure 5.1, i.e. at $x = L_i$ where L_i is the length of the i th terminal segment.

How the convolution integral will be evaluated when solving the model of the entire arterial tree, consisting both of the smaller and the larger arteries, will be described in Chapter 9.

8.2 Non-dimensional formulation

Before solving or analyzing the equations in further detail it is convenient to make the equations non-dimensional. In order to do so, the following characteristic parameters are applied:

- $r_c = 1$ cm, the characteristic radius of the vessels.
- $q_c = 10$ cm³/s, the characteristic flow through aorta.
- $\rho = 1.06$ g/cm³, the density of the blood.

The latter two parameters are used in order to determine the characteristic pressure $\rho(q_c/r_c^2)^2$. Using these the following non-dimensional quantities can be defined:

$$\begin{aligned} \tilde{x} &= \frac{x}{r_c} & \tilde{t} &= \frac{t q_c}{r_c^3} \\ \tilde{r}_0 &= \frac{r_0}{r_c} & \tilde{A} &= \frac{A}{r_c^2} \\ \tilde{q} &= \frac{Q}{q_c} & \tilde{p} &= \frac{p r_c^4}{\rho q_c^2} \end{aligned}$$

The non-dimensional form of (7.31) is then given by

$$\frac{\partial(\tilde{A} \tilde{r}_c^2)}{\partial(\tilde{t} \tilde{r}_c^3 / q_c)} + \frac{\partial(\tilde{q} q_c)}{\partial(\tilde{x} r_0)} = 0$$

Dividing by q_c/r_c gives

$$\frac{\partial \tilde{A}}{\partial \tilde{t}} + \frac{\partial \tilde{q}}{\partial \tilde{x}} = 0 \quad (8.12)$$

The non-dimensional momentum equation (7.32) is

$$\frac{\partial(\tilde{q} q_c)}{\partial(\tilde{t} r_c^3/q_c)} + \frac{\partial}{\partial(\tilde{x} r_c)} \left(\frac{\tilde{q}^2 q_c^2}{\tilde{A} r_c^2} \right) + \frac{\tilde{A} r_c^2}{\rho} \frac{\partial(\tilde{p} \rho q_c^2/r_c^4)}{\partial(\tilde{x} r_c)} = -2\pi\nu \frac{\tilde{q} q_c}{\tilde{A} r_c^2} \frac{\tilde{r} r_c}{\tilde{\delta} r_c}$$

Multiplying by r_c^3/q_c^2 and inserting the Reynolds number $\mathcal{R} = \rho q_c/(\mu r_c) = q_c/(\nu r_c)$ yields

$$\frac{\partial \tilde{q}}{\partial \tilde{t}} + \frac{\partial}{\partial \tilde{x}} \left(\frac{\tilde{q}^2}{\tilde{A}} \right) + \tilde{A} \frac{\partial \tilde{p}}{\partial \tilde{x}} = -\frac{2\pi\tilde{r}}{\delta\mathcal{R}} \frac{\tilde{q}}{\tilde{A}} \quad (8.13)$$

If we drop the tildes the non-dimensional equations (8.12) and (8.13) can be rewritten as

$$\begin{aligned} \frac{\partial A}{\partial t} + \frac{\partial q}{\partial x} &= 0 \\ \frac{\partial q}{\partial t} + \frac{\partial}{\partial x} \left(\frac{q^2}{A} \right) + A \frac{\partial p}{\partial x} &= -\frac{2\pi r}{\delta\mathcal{R}} \frac{q}{A} \end{aligned} \quad (8.14)$$

As for the continuity equation the state equation and the equations for the boundary conditions can be written directly in terms of the non-dimensional quantities.

Using these quantities equations (8.14) can be rewritten on conservation form. Hence,

$$\begin{aligned} \frac{\partial}{\partial t} \begin{pmatrix} A \\ q \end{pmatrix} + \frac{\partial}{\partial x} \begin{pmatrix} q \\ \frac{q^2}{A} + f\sqrt{A_0 A} \end{pmatrix} &= \\ \left(-\frac{2\pi r}{\delta\mathcal{R}} \frac{q}{A} + \left(2\sqrt{A} \left(\sqrt{\pi} f + \sqrt{A_0} \frac{df}{dr_0} \right) - A \frac{df}{dr_0} \right) \frac{dr_0}{dx} \right) \end{pmatrix} &= 0 \end{aligned} \quad (8.15)$$

Chapter 9

Numerical methods for the larger arteries

In Chapter 7 we saw that the fluid dynamic equations for the larger arteries are quasi-linear and hyperbolic. Such a system can be solved numerically with several methods ranging from first-order finite difference schemes such as the method of characteristics to implicit methods. One should keep in mind that the wave-propagation is fast (of order 10 m/s) so the method will have to operate with relatively small time-steps. The most optimal approach to solve this system would be to use some implicit scheme which would make it possible to use large time-steps. However, since our focus is on the model, not the implementation, we have used explicit schemes which are much simpler to implement. Hence, our simulations are based on Richtmeyer's two-step version of the Lax-Wendroff method (henceforth simply referred to as the Lax-Wendroff method), but we use a first order method of characteristics for the right boundary, i.e. at the terminals of the larger arteries. Numerical experiments suggest that this choice ensures stable computations at the right boundary. In the following sections we describe both the method of characteristics and the Lax-Wendroff method. Finally, in Section 9.3 we discuss the convergence of the two methods for a single vessel.

9.1 Numerical method of characteristics

The ordinary differential equations (7.45) can be solved numerically using a method of characteristics based on specified intervals, i.e. on a fixed grid. Such a grid is shown in Figure 9.1. This grid has lines parallel to the axis whereas the method of characteristics in general uses a grid where the lines follow the characteristics. However, since we are interested in the propagation of the solution for fixed time-steps the fixed grid, or specified intervals, this approach has been chosen. Therefore, let $\Delta x = L/M$ where L is the length of the vessel and M is the number of points along the x -axis, denote the spatial discretization and $\Delta t = T/N$ where T is the length of the period and N is the number of time-steps in the period, denote the time-discretization. Hence, the solution is approximated at grid-points $(m\Delta x, n\Delta t)$ for $m = 0, 1, \dots, M$ and $n = 0, 1, \dots, N$.

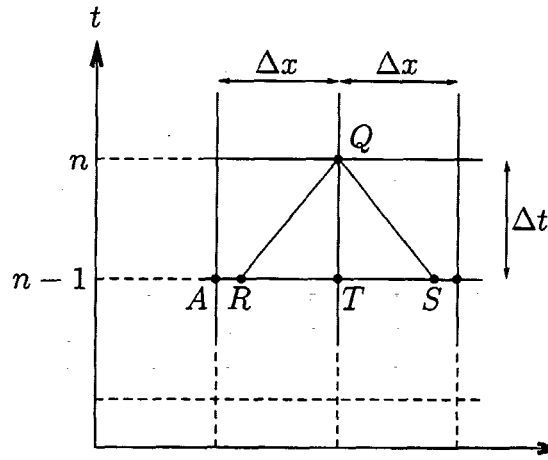


Figure 9.1: The figure shows the points of interest in the specified interval grid.

9.1.1 The interior

In order to find the solution, the system of ordinary differential equations (7.45), valid along the characteristics, should be approximated at any given point in the grid. Locally, the characteristics can be approximated at any given point Q at time-level n by straight lines with slopes determined by the characteristic wave speeds. These must intersect the line segments $|AT|$ and $|TB|$, respectively, in order for the numerical method to be convergent, see Figure 9.1. This is the geometrical expression of the requirement that the numerical domain of dependence should include the physical domain of dependence for any point in the (x, t) plane. If this is not possible Δx must be increased or Δt must be decreased. The points of intersection on the previous time-level $n - 1$ are called R and S respectively. Since the time-level can be inferred implicitly from the notation of the points Q , R , and S the dependent variables will not have the time indicated unless it is required by some special situation, e.g. $A_Q := A_Q^n$. The grid is shown in Figure 9.1. Using these definition the ordinary differential equations (7.45) together with the characteristic equations (7.41) and (7.42) can be solved. At the curve defined by $(x(t), t)$ Equation (7.42) can be approximated by

$$\Gamma_+ : \begin{cases} A_Q - A_R + \frac{q_Q - q_R}{-q_R/A_R + c_R} = H_R^+ \Delta t \\ x_Q - x_R = \left(\frac{q_R}{A_R} + c_R \right) \Delta t \end{cases} \quad (9.1)$$

$$\Gamma_- : \begin{cases} A_Q - A_S + \frac{q_Q - q_S}{-q_S/A_S - c_S} = H_S^- \Delta t \\ x_Q - x_S = \left(\frac{q_S}{A_S} - c_S \right) \Delta t \end{cases} \quad (9.2)$$

Thus, the problem stated in (7.45) is reduced to the treatment of the equations above. Assuming that the values of q and A are known at the points A, B and T then they can be determined at the point Q . In order to do so the terms A, q, c , and H must first be determined at S and R , respectively. Let η be either of the terms A, q, c , or H at R

then by linear interpolation

$$\frac{\eta_T - \eta_R}{\eta_T - \eta_A} = \frac{x_T - x_R}{x_T - x_A} \quad (9.3)$$

and

$$\frac{\eta_T - \eta_S}{\eta_T - \eta_B} = \frac{x_T - x_S}{x_T - x_B} \quad (9.4)$$

Multiplying (9.3) by $(q_Q/A_R \pm c_R)$ and $(dx/dt)^{-1} = (t_T - t_A)/(x_T - x_R) = (q_R/A_R + c_R)^{-1}$ gives

$$\eta_R = \eta_T - (\eta_T - \eta_A) \left(\frac{q_S}{A_S} + c_S \right) \theta_l$$

where $\theta_l = (t_Q - t_T)/(x_T - x_A)$. Similarly, (9.4) yields

$$\eta_S = \eta_T - (\eta_T - \eta_B) \left(\frac{q_S}{A_S} - c_S \right) \theta_s$$

where $\theta_r = (t_Q - t_T)/(x_T - x_B)$. Assuming that the spacing between the grid-points is equidistant then $\theta_l = \theta_r = \Delta t / \Delta x$. This only applies if

$$\frac{\Delta t}{\Delta x} \leq \left| \frac{q_i}{A_i} \pm c_i \right|^{-1} \quad \text{for } i = R, S$$

This is the so-called CFL-condition named after Courant, Friedrichs, and Lewy (Courant, Friedrichs and Lewy, 1928).

Substituting these expressions into (9.1) and (9.2) gives the following expressions for q_Q and A_Q , respectively.

$$q_Q = \left(\frac{1}{c_R - q_R/A_R} + \frac{1}{c_S + q_S/A_S} \right)^{-1} \quad (9.5)$$

$$\left(A_R - A_S + \frac{q_R}{c_R - q_R/A_R} + \frac{q_S}{c_S + q_S/A_S} + (H_R^+ - H_S^-) \Delta t \right)$$

and

$$A_Q = \left(c_R - \frac{q_R}{A_R} + c_S + \frac{q_S}{A_S} \right)^{-1} \quad (9.6)$$

$$\left(q_R - q_S + \left(c_R - \frac{q_R}{A_R} \right) A_R + \left(c_S + \frac{q_S}{A_S} \right) A_S + \right.$$

$$\left. \left(H_R^+ \left(c_R - \frac{q_R}{A_R} \right) + H_S^- \left(c_S + \frac{q_S}{A_S} \right) \right) \Delta t \right)$$

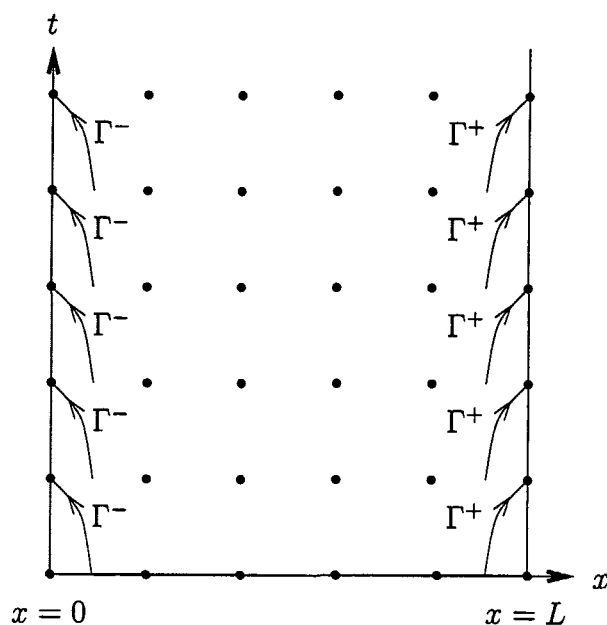


Figure 9.2: On the left boundary $x = 0$ only the Γ^- characteristics flow into the boundary as time increases. Analogously only the Γ^+ characteristics flow into the right boundary $x = L$.

9.1.2 Boundary conditions

At either of the boundaries, only one characteristic flows into the boundary as time increases, see Figure 9.2. Because there are two dependent variables (q and A) and because the characteristics are pointing in opposite directions one boundary condition is needed at each end of any vessel, i.e. at the inflow, at the bifurcations, and at the terminals of the arterial tree. The equations for these boundary conditions are as derived in Chapter 8. The numerical scheme for the bifurcation conditions uses the same approach as the one for the right boundary. Therefore, and because we do not use the method of characteristics for the entire arterial tree we will not describe this part of the numerical scheme in detail.

Inflow boundary condition

The inflow boundary condition, i.e. at $x_Q = 0$, can as discussed in Section 8.1, be modeled using the following periodic function

$$\begin{aligned} q(0, t) &= \bar{q}_0 t / \tau^2 \exp(-t^2 / (2\tau^2)), & 0 \leq t < T \\ q(0, t + jT) &= q(0, t), & j = 1, 2, 3, \dots \end{aligned} \quad (9.7)$$

where \bar{q}_0 is the cardiac output, τ is the time at which the maximal cardiac output is reached, and T is the length of the cardiac period. The discretization of the left

boundary condition only involves the negative characteristic Γ^- , i.e. the equations

$$\begin{aligned} x_Q - x_S &= (q_Q/A_S - c_S) \Delta t \\ A_Q - A_S + \frac{q_Q - q_S}{-q_S/A_S - c_S} &= H_S^- \Delta t \end{aligned} \quad (9.8)$$

where q_S , A_S , c_S and H_S^- are calculated as for the interior points and q_Q are determined using (9.7).

Outflow boundary condition

The outflow boundary condition for the larger arteries should be evaluated at each of the terminals marked by B in Figure 5.1, i.e. at $x_Q = L_i$ where L_i is the length of the i 'th terminal segment. It is determined from the convolution integral in (8.11). This can be rewritten in terms of the Fourier transform of the admittances $Y(x_Q, \omega) = Z(x_Q, \omega)^{-1}$, giving

$$q(x_Q, t) = \int_0^T p(x_Q, t - \tau) y(x_Q, \tau) d\tau \quad (9.9)$$

Since $t = n\Delta t = T/N$ where T is the length of the period and N is the number of time-steps and Δt is the length of the time-step. Then the equation above can be discretized by

$$\begin{aligned} q(x_Q, n\Delta t) = q_Q^n &= \sum_{k=0}^{N-1} p_Q^{<n-k>_N} y_Q^k \Delta t \\ &= p(Q, A_Q) y_Q^0 \Delta t + \sum_{k=1}^{N-1} p_Q^{<n-k>_N} y_Q^k \Delta t \end{aligned} \quad (9.10)$$

where N the symbol $<\cdot>_N$ denotes the modulus function defined such that $<n>_N \in \{0, 1, \dots, N-1\}$ for all $n \in \mathbb{Z}$, $N > 0$ and $p(Q, A_Q) = p(r_0(x_Q), A(x_Q, n\Delta t)) = p(x_Q, n\Delta t)$ should be evaluated using the state equation from (7.26). In practice the modulus is implemented by choosing values from the previous period when $n - k < 0$ and values from this period when $n - k \geq 0$. This is shown in Figure 9.4.

When initializing the computations p and q for $t = [0; T]$ contain the initial values; the flow and transmural pressure are zero. This is not physiological, and hence the pressure and flow profiles are not immediately reliable. Therefore, the model needs a few periods to stabilize itself. However, as shown in Figure 9.3 the simulations converges after only a few periods. The discretization of the right boundary condition only involves the positive characteristic Γ^+ . Hence,

$$\begin{aligned} x_Q - x_R &= \left(\frac{q_R}{A_R} + c_R \right) \Delta t \\ A_Q - A_R + \frac{q_Q - q_R}{-q_R/A_R + c_R} &= H_R^+ \Delta t \end{aligned} \quad (9.11)$$

Let

$$(q_{tms})^n = \sum_{k=1}^{N-1} p_Q^{<n-k>_N} y_Q^k \Delta t$$

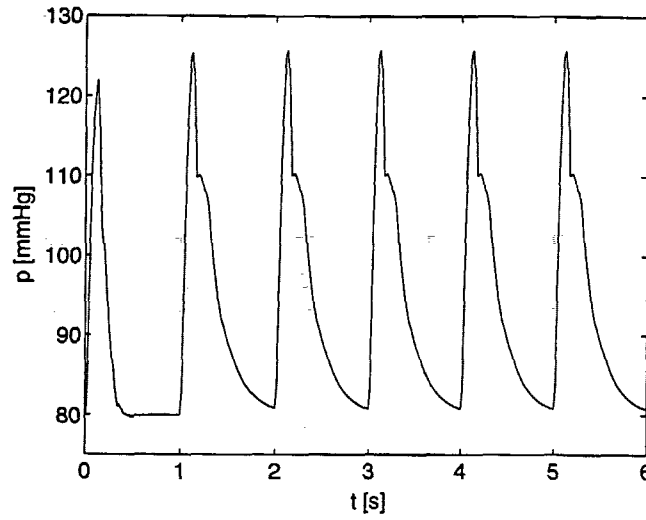


Figure 9.3: The pressure profiles stabilize after a few periods.

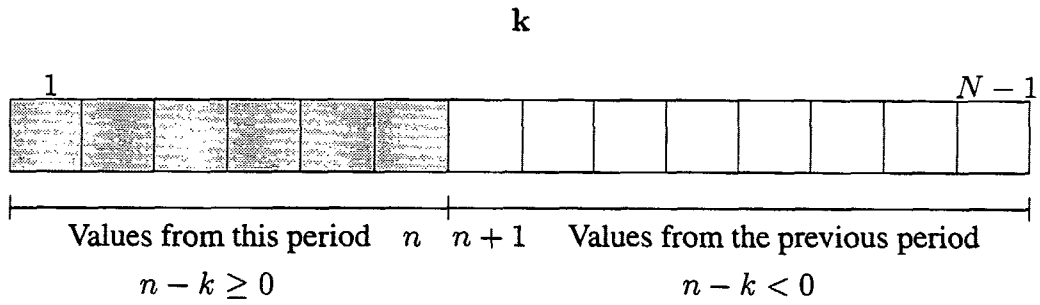


Figure 9.4: The discretized convolution integral runs over a whole period. For a given time $t = n\Delta t$ the values for p predicted from this period is used for $k = 1, \dots, n$ and the values predicted in the previous period for $k = n + 1, \dots, N - 1$.

then (9.11) can be written as

$$A_Q - A_R + \frac{p(Q, A_Q) y_Q^0 \Delta t + q_{tms}^n - q_R}{-q_R/A_R + c_R} = H_R^+ \Delta t \quad (9.12)$$

This is a non-linear equation in A_Q . Let $x_i = A_Q$, then the residual of (9.11) is given by

$$f(x_i) = x_i + \frac{p(Q, x_0) y_Q^0 \Delta t}{-q_R/A_R + c_R} + C$$

where

$$C = \frac{q_{tms}^n - q_R}{c_R - q_R/A_R} - A_R - H_R^+ \Delta t$$

Then

$$\frac{df}{dx_i} = 1 + \frac{dp(q, x_i)}{dx_i} \frac{y_Q^0 \Delta t}{-q_R/A_R + c_R}$$

Using these definitions x_i can be estimated using Newton's method, see e.g. Press, Teukolsky, Vetterling and Flannery (1989) or Stoer and Bulirsch (1980). It solves $f(x_i) = 0$ by extending the tangent line at some current guess for the root x_i until it crosses zero. Then it sets the next guess x_{i+1} to the abscissa of that zero-crossing. Algebraically, the method is derived from the Taylor series expansion of the function in the neighborhood of a point giving

$$x_{i+1} = x_i - \left(\frac{df(x_i)}{dx_i} \right)^{-1} f(x_i) \quad (9.13)$$

The indices i refer to the number of iterations, and x is the independent variable. This iteration is then continued until the error $|f(x_i) - f(x_{i-1})| < \epsilon$. However, one should note that this only works if $df/dx_i \neq 0$ and if it is possible to come up with a good initial guess x_0 . The latter is required because if the initial guess is too far from the root one often ends up finding some other root. A good initial guess for this situation is the value at the previous time-step, i.e. at $t = (n-1)\Delta t$.

9.2 The Lax-Wendroff method

In this section we will show how to solve the equations for the arterial tree using Richtmeyer's two-step version of the Lax-Wendroff explicit scheme (Peskin, 1976). This is a second-order method, and it requires that the equations are in conservation form, i.e. the equations in (8.15). Similar to the method of characteristics we need a basic scheme dealing with the interior of each vessels, a scheme for the inflow, one for the outflow, and one for the bifurcation conditions.

9.2.1 The interior

The solution at all points in the interior is determined by first determining some intermediate values at steps $(m+1/2, n+1/2)$ as shown in Figure 9.5.

From (8.15)

$$\begin{aligned} \frac{\partial}{\partial t} \begin{pmatrix} A \\ q \end{pmatrix} + \frac{\partial}{\partial x} \begin{pmatrix} q \\ \frac{q^2}{A} + f\sqrt{A_0 A} \end{pmatrix} = \\ \begin{pmatrix} 0 \\ -\frac{2\pi r_0}{\delta \mathcal{R}} \frac{q}{A} + \left(2\sqrt{A} \left(\sqrt{\pi} f + \sqrt{A_0} \frac{df}{dr_0} \right) - A \frac{df}{dr_0} \right) \frac{dr_0}{dx} \end{pmatrix} \end{aligned}$$

The non-dimensional version of the boundary and bifurcation conditions are identical to the dimensional equations. Now, let the dependent variables be represented by the vector \mathbf{U}

$$\mathbf{U} = (A, q),$$

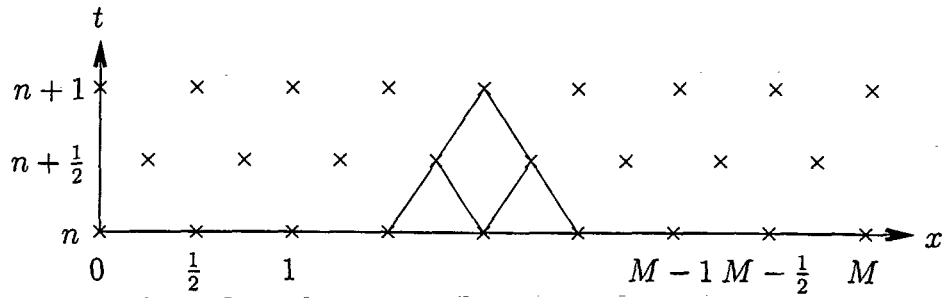


Figure 9.5: In order to determine the values of Q and A at $n + 1$, the intermediate values defined in (9.17) must be determined first.

the system flux by \mathbf{R}

$$\mathbf{R} = (R_1, R_2) = \left(q, \frac{q^2}{A} + B \right) = \left(q, \frac{q^2}{A} + f \sqrt{A_0 A} \right) \quad (9.14)$$

and the right hand side of the equations by \mathbf{S}

$$\mathbf{S} = (S_1, S_2) = \left(0, -\frac{2\pi r_0}{\delta \mathcal{R}} \frac{q}{A} + \left(2\sqrt{A} \left(\sqrt{\pi} f + \sqrt{A_0} \frac{df}{dr_0} \right) - A \frac{df}{dr_0} \right) \frac{dr_0}{dx} \right)$$

The system of equations (7.16) may then be written as

$$\frac{\partial}{\partial t} \mathbf{U} + \frac{\partial}{\partial x} \mathbf{R} = \mathbf{S} \quad (9.15)$$

Let $\mathbf{U}_m^n = \mathbf{U}(m\Delta x, n\Delta t)$ and similarly for \mathbf{R} and \mathbf{S} . Using a uniform grid, one can derive a four point formula, predicting the flow at time-level $(n + 1)$ as follows

$$\mathbf{U}_m^{n+1} = \mathbf{U}_m^n - \frac{\Delta t}{\Delta x} \left(\mathbf{R}_{m+1/2}^{n+1/2} - \mathbf{R}_{m-1/2}^{n+1/2} \right) + \frac{\Delta t}{2} \left(\mathbf{S}_{m+1/2}^{n+1/2} + \mathbf{S}_{m-1/2}^{n+1/2} \right) \quad (9.16)$$

Using two intermediate points at time-level $n + 1/2$ it is possible to determine

$$\begin{aligned} & \mathbf{R}_{m+1/2}^{n+1/2} \quad \mathbf{S}_{m+1/2}^{n+1/2} \\ & \mathbf{R}_{m-1/2}^{n+1/2} \quad \mathbf{S}_{m-1/2}^{n+1/2} \end{aligned}$$

using (9.14) and (9.15). This is done using the definition

$$\mathbf{U}_j^{n+1/2} = \frac{\mathbf{U}_{j+1/2}^n + \mathbf{U}_{j-1/2}^n}{2} + \gamma \left(-\frac{\mathbf{R}_{j+1/2}^n - \mathbf{R}_{j-1/2}^n}{h} + \frac{\mathbf{S}_{j+1/2}^n + \mathbf{S}_{j-1/2}^n}{2} \right) \quad (9.17)$$

for $j = m + 1/2$ and $j = m - 1/2$.

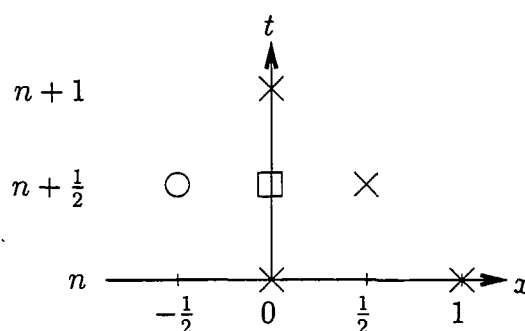


Figure 9.6: Left boundary: All variables are known at the points marked with a cross. In order to determine the value of A_0^{n+1} , we apply the boundary condition for $q_0^{n+1/2}$ at the point marked with a square, and from this it is possible to determine an approximate value at the ghost point marked with a circle. The latter is done by taking the average of the point marked by a circle and the point $(1/2, n + 1/2)$. The value of q_0^{n+1} can then be found using this construction and the boundary condition.

9.2.2 Boundary conditions

All three conditions will be described in the following sections. The details for these derivations will be left out here, but they are described in Appendix A.

Inflow boundary condition

The inflow into the aorta is described by the periodic function (8.2). Also in this case A will be determined using the boundary condition for q . In order to find A we need to evaluate $q_{-1/2}^{n+1/2}$. This can be found by introducing a ghost point, see Figure 9.6. Then

$$\begin{aligned} q_0^{n+1/2} &= \frac{1}{2} (q_{-1/2}^{n+1/2} + q_{1/2}^{n+1/2}) \Leftrightarrow \\ q_{-1/2}^{n+1/2} &= 2q_0^{n+1/2} - q_{1/2}^{n+1/2} \end{aligned} \quad (9.18)$$

and from (9.16)

$$A_0^{n+1} = A_0^n - \frac{\Delta x}{\Delta t} \left((R_1)_{1/2}^{n+1/2} - (R_1)_{-1/2}^{n+1/2} \right) + \frac{\Delta t}{2} \left((S_1)_{1/2}^{n+1/2} + (S_1)_{-1/2}^{n+1/2} \right)$$

where and $(S_1)_{-1/2}^{n+1/2}$ are given by

$$(R_1)_{-1/2}^{n+1/2} = q_{-1/2}^{n+1/2} \quad \text{and} \quad (S_1)_{-1/2}^{n+1/2} = 0$$

Outflow boundary condition

The convolution integral at the right boundary can be written as

$$q(M\Delta x, t) = \int_0^T p(M\Delta x, t - \tau) q(M\delta x, \tau) d\tau$$

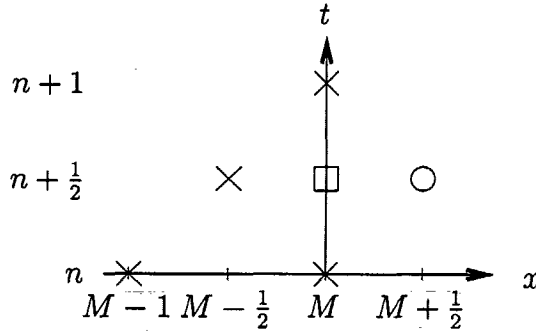


Figure 9.7: Right boundary: All variables are known at the points marked with a cross. In order to have enough equations to determine the values of Q and A at $(M, n+1)$, we need to add a ghost point, marked with a circle, and use the boundary condition at the point marked with a square. Similarly to the left boundary we determine the value at the point marked with a circle by averaging the square point over this and the point $(M-1/2, n+1/2)$.

and discretized by

$$q_M^n = p(M, A_M^n) y_M^0 \Delta t + (q_{tms})_M^n$$

where the current time is $t = n\Delta t$ and

$$(q_{tms})_M^n = \sum_{k=1}^{N-1} p_M^{<n-k>_N} y_M^k \Delta t$$

Here N is the number of time-steps per period, and $<\cdot>_N$ denotes the modulo operator, the range of which is the set $\{0, 1, \dots, N-1\}$. The sum contains the remaining terms from this and the previous period depending on the value of k , see Figure 9.4. Treating this boundary condition is a bit more tricky, since $q(x_M, t)$ is not known explicitly, but only as a function of the unknown p (and hence A).

From the numerical scheme (9.16) we had

$$\begin{aligned} A_M^{n+1} &= A_M^n - \frac{\Delta x}{\Delta t} \left((R_1)_{M+1/2}^{n+1/2} - (R_1)_{M-1/2}^{n+1/2} \right) + \frac{\Delta t}{2} \left((S_1)_{M+1/2}^{n+1/2} + (S_1)_{M-1/2}^{n+1/2} \right) \\ &= A_M^n - \frac{\Delta x}{\Delta t} \left((R_1)_{M+1/2}^{n+1/2} - (R_1)_{M-1/2}^{n+1/2} \right) \end{aligned} \quad (9.19)$$

since $S_1 = 0$, and

$$\begin{aligned} q_M^{n+1} &= \\ q_M^n - \frac{\Delta x}{\Delta t} \left((R_2)_{M+1/2}^{n+1/2} - (R_2)_{M-1/2}^{n+1/2} \right) + \frac{\Delta t}{2} \left((S_2)_{M+1/2}^{n+1/2} + (S_2)_{M-1/2}^{n+1/2} \right) \end{aligned} \quad (9.20)$$

The unknowns in these equations are

$$\begin{array}{cc} q_M^{n+1} & A_M^{n+1} \\ \mathbf{R} \left(q_{M+1/2}^{n+1/2}, A_{M+1/2}^{n+1/2} \right) & S_2 \left(q_{M+1/2}^{n+1/2}, A_{M+1/2}^{n+1/2} \right) \end{array}$$

As for the left boundary, these can be determined by establishing a ghost point, see Figure 9.7, such that

$$q_M^{n+1/2} = \frac{q_{M-1/2}^{n+1/2} + q_{M+1/2}^{n+1/2}}{2} \quad (9.21)$$

$$A_M^{n+1/2} = \frac{A_{M-1/2}^{n+1/2} + A_{M+1/2}^{n+1/2}}{2} \quad (9.22)$$

These equations add two more unknowns, namely $q_M^{n+1/2}$ and $A_M^{n+1/2}$ to the system. Hence, two more equations are needed. These can be found using the boundary condition at the time-levels $n + 1/2$ and $n + 1$.

$$q_M^{n+1/2} = p(M, A_M^{n+1/2}) y_M^0 \Delta t + (q_{tms})_M^{n+1/2} \quad (9.23)$$

$$q_M^{n+1} = p(M, A_M^{n+1}) y_M^0 \Delta t + (q_{tms})_M^{n+1} \quad (9.24)$$

The subscripts and superscripts are only mentioned if the respective variables depend on the corresponding parameter. The six equations (9.19–9.24) have the unknowns

$$\begin{array}{ccc} q_M^{n+1} & A_M^{n+1} & q_M^{n+1/2} \\ A_M^{n+1/2} & q_{M+1/2}^{n+1/2} & A_{M+1/2}^{n+1/2} \end{array}$$

The number of equations can be reduced by substituting (9.21) and (9.22) into (9.23). Hence, (9.23) can be written as

$$\frac{q_{M-1/2}^{n+1/2} + q_{M+1/2}^{n+1/2}}{2} = p\left(M, \frac{A_{M-1/2}^{n+1/2} + A_{M+1/2}^{n+1/2}}{2}\right) y_M^0 \Delta t + (q_{tms})_M^{n+1/2} \quad (9.25)$$

Thus, the four equations to be solved are (9.19), (9.20), (9.24), and (9.25), and the unknowns are

$$\begin{array}{ll} x_1 = q_{M+1/2}^{n+1/2} & x_2 = A_{M+1/2}^{n+1/2} \\ x_3 = q_M^{n+1} & x_4 = A_M^{n+1} \end{array}$$

The residual equations $f(x_i)$ for $i = 1 \dots 4$ and the Jacobian $Df(\mathbf{x})$ are derived in detail in Appendix A. As for the method of characteristics it is possible to find $x_1 - x_4$ using Newton's method. From (9.13) we had the following first-order accurate scheme

$$\mathbf{x}_{i+1} = \mathbf{x}_i - (Df(\mathbf{x}_i))^{-1} f(\mathbf{x}_i), \quad i = 0, 1, 2, 3, \dots \quad (9.26)$$

where the indices i refer to the number of iterations, and $\mathbf{x} = (x_1, x_2, x_3, x_4)$. As before, this method only applies if the Jacobian of $Df(\mathbf{x}_0)$ is nonsingular and if a good initial guess for \mathbf{x}_0 can be found. In this case an obvious initial guess is

$$\begin{array}{ll} (x_1)_0 = q_M^n & (x_2)_0 = A_M^n \\ (x_3)_0 = q_{M-1/2}^{n+1/2} & (x_4)_0 = A_{M-1/2}^{n+1/2} \end{array}$$

Bifurcation conditions

At the bifurcations there are an outflow (right) boundary for the parent vessel and an inflow (left) boundary for the daughter vessels. The prediction of q and A are still given as stated in (7.16). But in this case $\Xi_{M+1/2}^{n-1/2}$ and $\Xi_{M+1/2}^{n+1/2}$, Ξ being either R or S , originating from the daughter and parent vessels, respectively, can not be estimated. As for the left and right boundary conditions we introduce ghost points in order to get these estimates, see Figures 9.6 and 9.7. Using the ghost points, $(q^{(i)})_M^{n+1/2}$ and $(A^{(i)})_M^{n+1/2}$, where $i = p, d_1, d_2$, can be found by linear averaging as in (9.21) and (9.22).

The bifurcation conditions, at time-level $n + 1/2$ and $n + 1$, leads to the following equations. The conservation of flow gives

$$(q^{(p)})_M^j - (q^{(d_1)})_M^j = (q^{(d_2)})_M^j \quad (9.27)$$

and the assumption of continuous pressure across the bifurcation gives

$$(p^{(p)})_M^j = (p^{(d_1)})_M^j = (p^{(d_2)})_M^j \quad (9.28)$$

where $j = n + 1/2, n + 1$. These can be written in terms of A using the state equation (7.26).

$$(f^{(p)})_M \left(1 - \sqrt{\frac{(A_0^{(p)})_M}{(A^{(p)})_M^{n+1/2}}} \right) = (f^{(d_i)})_M \left(1 - \sqrt{\frac{(A_0^{(d_i)})_M}{(A^{(d_i)})_M^{n+1/2}}} \right) \quad (9.29)$$

and

$$(f^{(p)})_M \left(1 - \sqrt{\frac{(A_0^{(p)})_M}{(A^{(p)})_M^{n+1}}} \right) = (f^{(d_i)})_M \left(1 - \sqrt{\frac{(A_0^{(d_i)})_M}{(A^{(d_i)})_M^{n+1}}} \right) \quad (9.30)$$

where $i = d_1, d_2$ and $f(r_0) = 4Eh/(3r_0)$. Assuming that $i = p, d_1, d_2$ then the numerical scheme in (9.17), written out for q and A , gives

$$(q^{(i)})_M^{n+1} = (q^{(i)})_M^n + \frac{\Delta x}{\Delta t} \left((R_2^{(i)})_{M+\frac{1}{2}}^{n+\frac{1}{2}} + (R_2^{(i)})_{M-\frac{1}{2}}^{n+\frac{1}{2}} \right) + \quad (9.31)$$

$$\frac{\Delta t}{2} \left((S_2^{(i)})_{M+\frac{1}{2}}^{n+\frac{1}{2}} + (S_2^{(i)})_{M-\frac{1}{2}}^{n+\frac{1}{2}} \right) \quad (9.32)$$

and

$$(A^{(i)})_M^{n+1} = (A^{(i)})_M^n + \frac{\Delta x}{\Delta t} \left((R_1^{(i)})_{L+\frac{1}{2}}^{n+\frac{1}{2}} + (R_1^{(i)})_{L-\frac{1}{2}}^{n+\frac{1}{2}} \right) \quad (9.33)$$

because $S_1 = 0$. In case of a bifurcation we then have the following unknowns in the

system of equations

$$\begin{array}{lll}
 x_1 = (q^{(p)})_M^{n+1} & x_2 = (q^{(p)})_M^{n+1/2} & x_3 = (q^{(p)})_{M+1/2}^{n+1/2} \\
 x_4 = (q^{(d_1)})_M^{n+1} & x_5 = (q^{(d_1)})_M^{n+1/2} & x_6 = (q^{(d_1)})_{M-1/2}^{n+1/2} \\
 x_7 = (q^{(d_2)})_M^{n+1} & x_8 = (q^{(d_2)})_M^{n+1/2} & x_9 = (q^{(d_2)})_{M-1/2}^{n+1/2} \\
 x_{10} = (A^{(p)})_M^{n+1} & x_{11} = (A^{(p)})_M^{n+1/2} & x_{12} = (A^{(p)})_{M+1/2}^{n+1/2} \\
 x_{13} = (A^{(d_1)})_M^{n+1} & x_{14} = (A^{(d_1)})_M^{n+1/2} & x_{15} = (A^{(d_1)})_{M-1/2}^{n+1/2} \\
 x_{16} = (A^{(d_2)})_M^{n+1} & x_{17} = (A^{(d_2)})_M^{n+1/2} & x_{18} = (A^{(d_2)})_{M-1/2}^{n+1/2}
 \end{array}$$

Equations (9.21, 9.22, 9.27–9.33) comprise a system of eighteen non-linear equations in the variables listed above. The detailed derivation of the corresponding residual equations $f_r(x_i)$ for $i = 1 \dots 18$ and the Jacobian $Df_r(\mathbf{x}_0)$ can be found in Appendix A. Also in this case we solve the equations using Newton's method. From (9.26) we had

$$\mathbf{x}_{i+1} = \mathbf{x}_i - (Df_r(\mathbf{x}_i))^{-1} f_r(\mathbf{x}_i), \quad i = 0, 1, 2, 3, \dots$$

where the indices i refer to the number of iterations, and $\mathbf{x} = (x_1, x_2, x_3, \dots, x_{18})$. As mentioned before, this method only applies if the Jacobian $Df_r(\mathbf{x}_0)$ is nonsingular, and if it is possible to find good initial approximations for \mathbf{x}_0 .

It should, however, be noted that this system of equations can be split into a linear part which can be solved analytically and a much smaller non-linear part which should be solved numerically. This has not been done for the present work but it would be an obvious simplification.

9.3 Convergence of the two methods

In order to test the convergence of the two methods we conduct the following experiment. Let

$$q = A = x + t + 1$$

Then equations (8.15) can be satisfied if their right hand sides and boundary conditions are modified accordingly. This gives

$$\begin{aligned}
 \frac{\partial A}{\partial t} + \frac{\partial q}{\partial x} &= 2 \\
 \frac{\partial q}{\partial t} + \frac{\partial}{\partial x} \left(\frac{q^2}{A} \right) + A \frac{\partial p}{\partial x} &= 2 + f \sqrt{\frac{A_0}{A}}
 \end{aligned}$$

or on conservation form (8.15)

$$\frac{\partial}{\partial t} \begin{pmatrix} A \\ q \end{pmatrix} + \frac{\partial}{\partial x} \begin{pmatrix} q \\ \frac{q^2}{A} + f\sqrt{A_0 A} \end{pmatrix} = \begin{pmatrix} 2 \\ 2 + f\sqrt{\frac{A_0}{A}} + \left(2\sqrt{A} \left(\sqrt{\pi} f + \sqrt{A_0} \frac{df}{dr_0} \right) - A \frac{df}{dr_0} \right) \frac{dr_0}{dx} \end{pmatrix}$$

where p is given using the state equation in (7.26), $f(r_0) = 4Eh/(3r_0)$, and $A_0 = \pi r_0^2$ as described in Chapter 7. For both systems the corresponding boundary conditions are given by

$$\begin{aligned} A(0, t) &= q(0, t) = t + 1 \\ A(L, t) &= q(L, t) = t + 2 \end{aligned}$$

and the initial condition is

$$A(x, 0) = q(x, 0) = x + 1$$

In these experiments we have used the infinity norm to determine the rate of convergence. Let \mathbf{U} denote the approximate computed solution, and \mathbf{u} the exact solution. Furthermore, let the interval $[0; 1]$ be divided into M intervals. Hence, $\Delta x = 1/M$.

Assume that $\|\mathbf{U} - \mathbf{u}\|_\infty$ is $\mathcal{O}(\Delta x^n)$. Then

$$\begin{aligned} \|\mathbf{U} - \mathbf{u}\|_\infty &\leq c\Delta x^n = c\left(\frac{1}{M}\right)^n \Leftrightarrow \\ \log(\|\mathbf{U} - \mathbf{u}\|_\infty) &= \log c - n \log M \end{aligned}$$

where c is some positive constant. The order of convergence n can then be read off the graphs as the negative slope of $\log \|\mathbf{U} - \mathbf{u}\|_\infty$ plotted as a function of $\log M$. Furthermore, the constant c can be determined from the intersection of the graph with the line $\log M = 1$. As shown in Figure 9.8, $n \approx 1$ for the method of characteristics, and $n \approx 2$ asymptotically for the Lax-Wendroff method. These are the expected values because the method of characteristics is a first-order method and the Lax-Wendroff method is a second-order method.

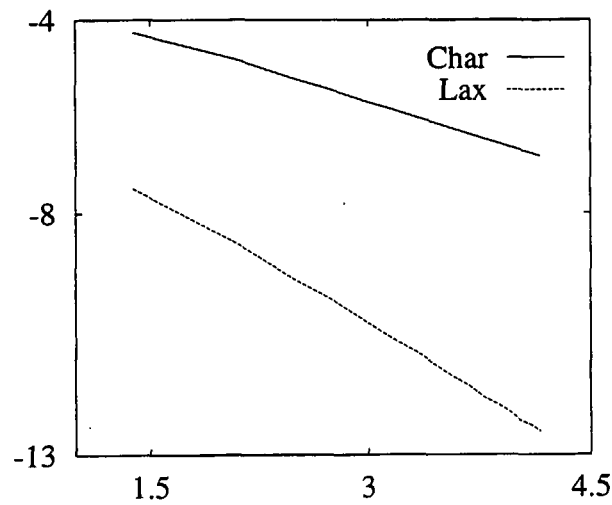


Figure 9.8: The figure shows a plot of $\log \|U - u\|_\infty$ (the y -axis) as a function of $\log M$ (the x -axis) for both the Lax-Wendroff method and the method of characteristics. From this plot one gets that the convergence rate (n) for the Lax-Wendroff method is $n \approx 2$ and $\log c \approx -4.5$, and that $n \approx 1$ and $\log c \approx -3$ for the method of characteristics.

Chapter 10

Fluid dynamical model of a small artery

In this chapter we present the system of equations describing flow and pressure in the smaller arteries. It consists of a continuity equation and an x -momentum equation. They are derived by combining the axisymmetric Navier-Stokes equations for flow in an elastic cylinder with a wall-equation balancing the forces of the elastic wall with those acting on the fluid inside.

In Chapters 7 and 8 we derived a similar model of the larger arteries. This model can, however, not be used for the smaller arteries. First, because solving a non-linear model for such a large tree is not computationally feasible, (see Section 6.2) and second, because it does not model the wall shear stresses in a satisfactory way. Therefore, we need a model which is simpler in some respects, but which at the same time models the boundary layer in more detail.

A good way to simplify the model is to linearize it. A direct linearization of the non-linear equations will, however, not be adequate. In the model of the larger arteries the wall shear stress was accounted for in the same approximate way by assuming a given velocity profile. This gave rise to a friction term on the right hand side of the equation, see Section 7.1. In this case we include the viscosity in the derivations and do not simplify them until very late in the approximations. This is important since the wall shear stress is more dominant in the smaller arteries and thus cannot be dealt with in the approximate way. We have decided to base our study on the linear model by Womersley (1957). This is rather comprehensive, and hence we give a rather detailed description of the derivations. Since Womersley originally derived his model a number of papers have been elaborating on it. Especially thorough treatments are presented in Atabek and Lew (1966), Atabek (1968), Pedley (1980), Lighthill (1989), and more recently by Berger (1993).

In Sections 10.1–10.6 we derive the equations for flow and pressure and in Sections 10.7–10.10 we solve the equations analytically and find the impedance at the root of the vessel. The derivation in this chapter is primarily based on Atabek and Lew (1966), Atabek (1968), and Pedley (1980). Sections 10.1–10.7 are very technical and the reader may wish to jump directly to Section 10.8 where the simplified momentum equation is described.

10.1 Model assumptions and basic equations

An artery is essentially an elastic vessel filled with fluid that interacts with the vessel walls. Thus, the mathematical model of the smaller arteries can be established by three equations, describing:

- The motion of the fluid.
- The motion of the vessel walls.
- The interaction between the fluid and the walls.

Except for the modeling of the boundary layers we let the assumptions for the smaller arteries match those used for the larger arteries. However, in our attempt to simplify the model we neglect the assumption of tapering vessels, i.e. the vessel radius is no longer dependent on x . Hence, p is a function of A only. Moreover, we assume that the fluid is Newtonian and incompressible.

10.2 Motion of the fluid

The fluid dynamic equations are derived using cylindrical coordinates (r, x, θ) . We assume that the flow is axisymmetric (no dependence on θ) and also without swirl (no theta component). Hence, the velocity in the radial and longitudinal directions are given by $\mathbf{u} = [u(r, x, t), w(r, x, t)]$, and the pressure by $p(r, x, t)$. Furthermore, we assume that no body forces are acting on the system. Hence, the Navier-Stokes equations take the form

$$\frac{\partial u}{\partial t} + u \frac{\partial u}{\partial r} + w \frac{\partial u}{\partial x} = -\frac{1}{\rho} \frac{\partial p}{\partial r} + \nu \left(\frac{\partial^2 u}{\partial r^2} + \frac{1}{r} \frac{\partial u}{\partial r} + \frac{\partial^2 u}{\partial x^2} - \frac{u}{r^2} \right) \quad (10.1)$$

$$\frac{\partial w}{\partial t} + u \frac{\partial w}{\partial r} + w \frac{\partial w}{\partial x} = -\frac{1}{\rho} \frac{\partial p}{\partial x} + \nu \left(\frac{\partial^2 w}{\partial r^2} + \frac{1}{r} \frac{\partial w}{\partial r} + \frac{\partial^2 w}{\partial x^2} \right) \quad (10.2)$$

$$\frac{1}{r} \frac{\partial}{\partial r}(ru) + \frac{\partial w}{\partial x} = 0 \quad (10.3)$$

10.3 Motion of the vessel walls

Since the vessel wall is elastic it will be deformed as the pulse-wave travels along it. These deformations are balanced by the external strain and the corresponding internal elastic stresses.

The movement of the vessel wall can be described by balancing the internal and external forces on a surface element of the vessel wall in its deformed state. It is convenient to change the variables to a coordinate system connected to the surface of the vessel. This is shown in Figure 10.1. Let H be any vector pointing to the middle surface shown in Figure 10.1, then

$$H = x\hat{x} + R\hat{r}$$

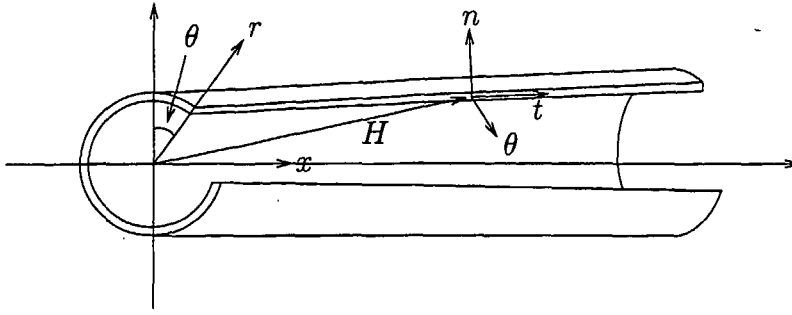


Figure 10.1: The original (r, x, θ) and the new (n, t, θ) coordinates.

where \hat{x} and \hat{r} are the unit vectors in the cylindrical coordinate system in the longitudinal and radial directions, respectively, and $R(x, t)$ is radius of the vessel. The new coordinates (n, t, θ) can be determined from H .

By the assumption of axial symmetry all equations can be expressed in terms of \hat{t} and \hat{n} . The unit vector \hat{t} is given by

$$\hat{t} = \frac{\frac{\partial H}{\partial x}}{\left| \frac{\partial H}{\partial x} \right|} = \frac{\hat{x} + \frac{\partial R}{\partial x} \hat{r}}{\left| \hat{x} + \frac{\partial R}{\partial x} \hat{r} \right|} = \frac{\hat{x} + \frac{\partial R}{\partial x} \hat{r}}{\left[1 + \left(\frac{\partial R}{\partial x} \right)^2 \right]^{1/2}} \quad (10.4)$$

and

$$\hat{n} = \frac{\hat{r} - \frac{\partial R}{\partial x} \hat{x}}{\left[1 + \left(\frac{\partial R}{\partial x} \right)^2 \right]^{1/2}} \quad (10.5)$$

because \hat{n} and \hat{t} are orthogonal. Equations for motion of the vessel are derived by balancing the internal and external forces on an infinitesimal surface element of the vessel wall. This is described in the following sections.

10.3.1 Internal forces

The internal forces on an infinitesimal surface element ($dx \times d\theta$) are composed of three components; a force N across the vessel wall, a shearing force S on the sides of the element, and a force T normal to each of the edges, see Figure 10.2. Most of these components are zero. The vessel wall is thin so any variation in the force across the wall can be neglected, i.e. $N_t = N_\theta = 0$, and the flow is axisymmetric. Hence, no shearing force will be acting on the side of the element, i.e. $S_t = S_\theta = 0$. The only forces left are T_t and T_θ , the normal forces to each of the edges, see Figure 10.3.

10.3.2 External forces

The internal forces must be balanced by external forces acting on the element. If these are denoted by P they are given by

$$P = P_t \hat{t} + P_n \hat{n} \quad (10.6)$$

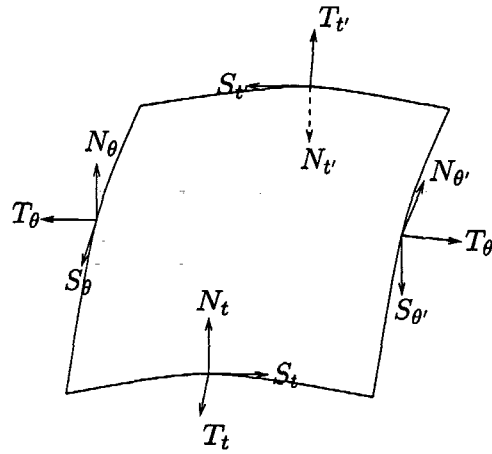


Figure 10.2: The forces on an infinitesimal surface element. N is the force acting across the vessel wall, S is the shearing force acting on the side of the element, and T is the force acting normal to each of the edges. The subscripts t and θ indicate the direction according to the coordinate system following the surface of the vessel and the superscript $'$ indicate that the force is acting in the negative direction.

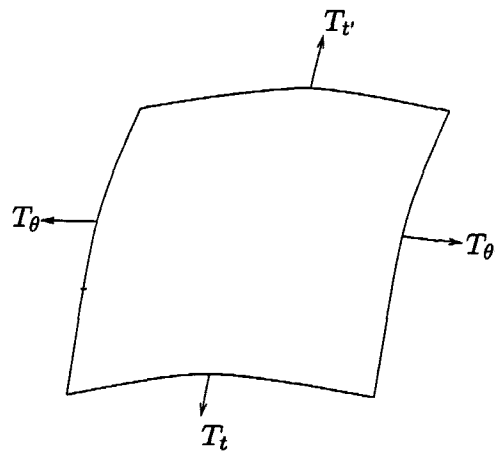


Figure 10.3: In case of an axisymmetric vessel with thin walls the only internal forces on any infinitesimal surface element are the forces normal to each of the edges.

in the (n, t, θ) coordinate system. Since the system is axisymmetric and without swirl there is no dependence on θ or components in the θ direction.

The forces can be split into three groups; the inertia forces, the tethering forces, and the surface forces. In the following sections, these will be analyzed separately.

Inertia forces

Let $\xi(r, x, t)$ and $\eta(r, x, t)$ be the longitudinal and radial displacement of the wall. The inertia force per unit area (Atabek and Lew, 1966) is then given by

$$-\rho_0 h \left(\frac{\partial^2 \xi}{\partial t^2} \hat{x} + \frac{\partial^2 \eta}{\partial t^2} \hat{r} \right) \quad (10.7)$$

where ρ_0 is the density of the wall and h is the thickness of the wall (because of the thin wall approximation h must be small compared with the vessel radius). We assume that both ρ_0 and h are constant along any vessel of a given radius.

Tethering forces

As mentioned previously, the arteries in the human body do not move freely because they are tethered to the surrounding tissue. Therefore, the motion of the arterial wall can be considered as an interaction between two viscoelastic media; the vessel wall and the surrounding tissue. However, as we also discussed earlier, modeling the exact viscoelastic behavior is rather complicated. Therefore, it is assumed (according to Atabek, 1968) that the tethering force T_{FT} can be modeled using a simple mechanical model consisting of a spring, a dash-pot and some lumped additional mass. The tethering force (per unit area) acting in the radial and longitudinal directions is

$$T_{FT} = \quad (10.8)$$

$$- \left[\left(M_a \frac{\partial^2 \xi}{\partial t^2} + L_x \frac{\partial \xi}{\partial t} + K_x \xi \right) \hat{x} + \left(M_a \frac{\partial^2 \eta}{\partial t^2} + L_r \frac{\partial \eta}{\partial t} + K_r \eta \right) \hat{r} \right]$$

where K_i and L_i , $i = x, r$, are the spring and the frictional coefficients of the dash-pot in the i th direction, and M_a is the additional mass of the system. This is assumed to be the same in both directions.

Since both inertia and tethering forces act in the same direction it is convenient to add them before projecting the forces in the normal and tangential directions. The resultant force is given by

$$T_{FT_{res}} = \quad (10.9)$$

$$- \left[\left(M_0 \frac{\partial^2 \xi}{\partial t^2} + L_x \frac{\partial \xi}{\partial t} + K_x \xi \right) \hat{x} + \left(M_0 \frac{\partial^2 \eta}{\partial t^2} + L_r \frac{\partial \eta}{\partial t} + K_r \eta \right) \hat{r} \right]$$

where

$$M_0 = M_a + \rho_0 h$$

Solving (10.4) and (10.5) for \hat{x} and \hat{r} gives

$$\begin{aligned} \begin{bmatrix} 1 & \frac{\partial R}{\partial x} \\ -\frac{\partial R}{\partial x} & 1 \end{bmatrix} \begin{bmatrix} \hat{x} \\ \hat{r} \end{bmatrix} &= \begin{bmatrix} \hat{t} \left[1 + \left(\frac{\partial R}{\partial x} \right)^2 \right]^{1/2} \\ \hat{n} \left[1 + \left(\frac{\partial R}{\partial x} \right)^2 \right]^{1/2} \end{bmatrix} \Leftrightarrow \\ \begin{bmatrix} \hat{x} \\ \hat{r} \end{bmatrix} &= \begin{bmatrix} (\hat{t} - \hat{n} \frac{\partial R}{\partial x}) / \left[1 + \left(\frac{\partial R}{\partial x} \right)^2 \right]^{1/2} \\ (\hat{n} + \hat{t} \frac{\partial R}{\partial x}) / \left[1 + \left(\frac{\partial R}{\partial x} \right)^2 \right]^{1/2} \end{bmatrix} \end{aligned} \quad (10.10)$$

Inserting these solutions in (10.9) gives the resultant inertia and tethering force in the tangential and normal directions, respectively

$$\begin{aligned} T_{F_{T_{res}}} \cdot \hat{t} &= - \left[1 + \left(\frac{\partial R}{\partial x} \right)^2 \right]^{-1/2} \\ &\quad \left[M_0 \frac{\partial^2 \xi}{\partial t^2} + L_x \frac{\partial \xi}{\partial t} + K_x \xi + \left(M_0 \frac{\partial^2 \eta}{\partial t^2} + L_r \frac{\partial \eta}{\partial t} + K_r \eta \right) \frac{\partial R}{\partial x} \right] \end{aligned} \quad (10.11)$$

and

$$\begin{aligned} T_{F_{T_{res}}} \cdot \hat{n} &= \left[1 + \left(\frac{\partial R}{\partial x} \right)^2 \right]^{-1/2} \\ &\quad \left[\left(M_0 \frac{\partial^2 \xi}{\partial t^2} + L_x \frac{\partial \xi}{\partial t} + K_x \xi \right) \frac{\partial R}{\partial x} - \left(M_0 \frac{\partial^2 \eta}{\partial t^2} + L_r \frac{\partial \eta}{\partial t} + K_r \eta \right) \right] \end{aligned} \quad (10.12)$$

Surface forces

The surface force is a result of the fluids interaction with the vessel wall. If the stress tensor of the fluid is given by \mathbf{T}_F , then the interaction with the inner vessel wall (i.e. at $r = R - h/2 = a$) is given by $-\mathbf{T}_F \cdot \hat{n}$. Assume that the stress tensor can be separated into the radial and longitudinal directions such that

$$(-\mathbf{T}_F \cdot \hat{n}) \cdot \hat{t}, \quad (-\mathbf{T}_F \cdot \hat{n}) \cdot \hat{n} \quad (10.13)$$

As seen in Chapter 7 the surface stress tensor for incompressible flow is given by Ockendon and Ockendon (1995)

$$\sigma_{ij} = -p\delta_{ij} + \mu \left(\frac{\partial u_i}{\partial x_j} + \frac{\partial u_j}{\partial x_i} \right)$$

In cylindrical coordinates the surface stress tensor becomes

$$\mathbf{T}_F = \begin{bmatrix} T_{rr} & T_{rx} \\ T_{rx} & T_{xx} \end{bmatrix} = \begin{bmatrix} -p + 2\mu \frac{\partial u}{\partial r} & \mu \left(\frac{\partial w}{\partial r} + \frac{\partial u}{\partial x} \right) \\ \mu \left(\frac{\partial w}{\partial r} + \frac{\partial u}{\partial x} \right) & -p + 2\mu \frac{\partial w}{\partial x} \end{bmatrix}_a \quad (10.14)$$

Using (10.5) and (10.14)

$$\begin{aligned} -\mathbf{T}_F \cdot \hat{n} &= - \left[1 + \left(\frac{\partial R}{\partial x} \right)^2 \right]^{-1/2} \begin{bmatrix} T_{rr} & T_{rx} \\ T_{rx} & T_{xx} \end{bmatrix}_a \begin{bmatrix} 1 \\ -\frac{\partial R}{\partial x} \end{bmatrix} \\ &= \left[1 + \left(\frac{\partial R}{\partial x} \right)^2 \right]^{-1/2} \left[-T_{rr} + T_{rx} \frac{\partial R}{\partial x}, -T_{rx} + T_{xx} \frac{\partial R}{\partial x} \right]_a \end{aligned}$$

Thus, the fluid stress in the \hat{n} and \hat{t} directions can be found as

$$\begin{aligned} &(-\mathbf{T}_F \cdot \hat{n}) \cdot \hat{t} \\ &= \left[1 + \left(\frac{\partial R}{\partial x} \right)^2 \right]^{-1} \left[-T_{rr} + T_{rx} \frac{\partial R}{\partial x}, -T_{rx} + T_{xx} \frac{\partial R}{\partial x} \right]_a \begin{bmatrix} \frac{\partial R}{\partial x} \\ 1 \end{bmatrix} \\ &= \left[1 + \left(\frac{\partial R}{\partial x} \right)^2 \right]^{-1} \left[(T_{xx} - T_{rr}) \frac{\partial R}{\partial x} + T_{rx} \left(\left(\frac{\partial R}{\partial x} \right)^2 - 1 \right) \right]_a \quad (10.15) \end{aligned}$$

and

$$\begin{aligned} &(-\mathbf{T}_F \cdot \hat{n}) \cdot \hat{n} \\ &= \left[1 + \left(\frac{\partial R}{\partial x} \right)^2 \right]^{-1} \left[-T_{rr} + T_{rx} \frac{\partial R}{\partial x}, -T_{rx} + T_{xx} \frac{\partial R}{\partial x} \right]_a \begin{bmatrix} 1 \\ -\frac{\partial R}{\partial x} \end{bmatrix} \\ &= \left[1 + \left(\frac{\partial R}{\partial x} \right)^2 \right]^{-1} \left[2 T_{rx} \frac{\partial R}{\partial x} - T_{rr} - T_{xx} \left(\frac{\partial R}{\partial x} \right)^2 \right]_a \quad (10.16) \end{aligned}$$

Total external forces

The total external force can now be found by adding the inertia and tethering forces (10.11) and (10.12) as well as the surface forces (10.15) and (10.16). Equation (10.6) gives

$$P = P_t \hat{t} + P_n \hat{n} = ((-\mathbf{T}_F \cdot \hat{n}) + T_{F_{Tres}}) \cdot \hat{t} + ((-\mathbf{T}_F \cdot \hat{n}) + T_{F_{Tres}}) \cdot \hat{n}$$

The tangential component is

$$\begin{aligned} P_t &= \left[1 + \left(\frac{\partial R}{\partial x} \right)^2 \right]^{-1} \left[(T_{xx} - T_{rr}) \frac{\partial R}{\partial x} + T_{rx} \left(\left(\frac{\partial R}{\partial x} \right)^2 - 1 \right) \right]_a - \\ &\quad \left[1 + \left(\frac{\partial R}{\partial x} \right)^2 \right]^{-1/2} \quad (10.17) \\ &\quad \left[M_0 \frac{\partial^2 \xi}{\partial t^2} + L_x \frac{\partial \xi}{\partial t} + K_x \xi + \left(M_0 \frac{\partial^2 \eta}{\partial t^2} + L_r \frac{\partial \eta}{\partial t} + K_r \eta \right) \frac{\partial R}{\partial x} \right] \end{aligned}$$

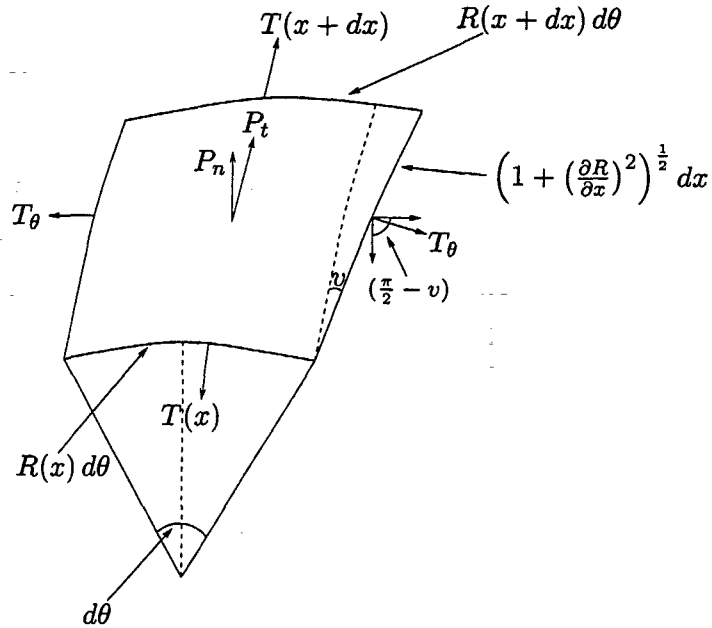


Figure 10.4: A volume element and its internal (T_i) and external (P_i) forces.

and the normal component is

$$\begin{aligned}
 P_n = & \left[1 + \left(\frac{\partial R}{\partial x} \right)^2 \right]^{-1} \left[2 T_{rx} \frac{\partial R}{\partial x} - T_{rr} - T_{xx} \left(\frac{\partial R}{\partial x} \right)^2 \right]_a + \\
 & \left[1 + \left(\frac{\partial R}{\partial x} \right)^2 \right]^{-1/2} \\
 & \left[\left(M_0 \frac{\partial^2 \xi}{\partial t^2} + L_x \frac{\partial \xi}{\partial t} + K_x \xi \right) \frac{\partial R}{\partial x} - \left(M_0 \frac{\partial^2 \eta}{\partial t^2} + L_r \frac{\partial \eta}{\partial t} + K_r \eta \right) \right]
 \end{aligned} \quad (10.18)$$

10.3.3 Balancing internal and external forces

Equation (10.6) gives the total load on the system. When a wave is propagated along a vessel it will dilate. Hence, the surface will look as shown in Figure 10.4. Considering this surface we can derive the equilibrium equations. As for the external forces the balancing of internal and external forces will be carried out in two parts; one for the tangential contributions and one for the normal contributions.

Balancing tangential components of the internal and external forces

The area of the surface in Figure 10.4 is given by $R d\theta dx \sqrt{1 + (\partial R / \partial x)^2}$ and the tangential part of the external strain P_t is given by

$$P_{tan} = R d\theta dx \left[1 + \left(\frac{\partial R}{\partial x} \right)^2 \right]^{1/2} P_t$$

This is pointing in the direction of the normal to the surface. Hence, the pressure load on any given volume element is given by $-P_{ext}$. This should be balanced by the internal stress over the surface element projected on the tangential direction. Thus, the stress over the surface in the tangential direction is given by

$$\begin{aligned} T_{tan_1} &= -T_t(x)R(x)d\theta + T_t(x+dx)R(x+dx)d\theta \\ &= \frac{\partial}{\partial x}(T_t R) dx d\theta \end{aligned}$$

if the last equality is approximated using a first order Taylor expansion for $T_t(x+dx)R(x+dx)$.

Furthermore, the stress from the radial tension also contributes. As seen on the right side of the surface element in Figure 10.4 the radial tension T_θ gives contributions both in the tangential and radial directions. Of course, since we have axial symmetry, the net tension around the vessel at any location is zero. The part of T_θ pointing backwards in the tangential direction is given by

$$\begin{aligned} T_{tan_2} &= -T_\theta dx \left[1 + \left(\frac{\partial R}{\partial x} \right)^2 \right]^{1/2} \cos(\pi/2 - v) \\ &= -T_\theta dx \left[1 + \left(\frac{\partial R}{\partial x} \right)^2 \right]^{1/2} \frac{\partial R}{\partial x} \left[1 + \left(\frac{\partial R}{\partial x} \right)^2 \right]^{-1/2} d\theta \\ &= -T_\theta dx d\theta \frac{\partial R}{\partial x} \end{aligned}$$

where v is defined as shown in Figure 10.4. Balancing T_{tan_1} and T_{tan_2} with P_{tang} and dividing by $dx d\theta$ gives

$$-\frac{\partial R}{\partial x} T_\theta + \frac{\partial}{\partial x}(R T_t) + R \left[1 + \left(\frac{\partial R}{\partial x} \right)^2 \right]^{1/2} P_t = 0 \quad (10.19)$$

Balancing normal components of the internal and external forces

The balancing of the normal internal stresses with the normal external strain gives

$$T_\theta \kappa_\theta + T_t \kappa_t$$

where κ_i , $i = \theta, t$, is the curvature in the i direction. As seen in Figure 10.5, the curvature in the longitudinal direction is given by

$$\kappa_\theta = -\frac{\partial^2 R}{\partial x^2} \left[1 + \left(\frac{\partial R}{\partial x} \right)^2 \right]^{-3/2}$$

and in the angular direction by

$$\kappa_t = \frac{1}{R} \left[1 + \left(\frac{\partial R}{\partial x} \right)^2 \right]^{-1/2}$$

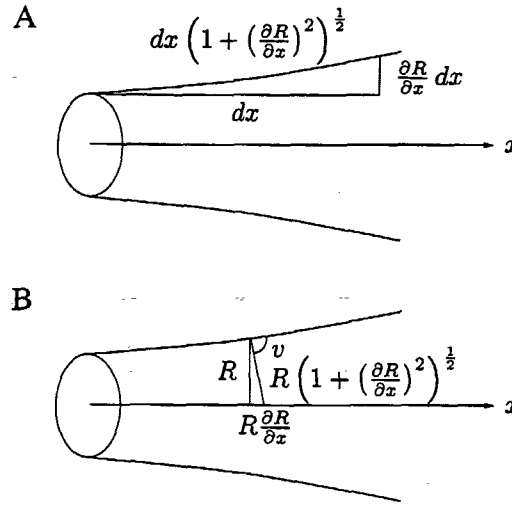


Figure 10.5: The curvature of the vessel. The longitudinal curvature (in A) is given by $\kappa_\theta = (\partial^2 R / \partial x^2) (1 + (\partial R / \partial x)^2)^{-3/2}$ and the tangential curvature normal to the surface (in B) is given by $\kappa_t = (1/R) (1 + (\partial R / \partial x)^2)^{-1/2}$.

Hence, the balancing equation becomes

$$T_\theta \kappa_t + T_t \kappa_\theta - P_n = 0 \quad \Leftrightarrow$$

$$\frac{T_\theta}{R} \left[1 + \left(\frac{\partial R}{\partial x} \right)^2 \right]^{-1/2} - T_t \frac{\partial^2 R}{\partial x^2} \left[1 + \left(\frac{\partial R}{\partial x} \right)^2 \right]^{-1/2} - P_n = 0 \quad (10.20)$$

Inserting (10.17) and (10.18) in (10.19) and (10.20) gives

$$-\frac{\partial R}{\partial x} T_\theta + \frac{\partial}{\partial x} (R T_t) -$$

$$R \left(M_0 \frac{\partial^2 \xi}{\partial t^2} + L_x \frac{\partial \xi}{\partial t} + K_x \xi + \left(M_0 \frac{\partial^2 \eta}{\partial t^2} + L_r \frac{\partial \eta}{\partial t} + K_r \eta \right) \frac{\partial R}{\partial x} \right) +$$

$$R \left[1 + \left(\frac{\partial R}{\partial x} \right)^2 \right]^{-1/2} \left[(T_{xx} - T_{rr}) \frac{\partial R}{\partial x} + T_{rx} \left(\left(\frac{\partial R}{\partial x} \right)^2 - 1 \right) \right]_a = 0 \quad (10.21)$$

$$\frac{T_\theta}{R} \left[1 + \left(\frac{\partial R}{\partial x} \right)^2 \right]^{-1/2} - T_t \frac{\partial^2 R}{\partial x^2} \left[1 + \left(\frac{\partial R}{\partial x} \right)^2 \right]^{-1/2} - \left[1 + \left(\frac{\partial R}{\partial x} \right)^2 \right]^{-1/2}$$

$$\left(\left(M_0 \frac{\partial^2 \xi}{\partial t^2} + L_x \frac{\partial \xi}{\partial t} + K_x \xi \right) \frac{\partial R}{\partial x} - \left(M_0 \frac{\partial^2 \eta}{\partial t^2} + L_r \frac{\partial \eta}{\partial t} + K_r \eta \right) \right) -$$

$$\left[1 + \left(\frac{\partial R}{\partial x} \right)^2 \right]^{-1} \left[2 \frac{\partial R}{\partial x} T_{rx} - T_{rr} - \left(\frac{\partial R}{\partial x} \right)^2 T_{xx} \right]_a = 0 \quad (10.22)$$

10.4 Elasticity Relations

The purpose of this section is to set up stress-strain relations such that the stress components T_i can be related to the displacements of the wall (ξ, η) . These are measured from some reference state, but still in the situation where the vessel is placed inside the body. The reason is that a loose piece of artery (unstressed) requires very large deformations to be brought to its original stressed state. This gives some problems since the general theory of elasticity only applies for small deformations, see e.g. Landau and Lifshitz (1986). These problems can be avoided by making the derivations depart from some initial stressed state, i.e. not going all the way back to the initial unstressed state of the material. Hence, it is assumed that when a wave moves along the artery then it only undergoes small deformations from its reference state. The initial state is chosen to be the state where the transmural pressure of the artery is zero. Furthermore, it is assumed that it is adequate to apply a linear relation between stress and strain.

Let the reference state of the stresses in the longitudinal and circumferential directions be denoted by T_{t_0} and T_{θ_0} . Then the following relations can be obtained

$$T_{\theta} - T_{\theta_0} = \frac{E_{\theta} h}{1 - \sigma_{\theta} \sigma_x} (\epsilon_r + \sigma_{\theta} \epsilon_x) \quad (10.23)$$

$$T_t - T_{t_0} = \frac{E_x h}{1 - \sigma_{\theta} \sigma_x} (\epsilon_x + \sigma_x \epsilon_r) \quad (10.24)$$

where E_i , $i = \theta, t$, is Young's modulus in the i th direction, h is the wall with thickness, σ_i , $i = \theta, t$ is the Poisson ratio in the i th direction, and ϵ_i , $i = \theta, t$, is the displacement relative to the reference state, see e.g. Landau and Lifshitz (1986). The relative circumferential displacement is given by

$$\epsilon_r = \frac{\eta}{R}$$

and in the longitudinal direction it is

$$\epsilon_x = \frac{\partial \xi}{dx}$$

10.5 Balancing fluid and wall motions

Boundary conditions linking the velocity of the wall to the velocity of the fluid remains to be specified. Assume that the fluid particles are at rest at the wall. Hence,

$$[u]_{r=a} = \frac{\partial \eta}{\partial t} \quad (10.25)$$

$$[w]_{r=a} = \frac{\partial \xi}{\partial t} \quad (10.26)$$

Furthermore, assume that the component of the fluid velocity normal to the wall is equal to the normal velocity of the inner surface of the vessel. Hence, the normal velocity of the wall, i.e. at $a = R - h/2$, is given by

$$\frac{d}{dt} \left(r - R + \frac{h}{2} \right) = 0 \quad \Leftrightarrow$$

$$[u]_{r=a} - [w]_{r=a} \frac{\partial R}{\partial x} - \frac{\partial R}{\partial t} = 0$$

10.6 Linearization

In principle the right number of equations and boundary conditions are present. However, in their present form they are too complicated to solve analytically, and as discussed earlier, the purpose was to set up a simple system of equations for the smaller arteries. Therefore, following Atabek and Lew (1966) we have chosen to linearize them.

The linearization is based on expansion of the dependent variables, in power series of a small parameter ϵ , around a known solution. This is defined by a situation where the fluid is at rest and the vessel is inflated and stretched. Furthermore, if $\epsilon = 0$ then all dependent variables give the known solution.

$$\begin{aligned}
 u &= u_1\epsilon + u_2\epsilon^2 + \dots \\
 w &= w_1\epsilon + w_2\epsilon^2 + \dots \\
 p &= p_0 + p_1\epsilon + p_2\epsilon^2 + \dots \\
 \xi &= \xi_1\epsilon + \xi_2\epsilon^2 + \dots \\
 \eta &= \eta_1\epsilon + \eta_2\epsilon^2 + \dots \\
 R &= R_0 + R_1\epsilon + R_2\epsilon^2 + \dots \\
 T_\theta &= T_{\theta_0} + T_{\theta_1}\epsilon + T_{\theta_2}\epsilon^2 + \dots \\
 T_t &= T_{t_0} + T_{t_1}\epsilon + T_{t_2}\epsilon^2 + \dots \\
 T_{rr} &= T_{rr_0} + T_{rr_1}\epsilon + T_{rr_2}\epsilon^2 + \dots \\
 T_{xx} &= T_{xx_0} + T_{xx_1}\epsilon + T_{xx_2}\epsilon^2 + \dots \\
 T_{rx} &= T_{rx_1}\epsilon + T_{rx_2}\epsilon^2 + \dots
 \end{aligned} \tag{10.27}$$

where $p_0, R_0, T_{\theta_0}, T_{t_0}$ are constants defining the reference state at zero transmural pressure. Let $f(r, x, t)$ be either of the functions in (10.27). In order to accomplish the linearization the $f(r, x, t)$ must be evaluated at $r = a = R - h/2$. The power series expansion together with Taylor series expansion to first order yield

$$\begin{aligned}
 f(r, x, t) &\approx f(a, x, t) + f'(a, x, t)(r - a) \\
 &= f_0(a, x, t) + kf'_0(a, x, t) + \\
 &\quad \epsilon ([f_1(a, x, t) - R_1 f'_0(a, x, t) + k f'_1(a, x, t)])
 \end{aligned} \tag{10.28}$$

where $k = r - R_0 + h/2$. Using (10.27) and (10.28), the zeroth and first order equations can be obtained by assembling terms to the respective powers of ϵ of the non-linear equations (10.1), (10.2), (10.3), (10.21), and (10.22).

10.6.1 Terms of zeroth order approximations

From the fluid equations (10.1), (10.2), and (10.3) only the pressure terms contributes since the expansions for u and w has no zero-order terms. Hence,

$$\frac{\partial p_0}{\partial r} = 0, \quad \frac{\partial p_0}{\partial x} = 0$$

From the shell equations only (10.22) contributes, namely

$$\frac{T_{\theta_0}}{R_0} - p_0 = 0 \tag{10.29}$$

10.6.2 Terms of first order approximations

In this case all equations give some contributions. The momentum equations (10.1) and (10.2) gives

$$\frac{\partial u_1}{\partial t} = -\frac{1}{\rho} \frac{\partial p_1}{\partial r} + \nu \left(\frac{\partial^2 u_1}{\partial r^2} + \frac{1}{r} \frac{\partial u_1}{\partial r} + \frac{\partial^2 u_1}{\partial x^2} - \frac{u_1}{r^2} \right) \quad (10.30)$$

$$\frac{\partial w_1}{\partial t} = -\frac{1}{\rho} \frac{\partial p_1}{\partial x} + \nu \left(\frac{\partial^2 w_1}{\partial r^2} + \frac{1}{r} \frac{\partial w_1}{\partial r} + \frac{\partial^2 w_1}{\partial x^2} \right) \quad (10.31)$$

and the continuity equation (10.3) gives

$$\frac{1}{r} \frac{\partial}{\partial r}(ru_1) + \frac{\partial w_1}{\partial x} = 0 \quad (10.32)$$

Expansion of the shell equation (10.21) to first order yields

$$\begin{aligned} & - (T_{\theta_0} + T_{\theta_1}\epsilon) \frac{\partial(R_1\epsilon)}{\partial x} + \frac{\partial((R_0 + R_1\epsilon)(T_{t_0} + T_{t_1}\epsilon))}{\partial x} - \\ & (R_0 + R_1\epsilon) \left(M_0 \frac{\partial^2(\xi_1\epsilon)}{\partial t^2} + L_x \frac{\partial(\xi_1\epsilon)}{\partial t} + K_x \xi_1\epsilon + \right. \\ & \left. \left(M_0 \frac{\partial^2(\eta_1\epsilon)}{\partial t^2} + L_r \frac{\partial(\eta_1\epsilon)}{\partial t} + K_r \eta_1\epsilon \right) \frac{\partial(R_1\epsilon)}{\partial x} \right) + \\ & (R_0 + R_1\epsilon) \left[1 + \left(\frac{\partial(R_0 + R_1\epsilon)}{\partial x} \right)^2 \right]^{-1/2} \\ & \left[(T_{xx_0} + T_{xx_1}\epsilon - T_{rr_0} - T_{rr_1}\epsilon) \frac{\partial(R_1\epsilon)}{\partial x} + (T_{rx_0} + T_{rx_1}\epsilon) \left(\left(\frac{\partial(R_1\epsilon)}{\partial x} \right)^2 - 1 \right) \right]_a \approx 0 \end{aligned}$$

The first order terms are

$$\begin{aligned} & -T_{\theta_0} \frac{\partial R_1}{\partial x} + \frac{\partial}{\partial x}(R_0 T_{t_1} + R_1 T_{t_0}) - \\ & R_0 \left(M_0 \frac{\partial^2 \xi_1}{\partial t^2} + L_x \frac{\partial \xi_1}{\partial t} + K_x \xi_1 \right) - R_0 [T_{rx_1}]_a = 0 \quad \Leftrightarrow \\ & M_0 \frac{\partial^2 \xi_1}{\partial t^2} + L_l \frac{\partial \xi_1}{\partial t} + K_l \xi_1 = \frac{\partial T_{t_1}}{\partial x} + \frac{T_{t_0} - T_{\theta_0}}{R_0} \frac{\partial R_1}{\partial x} - \mu \left[\frac{\partial w_1}{\partial r} + \frac{\partial u_1}{\partial x} \right]_a \quad (10.33) \end{aligned}$$

where the first order approximation of (10.14) is inserted for the surface stresses. We do not get any contributions from the terms involving T_{xx_0} and T_{rr_0} since the zeroth

order terms cancel. Equation (10.22) gives

$$\begin{aligned} & \frac{T_{\theta_0} + T_{\theta_1}\epsilon}{R_0 + R_1\epsilon} \left[1 + \left(\frac{\partial(R_1\epsilon)}{\partial x} \right)^2 \right]^{-1/2} - (T_{t_0} + T_{t_1}\epsilon) \frac{\partial^2(R_1\epsilon)}{\partial x^2} \left[1 + \left(\frac{\partial(R_1\epsilon)}{\partial x} \right)^2 \right]^{-3/2} - \\ & \left[1 + \left(\frac{\partial(R_1\epsilon)}{\partial x} \right)^2 \right]^{-1/2} \left(\left(M_0 \frac{\partial^2(\xi_1\epsilon)}{\partial t^2} + L_x \frac{\partial(\xi_1\epsilon)}{\partial t} + K_x \xi_1\epsilon \right) \frac{\partial(R_1\epsilon)}{\partial x} - \right. \\ & \quad \left. \left(M_0 \frac{\partial^2(\eta_1\epsilon)}{\partial t^2} + L_r \frac{\partial(\eta_1\epsilon)}{\partial t} + K_r \eta_1\epsilon \right) \right) - \\ & \left[1 + \left(\frac{\partial(R_1\epsilon)}{\partial x} \right)^2 \right]^{-1} \left[2 \frac{\partial(R_1\epsilon)}{\partial x} T_{rx_1}\epsilon - T_{rr_0} - T_{rr_1}\epsilon + \left(\frac{\partial(R_1\epsilon)}{\partial x} \right)^2 (T_{xx_0} + T_{xx_1}\epsilon) \right]_a \end{aligned}$$

where the first term can be approximated by

$$\begin{aligned} \frac{T_{\theta_0} + T_{\theta_1}\epsilon}{R_0 + R_1\epsilon} \left[1 + \left(\frac{\partial(R_1\epsilon)}{\partial x} \right)^2 \right]^{-1/2} & \approx \frac{T_{\theta_0} + T_{\theta_1}\epsilon}{R_0 \left(1 + \frac{R_1}{R_0}\epsilon \right)} \approx \\ \frac{T_{\theta_0} + T_{\theta_1}\epsilon}{R_0} \left(1 - \frac{R_1}{R_0}\epsilon \right) & \approx \frac{T_{\theta_0}}{R_0} + \left(\frac{T_{\theta_1}}{R_0} - T_{\theta_0} \frac{R_1}{R_0^2} \right) \epsilon \end{aligned}$$

Using this, the following first order approximations can be obtained

$$\begin{aligned} M_0 \frac{\partial^2 \eta_1}{\partial t^2} + L_r \frac{\partial \eta_1}{\partial t} + K_r \eta_1 = \\ - \frac{T_{\theta_1}}{R_0} + T_{\theta_0} \frac{R_1}{R_0^2} + T_{t_0} \frac{\partial^2 R_1}{\partial x^2} + \left[p - 2\mu \frac{\partial u_1}{\partial r} \right]_a \end{aligned} \quad (10.34)$$

where again the first order approximation of (10.14) is inserted for the stress exerted on the wall.

Assuming that the first order perturbations (indexed with 1) are small enough to neglect the second order perturbations, then ϵ can be incorporated in the dependent variables and we can set it to 1. For any (x, t) the first order Taylor expansion of $R(x + \xi, t)$ gives

$$R(x + \xi, t) = R(x, t) + \frac{\partial R}{\partial x} \xi = R_0 + \eta$$

as seen in Figure 10.6. The corresponding first-order expansion of R is given by

$$R(x, t) = R_0 + R_1\epsilon + \mathcal{O}(\epsilon^2) = R_0 + \eta_1\epsilon + \mathcal{O}(\epsilon^2)$$

since η has no zeroth order term. Furthermore, R_0 is approximated by the inner radius $a = R_0 - h/2$, but, since the walls are assumed to be thin compared with the vessel radius i.e. $h \ll a$, the error is negligible. Finally, the indices 1 are dropped and the definitions in (10.23) and (10.24) are used for T_{θ_1} and T_{t_1} . The linearized equations

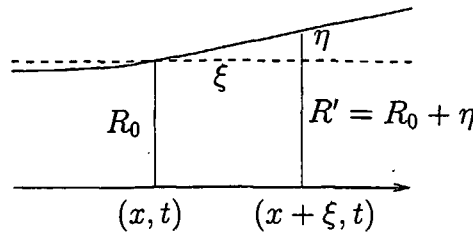


Figure 10.6: Estimation of $R(x + \xi, t)$ using the definitions of ξ and η .

can then be obtained from their first order approximations, i.e. (10.33) and (10.34) becomes

$$M_0 \frac{\partial^2 \xi}{\partial t^2} + L_l \frac{\partial \xi}{\partial t} + K_l \xi = \frac{E_x h}{1 - \sigma_\theta \sigma_x} \left(\frac{\partial^2 \xi}{\partial x^2} + \frac{\sigma_x}{a} \frac{\partial \eta}{\partial x} \right) + \frac{\partial \eta}{\partial x} \frac{T_{t_0} - T_{\theta_0}}{a} - \mu \left[\frac{\partial w}{\partial r} + \frac{\partial u}{\partial x} \right]_a \quad (10.35)$$

$$M_0 \frac{\partial^2 \eta}{\partial t^2} + L_r \frac{\partial \eta}{\partial t} + K_r \eta = -\frac{E_\theta h}{1 - \sigma_\theta \sigma_x} \left(\frac{\eta}{a^2} + \frac{\sigma_\theta}{a} \frac{\partial \xi}{\partial x} \right) + T_{\theta_0} \frac{\eta}{a^2} + T_{t_0} \frac{\partial^2 \eta}{\partial x^2} + \left[p - 2\mu \frac{\partial u}{\partial r} \right]_a \quad (10.36)$$

10.7 Solution of the linearized equations

Equations (10.30), (10.31), and (10.32) for the fluid motion must be solved first because the equations for the wall motion (10.35) and (10.36) couple to the fluid equations. Propagation of blood flow and pressure in human arteries is periodic and hence the solutions can be constructed from simple harmonic functions, i.e. u , w , p , ξ , and η can be written as propagating waves harmonic in both x and t . Therefore, we seek solutions of the form

$$\begin{aligned} u(r, x, t) &= u_r(r) e^{i\omega_k(t-x/c)} \\ w(r, x, t) &= w_r(r) e^{i\omega_k(t-x/c)} \\ p(r, x, t) &= p_r(r) e^{i\omega_k(t-x/c)} \\ \xi(x, t) &= \xi_1 e^{i\omega_k(t-x/c)} \\ \eta(x, t) &= \eta_1 e^{i\omega_k(t-x/c)} \end{aligned} \quad (10.37)$$

where $\omega_k = 2\pi k/T$ is the angular frequency. More general solutions can be found by superposition of solutions of this form (Whitham, 1974). Inserting these in (10.30–

10.32) for each $\omega = \omega_k$ gives

$$\begin{aligned} i\omega u_r &= -\frac{1}{\rho} \frac{dp_r}{dr} + \nu \left(\frac{d^2 u_r}{dr^2} + \frac{1}{r} \frac{du_r}{dr} + \frac{i^2 \omega^2 u_r}{c^2} - \frac{u_r}{r^2} \right) \\ i\omega w_r &= \frac{i\omega p_r}{\rho c} + \nu \left(\frac{d^2 w_r}{dr^2} + \frac{1}{r} \frac{dw_r}{dr} + \frac{i^2 \omega^2 w_r}{c^2} \right) \\ \frac{1}{r} \frac{d}{dr} (u_r r) &= \frac{i\omega w_r}{c} \end{aligned}$$

Let $\beta_0 = i a \omega / c$, $w_0^2 = i^3 a^2 \omega / \nu$ be dimensionless parameters. Multiplying the equations above by a^2 / ν and use $y = r/a$ then give the following inhomogeneous Bessel equations

$$\frac{a}{\mu} \frac{dp_r}{dy} = \frac{d^2 u_r}{dy^2} + \frac{1}{y} \frac{du_r}{dy} + (w_0^2 + \beta_0^2) u_r - \frac{u_r}{y^2} \quad (10.38)$$

$$\frac{R\beta_0}{\mu} p_r = \frac{d^2 w_r}{dy^2} + \frac{1}{y} \frac{dw_r}{dy} + (w_0^2 + \beta_0^2) w_r \quad (10.39)$$

$$\frac{1}{y} \frac{d}{dy} (u_r y) - \beta_0 w_r = 0 \quad (10.40)$$

The solutions to the corresponding homogeneous equations are

$$\begin{aligned} u_r &= u_c \frac{J_1 \left(\frac{r}{a} \sqrt{w_0^2 + \beta_0^2} \right)}{J_0(w_0)} \\ w_r &= w_c \frac{J_0 \left(\frac{r}{a} \sqrt{w_0^2 + \beta_0^2} \right)}{J_0(w_0)} \end{aligned} \quad (10.41)$$

The divergence of (10.31) gives

$$\begin{aligned} \nabla^2 p &= \frac{1}{r} \frac{d}{dr} \left(r \frac{dp}{dr} \right) + \frac{d^2 p}{dx^2} = 0 \Leftrightarrow \\ \frac{d^2 p_r}{dr^2} + \frac{1}{r} \frac{dp_r}{dr} + \frac{\beta_0^2}{a^2} p_r &= 0 \end{aligned}$$

which has the solution

$$p_r = p_1 J_0 \left(\frac{\beta_0 r}{a} \right) \quad (10.42)$$

Assume that the particular solution has the form

$$u_r = u_{cp} J_1 \left(\frac{\beta_0 r}{a} \right) \quad (10.43)$$

$$w_r = w_{cp} J_0 \left(\frac{\beta_0 r}{a} \right) \quad (10.44)$$

Inserting (10.42) together with (10.43) and (10.44) in (10.38) and (10.39), and using (10.40) to determine the constants gives the following solutions

$$u_r = \left[-\frac{a p_c \beta_0}{\mu w_0^2} J_1 \left(\frac{\beta_0 r}{a} \right) + \frac{A p_c \beta_0}{w_0 J_0(w_0)} J_1 \left(\frac{r}{a} \sqrt{w_0^2 + \beta_0^2} \right) \right] \quad (10.45)$$

$$w_r = \left[-\frac{a p_c \beta_0}{\mu w_0^2} J_0 \left(\frac{\beta_0 r}{a} \right) + \frac{A p_c \sqrt{w_0^2 + \beta_0^2}}{w_0 J_0(w_0)} J_0 \left(\frac{r}{a} \sqrt{w_0^2 + \beta_0^2} \right) \right] \quad (10.46)$$

$$p_r = p_c J_0 \left(\frac{\beta_0 r}{a} \right)$$

where $J_0(x)$ and $J_1(x)$ denote the zeroth and first order Bessel functions and A and p_c are the integration constants. w_0 and β_0 are dimensionless parameters given by

$$w_0^2 = i^3 \frac{a^2 \omega}{\nu} = i^3 w^2$$

where w is the Womersley number. Furthermore, assume that $A = \tilde{A}/(c_0 \rho)$, where c_0 is the Moens-Korteweg wave propagation velocity. However, we will reuse the letter A in order to avoid writing the tildes. Inserting the expressions above for u , w , p , and A into the boundary conditions (10.25) and (10.26) gives

$$\begin{aligned} -\frac{a p_c \beta_0}{\mu w_0^2} J_1(\beta_0) + \frac{A p_c \beta_0}{c_0 \rho} \frac{J_1 \left(\sqrt{w_0^2 + \beta_0^2} \right)}{w_0 J_0(w_0)} - i \omega \eta_1 &= 0 \\ -\frac{a p_c \beta_0}{\mu w_0^2} J_0(\beta_0) + \frac{A p_c \sqrt{w_0^2 + \beta_0^2}}{c_0 \rho} \frac{J_0 \left(\sqrt{w_0^2 + \beta_0^2} \right)}{w_0 J_0(w_0)} - i \omega \xi_1 &= 0 \end{aligned}$$

The system has four unknowns p_c , A , ξ_1 , and η_1 . Therefore, two more equations are needed. They stem from the equations for motion of the wall (10.35) and (10.36). Expanding ξ and η as in (10.37) and using u_r and w_r from (10.45) and (10.46) gives

$$\begin{aligned} p_c \left[J_0(\beta_0) + \frac{\beta_0^2}{w_0^2} (J_0(\beta_0) - J_2(\beta_0)) \right] - \\ \frac{A p_c \beta_0 \mu}{a c_0 \rho} \frac{\sqrt{w_0^2 + \beta_0^2}}{w_0 J_0(w_0)} \left[J_0 \left(\sqrt{w_0^2 + \beta_0^2} \right) - J_2 \left(\sqrt{w_0^2 + \beta_0^2} \right) \right] + \\ \eta_1 \left[\frac{T_{t_0} \beta_0^2 + T_{\theta_0} - B_{11}}{a^2} + \omega^2 \left(M_0 - i \frac{L_r}{\omega} - \frac{K_r}{\omega^2} \right) \right] + \frac{B_{12} \xi_1 \beta_0}{a^2} = 0 \quad (10.47) \end{aligned}$$

$$\begin{aligned} -\frac{2 p_c \beta_0^2}{w_0^2} J_1(\beta_0) + \frac{A p_c \mu (w_0^2 + \beta_0^2)}{a c_0 \rho w_0 J_0(w_0)} J_1 \left(\sqrt{w_0^2 + \beta_0^2} \right) - \frac{(B_{21} + T_{t_0} - T_{\theta_0}) \eta_1 \beta_0}{a^2} + \\ \xi_1 \left[\frac{B_{22} \beta_0^2}{a^2} + \omega^2 \left(M_0 - i \frac{L_x}{\omega} - \frac{K_x}{\omega^2} \right) \right] = 0 \quad (10.48) \end{aligned}$$

where

$$\begin{aligned} B_{11} &= \frac{E_\theta h}{1 - \sigma_x \sigma_\theta} & B_{22} &= \frac{E_x h}{1 - \sigma_x \sigma_\theta} \\ B_{12} &= \frac{E_\theta h \sigma_x}{1 - \sigma_x \sigma_\theta} & B_{21} &= \frac{E_x h \sigma_\theta}{1 - \sigma_x \sigma_\theta} \end{aligned}$$

These provide the last two equations for the four unknowns ξ_1 , η_1 , p_c and A . They are, however, still too complicated but they can be simplified using a long-wave approximation. This rests on the assumption

$$|\beta_0| = \left| \frac{a\omega}{c} \right| \ll 1$$

Hence,

$$\begin{aligned} J_0(\beta_0) &\approx 1 \\ J_1(\beta_0) &\approx \frac{\beta_0}{2} \\ J_2(\beta_0) &\approx \frac{\beta_0^2}{8} \\ w_0^2 + \beta_0^2 &\approx w_0^2 \end{aligned}$$

which gives

$$p_c \left(-\frac{a\beta_0^2}{2\mu w_0^2} + \frac{A\beta_0 F_J}{2c_0\rho} \right) - i\omega\eta_1 = 0 \quad (10.49)$$

$$p_c \left(-\frac{a\beta_0}{\mu w_0^2} + \frac{A}{c_0\rho} \right) - i\omega\xi_1 = 0 \quad (10.50)$$

$$\begin{aligned} p_c - \frac{A p_c \mu \beta_0}{a c_0 \rho} (2 - F_J) + \frac{B_{12} \beta_0 \xi_1}{a^2} + \\ \eta_1 \left[\frac{T_{t_0} \beta_0^2 + T_{\theta_0} - B_{11}}{a^2} + \omega^2 \left(M_0 - i \frac{L_r}{\omega} - \frac{K_r}{\omega^2} \right) \right] = 0 \end{aligned} \quad (10.51)$$

$$\begin{aligned} -\frac{p_c \beta_0^3}{w_0^2} + \frac{A p_c \mu w_0^2 F_J}{2 a c_0 \rho} - \frac{(B_{21} + T_{t_0} - T_{\theta_0}) \beta_0 \eta_1}{a^2} + \\ \xi_1 \left[\frac{B_{22} \beta_0^2}{a^2} + \omega^2 \left(M_0 - i \frac{L_x}{\omega} - \frac{K_x}{\omega^2} \right) \right] = 0 \end{aligned} \quad (10.52)$$

where the recursion formula

$$J_{n+1}(x) = \frac{2n}{x} J_n(x) - J_{n-1}(x)$$

and

$$F_J = \frac{2J_1(w_0)}{w_0 J_0(w_0)}$$

have been used. Equations (10.49–10.52) comprise a complete system for the variables p_c , $A p_c / (c_0 \rho)$, η_1 , and ξ_1 . They have non-trivial solutions if the determinant is zero. Computing the determinant gives in fact an equation which has the complex propagation velocity as the only unknown. The determinant is given by

$$\begin{vmatrix}
 -\frac{a\beta_0^2}{2\mu W_0^2} & \frac{\beta_0 F_J}{2} & -i\omega & 0 \\
 -\frac{a\beta_0}{\mu W_0^2} & 1 & 0 & -i\omega \\
 1 & -\frac{\mu\beta_0}{a}(2-F_J) & \frac{T_{t_0}\beta_0^2+T_{\theta_0}-B_{11}}{a^2} + \omega^2 K'_r & \frac{B_{12}\beta_0}{a^2} \\
 -\frac{\beta_0^3}{W_0^2} & \frac{\mu W_0^2 F_J}{2a} & -\frac{(B_{21}+T_{t_0}-T_{\theta_0})\beta_0}{a^2} & \frac{B_{22}\beta_0^2}{a^2} + \omega^2 K'_x
 \end{vmatrix} \quad (10.53)$$

where $K'_r = M_0 - iL_r/\omega - K_r/\omega^2$ and $K'_x = M_0 - iL_x/\omega - K_x/\omega^2$. In order to simplify (10.53) we analyze the magnitude of the terms in order to neglect the smaller ones and perform a number of row/column operations on the determinant.

First, it should be noted that $T_{t_0}\beta_0^2/a^2$ is much smaller than the other parts, which are of order one. Hence, this can be neglected. Second, $w_0^2 = i^3 w^2$ and $\beta_0 = i\beta$ are expanded and the following operations are performed:

1. Multiply the first column by $\mu w^2/(\beta a)$, the third column by β/w , and the fourth column by i/ω .
2. Multiply the second row by $1/(i\beta)$, the third row by $\beta a/(\mu w^2)$, and the fourth row by ia/μ .
3. Replace the second row by the first row minus twice the second row, and the third row by the first row minus the third row.

Thus, the determinant becomes

$$\begin{vmatrix}
 1 & 1 & 0 & 1 \\
 0 & 1-F_J & 2 & 1 \\
 0 & 1 + \frac{i\beta^2(2-F_J)}{w^2} & -\frac{(T_{\theta_0}-B_{11})\beta^2}{a\omega\mu W^2} - \frac{a\omega\beta^2 K'_r}{\mu W^2} & 1 + \frac{B_{12}\beta^2}{a\omega\mu W^2} \\
 -\beta^2 i & \frac{w^2 F_J}{2} & \frac{(B_{21}+T_{t_0}+T_{\theta_0})\beta^2}{a\omega\mu} & \frac{B_{22}\beta^2}{a\omega\mu} - \frac{\omega a K'_x}{\mu}
 \end{vmatrix} \quad (10.54)$$

A further analysis of the magnitude of the terms yields that $1 + \beta^2 i(2-F_J)/w^2 \approx 1$. Expanding the determinant after first column gives two sub-determinants with the same order of magnitude. Hence, the one arising from $-i\beta^2$ can be neglected. The remaining sub-determinant is

$$\begin{vmatrix}
 1-F_J & 2 & 1 \\
 1 & -\frac{(T_{\theta_0}-B_{11})\beta^2}{a\omega\mu W^2} - \frac{a\omega\beta^2 K'_r}{\mu W^2} & 1 + \frac{B_{12}\beta^2}{a\omega\mu W^2} \\
 \frac{w^2 F_J}{2} & \frac{(B_{21}+T_{t_0}+T_{\theta_0})\beta^2}{a\omega\mu} & \frac{B_{22}\beta^2}{a\omega\mu} - \frac{\omega a K'_x}{\mu}
 \end{vmatrix} = 0 \quad (10.55)$$

Let

$$\begin{aligned} B'_{11} &= \frac{B_{11} - T_{\theta_0}}{ac_0^2\rho} & B'_{12} &= \frac{B_{12}}{ac_0^2\rho} \\ B'_{21} &= \frac{B_{21} + T_{t_0} - T_{\theta_0}}{ac_0^2\rho} & B'_{22} &= \frac{B_{22}}{ac_0^2\rho} \\ K'_x &= \frac{\omega^2 a}{\rho c_0^2} \left(-M_0 + \frac{iL_x}{\omega} + \frac{K_x}{\omega^2} \right) & K'_r &= \frac{\omega^2 a}{\rho c_0^2} \left(-M_0 + \frac{iL_r}{\omega} + \frac{K_r}{\omega^2} \right) \end{aligned}$$

where K'_r and K'_x have been redefined. Inserting these and expanding $w^2 = a^2\omega/\nu$, $\beta = a\omega/c$ gives

$$\begin{vmatrix} 1 - F_J & 2 & 1 \\ 1 & (k')^2(B'_{11} + K'_r) & 1 + (k')^2 B'_{21} \\ \frac{F_J}{2} & (k')^2 B'_{21} & (k')^2 B'_{22} + \frac{K'_x c_0^2}{a^2 \omega^2} \end{vmatrix} = 0 \quad (10.56)$$

where $k' = c_0/c$ and $\rho = \mu/\nu$. Thus, the resulting determinant is

$$\begin{aligned} & (k')^4(1 - F_J) [B'_{22}(B'_{11} + K'_r) - B'_{12}B'_{21}] + \\ & (k')^2 \left[F_J \left(B'_{12} + B'_{21} - \frac{B'_{11} + K'_r}{2} \right) - 2B'_{22} + \frac{c_0^2}{a^2 \omega^2} K'_x (B'_{11} + K'_r)(1 - F_J) \right] + \\ & F_J + \frac{2c_0^2}{\omega^2 a^2} K'_x = 0 \end{aligned} \quad (10.57)$$

This is the dispersion relation for the waves and it is equivalent to the result obtained by Pedley (1980).

The original equations can be simplified by neglecting the terms corresponding to the simplifications that led to (10.55). This gives the following system of equations, which can also be found in Pedley (1980).

$$p_c \left(-\frac{\beta_0^2 a}{2\mu w_0^2} + \frac{AF_J}{2c_0\rho} \right) - i\omega\eta_1 = 0 \quad (10.58)$$

$$p_c \left(-\frac{\beta_0 a}{\mu w_0^2} + \frac{A}{c_0\rho} \right) - i\omega\xi_1 = 0 \quad (10.59)$$

$$p_c + \left[\frac{T_{\theta_0} - B_{11}}{a^2} + (M_0\omega^2 - iL_r\omega - K_r) \right] \eta_1 + \frac{B_{12}\beta_0\xi_1}{a^2} = 0 \quad (10.60)$$

$$\begin{aligned} & \frac{A p_c \mu w_0^2 F_J}{2 a c_0 \rho} - \frac{(B_{21} + T_{t_0} - T_{\theta_0})\beta_0\eta_1}{a^2} + \\ & \left[\frac{B_{22}\beta_0^2}{a^2} + (M_0\omega^2 - iL_x\omega - K_x\omega^2) \right] \xi_1 = 0 \end{aligned} \quad (10.61)$$

Generally k' is a complex number

$$\frac{c_0}{c} = k'_{re} + ik'_{im}$$

Giving

$$\exp(i\omega(t - x/c)) = \exp(i\omega(t - xk'_{re}/c_0)) \exp(-x\omega k'_{im}/c_0) \quad (10.62)$$

The real part of the wave propagation can be written as

$$\frac{c_0}{k'_{re}} = \frac{\omega}{k}$$

where k is the wave number. Hence, (10.62) becomes

$$\exp(i\omega(t - x/c)) = \exp(i\omega(t - xk'_{re}/c_0)) \exp(-2\pi k'_{im}x/(\lambda k'_{re}))$$

where $\lambda = 2\pi/k$ is the wavelength. The last exponential represents the transmission per wavelength. The fourth order equation (10.57) gives two solutions for $(k')^2$, but only one of them represents the pressure wave. If $x > 0$ the solutions represent the outgoing waves, and if $x < 0$ the solutions represent the incoming waves. Since we want to study the waves propagating distally (from the heart towards the peripheral vessels) we will only consider the solutions representing the outgoing waves.

In any case the solutions depends on w , the Womersley number, through F_J . The ratio of the vessel radius to the thickness of the oscillating Stokes boundary layer is proportional to w . If w is large, the boundary layer is thin and the velocity profile is almost flat across the core vessel; if w is small, the boundary layer is thick (the vessel is fully occupied by the innermost portion of the boundary layer) and the flow becomes quasi-steady. For $w \rightarrow 0$ a Poiseuille flow is obtained. The following asymptotic expansion can be derived for F_J for large and small values of w , respectively.

$$F_J(w) = \begin{cases} 2/(wi^{1/2}) [1 + (2w)^{-1} + \mathcal{O}(w^{-2})] & \text{for } w \rightarrow \infty \\ 1 - i(w^2/8) - (w^4/48) + \mathcal{O}(w^6) & \text{for } w \rightarrow 0 \end{cases} \quad (10.63)$$

This system is still too complicated to solve for any real applications. Therefore, it must be simplified further. This can be done by assuming longitudinal tethering. Hence, $T_{t_0} = 0$, $T_{\theta_0} = 0$, and

$$c_0^2 = \frac{E_\theta h}{2\rho a}$$

Thus, B'_{ij} are

$$\begin{aligned} B'_{11} &= \frac{2}{1 - \sigma_x \sigma_\theta} & B'_{12} &= \frac{2\sigma_x}{1 - \sigma_x \sigma_\theta} \\ B'_{21} &= \frac{2E_x/E_\theta \sigma_\theta}{1 - \sigma_x \sigma_\theta} & B'_{22} &= \frac{2E_x/E_\theta}{1 - \sigma_x \sigma_\theta} \end{aligned}$$

These quantities are of order one. According to Bergel (1972) good estimates are $\sigma_x = \sigma_\theta = 0.29$ and $E_x/E_\theta = 1.2$. This yields

$$B'_{11} = 2.18, \quad B'_{22} = 2.62, \quad B'_{12} = 0.63, \quad B'_{21} = 0.76$$

Bergel also gives values for the tethering constants,

$$\begin{aligned} K_{r,x} &\approx 33 \times 10^3 \text{ kg/(s}^2\text{m}^2) \\ L_{r,x} &\approx 17 \times 10^3 \text{ kg/(s m}^2) \\ M_0 &\approx 4 \text{ kg/m}^2 \end{aligned}$$

Consequently, M_0 is negligible compared with $K_{r,x}$ and $L_{r,x}$. Hence,

$$K'_{r,x} \approx \frac{(33 + 17i\omega) a}{\rho c_0^2} \times 10^3 \text{ kg/(s}^2\text{m}^2)$$

In the smaller arteries $a \approx 10^{-3}$ m, $\rho \approx 10^3$ kg/m³, $c_0 \approx 5$ m/s, and $\omega \approx 4\pi\text{s}^{-1}$, hence $|K'_{r,x}| \approx 0.009$. These data are as estimated by Pedley (1980). From these estimates we see that $K'_r \ll B'_{ij}$ and hence K'_r can be neglected in (10.57). The term involving K'_x appear as $c_0^2/(\omega^2 a^2) K_x \approx 1400$ which is large compared to the other terms. Therefore, the dispersion relation (10.57) reduces to:

$$a_0(k')^4 + (a_1 K - a_2)(k')^2 - \frac{2K}{1 - F_J} = 0 \quad (10.64)$$

where

$$\begin{aligned} a_0 &= B'_{22}B'_{11} - B'_{12}B'_{21} \\ a_1 &= B'_{11} \\ a_2 &= F_J \left(B'_{12} + B'_{21} - \frac{B'_{11}}{2} \right) - 2B'_{22} \end{aligned}$$

and

$$K = \frac{c_0^2}{a^2 \omega^2} K'_x$$

Since K is large, a_2 can be neglected as well and we are left with

$$a_0(k')^4 + a_1 K(k')^2 - \frac{2K}{1 - F_J} = 0$$

which has the approximative solutions

$$\begin{aligned} (k')^2 &\approx -\frac{a_1 K}{a_0} \left(1 \pm \left(1 - \frac{2}{K(1 - F_J)a_1} \right) \right) \Leftrightarrow \\ (k')^2 &\approx \frac{2}{(1 - F_J)a_1}, -\frac{a_1 K}{a_0} \end{aligned} \quad (10.65)$$

The first of these solutions is the pressure wave. This can be compared to the result found by Lighthill (1989), where the wall is assumed to be an isotropic elastic solid, i.e. $a_1 = B'_{11} = 2/(1 - \sigma^2)$ and $w \rightarrow \infty$ such that $F_J \approx 0$. Then (10.65) gives $(k')^2 = 1 - \sigma^2$ or equivalently $c^2 = c_0/(1 - \sigma^2)$.

The solution can also be found by letting $K \rightarrow \infty$ directly in (10.58–10.61). However, this is possible only if $\xi = 0$. Hence, from (10.61) one finds (still neglecting K'_r) that

$$B'_{11}\eta_1 = \frac{ap_c}{\rho c_0^2}$$

From (10.58)

$$A = -k'$$

and from (10.59)

$$(k')^2 = \frac{2\eta_1}{(1 - F_J)ap_c/\rho c_0^2} = \frac{2}{(1 - F_J)B'_{11}}$$

which is consistent with (10.65). Finally, from (10.60)

$$B'_{21}\eta_1 = -\frac{F_Jap_c}{2c_0^2\rho}$$

10.8 Momentum equation

The one-dimensional flow associated with the longitudinal velocity w_r is given by

$$Q = \int_0^a w_r 2\pi r dr \quad (10.66)$$

The long-wave approximation, see page 110, gives rise to the following approximations

$$\begin{aligned} J_0\left(\frac{\beta_0 r}{a}\right) &\approx 1 \\ J_1\left(\frac{\beta_0 r}{a}\right) &\approx \frac{\beta_0 r}{2a} \\ J_i\left(\frac{r}{a}\sqrt{w_0^2 + \beta_0^2}\right) &\approx J_i\left(\frac{w_0 r}{a}\right) \end{aligned}$$

for $i = 0, 1$. Inserting these in (10.41) gives

$$w_r = \frac{p_c}{w_0} \left(-\frac{\beta_0^2 a}{\mu w_0} + \frac{A}{J_0(w_0)} J_0\left(\frac{w_0 r}{a}\right) \right) \quad (10.67)$$

Expanding w_0 and β_0 and inserting $A = k'$ in (10.67) gives

$$w_r = \frac{p_c}{c_0 \rho} k' \left[1 - \frac{J_0\left(\frac{w_0 r}{a}\right)}{w_0 J_0(w_0)} \right] \quad (10.68)$$

Integrating over the cross-sectional area yields

$$Q = \frac{-A_0 p_c}{\rho c_0} k' (1 - F_J) \quad (10.69)$$

where $A_0 = \pi a^2$ is the cross-sectional area of the vessel, $k'/c_0 = 1/c$,

$$\frac{-i\omega p_c}{c} = \frac{\partial P}{\partial x} \quad (10.70)$$

is the complex pressure gradient, and F_J is defined according to (10.63). In Pedley (1980) it is shown that it is reasonable to use the lower expression in (10.63) when $w \leq 4$ and the upper expression in (10.63) when $w > 4$. This function is not continuous at $w = 4$ because it is derived as approximations for the limits of w . However, splitting at $w = 4$ seems very crude. Instead we have set up a continuous equation by using the upper equation for $w > 3$ and the lower equation for $w \leq 2$ and making a linear interpolation between the two values.

The final momentum equation is obtained by inserting (10.70) in (10.69)

$$i\omega Q = \frac{-A_0}{\rho} \frac{\partial P}{\partial x} (1 - F_J) \quad (10.71)$$

10.9 Continuity equation

The one-dimensional continuity equation for the smaller arteries is the same as for the larger arteries, namely

$$\frac{\partial A}{\partial t} + \frac{\partial q}{\partial x} = 0$$

We use the Fourier series expansions from (8.7) and (8.8)

$$p(x, t) = \sum_{k=-\infty}^{\infty} P(x, \omega_k) e^{i\omega_k t}$$

$$q(x, t) = \sum_{k=-\infty}^{\infty} Q(x, \omega_k) e^{i\omega_k t}$$

with Fourier coefficients given by

$$P(x, \omega_k) = \frac{1}{T} \int_{-T/2}^{T/2} p(x, t) e^{-i\omega_k t} dt$$

$$Q(x, \omega_k) = \frac{1}{T} \int_{-T/2}^{T/2} q(x, t) e^{-i\omega_k t} dt$$

where $\omega_k = 2\pi k/T$ is the angular frequency. These are equivalent to the Fourier expansion in (10.37). For each $\omega = \omega_k$ the continuity equation can be transformed to

$$i\omega CP + \frac{\partial Q}{\partial x} = 0 \quad (10.72)$$

where C is the compliance. This can be approximated by

$$C = \frac{dA}{dp} = \frac{3A_0 a}{2Eh} \left(1 - \frac{3pa}{4Eh}\right)^{-3} \approx \frac{3A_0 a}{2Eh}$$

which applies since $Eh \gg pa$.

10.10 Solutions of the linear model

For each vessel in the smaller arteries (10.72) and (10.71) must be solved. The equations comprise a continuity and a momentum equation determining the flow resulting from an oscillatory pressure gradient in a non-tapering vessel where the amplitude and the phase depend on the wall distensibility and viscoelasticity through the factor k' . These are

$$i\omega CP + \frac{\partial Q}{\partial x} = 0 \quad (10.73)$$

$$i\omega Q + \frac{A_0(1 - F_J)}{\rho} \frac{\partial P}{\partial x} = 0 \quad (10.74)$$

These equations are periodic with period T and apply for any vessels of length L . Differentiating (10.74) with respect to x and inserting the result in (10.73) give

$$\frac{\omega^2}{c^2} Q + \frac{\partial^2 Q}{\partial x^2} = 0 \quad \text{or} \quad \frac{\omega^2}{c^2} P + \frac{\partial^2 P}{\partial x^2} = 0 \quad (10.75)$$

with the wave propagation velocity

$$c = \sqrt{\frac{A_0(1 - F_J)}{\rho C}} \quad (10.76)$$

Solving (10.75) yields

$$\begin{aligned} Q(x, \omega) &= a \cos(\omega x/c) + b \sin(\omega x/c) \\ P(x, \omega) &= i \sqrt{\frac{\rho}{C A_0(1 - F_J)}} (-a \sin(\omega x/c) + b \cos(\omega x/c)) \end{aligned}$$

where a and b are arbitrary constants of integration. As stated in (8.6) the impedance $Z(x, \omega)$ for any Fourier mode can be defined by the relation

$$P(x, \omega) = Z(x, \omega) Q(x, \omega)$$

Hence, the impedance can found by

$$Z(x, \omega) = \frac{ig^{-1}(b \cos(\omega x/c) - a \sin(\omega x/c))}{a \cos(\omega x/c) + b \sin(\omega x/c)} \quad (10.77)$$

where

$$g = \sqrt{C A_0(1 - F_J)/\rho} \quad (10.78)$$

At $x = L$

$$Z(L, \omega) = \frac{ig^{-1}(b \cos(\omega L/c) - a \sin(\omega L/c))}{a \cos(\omega L/c) + b \sin(\omega L/c)}$$

and at $x = 0$

$$Z(0, \omega) = \frac{i b}{g a} \quad (10.79)$$

Assuming that $Z(L, \omega)$ is known b/a can be found using (10.77).

$$\frac{b}{a} = \frac{\sin(\omega L/c) - igZ(L, \omega) \cos(\omega L/c)}{\cos(\omega L/c) + igZ(L, \omega) \sin(\omega L/c)}$$

Then, the root impedance for any vessel can be found from (10.79).

$$Z(0, \omega) = \frac{ig^{-1} \sin(\omega L/c) + Z(L, \omega) \cos(\omega L/c)}{\cos(\omega L/c) + igZ(L, \omega) \sin(\omega L/c)} \quad (10.80)$$

For any vessel, the input impedance for zero frequency, or in the electrical terminology the DC impedance, can be found as

$$\begin{aligned} Z(0, 0) &= \lim_{\omega \rightarrow 0} Z(0, \omega) \\ &= \lim_{\omega \rightarrow 0} (ig^{-1} \sin(\omega L/c) + Z_L(L, \omega) \cos(\omega L/c)) \\ &= \lim_{\omega \rightarrow 0} \left(i\omega L \frac{\rho}{A_0} \frac{8\nu}{ir^2\omega} + Z_L(L, \omega) \right) \\ &= \frac{8\mu L}{\pi r_0^4} + Z(L, 0) \\ &= \frac{8\mu l_{rr}}{\pi r_0^3} + Z(L, 0) \end{aligned} \quad (10.81)$$

where $l_{rr} = L/r_0$ is the length to radius ratio, as discussed in Chapter 6. Equation (10.81) suggests that in general, for any network, the root impedance will be proportional to r_0^{-3} . Since we terminate the structured tree when the radius of the leaves is smaller than some given minimum value $r < r_{min}$, the constant of proportionality can not be derived analytically. In the special case of a symmetric tree, i.e. where all vessels scale such that $r_j = \alpha^j r_0$, with N generations and where the impedance at the terminal vessels are zero (when $Z_N(L, 0) = 0$), we get

$$Z(0, 0) = \frac{8\mu l_{rr}}{\pi r_0^3} \sum_{j=0}^N \left(\frac{1}{2\alpha^3} \right)^j = \frac{8\mu l_{rr}}{\pi r_0^3} \frac{2\alpha^3 - \left(\frac{1}{2\alpha^3} \right)^N}{2\alpha^3 - 1} \quad (10.82)$$

Chapter 11

Flow and pressure in the tree of smaller arteries

In analogy to the larger arteries we could now solve (10.73) and (10.74) with appropriate boundary conditions and predict the blood flow and pressure at any site along the smaller arteries. However, we are only interested in the impedance at the root of the structured tree as explained in Chapter 10. Equation (10.80) gives $Z(0, \omega) = f(Z(L, \omega))$ for any of the smaller arteries. The aim of this chapter is to determine an expression for the root impedance of the structured trees comprising the smaller arteries. This is done by imposing appropriate boundary conditions combining the smaller arteries into the structured tree. These are:

- A bifurcation condition.
- A terminal boundary condition.

11.1 Bifurcation condition

Setting up the bifurcation condition does not require much more than we have already established. As for the larger arteries we assume that pressure is continuous and that no flow is leaking at the bifurcation, see Section 8.1.2. Hence, the bifurcation is analogous to a transmission-line network and the admittances add, i.e.

$$\frac{1}{Z_p} = \frac{1}{Z_{d_1}} + \frac{1}{Z_{d_2}} \quad (11.1)$$

where as before the subscript p refers to the parent vessel and the subscripts d_1, d_2 refer to the daughter vessels.

11.2 Outflow boundary condition

Because of the viscous treatment of blood in the smaller arteries the structured tree yields a resistance by itself and we can assume a zero impedance at the leaves of the structured tree. Because various parts of the body serve different needs and hence show a variation in the peripheral resistance, the approach above requires that the minimum

radii (r_{min}) applied at the terminals are chosen individually for each of the structured trees. While r_{min} may vary for the different structured trees it is kept constant in each of them. Alternatively, one could choose a common minimum radius and then vary the total impedance by applying a variable terminal impedance at the bottom of the vessels and then propagate this back through the tree together with the induced dynamic impedance.

11.3 Root impedance of the structured tree

Because of the structure of the tree, all parameters are determined as functions of the vessel radius. Hence, both g , defined in (10.78), and the length L for each vessel can be determined as functions of the vessel radius. Furthermore, because of the geometric self-similarity it is very easy to compute the root impedance $Z(0, \omega)$ by solving, (10.80) and (11.1) recursively. However, in order to do so all basic parameters must be initialized. These are:

- The scaling parameters α and β which are given by (6.4).
- The terminal resistance Z_t (see discussion on page 122).
- The minimum radius r_{min} , at which all vessels of the structured tree are truncated.
- The root radius r_{root} .

Recall that the root impedance should be used with the outflow boundary condition for the larger arteries, i.e. when evaluating the convolution integral in (8.11). Since we assumed that the wave propagation of the larger arteries is periodic the impedance should be determined for all $0 \leq t \leq T$. Hence, in the frequency domain this translates to discrete angular frequencies $\omega_k = 2\pi k/T$, for $k = -N/2, \dots, N/2$ where N is the number of time-steps per period. Now, because of the possibility to apply self conjugation

$$Z(0, \omega_{-k}) = \overline{Z(0, \omega_k)}$$

we only need to determine $Z(0, \omega_k)$ for $k = 0, 1, \dots, N/2$.

Finally, before describing an algorithm for determining the root impedance we will describe how to take advantage of the fact that the tree of smaller arteries is structured. A binary tree with N generations would have 2^N terminal leaves. In our case the tree is structured such that the radius of any vessel at the n th generation is scaled with the factor:

$$\alpha^k \beta^{n-k} \quad \text{for } k \in [0; n]$$

Each scaling factor appears with frequency

$$\text{Freq} = \frac{n!}{k!(n-k)!}$$

For a tree with N generations there are

$$\sum_{n=0}^N \sum_{k=0}^n 1 = \mathcal{O}(N^2)$$

different impedances which must be calculated. This is illustrated in Figure 6.1. This should be seen in contrast to a general binary tree in which all vessels may have different impedances. In this case the complexity is $\mathcal{O}(2^N)$. Thus, the simplifications achieved by storing (e.g. in the table computed) each of the impedances once they have been calculated is what makes the algorithm computationally feasible. However, it should be noted, that the estimates above are for a tree with a fixed number of generations. Since the structured trees are truncated when the radius of any given vessel becomes smaller than some minimum radius, however, these estimates are not exact, but for most practical situations they are still valid. In any case, the savings obtained from reusing the pre-computed values are crucial to this approach.

The recursive algorithm can thus be written as:

Algorithm 1: Computes the root impedance $Z_0(\omega_k, p_\alpha, p_\beta)$ recursively.

- Determine all parameters for the vessel (as described in Chapter 6):
 - The radius $r = \alpha^{p_\alpha} \beta^{p_\beta} r_{root}$.
 - The cross-sectional area $A = \pi r^2$.
 - The elasticity relation $f(r) = Eh/\tau$, see (5.4).
 - The length $l = r l_{rr}$ where l_{rr} is the length to radius ratio.
 - The viscosity μ .
- Determine the wave propagation speed c and the scalar g as given in (10.76) and (10.78). These depend on F_J , defined in (10.63) and thus on the Womersley number w .
- The recursive algorithm:
 - If $r < r_{min}$ then
 - $Z_L(\omega_k, p_\alpha, p_\beta) = \text{terminal resistance.}$
 - else
 - If the root impedance of the left daughter $(p_\alpha + 1, p_\beta)$ has been previously computed then
 - $Z_0(\omega_k, p_\alpha + 1, p_\beta) = \text{computed}(p_\alpha + 1, p_\beta)$
 - else
 - Compute the root impedance of the left daughter by calling $Z_0(\omega_k, p_\alpha + 1, p_\beta)$ recursively.
 - If the root impedance of the right daughter $(p_\alpha + 1, p_\beta)$ has been computed previously then

$$Z_0(\omega_k, p_\alpha, p_\beta + 1) = \text{computed}(p_\alpha, p_\beta + 1)$$

◦ else

Compute the root impedance of the right daughter by calling $Z_0(\omega_k, p_\alpha, p_\beta + 1)$ recursively.

$$\blacksquare Z_L(\omega_k, p_\alpha, p_\beta) = 1 / (Z_0^{-1}(\omega_k, p_\alpha + 1, p_\beta) + Z_0^{-1}(\omega_k, p_\alpha, p_\beta + 1))$$

• If $\omega_k \neq 0$ then

$$\blacksquare Z_0(\omega_k, p_\alpha, p_\beta) = f(Z_L(\omega_k, p_\alpha, p_\beta)) \text{ using (10.80).}$$

• else, if $\omega_k = 0$ then

$$\blacksquare Z_0(\omega_k, p_\alpha, p_\beta) = f(Z_L(\omega_k, p_\alpha, p_\beta)) \text{ using (10.81).}$$

• Update the table of pre-computed values:

$$\text{computed}(p_\alpha, p_\beta) = Z_0(\omega_k, p_\alpha, p_\beta).$$

For most of our simulations the terminal resistance is taken to be zero and the impedance is predicted solely from the structured tree. However, it is easy to modify the algorithm to incorporate an additional terminal impedance beyond that provided by the tree itself. Assume for example that the total terminal impedance Z_t is given and that it is distributed evenly over all terminals. The terminal impedance for each terminal Z_{t_i} is then

$$Z_{t_i} = N_t Z_t$$

where N_t is the total number of terminals. This applies since the admittances add to give the total admittance, and impedance is the reciprocal of admittance. Because we have chosen to terminate the structured tree when the radius $r < r_{min}$ the number of terminals cannot be determined analytically. However, it can be counted recursively as shown in Algorithm 2 by calling the subroutine `count(0, 0)` where the zeros refer to the root of the tree.

Algorithm 2: `count(p_α, p_β)`. Counts the number of terminals of an asymmetric binary tree truncated when the radius $r < r_{min}$. The algorithm assumes that N_t , the number of terminals, is initialized to 0 when called at the top level:

• Let $r = \alpha^{p_\alpha} \beta^{p_\beta} r_{root}$.

• If $r < r_{min}$ then

$$\blacksquare N_t = N_t + 1$$

• else

■ Count the number of terminals of the left subtree by calling `count($p_\alpha + 1, p_\beta$)`.

■ Count the number of terminals of the right subtree by calling `count($p_\alpha, p_\beta + 1$)`.

By inverse Fourier transform of the root impedance $Z(0, \omega)$ the response function $z(0, t)$ in the time-domain and hence the impedance that appears in the convolution integral in (8.11) can now be found. Thus, the boundary condition for the larger arteries can be determined and this closes our model. Another possibility is to investigate if the equations can be solved using a self-similar approach. This is not quite possible due to the viscous treatment of the momentum equation. However, this approach gives some insight which could be used for other purposes. Therefore, we have chosen to show the self-similar solution to the inviscid wave equation in Appendix C.

Chapter 12

Results

In this chapter we will present a selection of results which elucidate our hypothesis. Our main aim was to show that the structured tree model is a feasible outflow boundary condition for determining blood flow and pressure in the larger arteries.

Therefore, we will show that our model captures all essential features characterizing the arterial pulse. In addition, we compare our model with a pure resistance and a three element Windkessel model as well as with measured data.

As discussed in Chapter 2 the characteristic features of the arterial pulse are:

- The maximum pressure of the larger arteries increases away from the heart towards the periphery because of tapering of the vessels.
- The mean pressure of the arteries drops according to the distribution of flow impedance of the vascular bed (Noordergraaf, 1978).
- The steepness of the incoming pressure profile increases towards the periphery. This is a result of the pressure dependence of the wave propagation velocity $c(p)$ such that the part of the wave with higher pressure travels faster than that with lower pressure.
- The reflected dicrotic wave separates from the incoming pressure wave and is more prominent at peripheral locations than at proximal locations.

All results shown in this chapter represent solutions of the non-dimensional fluid dynamics equations (8.15) with the state equation (7.26) and boundary conditions (8.2) and (8.11). The outflow boundary condition will be determined by the structured tree model, a pure resistance model, or a three element Windkessel model.

This chapter is divided into three sections: In Section 12.1 we show some results based on the parameters discussed in Chapters 5 and 6. These data reflect typical patient data. However, in real life the resulting flow and pressure profiles vary significantly among normal healthy human subjects. Therefore, a model for a particular case would require an investigation of the data for the patient in question. In Section 12.2 we compare our structured tree model with a pure resistance and a Windkessel model. Finally, in Section 12.3 we investigate the impact of variation of some of the important parameters.

12.1 Results from the model problem

The results presented here are based on the following choices:

- The geometrical data for the larger arteries are as described in Table 5.2.
- The parameters for the structured tree follow the choices in Chapter 6.
- The terminal resistance for the smaller arteries is set to zero.
- The minimum radius r_{min} is chosen to be 0.04 cm for all structured trees.
- The ratio for Young's modulus times the wall-thickness to radius, Eh/r_0 , is chosen as shown in Figure 5.2.
- The viscosity is kept constant for the reasons discussed in Chapter 3. The effect of a radius dependent viscosity will be studied in Section 12.3.

We have restricted the presentation to flow and pressure profiles for a few representative vessels. These are flow and pressure in the aorta (see Figure 12.1) as well as the iliac and femoral arteries (see Figure 12.2). All profiles capture the characteristics described in the beginning of this chapter, but it should be noted that the outflow boundary condition is applied at the bottom of the femoral arteries, i.e. the tibial arteries are not included in this simulation as discussed on page 34. Furthermore, our results show a small negative flow peripherally even though back-flow into the left ventricle is not included in the model, see Figure 8.2. It can be difficult to see all of these characteristics in the three-dimensional figures. In particular, it is not easy to see the steepening of the wave front. However, this can be seen in Figure 12.3, where two-dimensional cross-sections of flow and pressure profiles are plotted as functions of time at five equidistant locations along the aorta, iliac, and femoral arteries. Furthermore, the two-dimensional plots are more easily compared with measurements which are normally presented as such.

From McDonald (1974) we have results for flow and pressure at various locations along the aorta and femoral arteries in dogs, see Figure 12.4. For comparison, Figure 12.5 shows pressure profiles at various locations along the human aorta and iliac artery. These profiles, which are recorded from a single patient by Pedersen (1997), are typical for a healthy human adult. Both the measured and our computed results show the characteristics discussed in the introduction to this chapter even though the actual profiles vary.

12.2 Comparison of the structured tree, the Windkessel, the pure resistance models, and measured data

In order to investigate the performance of the structured tree model, we will compare it with two other models:

1. A pure resistance model

$$Z_L(\omega) = R_T$$

where R_T is a constant representing the peripheral resistance.

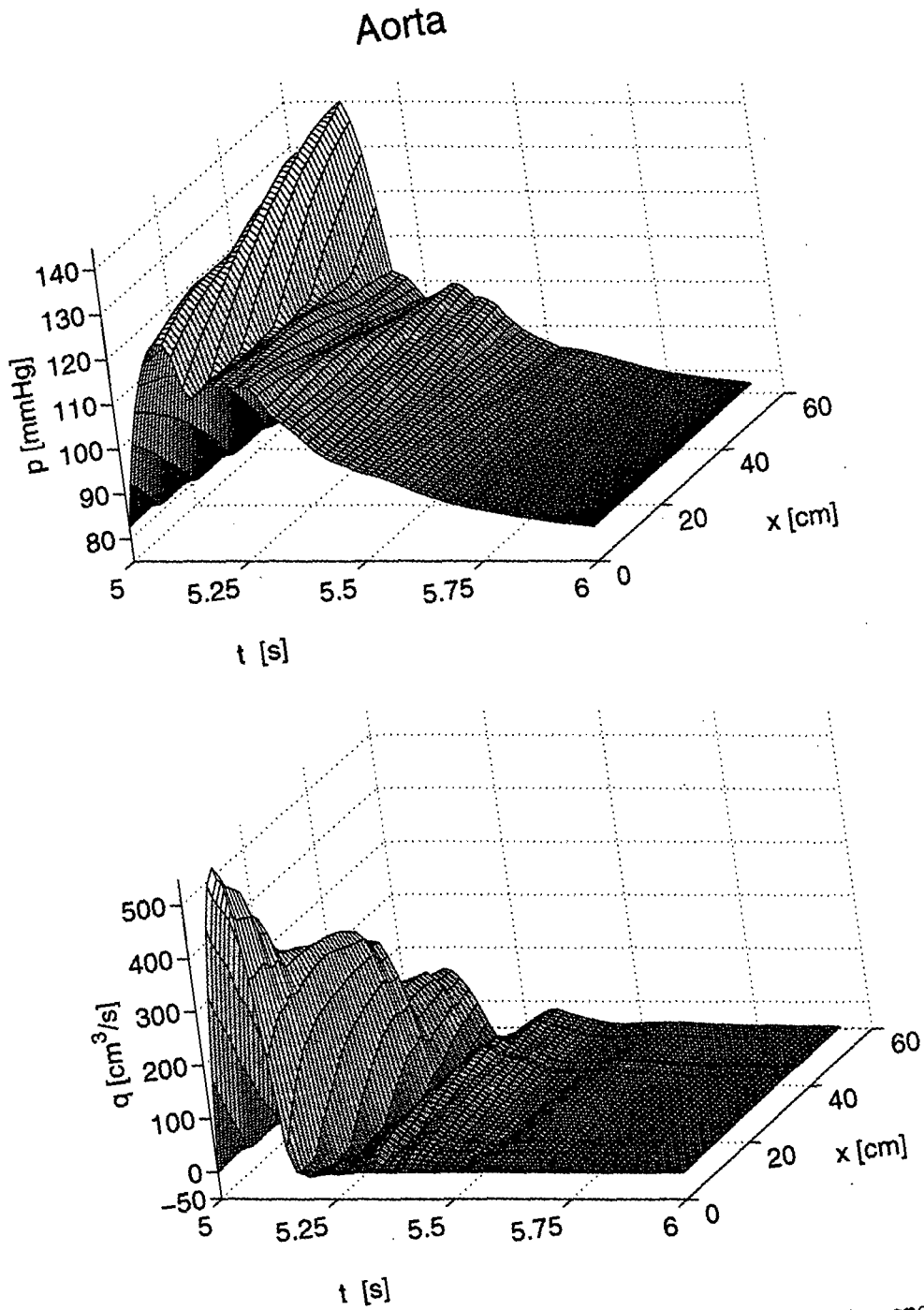


Figure 12.1: Pressure and flow in the aorta as functions of x and t during one period.

Iliac and Femoral arteries

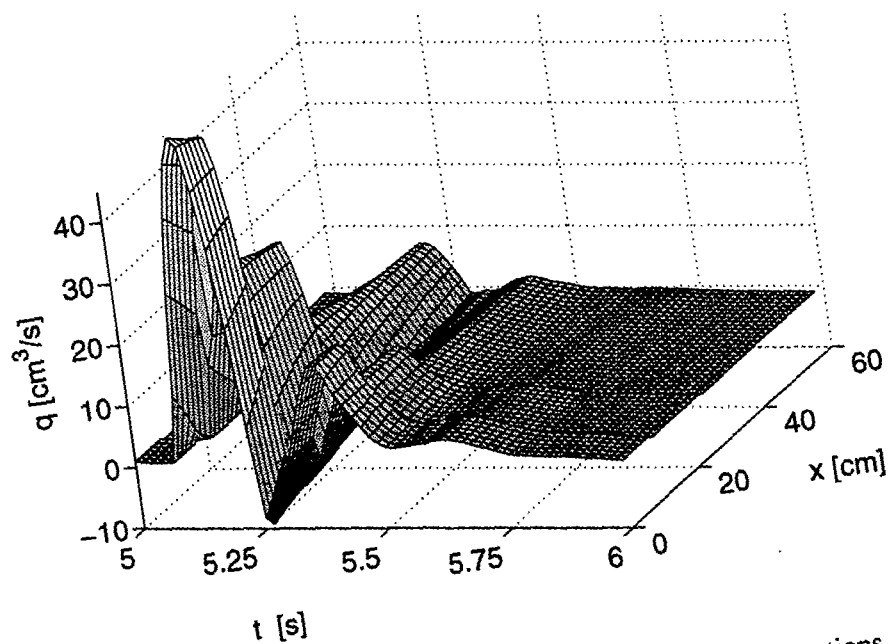
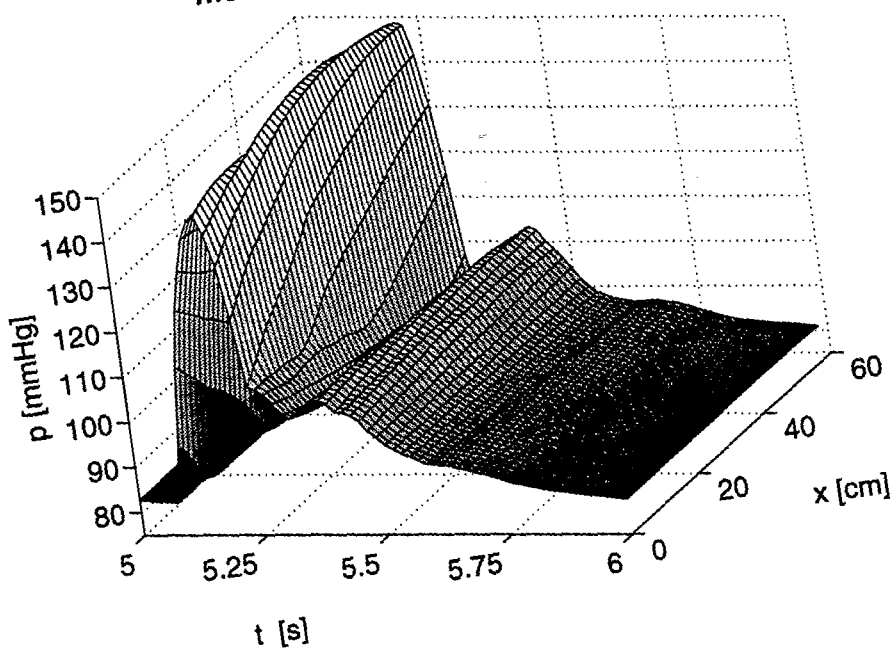


Figure 12.2: Pressure and flow in the iliac and femoral arteries as functions of x and t during one period. The structured tree model is applied at the bottom of the femoral arteries.

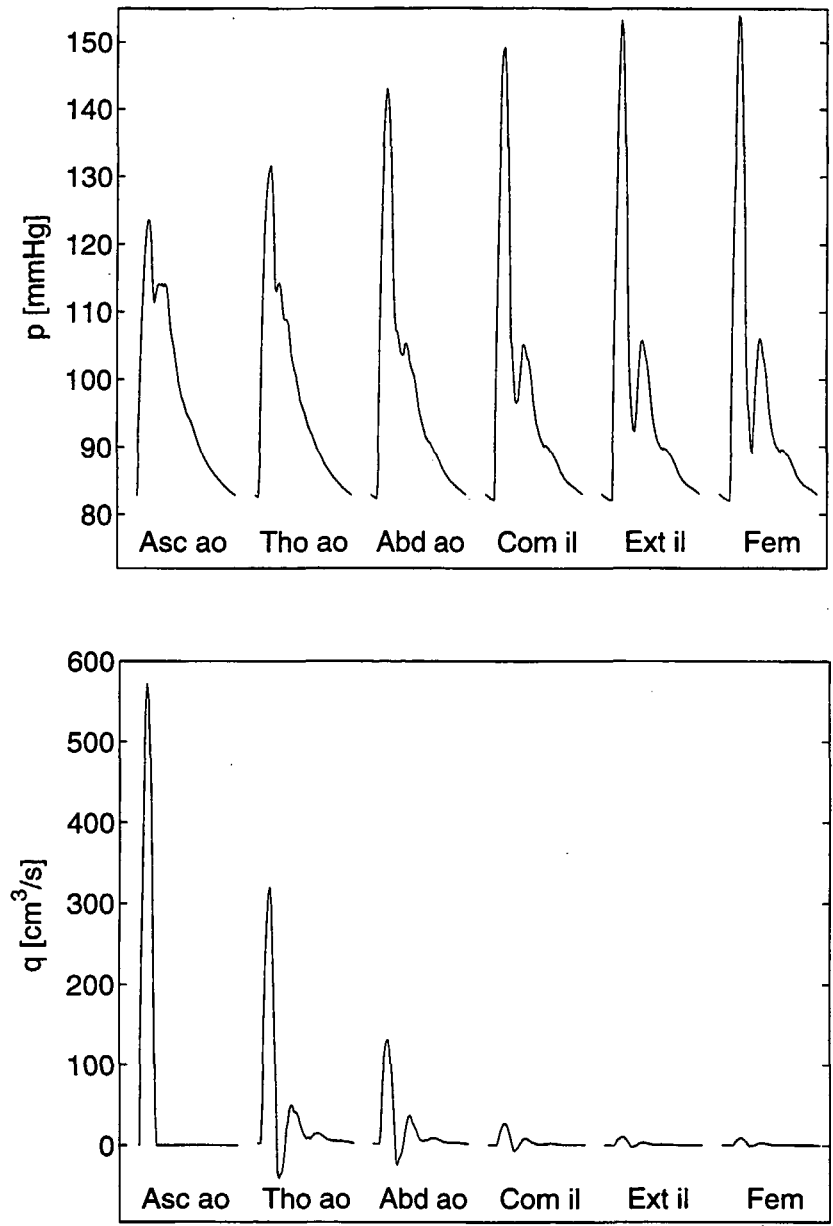


Figure 12.3: Time dependent pressure and flow in the ascending, thoracic, and abdominal aorta, the common and external iliac, and the femoral arteries; all given for one period. These graphs are cross sections of the 3D plots of Figure 12.1 and 12.2.

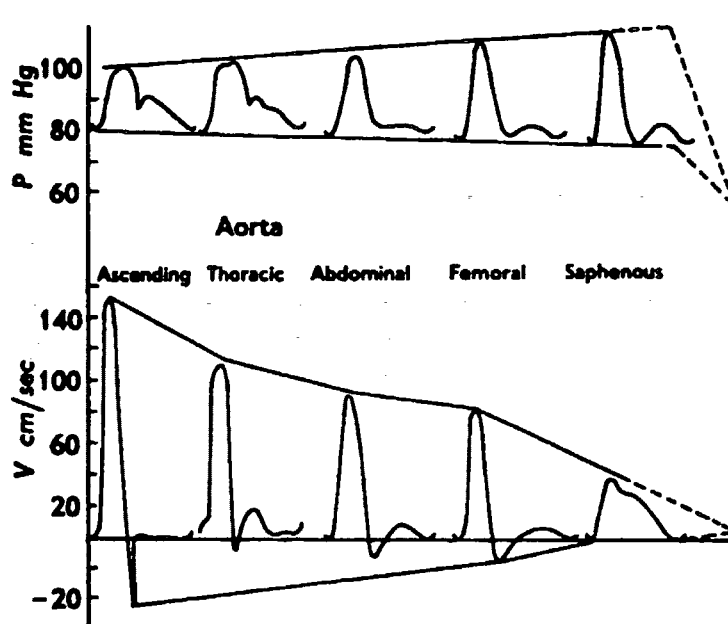


Figure 12.4: Time dependent pressure and flow in the ascending, thoracic, and abdominal aorta, as well as the femoral and saphenous arteries in dogs. The curves are plotted at fixed locations during one period. From McDonald (1974).

2. A three element Windkessel model, which is a lumped model predicting the impedance as a result of a resistive and a compliant behavior of the smaller arteries, i.e.

$$Z_L(\omega) = \frac{R_1 + R_2 + i\omega C_T R_1 R_2}{1 + i\omega C_T R_2}$$

where $R_T = R_1 + R_2$ is the total peripheral resistance, C_T is the total peripheral compliance. This is discussed in detail in Section 8.1.3.

The comparison falls into three parts:

- A comparison of the three outflow boundary conditions applied to a single isolated vessel, see Section 12.2.1.
- A comparison of the Windkessel model, the structured tree model, and measured data for the impedance in humans, see Section 12.2.2.
- A comparison of the Windkessel model and the structured tree model using data by Stergiopoulos et al. (1992), see Section 12.2.3.

12.2.1 Comparison of the three outflow boundary conditions for a single isolated vessel

The advantage of both the pure resistance and the Windkessel models is that they are easy to understand and computationally inexpensive. The disadvantage of the Wind-

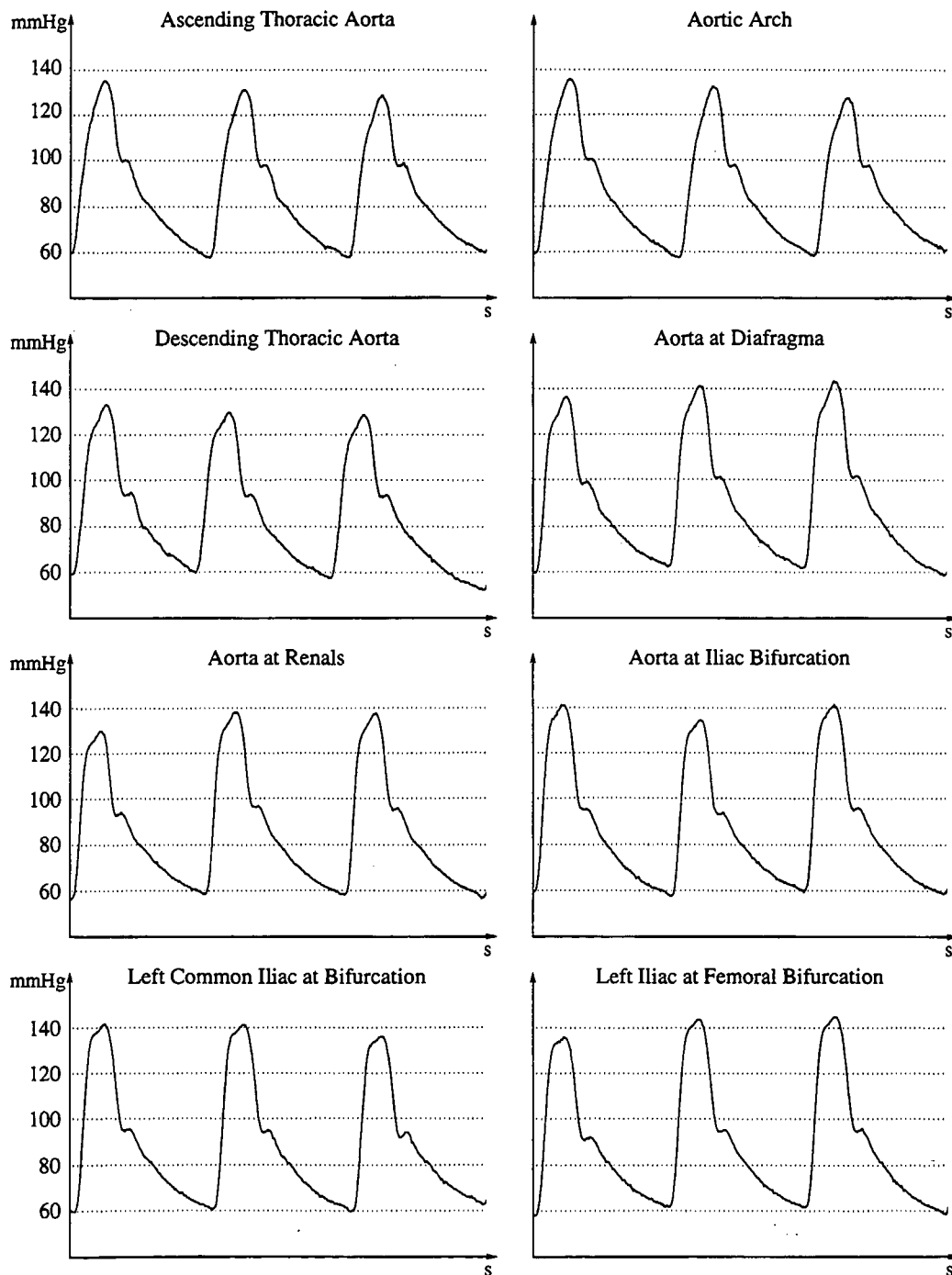


Figure 12.5: Pressure in the aorta and iliac artery for a female human. From Pedersen (1997).

kessel and the pure resistance models is that they are not able to capture the wave propagation phenomena in the part of the arterial system that they model. Furthermore, neither the pure resistance nor the Windkessel model can account for the phase-lag between flow and pressure. The Windkessel model requires estimates of the total arterial resistance, R_T , and compliance, C_T , for each terminal segment and the pure resistance model needs the total arterial resistance. Still, when coupled to the non-linear equations for the larger arteries both models are able to capture the overall behavior of the system. For the Windkessel model it is even possible to get a good estimate of the impedance and as we will see in the next section using the data given by Stergiopoulos et al. (1992) good agreement can be obtained between the two models.

In order to show the differences between the three models we have (for simplicity) used a single tapering vessel of length 100 cm, with top radius 0.4 cm, and with bottom radius of 0.25. Then we have applied all three models as different outflow boundary conditions to this vessel. In order to make them match as well as possible we have estimated the parameters for the Windkessel and the pure resistance models from the root impedance determined by the structured tree model. The total resistance R_T (the DC term from the structured tree model) is the same for all three models and the total compliance C_T for the Windkessel model is fitted empirically to match that which is given by the structured tree model. It should be emphasized that this study is theoretical and hence the parameters should not be compared with physiological values. However, the same differences can be seen when applying the three models to the whole tree.

We have made the following plots:

- Pressure versus flow, see Figure 12.6.
- Impedance (both modulus and phase) versus frequency at the boundary, see Figure 12.9. Since the pure resistance model does not depend on the frequency this plot only comprises the structured tree and the Windkessel models.
- Pressure as a function of x and t during one period, see Figure 12.7.
- Flow as a function of x and t during one period, see Figure 12.8.

The pressure versus flow curves in Figure 12.6 show the phase lag between flow and pressure for a single vessel. The top figure is for the pure resistance model, the middle one for the Windkessel model, and the lower one for the structured tree model. Comparing these, the most striking difference is that the pure resistance model affects the overall shape of the curve. The forced in-phase condition at the outflow boundary results in a narrowing of the width of the loop back through the vessel. Furthermore, it is worth noticing that the pure resistance model to some extent can be viewed as a simplification of the Windkessel model incorporating only the DC resistance. For the Windkessel model the flow and pressure are also nearly in phase, but the narrowing is not reflected back through the vessel. Finally, it is observed that the structured tree model does indeed keep some phase lag between flow and pressure. However, the pressure-flow plots look fairly similar for the Windkessel and the structured tree models. The reason for this is that the local dynamics of the impedance can not be seen on such a plot. This has to do with the fact that the structured tree model includes wave propagation effects for the entire tree, which the Windkessel model cannot do. Hence,

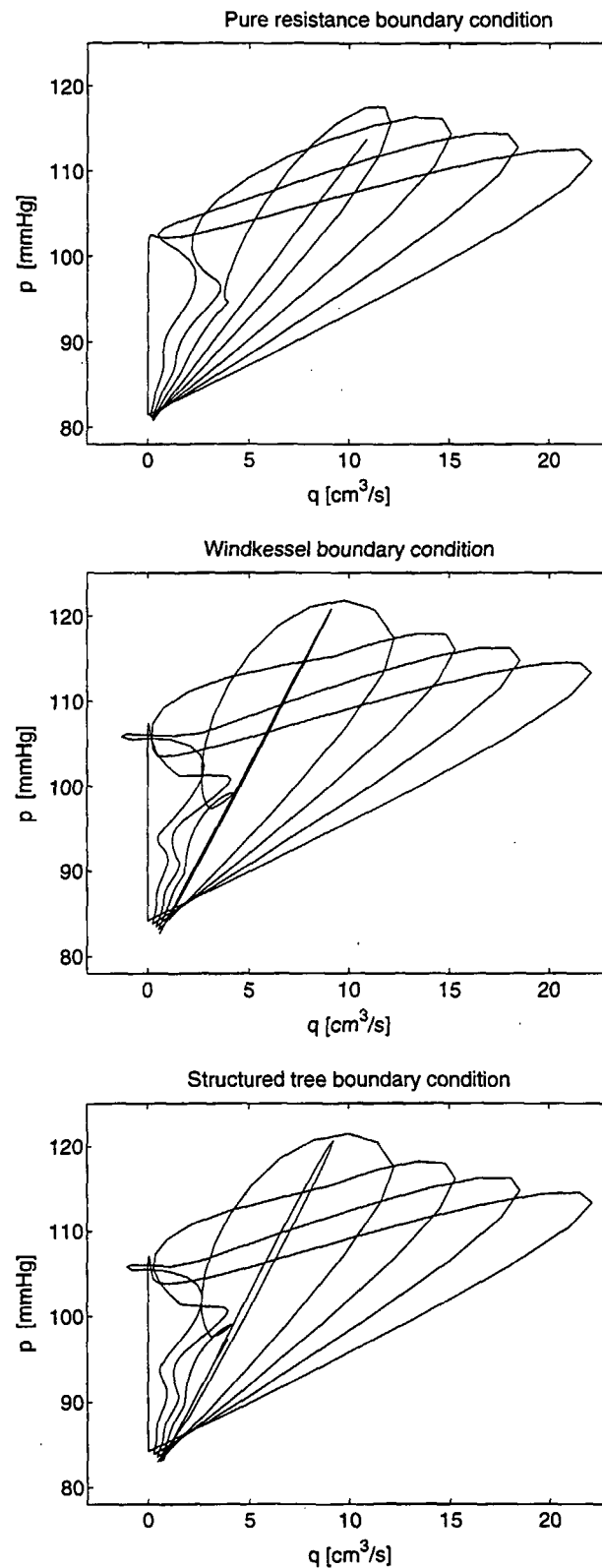


Figure 12.6: Pressure versus flow in a single vessel at six equidistant locations, i.e. for a vessel of length L , $x = 0, L/4, L/2, 3L/4, L$. both flow and pressure are plotted as functions of time during one cardiac cycle. The top graph is from the pure resistance model, the middle one from the Windkessel model, and the bottom one from the structured tree model.

it is possible that the Windkessel model will introduce more artificial reflections than the structured tree model. When we compare the result for the aortic pressure and flow waves (see Figures 12.7 and 12.8) this is exactly what we see as a difference between the two models. The reflections from the pressure when using the Windkessel model are slightly more pronounced than for the structured tree model, but seen from an overall point of view, the differences are small. However, if we instead make a so-called Bode plot of the impedance at the bottom of the large vessel, $Z_L(\omega)$, versus the angular frequency, ω , i.e. making a plot of $\log(|Z_L(\omega)|)$ versus $\log(\omega)$ and a plot of $\text{phase}(Z)$ versus $\log(\omega)$, the differences between the two models become more clear. The impedances are computed as functions of all frequencies needed in order to evaluate the outflow condition in (8.6). For example, if the number of time-steps in a period of 1 s is $N = 2048$ then $\omega \in [-2\pi N/2, 2\pi N/2]$. First of all it is seen that the Windkessel model cannot predict any of the dynamic behavior resulting in oscillations at high frequencies. But in this academic case where the peripheral resistance is rather low these oscillations are significant. The question which then arises is whether such oscillations actually occur in human data.

12.2.2 Comparison of structured tree and the Windkessel models with measured data

In Nichols and O'Rourke (1998) they have a whole chapter discussing the impedance of the larger arteries and we have compared our results with those obtained there. Nichols and O'Rourke (1998) results for humans are mainly from the larger arteries. In order to directly show the difference between the Windkessel and the structured tree models we have applied the two models directly as outflow boundary conditions for these larger arteries even though the outflow boundary conditions usually are applied further down-stream.

The comparisons of the Windkessel, the structured tree, and the measured data are made for the brachiocephalic, the subclavian, and the femoral arteries. However, since the structured tree model is not designed to be valid for these large arteries one should not assume perfect matches without some adjustments of the parameters.

For the brachiocephalic and subclavian arteries we had to modify the length to radius ratio to 130. This much larger length to radius ratio corresponds with the arteries of the arm: From table 5.2 we see that starting from the subclavian artery no large side branches occur before the bifurcation between the ulnar and interosseus arteries. Hence the combined length of the subclavian and brachial arteries is 43.25 cm and the average radius is 0.32 cm. This results in a length to radius ratio of 135. Now, starting at the brachiocephalic artery we have a major bifurcation after only 3.5 cm resulting in a very short length to radius ratio. However, this is then followed by a rather long length to radius ratio. This is not taken into account here. Instead we have kept the same length to radius ratio as for the subclavian artery. These large variations, confirm what we discussed in Section 6.3, namely that it is not easy to find a universal length to radius for the larger arteries. However, since we know that the length to radius ratio gets smaller for the smaller arteries further studies might be able to reveal some functional dependence, e.g. on the radius, of the length to radius ratio.

For the brachiocephalic artery we have chosen an input radius of 0.5 cm and a minimum radius of 0.025 cm. An input radius of 0.5 cm is rather small, but it is not

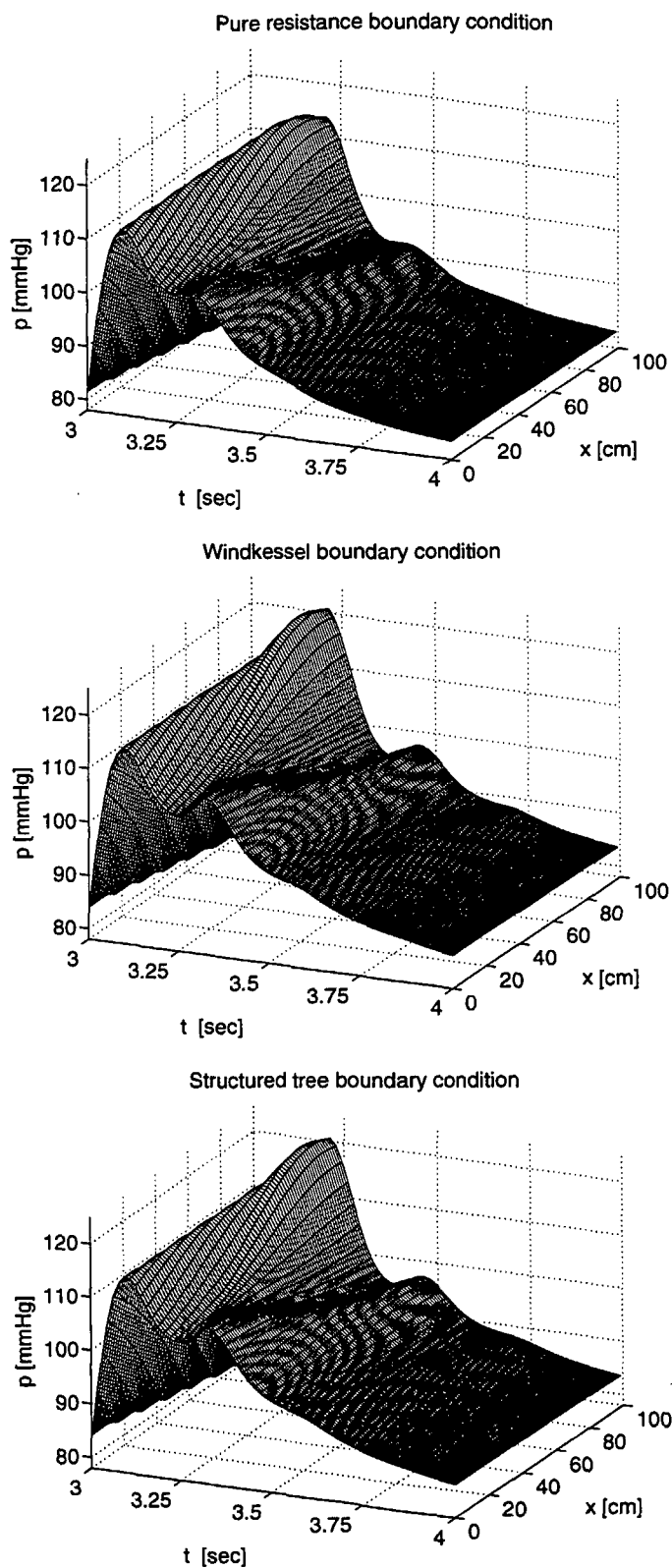
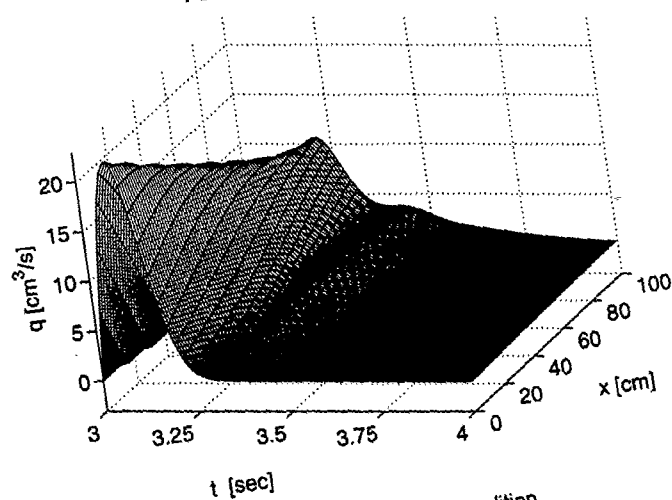
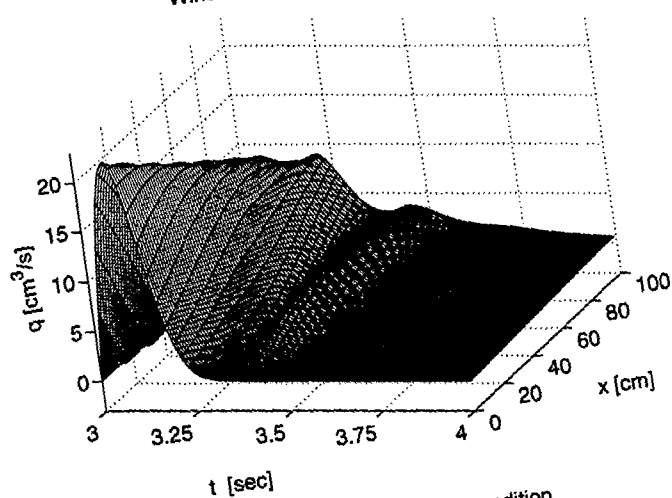


Figure 12.7: Pressure in a single vessel as a function of x and t during one period.

Pure resistance boundary condition



Windkessel boundary condition



Structured tree boundary condition

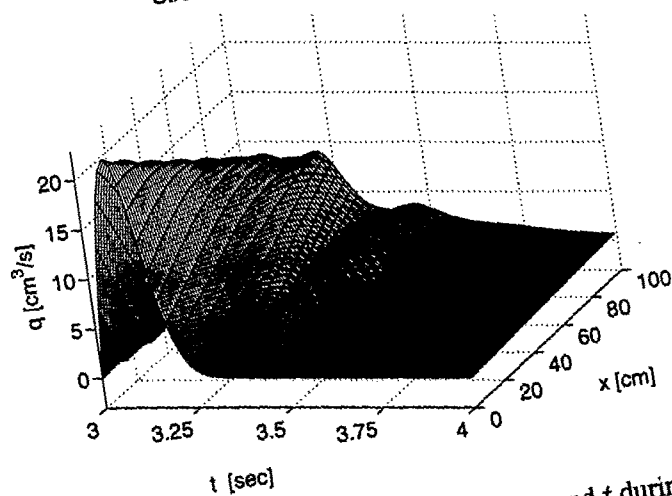


Figure 12.8: Flow in a single vessel as a function of x and t during one period.

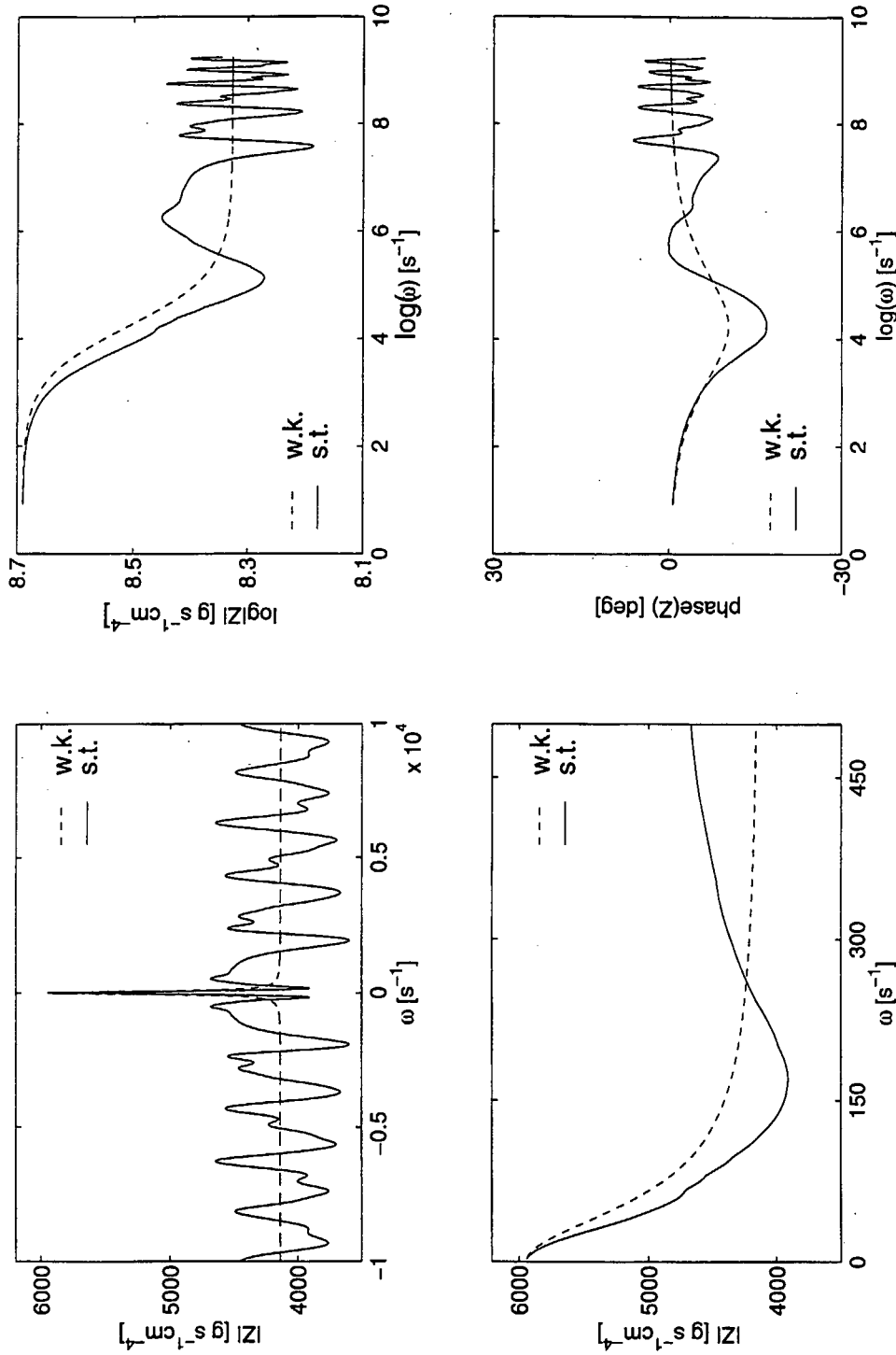


Figure 12.9: The left graphs show the impedance needed for the outflow boundary condition and a zoom showing the impedance for a range of frequencies. The right graphs show Bode plots; i.e. a log log plot of the modulus of the impedance versus the frequency and a single log plot of the phase of the impedance versus the frequency. Note, that all frequencies are angular frequencies. The dotted lines signifies results from the Windkessel model (w.k.) and the solid lines signifies results from the structured tree (s.t.).

specified exactly where the measurements have been carried out. Thus the comparisons should be interpreted with all of these reservations in mind. For the vessel wall parameters we have let $Eh/r_0 = k_1 \exp(k_2 r_0) + k_3$ as shown in Figure 5.2. The results for these comparisons are shown in Figures 12.10 and 12.11.

For the femoral artery we have, using a similar argument as before, assumed a length to radius ratio of 210. This corresponds to a length of the femoral arteries of 58.5 cm and a mean radius of 0.28 cm. The top radius is 0.370 cm and the minimum radius is 0.025 cm.

It becomes clear from all of these figures that the structured tree model is, in fact, able to capture some of the observed oscillatory dynamics in the impedance which cannot be captured by the Windkessel model.

12.2.3 Comparison with Stergiopulos model

We will now compare our structured tree model with the three element Windkessel model discussed by (Stergiopulos et al., 1992) when used with a full arterial tree. In Figures 12.13 and 12.14 we have plotted the the impedance as a function of the angular frequency for the renal and the femoral arteries. As for the previous graphs we have plotted the modulus for the entire spectra needed for the outflow boundary condition, a zoom, as well as Bode plots of the impedance modulus and phase.

From the plots showing only the impedance modulus versus the frequency of the renal artery (Figure 12.13), we see that the two Windkessel curves compare well with the curves resulting from the structured tree model (see Table 12.1). However, as we saw earlier, the Windkessel model does not exhibit the high frequency oscillations which are observed in actual measurements. It should be noted that these plots are made at the points where the outflow boundary conditions are attached. Unfortunately, for these small arteries we do not have any measured data to compare with. But if we compare these results with the measured data further proximal in the system we do see similar patterns in the Bode plots suggesting that the structured tree model is able to represent the dynamics in more detail.

In Figure 12.14 we see a slightly slower decay of the fitted impedance than what is expected from the Windkessel model. This shows in the Bode plots as an earlier minimum for the phase and an earlier decay for the impedance. A more detailed analysis could be done by fitting the structured tree model with data, but, even with this crude fitting, adjusting Young's modulus and the minimum radius the results do correspond within orders of magnitude.

Generally, the comparison show that there are two parameters of the structured tree which are essential, Young's modulus, E , and the minimal radius, r_{min} , determining when to terminate the structured tree. In order to get the best agreement between the structured tree and the Windkessel data E and r_{min} must be determined individually for each terminal branch of the larger arteries.

In order to compare the result from our model with one where the Windkessel model is applied as outflow boundary conditions for the entire arterial tree we have fitted parameters for the structured tree to all of the outflow branches present in the model by Stergiopulos et al. (1992). After adjusting Young's modulus as well as the minimum radius for each outflow vessel we are able to get a similar behavior for all outflow vessels. Especially the total resistances have a very good agreement varying

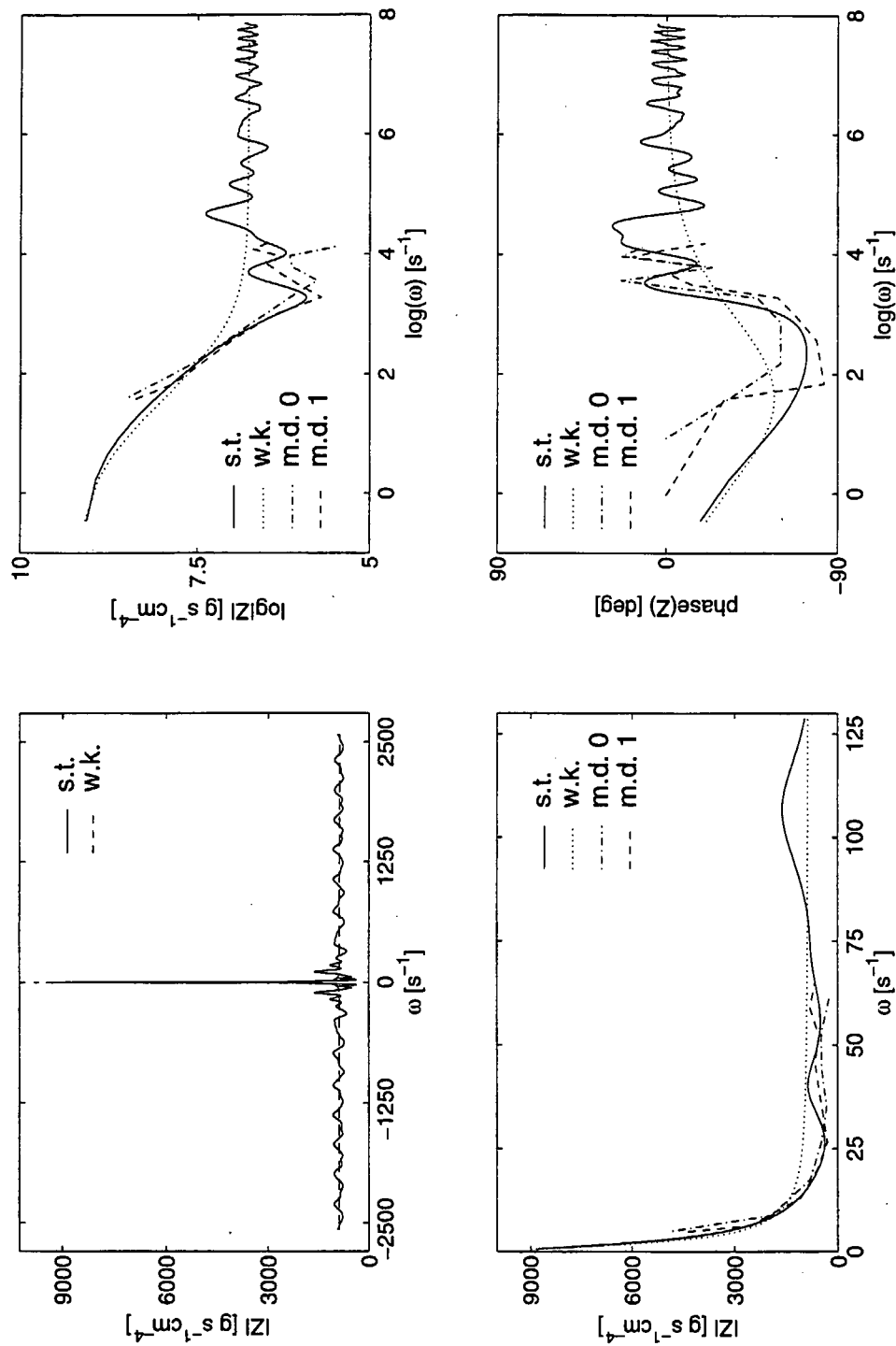


Figure 12.10: Impedance Bode plots for the brachiocephalic artery compared with measured data. The measured data (m.d.0 and m.d.1) are from (Nichols and O'Rourke, 1998). The dotted lines signifies results from the Windkessel model (w.k.) and the solid lines signifies results from the structured tree (s.t.).

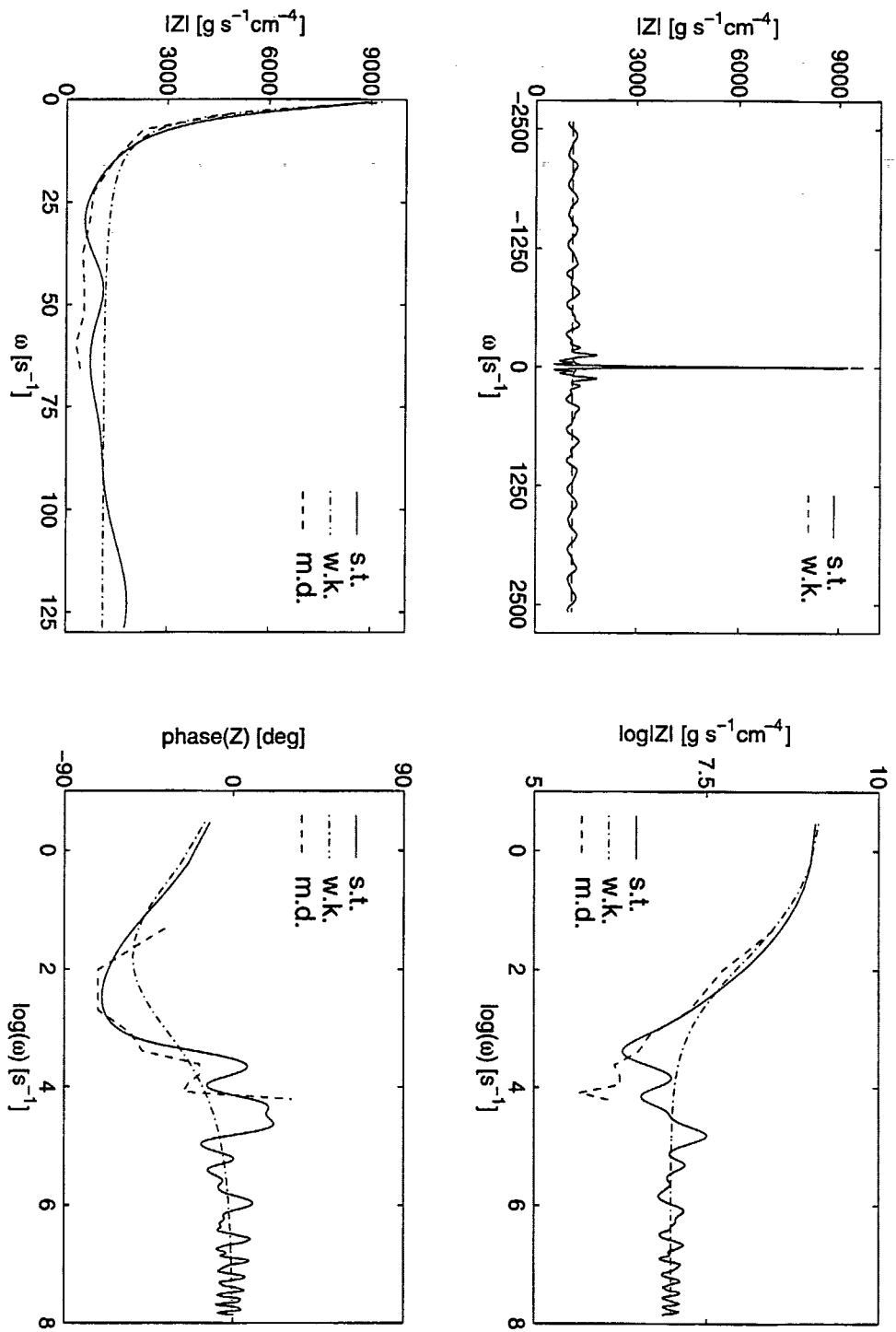


Figure 12.11: Impedance and Bode plots for the subclavian artery compared with measured data. The measured data (m.d.) are from (Nichols and O'Rourke, 1998)

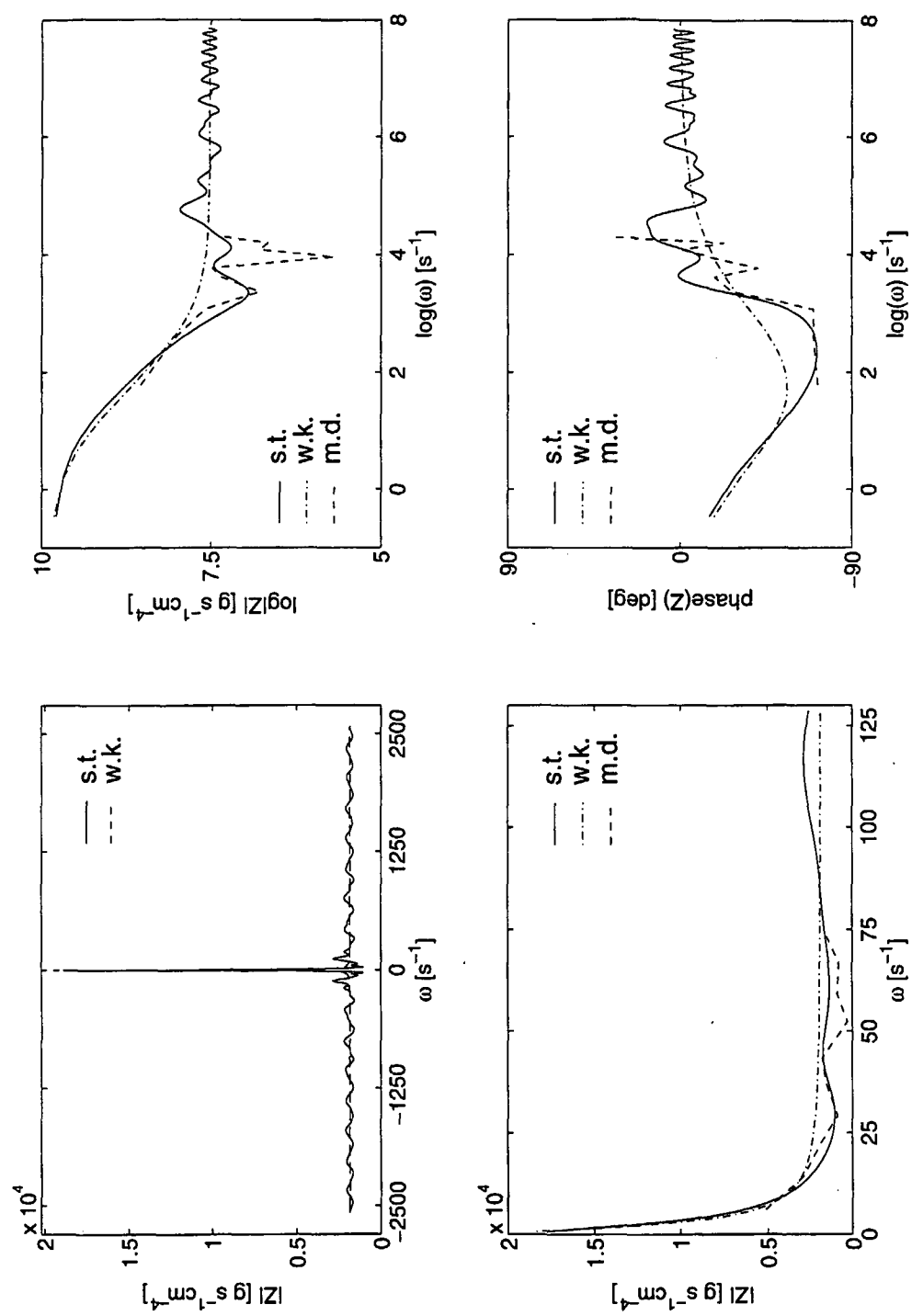


Figure 12.12: Impedance and Bode plots for the femoral artery compared with measured data. The measured data (m.d.) are from (Nichols and O'Rourke, 1998)

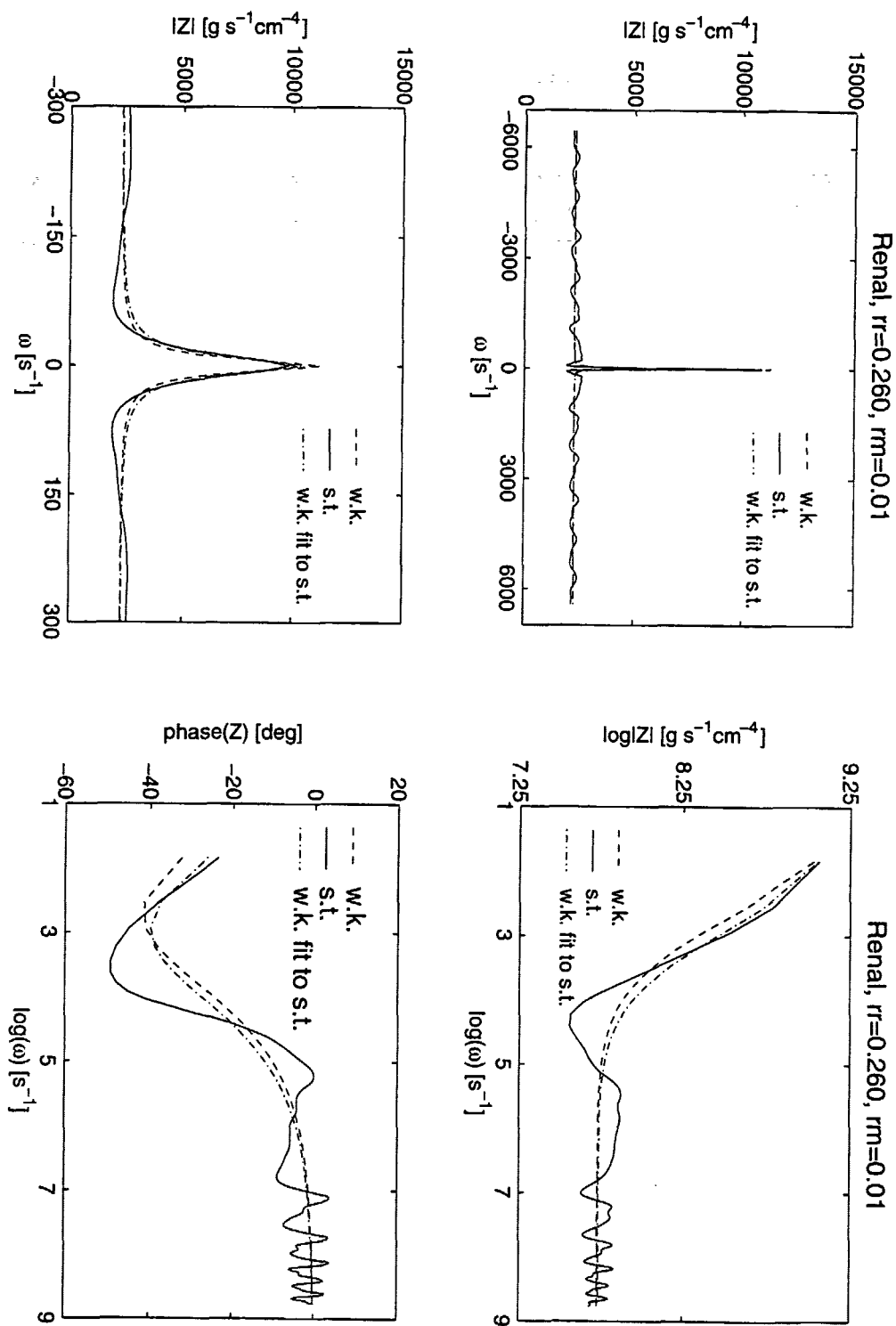


Figure 12.13: Impedance and Bode plots for the renal artery, the root radius is 0.260 cm and the radius at which the structured tree is truncated is 0.01 cm.

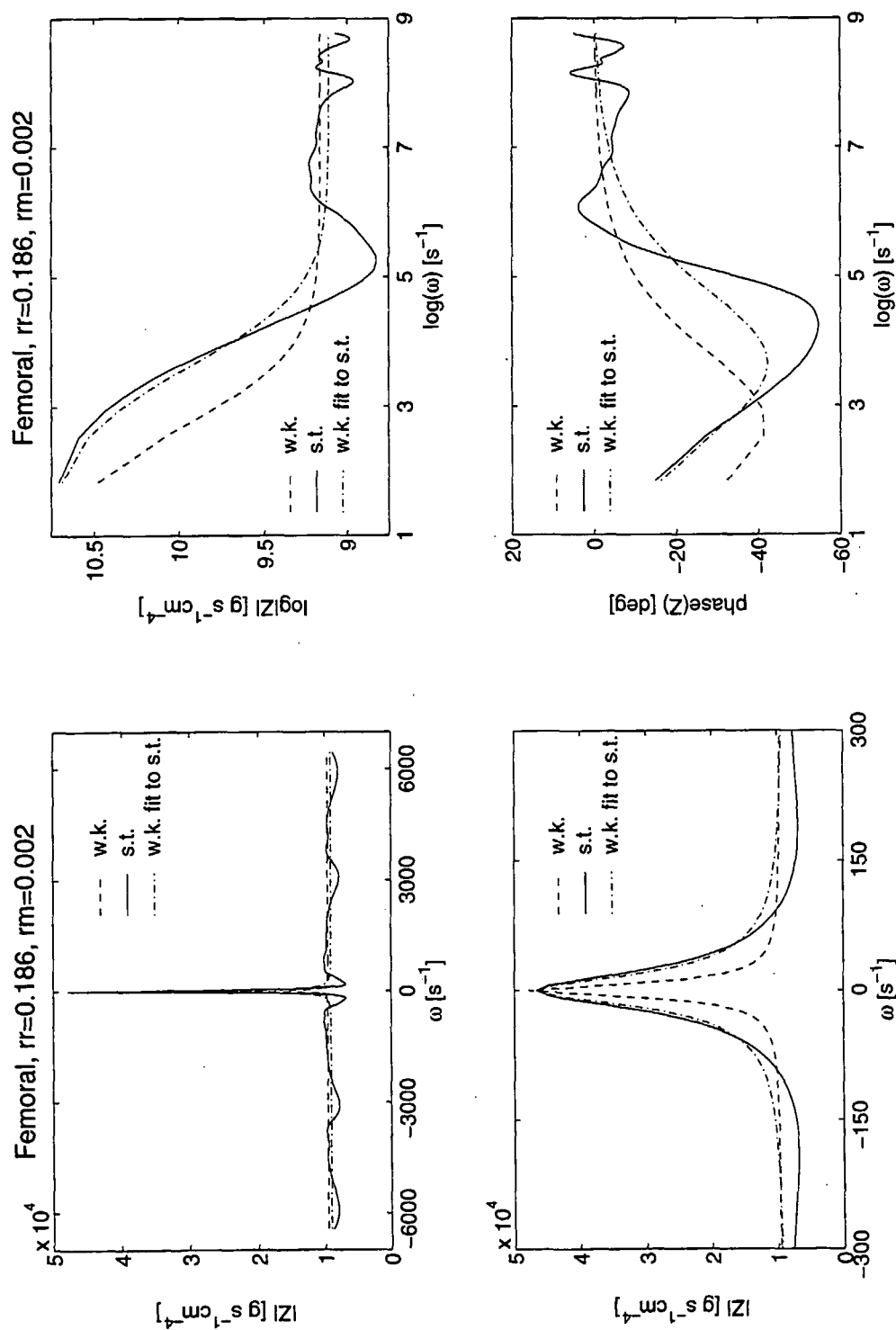


Figure 12.14: Impedance and Bode plots for the femoral artery, the root radius is 0.186 cm and the radius at which the structured tree is truncated is 0.002 cm.

less than five percent from the measured data. However, the compliances do not have as good a correspondence; on the average they vary about 50-60 % from the measured data. The compliance error is seen in Figure 12.14 as the difference between the spike width of the two Windkessel profiles; the one based on measurements and the one fitted to the structured tree. All parameters are fitted in a least squares sense using the Curvefit function available in Matlab. Due to the large differences in order of magnitude between the compliance and the resistance data it is difficult to get a more precise estimate, without applying some local method.

As we saw for the one vessel comparison, the Windkessel model can not include the high frequency oscillations present in real human data. But again, seen from an overall point of view, the differences between the pressure and flow profiles of the larger arteries are small. The same results apply to the more peripheral vessels, i.e. that the overall shape of the pressure and flow are similar, but that the reflections and the maximum pressure are more damped for the structured tree model.

In both cases we have used the geometrical data shown in Tables 12.1 and 12.2 and the radius dependent relation for Eh/r_0 , see (5.2), for the larger arteries. The radius dependent relation for Eh/r_0 is based on Stergiopoulos et al. (1992) such that we get as good fits as possible for all outflow vessels. This is chosen in order to facilitate the comparisons in this case. Table 12.1 shows that the fitted values for r_{min} fall in four distinct classes depending on their order of magnitude. Hence, the corresponding peripheral resistances can be organized into four groups as follows:

Peripheral resistance group	Typical r_{min} (cm)
very low	0.05
Low	0.01
Medium	0.002
High	0.0005

It is common knowledge that organs have different peripheral resistances reflecting the physiological characteristics of the organs which they supply and that these fall into groups such as the ones mentioned here. Hence, r_{min} is chosen from knowledge of resistance only. For example the renals have a small peripheral resistance reflected in a large minimum terminal radius and the Femoral artery has a large peripheral resistance reflected in a small minimal terminal radius.

In contrast to this, the Windkessel model needs estimates of arterial resistance and compliance, which are often less accessible because they require sophisticated measurements.

12.3 Parameter variation

Both models, i.e. models of the smaller and the larger arteries, include parameters affecting the overall behavior in various ways.

Parameters for the smaller arteries are:

- The exponent $\xi = 2.7$ used in the radius power law (6.1).
- The asymmetry ratio $\gamma = r_{d_2}^2/r_{d_1}^2 = 0.4048$, from (6.3).

Branch	Group	$r_{root}, \text{ cm}$	$r_{min}, \text{ cm}$	$E, \frac{10^6 \text{ g}}{\text{s}^2 \text{ cm}}$	$ R_{Tf} , \frac{10^4 \text{ g}}{\text{s cm}^4}$	$ R_T , \frac{10^4 \text{ g}}{\text{s cm}^4}$	$ C_f , \frac{10^{-6} \text{ cm}^4 \text{ s}^2}{\text{g}}$	$ C , \frac{10^{-6} \text{ cm}^4 \text{ s}^2}{\text{g}}$
Carotid	low	0.083	0.010	2.5	16.25	13.90	0.19	1.34
Interosseus ^a	low	0.091	0.020	1.6	8.68	8.43	0.33	0.22
Tibial anterior	low	0.130	0.010	2.7	5.47	5.59	0.91	3.33
Tibial posterior	low	0.141	0.010	2.7	4.51	4.77	1.23	3.90
Radial	low	0.142	0.010	3.2	4.41	5.28	1.09	3.52
Intercostals	very low	0.150	0.050	0.3	1.33	1.39	5.43	13.38
Inferior Mesenteric	medium	0.160	0.002	9.5	6.84	6.88	0.85	2.70
Gastric	medium	0.180	0.002	9.5	5.00	5.41	1.29	3.44
Ulnar	medium	0.183	0.001	13.0	6.32	6.01	1.08	3.10
Vertebral	medium	0.183	0.002	10.0	4.79	5.28	1.32	3.52
Femoral	medium	0.186	0.002	8.0	4.65	4.77	1.49	3.90
Iliac	high	0.200	0.0005	34.0	6.40	7.94	0.75	2.34
Hepatic	medium	0.220	0.001	10.5	3.86	3.63	2.38	5.13
Renal	low	0.260	0.010	2.0	1.03	1.13	13.92	16.46
Splenic	medium	0.275	0.001	10.0	2.15	2.32	5.47	8.02
Superior Mesenteric	high	0.435	0.0004	11.0	0.92	0.93	23.91	20.00

Table 12.1: The data for the terminal segments. The first column refers to the level of peripheral resistance. The next two columns give the root and the minimum radii for the structured tree. The fourth column give Young's modulus, and the last four columns give the total terminal resistance and the compliance. The ones with the subscript f are fitted to the arterial tree and the others are as given in Stergiopoulos et al. (1992).

^aIt should be noted that we have changed the order of magnitude of the peripheral resistance from 10^6 g/s/cm^4 to 10^5 g/s/cm^4 in order to be able to make any estimate for this vessel. We assume that there is a printing error in the table, however, this could also be in one of the other parameters; the terminal radius or the peripheral resistance. The reason for assuming that there might be a printing error is because a structured tree fitted to the actual data required a structured tree with a minimum radius less than 0.0002 cm and a Young's modulus of more than $150 \times 10^6 \text{ g/s}^2/\text{cm}$ which has no physiological basis.

#	Artery	L (cm)	r_{top} (cm)	r_{bot} (cm)
1	Ascending Aorta	1.00	1.470	1.440
3	Ascending Aorta	3.00	1.440	1.353
4	Aortic arch	2.00	1.353	1.300
12	Aortic arch	4.00	1.300	1.194
14	Thoracic Aorta	5.25	1.194	1.071
15	Thoracic Aorta	10.50	1.071	0.861
27	Abdominal Aorta	5.25	0.861	0.772
29	Abdominal Aorta	1.00	0.772	0.756
31	Abdominal Aorta	1.00	0.756	0.740
33	Abdominal Aorta	10.00	0.740	0.601
35	Abdominal Aorta	7.00	0.601	0.520
36	External Iliac	5.75	0.368	0.347
37	Femoral	14.50	0.347	0.299
40	Femoral	44.25	0.299	0.190
38	Internal Iliac	5.00	0.200	0.200
39	Deep femoral	12.50	0.255	0.186
43	Posterior Tibal	32.00	0.247	0.141
44	Anterior Tibal	34.25	0.130	0.130
2	Coronaries	10.00	0.350	0.300
5	Brachiocephalic	3.50	0.620	0.620
6, 17	R. + L. Subclavian	3.50	0.423	0.423
9, 19	R. + L. Brachial	42.25	0.403	0.236
10, 21	R. + L. Radial	23.50	0.174	0.142
11, 20	R. + L. Ulner	6.75	0.215	0.215
46, 47	R. + L. Ulner	17.00	0.203	0.183
45, 48	R. + L. Interosseus	8.00	0.091	0.091
8, 18	R. + L. Vertebral	14.75	0.188	0.183
7	R. com. Carotid	17.75	0.370	0.370
13	L. com. Carotid	20.75	0.370	0.370
41, 42	Ext. + int. Carotid	17.75	0.177	0.083
16	Intercostals	8.00	0.200	0.150
28	Superior Mesenteric	6.00	0.435	0.435
22	Celiac axis	1.00	0.390	0.390
23	Hepatic	1.00	0.220	0.220
24	Hepatic	6.50	0.220	0.220
25	Gastric	7.00	0.180	0.180
26	Splenic	6.25	0.275	0.275
30, 32	R. + L. Renal	3.25	0.260	0.260
34	Inferior Mesenteric	5.00	0.160	0.160

Table 12.2: Data for the length, top and bottom radii for the larger arteries. As for Table 5.2 the numbers of the left column refer to Figure 5.1. From Stergiopoulos et al. (1992).

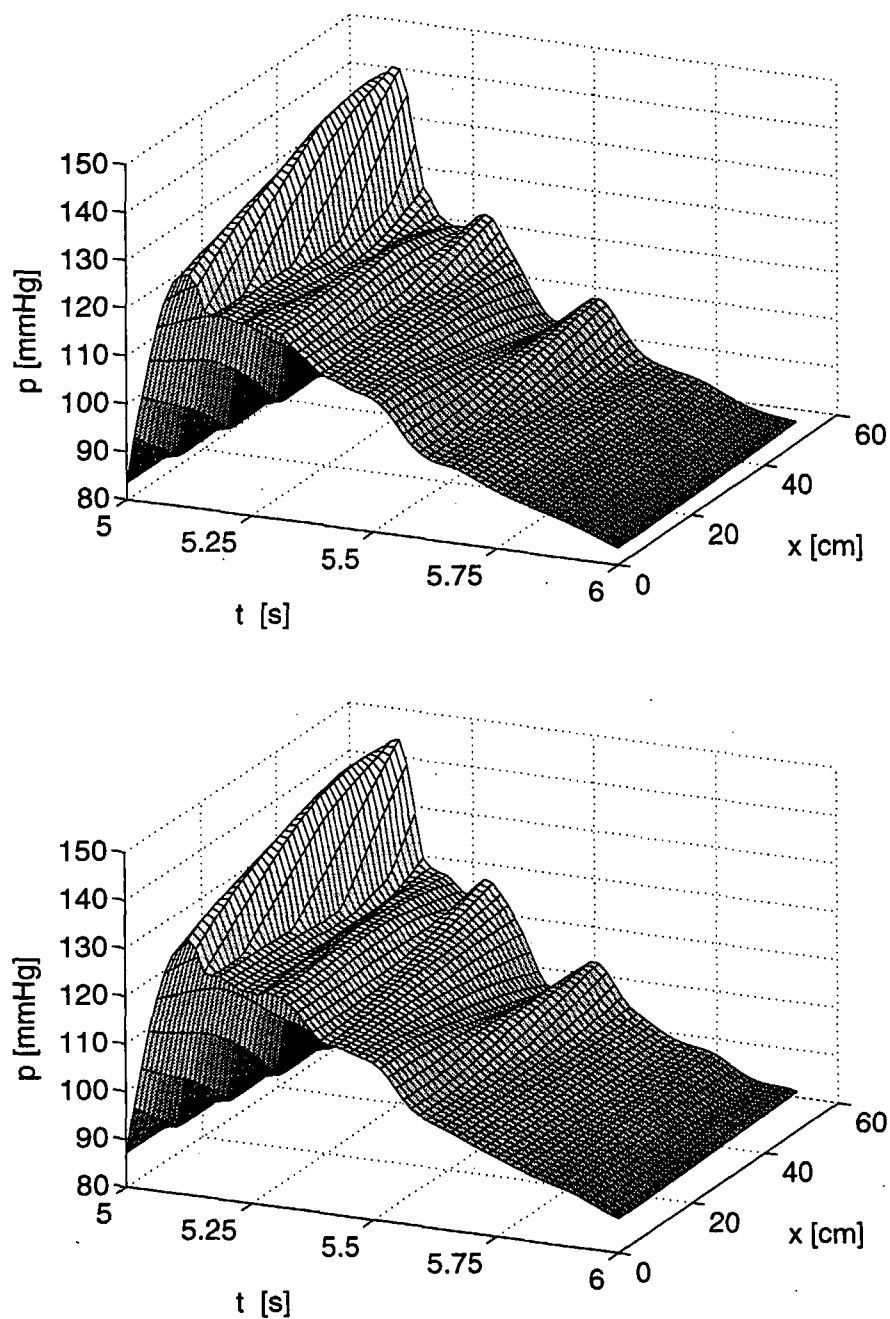


Figure 12.15: Pressure in the aorta using for the top graph the structured tree model as outflow boundary condition and for the bottom graph the Windkessel model is used as outflow boundary condition. Both curves are plotted as functions of x and t during one period.

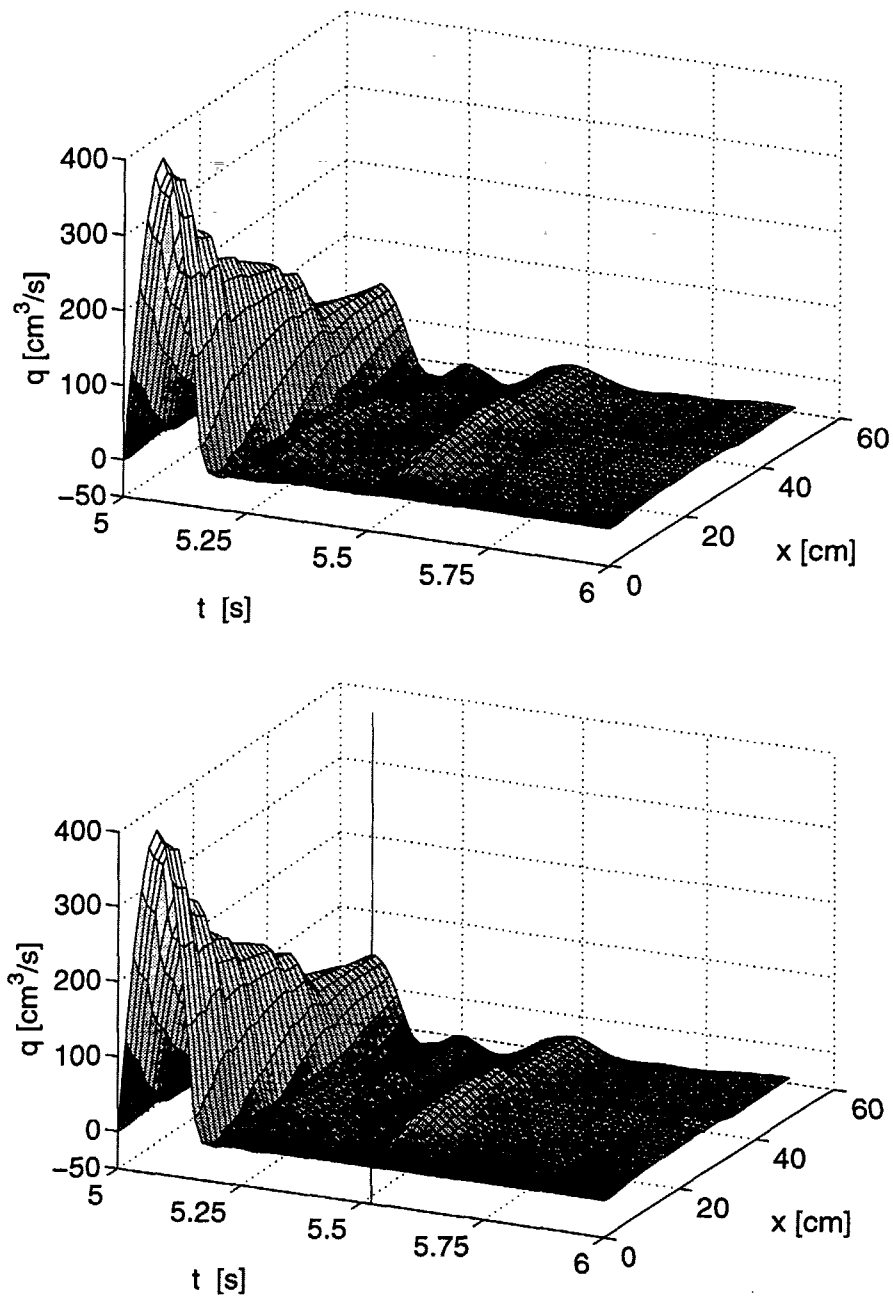


Figure 12.16: Flow in the aorta using for the top graph the structured tree model as outflow boundary condition and for the bottom graph the Windkessel model is used as outflow boundary condition. Both curves are plotted as functions of x and t during one period.

- The length to radius relation $l_{rr} = 50$, from (6.5).
- The minimum radius $r_{min} = 0.04$ cm, see Section 12.1.

Parameters for the larger arteries are:

- The ratio of Young's Modulus times the wall thickness to the radius: $Eh/r_0 = k_1 \exp(k_2 r_0) + k_3$, where $k_1 = 2.00 \times 10^7$ g/s²/cm, $k_2 = -22.53$ cm⁻¹, and $k_3 = 0.87 \times 10^6$ g/s²/cm, see Figure 5.2.
- The cardiac output, which is 3.5 l/min for our standard model described in Section 12.1 and 2.5 l/min for the model using Stergiopulos' data.
- The period $T = 1$ s.

The parameters given above all match the arterial system in its healthy state and these are the choices used throughout the previous two sections. However, perturbations of these parameters might be used to simulate various diseased states, such as stiff arteries which is one of the indications of diabetes as discussed Chapter 2. Therefore, the purpose of the following sections is to investigate how the model reacts to variations in the above mentioned parameters.

12.3.1 Parameters for the smaller arteries

Radius power law exponent

Figure 12.17 shows the root impedance computed for $\xi = 2.3, 2.5, 2.7, 2.9$. The effect is not profound; the side-lobes are unchanged and only the height of the spike $Z(0,0)$ is affected. Figure 12.18 shows a linear interpolation of $Z(0,0)$ as a function of ξ . The graph suggests a maximum at $\xi = 2.4$. However, none of these values vary more than 20 % from $\xi = 2.7$ which is the exponent we have chosen.

Asymmetry ratio

Figure 12.19 shows the root impedance computed for $\gamma = 0.1, 0.2, \dots, 0.9$. As for ξ the percentual variation of the average impedance from the chosen $\gamma = 0.4$ is small; no more than 18%. It is interesting to observe that the oscillations of the side-lobes grow as the structured tree becomes more symmetric. This makes sense, since for a symmetric tree all branches are terminated at the same point and hence reflections will be superimposed on each other and thus tend to increase at the root of the structured tree. While the more asymmetric the tree gets the more the reflections will be spread out and as a result damp the reflections. When comparing this to the human body it makes sense that the arteries do not branch in symmetric trees.

Length to radius relation

Figure 12.21 shows the root impedance computed for $l_{rr} = 10, 20, \dots, 90$. The average root impedance $Z(0,0)$ grows with l_{rr} and the frequency of the side-lobes increases. This makes sense since we change the geometrical characteristics and hence the characteristics for the wave-propagation.

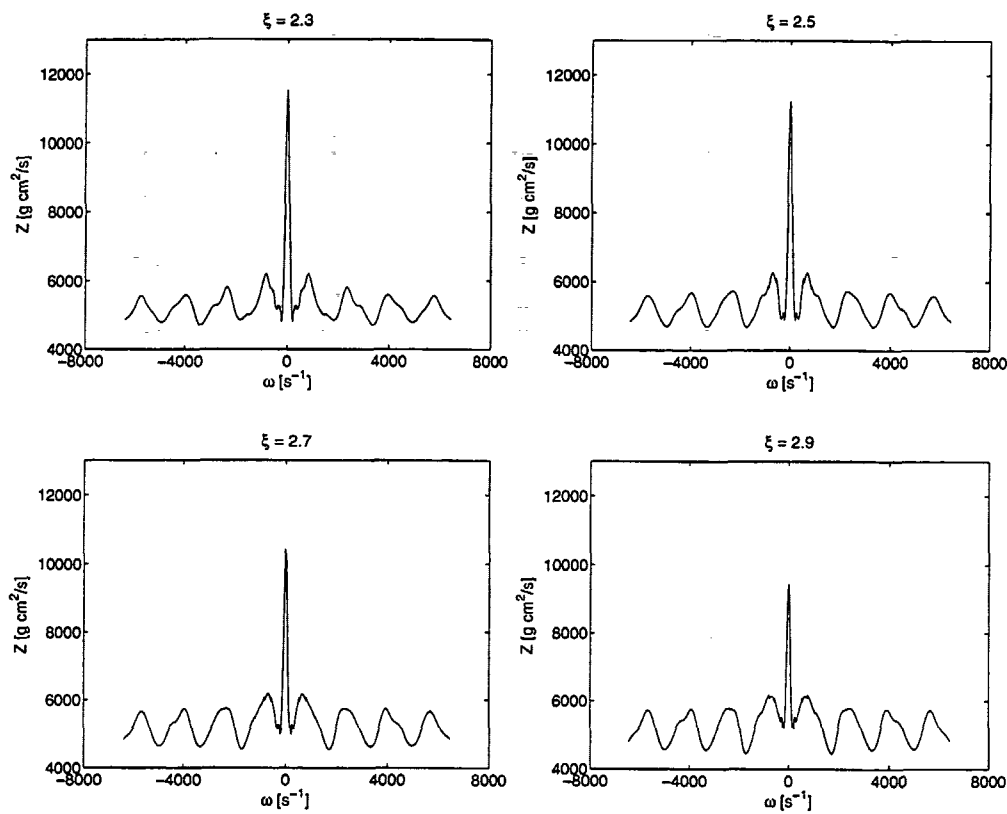


Figure 12.17: The root impedance $Z(0, \omega)$ for $\xi = 2.3, 2.5, 2.7, 2.9$, respectively.

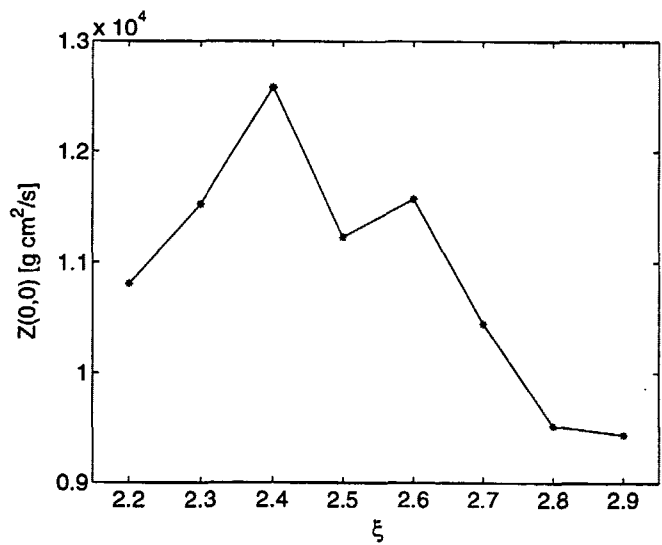


Figure 12.18: $Z(0, 0)$ as a function of ξ .

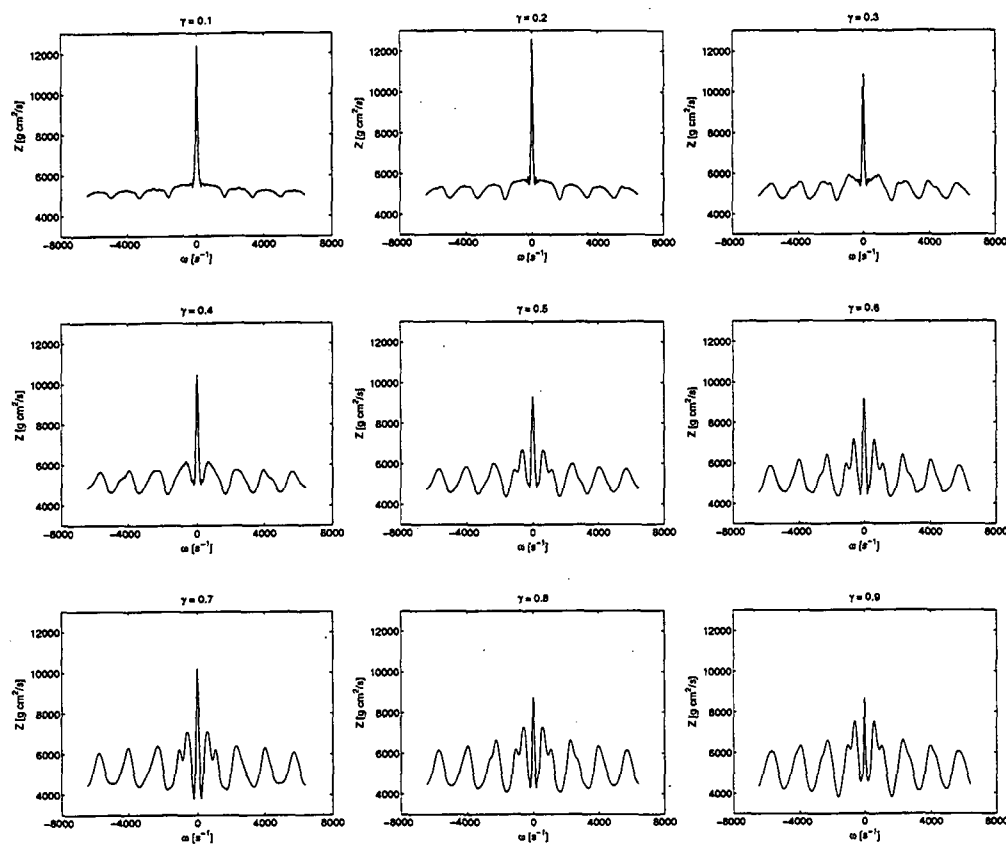


Figure 12.19: The root impedance for $\gamma = 0.1, 0.2, \dots, 0.9$, respectively.

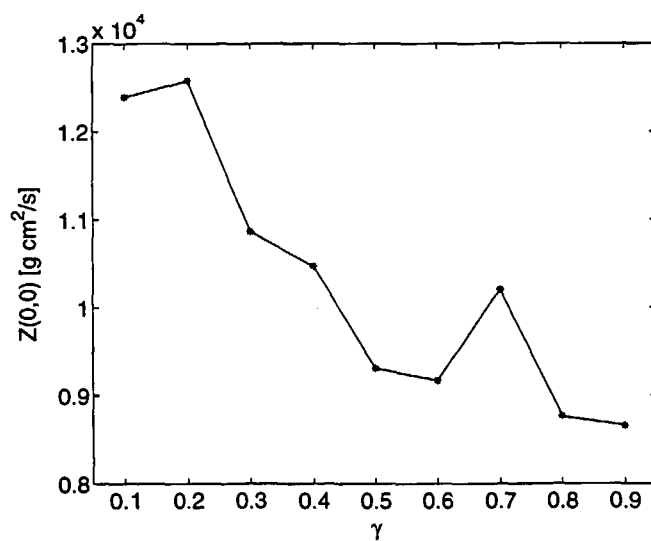


Figure 12.20: $Z(0,0)$ as a function of γ .

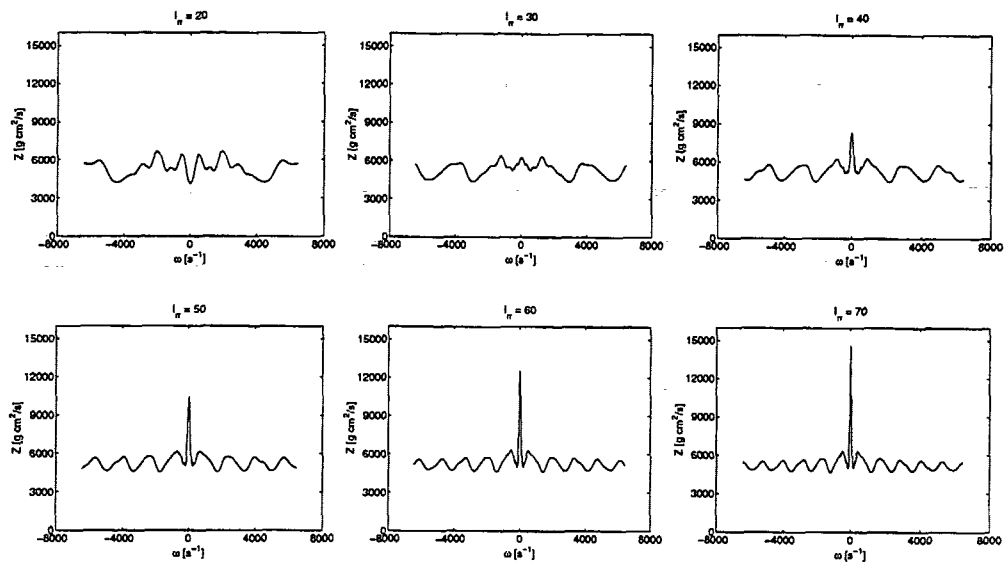


Figure 12.21: The root impedance for $l_{rr} = 20, 30, \dots, 70$, respectively.

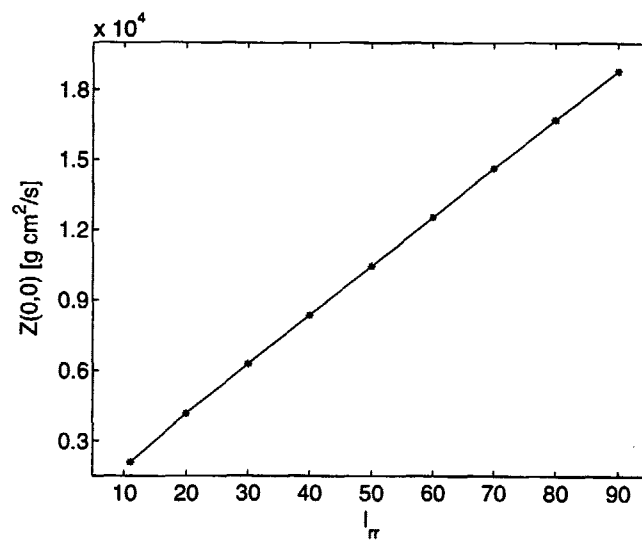


Figure 12.22: $Z(0,0)$ as a function of l_{rr} .

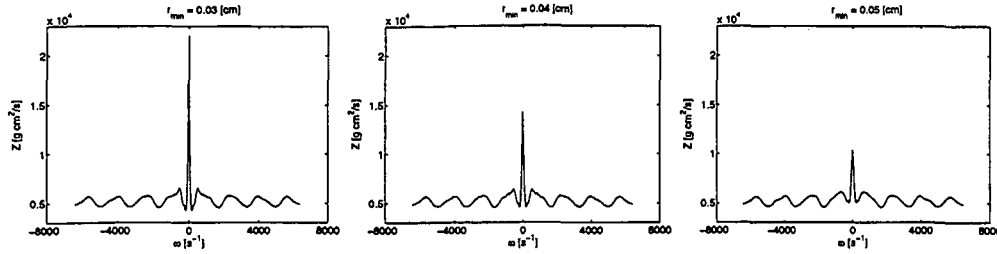


Figure 12.23: The root impedance for $r_{min} = 0.3, 0.4, 0.5$, respectively.

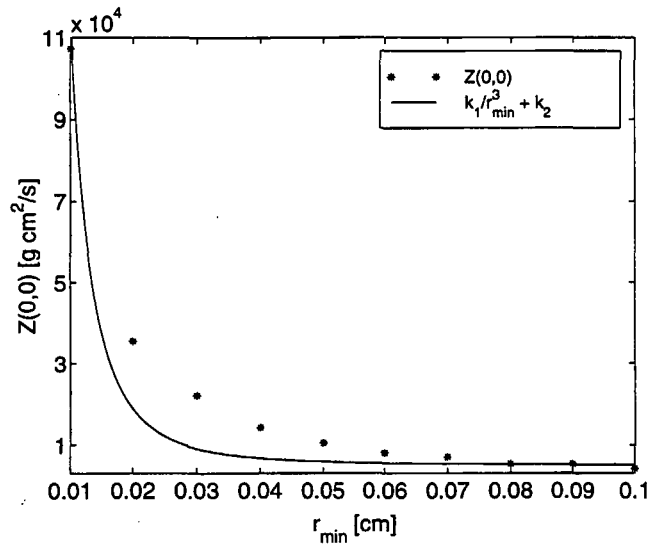


Figure 12.24: $Z(0,0)$ as a function of r_{min} shown together with $k_1/r_{min}^3 + k_2$, where $k_1 = 0.11 \text{ cm}^5/\text{s}$ and $k_2 = 5 \times 10^3 \text{ cm}^2/\text{s}$.

Furthermore, Figure 12.22 reveals that $Z(0,0)$ grows linearly with l_{rr} . This linear growth is expected since the root impedance for each branch is proportional to l_{rr} as shown in (6.5). The significance of this lies in the fact that long thin tubes yield a higher resistance than short, thick tubes. However, as the comparisons in Section 12.2 show the length to radius ratio differs for the larger arteries. This suggests that the length to radius ratio might vary with the radius throughout the arterial system. This should be considered in further studies.

Minimum radius

Figure 12.23 shows the root impedance computed for $r_{min} = 0.03, 0.04, 0.05$. A decrease in r_{min} implies an increase in the overall resistance of the outflow boundary condition provided by the structured tree while the side-lobes remain unaffected. Figure 12.24 shows $Z(0,0)$ as a function of r_{min} . Recall from (10.82) that for a symmetric tree with N generations $Z(0,0)$ is inversely proportional to r_{root}^3 and hence

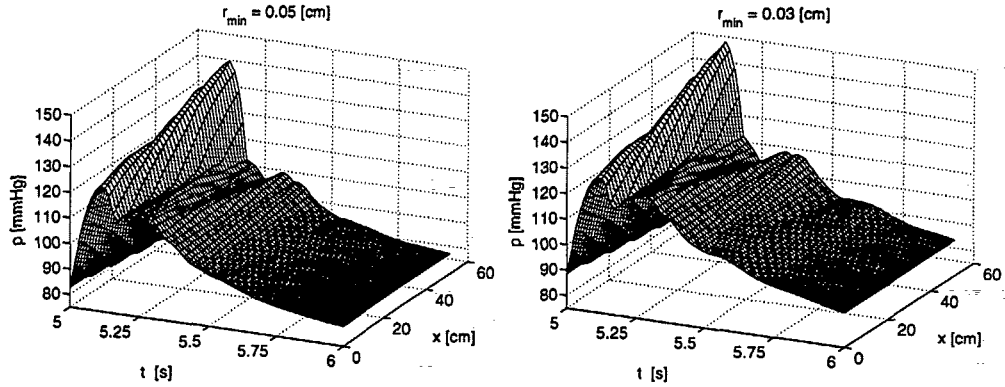


Figure 12.25: Pressure in the aorta as a function of x and t during one period. The two figures are for $r_{min} = 0.05$ and $r_{min} = 0.03$. The decreased r_{min} gives an increased average impedance, which results in an increase in both the systolic and diastolic pressures as well as an increase in the wave reflections.

to $\alpha^{-3N} r_{min}^3$ because of the linear scaling. However, as discussed in Section 10.10, this does not apply to the asymmetric tree. In Figure 12.24 we have plotted both the average root impedance for an asymmetry ratio of $\gamma = 0.4048$ and fitted the data to the function $f(r) = k_1/r_{min}^3 + k_2$, where $k_1 = 0.11 \text{ cm}^5 \text{ g/s}$ and $k_2 = 5 \times 10^3 \text{ cm}^2 \text{ g/s}$. From the fit it becomes clear that for the asymmetric tree the exponent is different from 3. Finally, we mention that a positive terminal resistance affects the results similarly to a decrease in r_{min} .

Generally, several of the results above imply a significant change in the average impedance $Z(0,0)$. For example, a 53% increase in $Z(0,0)$ (which is more than double the increase resulting from changes in the exponent ξ or the asymmetry ratio γ), effectuated by increasing r_{min} from 0.3 to 0.5 has the effect that both the systolic and diastolic pressures as well as the wave reflections are increased. This is seen in Figure 12.25 which shows the aortic pressure for the two choices of r_{min} .

From these studies we can conclude that the parameters having the most significant effect are the minimum radius and the length to radius relation, while the effect of changes in the exponent ξ or the asymmetry ratio γ is much less pronounced.

12.3.2 Parameters for the larger arteries

Young's modulus

An increase in Young's modulus and hence in the parameter Eh/r_0 corresponds to a stiffening of the arteries. This yields an increase in the systolic pressure and an attenuated dicrotic wave as illustrated in Figure 12.27 using the Stergiopulos data. Eh/r_0 has been increased by increasing the limit

$$\lim_{r_0 \rightarrow \infty} Eh/r_0$$

from $0.87 \times 10^6 \text{ g/s}^2/\text{cm}$ to $2 \times 10^6 \text{ g/s}^2/\text{cm}$ as shown in Figure 12.26.

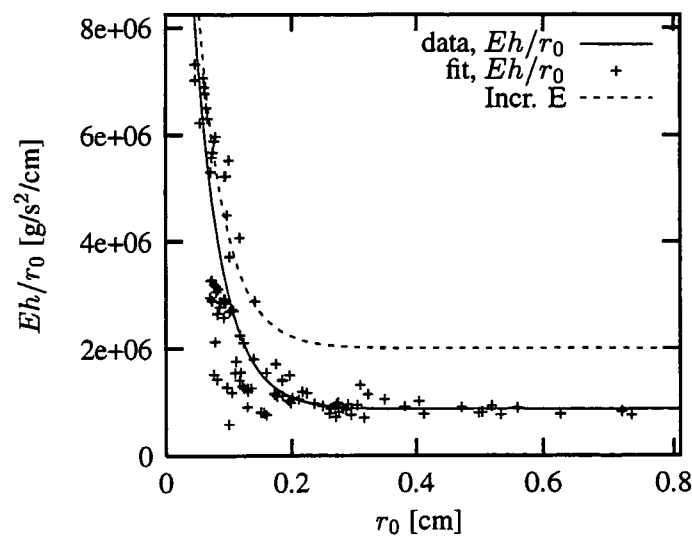


Figure 12.26: Young's modulus for the standard case, i.e. where we have fitted a function to the data by Stergiopoulos et al. (1992), and where the value approached for large r is doubled.

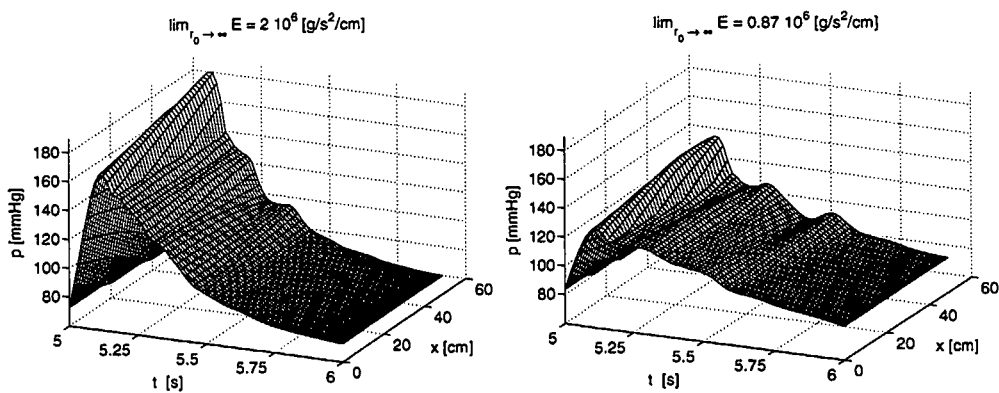


Figure 12.27: Pressure in the aorta as a function of x and t during one period. The two figures are for $\lim_{r_0 \rightarrow \infty} Eh/r_0 = 0.86 \times 10^6 \text{ g/s}^2/\text{cm}$ and $\lim_{r_0 \rightarrow \infty} Eh/r_0 = 2 \times 10^6 \text{ g/s}^2/\text{cm}$. The increase in Young's modulus implies an increase in the systolic pressure and attenuation of the reflected waves.

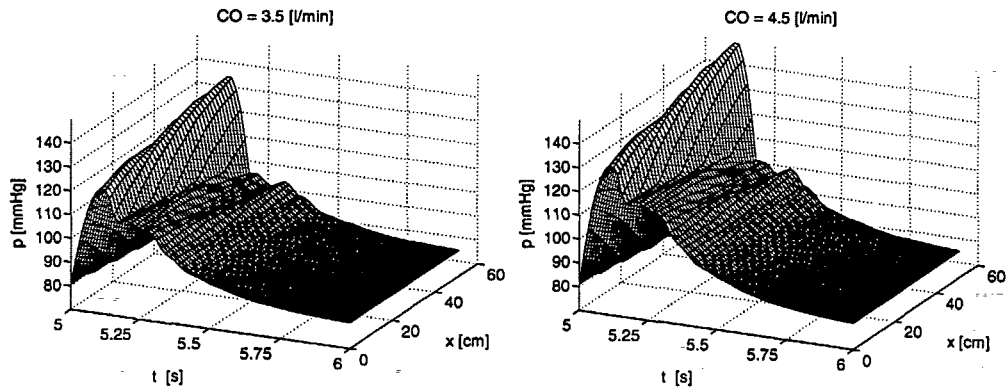


Figure 12.28: Pressure in the aorta as a function of x and t during one period. The two figures are for a cardiac output of $CO = 3.5 \text{ l/min}$ and $CO = 4.5 \text{ l/min}$. The increased cardiac output implies an increase in the systolic pressure as well as more pronounced reflected waves.

Cardiac output

An increase in the cardiac output causes an increase in the systolic pressure as well as an increase of the reflected waves. This is seen in Figure 12.28.

The period

In our standard model we have chosen the period $T = 1 \text{ s}$. An increase in the period implies that there are fewer bursts of blood into the arteries per minute and in order to maintain a given cardiac output more blood must enter the aorta at each systole. This implies that the systolic pressure increases and that the reflected waves become more pronounced.

A longer period leads to an increased pressure. This is shown in Figure 12.29.

12.3.3 Radius dependent viscosity

Finally, we have not included the variation of the apparent viscosity with radius in any of the computations above. The decrease in the viscosity for the very small vessels implies that the peripheral resistance obtained for a given minimum radius is decreased; hence this will also imply a decrease in both the systolic and diastolic pressures as well as attenuation of the reflected waves. This is seen in Figure 12.30 where pressure is plotted both for μ constant and for the radius dependent μ . Both plots are based on the Stergiopoulos data.

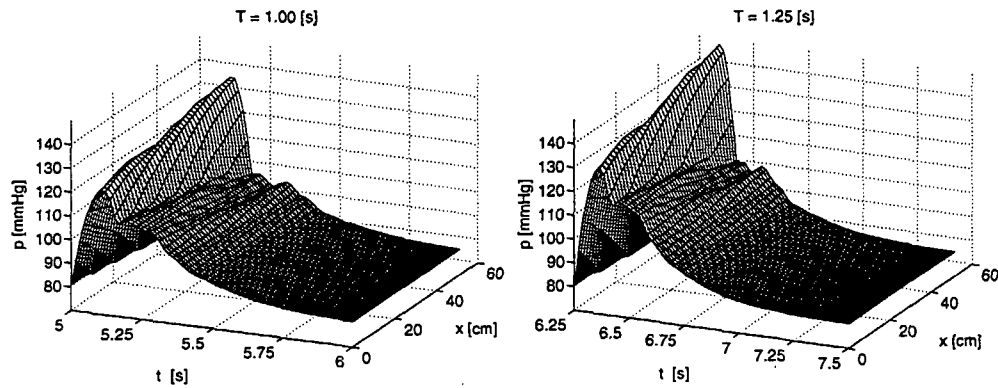


Figure 12.29: Pressure in the aorta as a function of x and t during one period. The two figures are for $T = 1.00$ s and $T = 1.25$ s. The decreased period implies a decrease in the systolic pressure as well as less pronounced reflected waves.

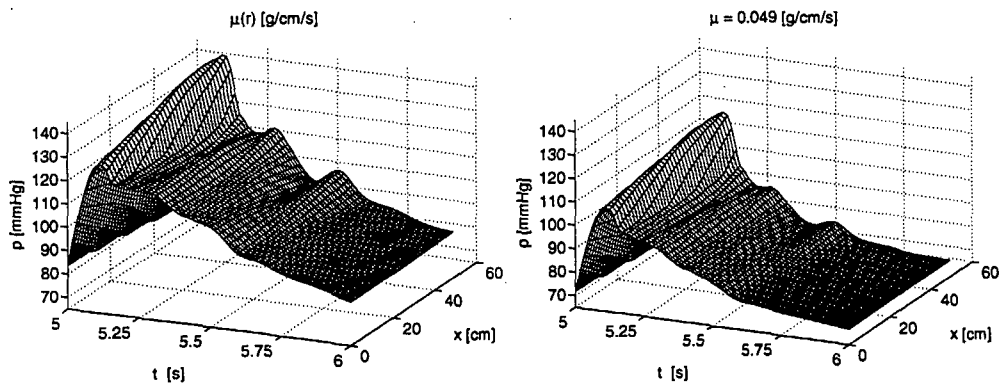


Figure 12.30: Pressure in the aorta using the structured tree as a function of x and t during one period. The left graph shows pressure for a constant viscosity and the right graph shows pressure for a radius dependent viscosity, see Chapter 3. The radius dependent viscosity causes a decrease in the peripheral resistance leading to a decrease in both the systolic and diastolic pressure as well as attenuation of the reflected waves.

Chapter 13

Conclusion

The purpose of this study was to develop a model, based on physiological principles, which can predict flow and pressure in the larger human systemic arteries. This has been achieved by constructing a fluid dynamical model, including both the larger and the smaller arteries, where the impedance of the smaller arteries constitute a boundary condition for the larger arteries. The smaller arteries are modeled as asymmetric structured trees while the larger arteries are modeled using actual data for the length, top, and bottom radii for each of the vessels. Flow and pressure in the larger arteries are found by solving the one-dimensional non-linear Navier-Stokes equations combined with a state equation predicting the relation between flow and pressure. For the smaller arteries we only compute the impedance which is found by solving a linearization of the one-dimensional Navier-Stokes equations combined with the same state equation as for the larger arteries.

It was shown in Chapter 12 that the resulting pressure and flow profiles all have the correct characteristics:

- The systolic pressure increases away from the heart.
- The mean pressure drops slowly.
- The steepness of the incoming pressure profile increases towards the periphery.
- The velocity of the wave propagation of the reflected dicrotic wave is slower than that of the main wave, and hence the dicrotic wave separates from the main wave peripherally.

In addition to showing the correct characteristics, see Figures 12.1, 12.2, and 12.3, our results reveal that the structured tree model provides a more dynamical impedance which is much closer to physiological behavior than can be obtained with the Windkessel model, see Figures 12.9–12.12. Furthermore, phase-lag between flow and pressure is retained, and correct quantitative as well as qualitative results for both flow and pressure are obtained, see Figure 12.6. However, it has been necessary to reduce the cardiac output to about 3.5 l/min in order to achieve these results. This is a natural consequence of the fact that we do not include all branches of the arteries and thus cannot account for the total cardiac output.

We have used a strictly positive function to generate the inflow profile and still observed the wanted reflected waves. Therefore, we can conclude that the primary

factor creating the wave reflections is not the appearance of a negative flow into the left ventricle but the tapering and bifurcations of the vessels combined with the peripheral resistance. However, as seen in the measurements in Figure 12.5 there is a small 'hump' near the apex of the measured curves. This results in a small extra reflected wave and, since it is not appearing in the simulated results, we assume that it is caused by the inflow discontinuity represented by the actual negative flow back into the heart.

The advantage of modeling the smaller arteries by applying structured trees at all terminals of the larger arteries is that it gives a physiological boundary condition which is able to include wave-propagation effects such that the impedance show the right dynamic behavior. Furthermore, it only has one parameter that needs to be estimated, namely the radius at which the structured tree must be terminated. However, this assumes that we are able to use a general functional dependence determining the elasticity of the vessel walls. This is a result of the viscous treatment of blood flow in the structured tree. Because we do not apply any resistance at the terminals of the structured tree the peripheral resistance of the larger arteries is obtained entirely from the solutions of the linearized equations in the asymmetric structured tree. However, we have also shown that it is important to estimate the minimum radii correctly. Furthermore, we have shown that it is possible to estimate the minimum radius by studying the overall terminal resistance of the organ in question.

As mentioned in the section describing the geometry of the structured tree, the diameter of the smaller arteries varies considerably and so does the peripheral resistance of these very small vessels which have a strong muscular wall. This is consistent with the observations (Guyton, 1991) that it is the arterioles, and not the capillaries, which generate the peripheral resistance. Furthermore, since the total peripheral resistance of the different organs vary it is important to choose the minimum radius individually for each of the structured trees, i.e. for each of the terminal branches of the larger arteries.

Our investigations of the model behavior under variations of the other parameters show that they affect the model as expected: For the smaller arteries we see that changes in both the radius exponent ξ as well as the asymmetry ratio γ does not have a significant effect. Hence, better estimates than those given in Table 6.1 are hardly justified. However, the choice of minimum radius r_{min} and length to radius relation l_{rr} is important. Especially our comparisons show that the length to radius relation might have a dependence on radius. Hence we propose to investigate this relation further. Generally, for the smaller arteries, most of the references agree with the relations we have used, see Section 6.3.

For the parameters of the overall system, i.e. the cardiac output, the length of the period, Young's modulus, and the actual geometry of the larger vessels we see that the model behaves as expected. An increase in the cardiac output causes an increase in the systolic pressure as well as more pronounced reflected waves. An increase in the period implies that there are few bursts of blood into the arteries per minute and in order to maintain a given cardiac output more blood is entering the aorta at each systole. This implies that the systolic pressure increases and that the reflected waves become more pronounced. Even though we in most cases used a very simple model of the Young's modulus we see the correct behavior when changing the parameter. In the results we showed that when letting Eh/r_0 grow with a decreasing vessel radius, then an increase of $\lim_{r_0 \rightarrow \infty} Eh/r_0$ correctly causes an increase in the systolic pressure and attenuation of the reflected waves. If the model is to be used for studying a more

local behavior of changes in the vessel elasticity, this function should be modeled more carefully.

The basic geometrical data for the larger arteries also have an impact on the results. The dimensions of the larger arteries in humans vary considerably, for example will the aorta of a 2 m tall man be much longer than that of a 1.5 m tall woman. However, for both persons the pressure profiles have the same characteristics provided that both are healthy.

In summary; the study has shown the feasibility of limiting the computational domain. Based entirely on physiological information we have succeeded in deriving a good boundary condition for the non-linear model predicting blood flow and pressure in the larger systemic arterial tree in such a way that even at the boundary the impedance shows the right characteristics even for high frequencies. Thus, we have confirmed the claim stated in the hypothesis.

It is possible to argue that the structured model is too complicated and that the much simpler Windkessel model is adequate because it provides a dynamic boundary condition as well. Furthermore, since measurements for both the total resistance and the compliance are available, the Windkessel model is simple and yet adequate as boundary condition for the larger arteries. In contrast, the structured tree model is more detailed, but it does not yield a decisive advantage over the Windkessel model. Finally, the Windkessel model is local in both time and space, while the structured tree model is periodic in time but local in space. Therefore, replacing the Windkessel model with a structured tree model comes at the cost of replacing an ordinary differential equation by a convolution integral.

However, we find the structured tree model has several important advantages. First of all because it is based on the underlying physiology, it includes wave propagation effects. This enables the model to capture the observed high frequency oscillations of the impedance in the part of the arterial system that it models. Second, the structured tree model can predict flow and pressure not only in the larger but also in the smaller arteries, i.e. shifting the purpose of the structured tree from being a boundary condition to being a more active part of the model.

The idea of using a structured tree in which a simpler set of equations is solved, could also be applied to other areas involving flow in tree-like structures such as flow and depth of water in a river delta. However, the use of the boundary condition stated here is only applicable to phenomena in which there is some scaling law that gives rise to a structured tree.

13.1 Perspectives

Several modifications and improvements can be made to the arterial model presented in the dissertation. In the following we will give a summary of some of these.

Order of the structured tree

We have shown that the minimum radius of the terminal trees should be varied in order to account for resistance of various organs. We also showed that the significant part of the difference in applying the various terminal minimum radii lies in the magnitude of

the average resistance. Therefore, it would be obvious to investigate the possibility of keeping one minimum radius common for all the smaller vessels and then adjust it to the various organs by attaching a variable pure resistance as a boundary condition at the terminals of the smaller arteries. In this way the dynamics generated by the structured tree is retained and a pure resistance need not be applied until at the arterioles where the flow and pressure are almost in phase. This also agrees with the physiological approach we have used when designing the model. Furthermore, having a pure resistance at the bottom makes it easier to adapt the model to various physiological conditions. For example, during exercise, the peripheral resistance of the various tissues decreases.

Another point which could be interesting to study is the correspondence between adapting the structured tree to yield a given resistance at its root and comparing the resulting minimum radius with the actual physiological radius at the arteriolar level of the given organ. In order to get a good agreement we believe that such a study requires a more detailed model of the elastic properties such that there is a close match between the structured tree in question and the organ it models.

13.1.1 Inflow boundary condition

In order to discuss the origin of the various reflected waves in actual measurements of the arterial pressure it would be useful to change the inflow condition such that it includes a negative flow into the left ventricle. This is not a leak but a result of the fact that before the aortic valve closes a small amount of blood flows from the aorta and back into the ventricle. Making a comparative study including an inflow accounting for the negative flow and one without would yield this information. Another way to facilitate this would be to combine this model with a heart model providing the inflow function. This could in turn also give some more detailed information on pressure in the aorta, since combining our model with such a model would yield contributions to both flow and pressure.

13.1.2 Young's modulus and the state equation

In this dissertation we have used a simple state equation based on linear elasticity theory, but where Eh/r_0 decreases exponentially with an increasing radius. The functional dependence between Young's modulus, the wall-thickness, and the radius is an improvement of the basic model, however, it is still not physiologically correct to use a pure elastic model for the arterial wall. As a result the wave propagation velocity decreases with an increasing pressure, which should be opposite, and when plotting the cross-sectional area $A(x_f, t)$ versus pressure $p(x_f, t)$ for some fixed x_f the graph curves the wrong way, see Section 7.2. However, this is not essential since the curve is almost a straight line. As a result the model exhibits an overall behavior which is correct and can thus we get the satisfactory results shown throughout this thesis. But, as discussed earlier, this may be improved by using an empirically based relation which allows for varying elastic properties for the individual arteries. This is probably reasonable, since even though the systemic arteries are all composed of the same basic material there are differences depending on their function. However, in order to develop a better empirical model a more detailed study must be performed such that the model parameters can be estimated correctly. A good suggestion to such a model is

the model by Langewouters et al. (1984) which is discussed in Section 7.2.2. Finally, it should be noted that it is easy to change the present state equation with some other relation and we highly recommend to investigate this further.

13.2 Pathological situations

In order to get a better idea of the validity of the arterial model one should use it for studying a number of pathological situations. Since our model is based on the assumption of laminar flow it would not be well suited for studying phenomena related to atherosclerosis since these often give rise to vortices and turbulence (Nichols and O'Rourke, 1998). However, it would be interesting to study effects arising from changes in the vascular wall. That could be aging, diabetes, vaso-constriction, or vaso-dilation. In Section 12.3.2 we looked at some of the phenomena resulting in a stiffening of the arteries, but the opposite should be studied as well e.g. vaso-dilation. In this case $\lim_{r_0 \rightarrow 0} Eh/r_0$ would be decreased, resulting in a stiffening of the smaller arteries such as the radial and femoral arteries but only little change in elasticity of the larger arteries such as aorta. This should result in a reduced systolic pressure and a reduction of wave reflections because due to a delay in the early reflections (Nichols and O'Rourke, 1998). However, if one wishes to study the implications for specific arteries, i.e. more local changes, a more sophisticated model of the elasticity of the arterial wall should be incorporated.

13.3 Comparison with measured data

Finally, one of the biggest problems with our treatment in this report is the lack of detailed comparisons with measured data. One study that we would suggest to do would be to measure pressure and maybe flow at a number of locations e.g. along the aorta. For each of these measurements one should then estimate the geometry of the larger arteries and then compare the results with simulations. Since it is easy to adjust the geometry of the model to the subject being measured, these measurements do not necessarily have to be on humans. However, in order to be able to use the same model assumptions comparisons should be made with relative large animals e.g. pigs or dogs. However, we did initiate such studies by measuring the pressure at number of locations along the aorta, see Figure 12.5. Unfortunately, we only managed to include one measurement.

13.4 Arterial modeling and anesthesia simulation

The model developed here fulfills our purpose of deriving a reference model of the larger arteries. However, we also wanted to derive a model which in various pathological situations could be used to calibrate the cardiovascular model in the anesthesia simulator. But, as discussed above it would be easy to set up a number of studies for certain groups of pathological situations, e.g. vaso-dilation and vaso-constriction.

It is not possible to directly include the model in the anesthesia simulator described in Chapter 2 since it would not be able to run in real time on a PC which is one of the

requirements for the simulator. Therefore, the cardiovascular model, and hence the arterial model, used in the anesthesia simulator is much simpler than what has been described in this study. The disadvantage of the simple model is that it is not able to predict the correct pressure and flow profiles for the large variety of situations needed in the simulator. The model in the simulator is mostly used to predict the systolic and diastolic pressures while the pressure profiles are generated from predefined profiles. Thus, the simulator contains a database with a large number of standard curves.

Reflecting the correct physiological behavior is thus difficult, and this is where the reference model will be most useful. Because of the flexible structure of our model it is possible to construct all of these standard cases by setting up parameters describing each of the scenarios.

Such information should include:

- The cardiac output.
- The frequency of the period.
- Young's modulus.
- The peripheral resistances for each of the organs such that the minimum radius for the structured trees can be chosen correctly.
- The actual geometry for the vessels of the larger arteries.

Simulations with these parameters can be used directly to verify or determine the actual pressure profiles but it is also possible to determine some of the basic parameters for the simplified model from profiles generated with our reference model.

The main use of the reference model is to create parameters as well as flow and pressure profiles for the anesthesia simulator. Moreover, the modeling process has generated much experience and knowledge about physiology. This has proven useful for evaluating the results of the simpler real time model in the simulator. Since the goal as stated in our hypothesis was to build and test a reference model for the cardiovascular model in the simulator we will conclude that we have accomplished our goal.

Appendix A

Derivation of non-linear equations for the Lax-Wendroff method

A.1 Outflow boundary condition

The residuals $((f_r)_1, (f_r)_2, (f_r)_3, (f_r)_4 \dots)$ needed to apply Newton's method are given by:

Equation 1 – from (9.25):

$$(f_r)_1 = p \left(M, \frac{A_{M-1/2}^{n+1/2} + x_2}{2} \right) y_M^0 \Delta t + (q_{tms})_M^{n+1/2} - \frac{q_{M-1/2}^{n+1/2} + x_1}{2} \quad (\text{A.1})$$

Let

$$\begin{aligned} k_1 &= (q_{tms})_M^{n+1/2} - \frac{q_{M-1/2}^{n+1/2}}{2} \\ k_2 &= y_M^0 \Delta t \\ k_3 &= A_{M-1/2}^{n+1/2} \end{aligned}$$

then $(f_r)_1$ can then be rewritten as

$$(f_r)_1 = k_1 + p \left(M, \frac{k_3 + x_2}{2} \right) k_2 - \frac{x_1}{2} \quad (\text{A.2})$$

Equation 2 – from (9.24):

$$(f_r)_2 = p(M, x_4) y_M^0 \Delta t + (q_{tms})_M^{n+1} - x_3 \quad (\text{A.3})$$

Let

$$k_4 = (q_{tms})_M^{n+1}$$

then $(f_r)_2$ can then be rewritten as

$$(f_r)_2 = k_4 + p(M, x_4) k_2 - x_3 \quad (\text{A.4})$$

Equation 3 – from (9.19):

$$(f_r)_3 = A_M^n - \theta \left(x_1 - (R_1)_{M-1/2}^{n+1/2} \right) - x_4 \quad (\text{A.5})$$

Let

$$k_5 = A_M^n + \theta (R_1)_{M-1/2}^{n+1/2}$$

then $(f_r)_3$ can be rewritten as

$$(f_r)_3 = k_5 - \theta x_1 - x_4$$

Equation 4 – from (9.20):

$$\begin{aligned} (f_r)_4 = & -x_3 + q_M^n - \theta \left(\frac{x_1^2}{x_2} + B_{(M+1/2, x_2)} - (R_2)_{M-1/2}^{n+1/2} \right) + \\ & \gamma \left(F_{(M+1/2, x_1, x_2)} + \frac{dB_{(M+1/2, x_2)}}{dx} + (S_2)_{M-1/2}^{n+1/2} \right) \end{aligned} \quad (\text{A.6})$$

where

$$F_{(M+1/2, x_1, x_2)} = -\frac{2\pi(r_0)_{M+1/2}}{\delta\mathcal{R}} \frac{x_1}{x_2}$$

$$B_{(M+1/2, x_2)} = f(r_0)_{M+1/2} \sqrt{x_2 (A_0)_{M+1/2}}$$

$$\begin{aligned} \frac{dB_{(M+1/2, x_2)}}{dx} &= \left(\frac{\partial B}{\partial r_0} \frac{dr_0}{dx} \right)_{M+1/2}^{n+1/2} \\ &= \left(2\sqrt{x_2} \left(\sqrt{\pi} f(r_0) + \sqrt{A_0} \frac{df}{dr_0} \right) - A \frac{df}{dr_0} \right)_{M+1/2} \left(\frac{dr_0}{dx} \right)_{M+1/2} \end{aligned}$$

Let

$$k_6 = q_M^n + \theta (R_2)_{M-1/2}^{n+1/2} + \gamma (S_2)_{M-1/2}^{n+1/2}$$

then $(f_r)_4$ can be written as

$$(f_r)_4 = -x_3 + k_5 - \theta \left(\frac{x_1^2}{x_2} + B_{(M+1/2, x_2)} \right) + \gamma \left(F_{(M+1/2, x_1, x_2)} + \frac{dB_{(M+1/2, x_2)}}{dx} \right)$$

The Jacobian Df_r is given by

$$Df_r = \begin{pmatrix} -\frac{1}{2} & \xi_1 & 0 & 0 \\ 0 & 0 & -1 & \xi_2 \\ -\theta & 0 & 0 & -1 \\ \xi_3 & \xi_4 & -1 & 0 \end{pmatrix}$$

where

$$\begin{aligned}\xi_1 &= k_2 \frac{dp(M(k_3 + x_2)/2)}{dx_2} \\ \xi_2 &= k_4 \frac{dp(M, x_4)}{dx_4} \\ \xi_3 &= -\theta \frac{2x_1}{x_2} + \gamma \frac{dF(M+1/2, x_1, x_2)}{dx_1} \\ \xi_4 &= \theta \left(\left(\frac{x_1}{x_2} \right)^2 + \frac{dB(M+1/2, x_2)}{dx_2} \right) + \gamma \left(\frac{dF(M+1/2, x_1, x_2)}{dx_2} + \frac{d^2B(M+1/2, x_2)}{dx dx_2} \right)\end{aligned}$$

A.2 Bifurcation conditions

The residuals $((f_r)_1, (f_r)_2, \dots, (f_r)_{18})$ needed to apply Newton's method are given by:

Equation 1 – from (9.32):

$$\begin{aligned}(f_r)_1 &= -x_1 + (q^{(p)})_M^n - \theta \left(\frac{x_3^2}{x_{12}} + B(M+1/2, x_{12}) - (R_2^{(p)})_{M-1/2}^{n+1/2} \right) + \\ &\quad \gamma \left(F(M+1/2, x_3, x_{12}) + \frac{dB(M+1/2, x_{12})}{dx} + (S_2^{(p)})_{M-1/2}^{n+1/2} \right)\end{aligned}$$

where

$$\begin{aligned}B(M+1/2, x_{12}) &= f(r_0)_{M+1/2} \sqrt{x_{12} (A_0)_{M+1/2}} \\ F(M+1/2, x_3, x_{12}) &= -\frac{2\pi(r_0)_{M+1/2} x_3}{\delta \mathcal{R} x_{12}} \\ \frac{dB(M+1/2, x_{12})}{dx} &= \left(\frac{\partial B}{\partial r_0} \frac{dr_0}{dx} \right)_{M+1/2}^{n+1/2} \\ &= \left(2\sqrt{x_{12}} \left(\sqrt{\pi} f(r_0) + \sqrt{A_0} \frac{df}{dr_0} \right) - A \frac{df}{dr_0} \right)_{M+1/2} \left(\frac{dr_0}{dx} \right)_{M+1/2}\end{aligned}$$

Then let

$$k_1 = (q^{(p)})_M^n + \theta (R_p^{(p)})_{M-1/2}^{n+1/2} + \gamma (S_2^{(p)})_{M-1/2}^{n+1/2}$$

and $(f_r)_1$ can be rewritten as

$$(f_r)_1 = k_1 - x_1 - \theta \left(\frac{x_3^2}{x_{12}} + B(M+1/2, x_{12}) \right) + \gamma \left(F(M+1/2, x_3, x_{12}) + \frac{dB(M+1/2, x_{12})}{dx} \right)$$

Equations 2 and 3 – from (9.32):

$$\begin{aligned}(f_r)_{2,3} &= -x_{4,7} + (q^{(d_1, d_2)})_M^n - \theta \left((R_2^{(d_1, d_2)})_{M+1/2}^{n+1/2} - B(-1/2, x_{15,18}) \right) + \\ &\quad \gamma \left((S_2^{(2,3)})_{M+1/2}^{n+1/2} + F(-1/2, x_{6,9}, x_{15,18}) + \frac{dB(-1/2, x_{15,18})}{dx} \right)\end{aligned}$$

Where B, F , and dB/dx are defined as above. Now let

$$k_{2,2a} = (q^{(d_1, d_2)})_M^n - \theta \left(R_2^{(d_1, d_2)} \right)_{M+1/2}^{n+1/2} + \gamma \left(S_2^{(d_1, d_2)} \right)_{M+1/2}^{n+1/2}$$

then

$$(f_r)_{2,3} = k_{2,2a} - x_{4,7} + \theta \left(\frac{x_{6,9}^2}{x_{15,18}} + B(-1/2, x_{15,18}) \right) + \gamma \left(F(-1/2, x_{6,9}, x_{15,18}) + \frac{dB(-1/2, x_{15,18})}{dx} \right)$$

Equation 4 – from (9.33):

$$(f_r)_4 = -x_{10} + (A^{(p)})_M^n - \theta \left(x_3 - \left(R_1^{(p)} \right)_{M-1/2}^{n+1/2} \right)$$

Let

$$k_3 = (A^{(p)})_M^n + \theta \left(R_1^{(p)} \right)_{M-1/2}^{n+1/2}$$

then

$$(f_r)_4 = -x_{10} - \theta x_3 + k_3$$

Equations 5 and 6 – from (9.33):

$$(f_r)_{5,6} = -x_{13,16} + (A^{(d_1, d_2)})_M^n - \theta \left(\left(R_1^{(d_1, d_2)} \right)_{M+1/2}^{n+1/2} - x_{6,9} \right)$$

Let

$$k_{4,4a} = (A^{(d_1, d_2)})_M^n - \theta \left(R_1^{(d_1, d_2)} \right)_{M+1/2}^{n+1/2}$$

Then we can rewrite $(f_r)_{5,6}$ as

$$(f_r)_{5,6} = -x_{13,16} + \theta x_{6,9} + k_{4,4a}$$

Equation 7 – from (9.21):

$$(f_r)_7 = -x_2 + \frac{(q^{(p)})_{M-1/2}^{n+1/2} + x_3}{2}$$

Let

$$k_5 = \frac{(q^{(p)})_{M-1/2}^{n+1/2}}{2}$$

then

$$(f_r)_7 = -x_2 + \frac{x_3}{2} + k_5$$

Equations 8 and 9 – from (9.21):

$$(f_r)_{8,9} = -x_{5,8} + \frac{x_{6,9} + (q^{(d_1, d_2)})_{M+1/2}^{n+1/2}}{2}$$

Let

$$k_{6,6a} = \frac{(q^{(d_1, d_2)})_{M+1/2}^{n+1/2}}{2}$$

Then

$$(f_r)_{8,9} = -x_{5,8} + \frac{x_{6,9}}{2} + k_{6,6a}$$

Equation 10 – from (9.22):

$$(f_r)_{10} = -x_{11} + \frac{(A^{(p)})_{M-1/2}^{n+1/2} + x_{12}}{2}$$

Let

$$k_7 = \frac{(A^{(p)})_{M-1/2}^{n+1/2}}{2}$$

then

$$(f_r)_{10} = -x_{11} + \frac{x_{12}}{2} + k_7$$

Equations 11 and 12 – from (9.22):

$$(f_r)_{11,12} = -x_{14,17} + \frac{x_{15,18} + (A^{(d_1, d_2)})_{M+1/2}^{n+1/2}}{2}$$

Let

$$k_{8,8a} = \frac{(A^{(d_1, d_2)})_{M+1/2}^{n+1/2}}{2}$$

Then

$$(f_r)_{11,12} = -x_{14,17} + \frac{x_{15,18}}{2} + k_{8,8a}$$

Equations 13 and 14 – from (9.27):

$$(f_r)_{13,14} = -x_{2,1} + x_{5,4} + x_{8,7}$$

Equations 15 and 16 – from (9.29):

$$(f_r)_{15,16} = -(f^{(p)})_M \left(1 - \sqrt{\frac{(A_0^{(p)})_M}{x_{11}}} \right) + (f^{(d_1, d_2)})_0 \left(1 - \sqrt{\frac{(A_0^{(d_1, d_2)})_0}{x_{14,17}}} \right)$$

where $f = Eh/\tau_0$. Let

$$\begin{aligned}k_{9,9a} &= -\left(f^{(p)}\right)_M + \left(f^{(d_1,d_2)}\right)_0 \\k_{10} &= \left(f^{(p)}\sqrt{A_0^{(p)}}\right)_M \\k_{11,11a} &= \left(f^{(d_1,d_2)}\sqrt{A_0^{(d_1,d_2)}}\right)_0\end{aligned}$$

Then $(f_r)_{15,16}$ can be rewritten as

$$(f_r)_{15,16} = \frac{k_{10}}{\sqrt{x_{11}}} - \frac{k_{11,11a}}{\sqrt{x_{14,17}}} + k_{9,9a}$$

Equations 17 and 18 – from (9.30):

$$(f_r)_{17,18} = -\left(f^{(p)}\right)_M \left(1 - \sqrt{\frac{(A_0^{(p)})_M}{x_{10}}}\right) + \left(f^{(d_1,d_2)}\right)_0 \left(1 - \sqrt{\frac{(A_0^{(d_2,d_3)})_0}{x_{13,16}}}\right)$$

Since neither f nor A_0 depends on t , we can reuse the constants $k_9 - k_{11a}$. Doing so, $(f_r)_{17,18}$ can be rewritten as

$$(f_r)_{17,18} = \frac{k_{10}}{\sqrt{x_{10}}} - \frac{k_{11,11a}}{\sqrt{x_{13,16}}} + k_{9,9a}$$

The Jacobian Df_r is given by

$$\begin{pmatrix} -1 & 0 & \xi_1 & 0 & 0 & 0 & 0 & 0 & 0 & 0 & 0 & \xi_2 & 0 & 0 & 0 & 0 & 0 \\ 0 & 0 & 0 & -1 & 0 & \xi_3 & 0 & 0 & 0 & 0 & 0 & 0 & 0 & 0 & \xi_4 & 0 & 0 \\ 0 & 0 & 0 & 0 & 0 & 0 & -1 & 0 & \xi_5 & 0 & 0 & 0 & 0 & 0 & 0 & 0 & \xi_6 \\ 0 & 0 & -\theta & 0 & 0 & 0 & 0 & 0 & 0 & -1 & 0 & 0 & 0 & 0 & 0 & 0 & 0 \\ 0 & 0 & 0 & 0 & 0 & \theta & 0 & 0 & 0 & 0 & 0 & 0 & -1 & 0 & 0 & 0 & 0 \\ 0 & 0 & 0 & 0 & 0 & 0 & 0 & 0 & \theta & 0 & 0 & 0 & 0 & 0 & 0 & -1 & 0 \\ 0 & -1 & \frac{1}{2} & 0 & 0 & 0 & 0 & 0 & 0 & 0 & 0 & 0 & 0 & 0 & 0 & 0 & 0 \\ 0 & 0 & 0 & 0 & -1 & \frac{1}{2} & 0 & 0 & 0 & 0 & 0 & 0 & 0 & 0 & 0 & 0 & 0 \\ 0 & 0 & 0 & 0 & 0 & 0 & 0 & -1 & \frac{1}{2} & 0 & 0 & 0 & 0 & 0 & 0 & 0 & 0 \\ 0 & 0 & 0 & 0 & 0 & 0 & 0 & 0 & 0 & 0 & -1 & \frac{1}{2} & 0 & 0 & 0 & 0 & 0 \\ 0 & 0 & 0 & 0 & 0 & 0 & 0 & 0 & 0 & 0 & 0 & 0 & -1 & \frac{1}{2} & 0 & 0 & 0 \\ 0 & 0 & 0 & 0 & 0 & 0 & 0 & 0 & 0 & 0 & 0 & 0 & 0 & 0 & 0 & -1 & \frac{1}{2} \\ 0 & -1 & 0 & 0 & 1 & 0 & 0 & 1 & 0 & 0 & 0 & 0 & 0 & 0 & 0 & 0 & 0 \\ -1 & 0 & 0 & 1 & 0 & 0 & 1 & 0 & 0 & 0 & 0 & 0 & 0 & 0 & 0 & 0 & 0 \\ 0 & 0 & 0 & 0 & 0 & 0 & 0 & 0 & 0 & 0 & \xi_7 & 0 & 0 & \xi_8 & 0 & 0 & 0 \\ 0 & 0 & 0 & 0 & 0 & 0 & 0 & 0 & 0 & 0 & \xi_7 & 0 & 0 & 0 & 0 & 0 & \xi_9 \\ 0 & 0 & 0 & 0 & 0 & 0 & 0 & 0 & 0 & \xi_{10} & 0 & 0 & \xi_{11} & 0 & 0 & 0 & 0 \\ 0 & 0 & 0 & 0 & 0 & 0 & 0 & 0 & 0 & \xi_{10} & 0 & 0 & 0 & 0 & 0 & \xi_{12} & 0 \end{pmatrix}$$

where

$$\begin{aligned}
\xi_1 &= -\theta \frac{2x_3}{x_{12}} + \gamma \frac{dF(M+1/2, x_3, x_{12})}{dx_3} \\
\xi_2 &= \theta \left(\frac{x_3^2}{x_{12}^2} - \frac{dB(M+1/2, x_{12})}{dx_{12}} \right) + \gamma \left(\frac{dF(M+1/2, x_3, x_{12})}{dx_{12}} + \frac{d^2 B(M+0.5, x_{12})}{dx dx_{12}} \right) \\
\xi_3 &= \theta \frac{2x_6}{x_{15}} + \gamma \frac{dF(-1/2, x_6, x_{15})}{dx_6} \\
\xi_4 &= \theta \left(-\frac{x_6^2}{x_{15}^2} + \frac{dB(-1/2, x_{15})}{dx_{15}} \right) + \gamma \left(\frac{dF(-1/2, x_6, x_{15})}{dx_{15}} + \frac{d^2 B(-1/2, x_{15})}{dx dx_{15}} \right) \\
\xi_5 &= \theta \frac{2x_9}{x_{18}} + \gamma \frac{dF(-1/2, x_9, x_{18})}{dx_9} \\
\xi_6 &= \theta \left(-\frac{x_9^2}{x_{18}^2} + \frac{dB(-1/2, x_{18})}{dx_{18}} \right) + \gamma \left(\frac{dF(-1/2, x_9, x_{18})}{dx_{18}} + \frac{d^2 B(-1/2, x_{18})}{dx dx_{18}} \right) \\
\xi_7 &= -\frac{dP(M, x_{11})}{dA} \\
\xi_8 &= \frac{dP(0, x_{14})}{dA} \\
\xi_9 &= \frac{dP(0, x_{17})}{dA} \\
\xi_{10} &= -\frac{dP(M, x_{10})}{dA} \\
\xi_{11} &= \frac{dP(0, x_{13})}{dA} \\
\xi_{12} &= \frac{dP(0, x_{16})}{dA}
\end{aligned}$$

and

$$\begin{aligned}
\frac{dB(l, x_i)}{dx_i} &= \frac{f(r_0)_l}{2} \sqrt{\frac{(A_0)_l}{x_i}} \\
\frac{d^2 B(l, x_i)}{dx dx_i} &= \left(\frac{1}{2\sqrt{x_i}} \left(f(r_0)_l \sqrt{\pi} + \left(\frac{df}{dr_0} \right)_l \sqrt{(A_0)_l} \right) - \left(\frac{df}{dr_0} \right)_l \right) \left(\frac{dr_0}{dx} \right)_l \\
\frac{dF(l, x_{i_1}, x_{i_2})}{dx_{i_2}} &= \frac{2\pi(r_0)_l}{\delta \mathcal{R}} \frac{x_{i_1}}{x_{i_2}^2} \\
\frac{dF(l, x_{i_1}, x_{i_2})}{dx_{i_1}} &= \frac{2\pi(r_0)_l}{\delta \mathcal{R}} \frac{1}{x_{i_2}} \\
\frac{dP(l, x_i)}{dx_i} &= -\frac{f(r_0)_l}{2} \sqrt{\frac{d(A_0)_l}{x_i^3}}
\end{aligned}$$

Appendix B

Gas dynamics analogy

There is an direct analogy between the equations for the one-dimensional fluid flow in distensible vessels and the one-dimensional gas-dynamic equations. This is described by Shapiro (1977) and Forbes (1981) among others.

Our point of departure are equations (7.9–7.10). However, we disregard both the outflow ($\Psi = 0$) and the wall-shear stress. The latter could easily be taken into the equations but is left out to simplify the equations. This is acceptable since the purpose of this section is to show the analogy not to derive our concrete model. Hence, the continuity and momentum equations are given by

$$\begin{aligned}\frac{\partial A}{\partial t} + \frac{\partial(Au)}{\partial x} &= 0 \\ \rho \left(\frac{\partial(Au)}{\partial t} + \frac{\partial(Au^2)}{\partial x} \right) + A \frac{\partial p}{\partial x} &= 0\end{aligned}$$

Dividing the momentum equation by ρ , and expanding the terms $\partial(Au)/\partial t$ and $\partial(Au^2)/\partial x$ gives

$$\begin{aligned}\frac{\partial A}{\partial t} + \frac{\partial(Au)}{\partial x} &= 0 \\ A \frac{\partial u}{\partial t} + u \left(\frac{\partial A}{\partial t} + \frac{\partial(Au)}{\partial x} \right) + Au \frac{\partial u}{\partial x} + \frac{A}{\rho} \frac{\partial p}{\partial x} &= 0\end{aligned}$$

If u times the continuity equation is subtracted the terms in the parenthesis cancel. Dividing the momentum equation by A yields

$$\frac{\partial A}{\partial t} + \frac{\partial(Au)}{\partial x} = 0 \quad (\text{B.1})$$

$$\frac{\partial u}{\partial t} + u \frac{\partial u}{\partial x} + \frac{1}{\rho} \frac{\partial p}{\partial x} = 0 \quad (\text{B.2})$$

Instead of using (7.26) it is assumed that p is a function of A only. Thus, the natural taper of the arteries is disregarded. Hence, Equations (B.1–B.2) can be reformulated such that they become identical to the unsteady one-dimensional gas dynamics equations. In order to do so the following change of variables must be made

$$\hat{\rho} = \rho A$$

where ρ is constant due to the incompressibility in the fluid approach, and

$$\hat{p} = \int A dp$$

Using these definitions the following one-dimensional gas dynamics equations are obtained

$$\frac{\partial \hat{p}}{\partial t} + \frac{\partial(\hat{\rho}u)}{\partial x} = 0 \quad (\text{B.3})$$

$$\frac{\partial u}{\partial t} + u \frac{\partial u}{\partial x} + \frac{1}{\hat{\rho}} \frac{\partial \hat{p}}{\partial x} = 0 \quad (\text{B.4})$$

In order to make the similarity complete we need to establish

$$\hat{p} = K \hat{\rho}^\gamma$$

This imposes the following restriction on the state equation $p(A)$.

For $\gamma \neq 1$

$$A(p) = \left(A(p^*)^{\gamma-1} + \frac{\gamma-1}{\gamma} \frac{p-p^*}{K \rho^\gamma} \right)^{1/(\gamma-1)} \quad (\text{B.5})$$

and for $\gamma = 1$

$$A(p) = A(p^*) \exp \left(\frac{p-p^*}{K \rho} \right)$$

where p^* is constant having the dimensions of pressure. Finally, if we let $\gamma = 1/2$, $K = (4/3) Eh \sqrt{\pi/\rho}$, and $p^* = 0$ it can be shown that equation (B.5) is identical to the "elastic" relation stated in equation (7.26).

Appendix C

The self-similar tree

The tree of smaller arteries can be regarded as self-similar if the equations for any given vessel can be determined as scaled versions of the corresponding equations for the parent vessel, see Figure C.1.

In this chapter we show that if the fluid in the smaller arteries is treated as inviscid then it is possible to derive a self-similar solution. However, blood is viscous and because viscosity can not be scaled self-similarity do not apply

In order for self-similarity to apply, the parameters of a given daughter vessel (indicated with subscript d) must be scaled versions of the corresponding parameters for the parent vessel (indicated with subscript p), i.e.

$$\begin{aligned} t_d = \alpha t_p \quad x_d = \alpha x_p \quad r_d = \alpha r_p \quad A_d = \alpha^2 A_p \quad C_d = \alpha^2 C_p \\ P_d = P_p \quad Q_d = \alpha^2 Q_p \quad \rho_d = \rho_p \quad \omega_d = \omega_p / \alpha \quad Z_d = Z_p / \alpha^2 \end{aligned} \quad (\text{C.1})$$

where α is the scaling factor ($\alpha < 1$). Thus, equations (10.73) and (10.74) scale as

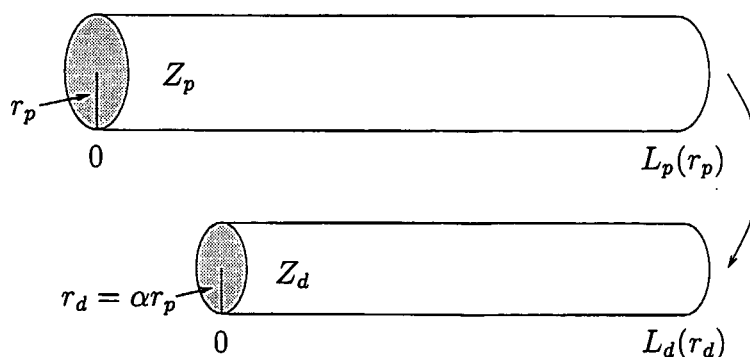


Figure C.1: The scaled vessels.

follows

$$\begin{aligned}
 & \left. \begin{aligned} i\omega_p Q_p + \frac{A_p(1-F_J)}{\rho_p} \frac{\partial P_p}{\partial x_p} &= 0 \\ i\omega_p C_p P_p + \frac{\partial Q_p}{\partial x_p} &= 0 \end{aligned} \right\} \Rightarrow \quad (C.2) \\
 & \left. \begin{aligned} i\alpha\omega_d(Q_d/\alpha^2) + \frac{(A_d/\alpha^2)(1-F_J)}{\rho_d} \frac{\partial P_d}{\partial(x_d/\alpha)} &= 0 \\ i\alpha\omega_d(C_d/\alpha^2)P_d + \frac{\partial(Q_d/\alpha^2)}{\partial(x_d/\alpha)} &= 0 \end{aligned} \right\} \Rightarrow \\
 & \begin{aligned} i\omega_d Q_d + \frac{A_d(1-F_J)}{\rho_d} \frac{\partial P_d}{\partial x_d} &= 0 \\ i\omega_d C_d P_d + \frac{\partial Q_d}{\partial x_d} &= 0 \end{aligned}
 \end{aligned}$$

The only term which does not immediately reveal whether it scales is F_J . From (10.63) we had

$$F_J = \begin{cases} 2/(wi^{1/2}) [1 + 1/(2w) + \mathcal{O}(w^{-2})] & \text{for } w \rightarrow \infty \\ 1 - i(w^2/8) - (w^4/48) + \mathcal{O}(w^6) & \text{for } w \rightarrow 0 \end{cases}$$

where the Womersley number $w = r\sqrt{\omega/\nu}$. In order for equations (C.2) to scale F_J and thus w must be invariant under the scalings by α . The scaling definitions in (C.1) gives $w_p = r_d/\alpha\sqrt{\omega_d\alpha/\nu_d} = w_d/\alpha$. This shows that unless the kinematic viscosity ν can be scaled such that $\nu_p = \nu_d/\alpha$, there is no self-similar solution to (C.2). Even though the viscosity, as shown in Figure 3.8, do depend on the vessel radius it does not scale linearly, so the viscous case does not exhibit self-similarity.

However, it is possible to find a self-similar solution to the inviscid fluid dynamic equations. These can be found from disregarding the friction term $2\pi\nu qRR/(A\delta)$ in (7.31) and (7.32)

$$\begin{aligned}
 \frac{\partial A}{\partial t} + \frac{\partial q}{\partial x} &= 0 \\
 \frac{\partial q}{\partial t} + \frac{\partial}{\partial x} \left(\frac{q^2}{A} \right) + \frac{A}{\rho} \frac{\partial p}{\partial x} &= 0
 \end{aligned}$$

These equations can be linearized by letting $\partial A/\partial t \approx C\partial p/\partial t$, disregarding the term $\partial(q^2/A)/\partial x$, and approximating the factor A/ρ by A_0/ρ . Hence,

$$C \frac{\partial p}{\partial t} + \frac{\partial q}{\partial x} = 0 \quad (C.3)$$

$$\frac{\partial q}{\partial t} + \frac{A_0}{\rho} \frac{\partial p}{\partial x} = 0 \quad (C.4)$$

The Fourier transform of these inviscid linear fluid dynamic equations yields exactly the same equations as (C.2) but without the factor F_J . Hence, the inviscid equations exhibit self-similarity.

The equations for the daughter arteries can be written in terms of the ones for the parent artery.

$$Z_d(x_d, \omega_d) = \frac{P_d(x_d, \omega_d)}{Q_d(x_d, \omega_d)} = \frac{P_p(x_p, \omega_p)}{\alpha^2 Q_p(x_p, \omega_p)} = \frac{Z_p(x_p, \omega_p)}{\alpha^2} =$$

Hence, the impedance at the inlet of the vessel, i.e. at $x = 0$, is given by

$$Z_d(0, \omega_d) = \frac{Z_p(0, \alpha\omega_p)}{\alpha^2}$$

As discussed in Chapter 6 the daughter vessels scale with ratios α and β , not necessarily the same. Hence,

$$Z_{d1}(0, \omega_{d1}) = \frac{Z_p(0, \alpha\omega_p)}{\alpha^2} \quad (\text{C.5})$$

$$Z_{d2}(0, \omega_{d2}) = \frac{Z_p(0, \beta\omega_p)}{\beta^2} \quad (\text{C.6})$$

In order to apply self-similarity the bifurcation-condition (11.1) must be scaled as well. Using (C.5) and (C.6) gives

$$\begin{aligned} \frac{1}{Z_p(L_p, \omega_p)} &= \frac{1}{Z_{d1}(0, \omega_{d1})} + \frac{1}{Z_{d2}(0, \omega_{d2})} \Rightarrow \\ \frac{1}{Z_p(L_p, \omega_p)} &= \frac{\alpha^2}{Z_p(0, \alpha\omega_p)} + \frac{\beta^2}{Z_p(0, \beta\omega_p)} \end{aligned} \quad (\text{C.7})$$

The comparison is made at the bottom of the parent vessel, at $x = L$ and at the top of the daughter vessels, i.e. at their *local* $x = 0$. Using (C.7) in (10.80) gives the following self-similar expression for the input impedance.

$$Z(0, \omega) = \frac{ig^{-1} \sin(\omega L/c) + \cos(\omega L/c) / \left(\frac{\alpha^2}{Z(0, \alpha\omega)} + \frac{\beta^2}{Z(0, \beta\omega)} \right)}{\cos(\omega L/c) + ig \sin(\omega L/c) / \left(\frac{\alpha^2}{Z(0, \alpha\omega)} + \frac{\beta^2}{Z(0, \beta\omega)} \right)} \quad (\text{C.8})$$

It is only possible to derive an analytical solution for the root impedance of the structured tree for the unscaled tree, i.e. where $\alpha = \beta = 1$. However, a general solution can be found numerically. In the remainder of this chapter the analytical solution for $\alpha = \beta = 1$ is presented along with solution algorithms for the more general symmetric ($\alpha = \beta$) and asymmetric (all α 's and β 's) trees.

C.1 Case 1: Unscaled bifurcations, ($\alpha = \beta = 1$)

In this case the self-similar impedance is found by inserting $\alpha = \beta = 1$ in (C.8). Hence,

$$\begin{aligned} Z(0, \omega) &= \frac{ig^{-1} \sin(\omega L/c) + Z(0, \omega) \cos(\omega L/c)/2}{\cos(\omega L/c) + ig Z(0, \omega) \sin(\omega L/c)/2} \Leftrightarrow \\ g^2 Z(0, \omega)^2 - ig \frac{\cos(\omega L/c)}{\sin(\omega L/c)} Z(0, \omega) - 2 &= 0 \end{aligned} \quad (\text{C.9})$$

for $\omega L/c \neq p\pi$.

This equation only has a solution if $g \neq 0$ and it depends on $\omega L/c$. If $\omega L/c = p\pi$ then (C.9) gives $Z(0, p\pi) = 0$. Otherwise, if $\omega L/c \neq p\pi$, the solution to the quadratic equation depends on the sign of the discriminant. Equation (C.9) can be simplified by letting $\tilde{Z}(0, \omega) = gZ(0, \omega)$. This gives

$$\begin{aligned} \tilde{Z}(0, \omega)^2 - i \cot(\omega L/c) \tilde{Z}(0, \omega) - 2 &= 0 \quad \Leftrightarrow \\ \tilde{Z}(0, \omega) &= \frac{i \cot(\omega L/c)}{2} \pm \sqrt{2 - \frac{\cot^2(\omega L/c)}{4}} \end{aligned}$$

Reinserting the original $Z(0, \omega)$ gives the following solutions:

1. If the discriminant $2 - \cot^2(\omega L/c)/4 = 0$ the solution is purely imaginary and given by

$$Z(0, \omega) = \frac{i \cot(\omega L/c)}{2g}$$

2. If the discriminant $2 - \cot^2(\omega L/c)/4 < 0$ the solution is also purely imaginary and given by

$$Z(0, \omega) \tag{C.10}$$

$$= \frac{i \cot(\omega L/c)}{2g} \pm \frac{i}{g} \sqrt{\frac{\cot^2(\omega L/c)}{4} - 2}$$

$$= \frac{i}{2g} \left(\cot(\omega L/c) \pm |\cot(\omega L/c)| \sqrt{1 - \frac{8}{\cot^2(\omega L/c) - 2}} \right) \tag{C.11}$$

Since both P and Q are the Fourier transforms of real functions they must be self-adjoint, i.e.

$$P(x, \omega) = \overline{P(x, -\omega)}, \quad Q(x, \omega) = \overline{Q(x, -\omega)}$$

for all x .

The same applies for $Z(x, \omega)$. Furthermore, the solutions above must approach 0 as $\omega L/c \rightarrow p\pi$.

When $|\cot(\omega L/c)|$ is large (i.e. when $\omega L/c$ is close to $p\pi$) the square-root in (C.11) can be approximated to first order and the solution becomes

$$Z(0, \omega) \approx \frac{i}{2g} \left(\cot(\omega L/c) \pm |\cot(\omega L/c)| \left(1 - \frac{4}{\cot^2(\omega L/c)} \right) \right)$$

In order to figure out which solutions to pick two situations must be studied

- (a) For $\cot(\omega L/c) > 0$, that is where $\omega L/c \in \cup_{p \in \mathbb{Z}} [p\pi, (p + \frac{1}{2})\pi]$ the impedance becomes:

$$Z(0, \omega) = \frac{i}{2g} \cot(\omega L/c) \left(1 \pm \left(1 - \frac{4}{\cot^2(\omega L/c)} \right) \right)$$

If the solution with the plus sign is chosen $Z(0, \omega)$ does not converge to 0 as $\omega L/c \rightarrow p\pi$. However, if the negative solution is chosen, the impedance becomes

$$Z(0, \omega) = \frac{2i}{g} \tan(\omega L/c) = -\frac{2i}{g} \tan(-\omega L/c) \quad (\text{C.12})$$

which converges to zero as it is supposed to. Finally, this solution is self-adjoint as required.

- (b) For $\cot(\omega L/c) < 0$, i.e. $\omega L/c \in \cup_{p \in \mathbb{Z}} [(p + \frac{1}{2})\pi, p\pi]$ the impedance becomes:

$$Z(0, \omega) = \frac{i}{2g} \left(\cot(\omega L/c) \pm (-\cot(\omega L/c)) \left(1 - \frac{4}{\cot^2(\omega L/c)} \right) \right)$$

In this case the positive solution must be chosen in order for the two conditions to be fulfilled and in this case the solution obtained is the same as (C.12).

3. If the discriminant $2 - \cot^2(\omega x/c)/4 > 0$ the solution has both a real part and an imaginary part. Thus, the impedance is given by

$$Z(0, \omega) = \frac{i \cot(\omega L/c)}{2g} \pm \sqrt{2 - \frac{\cot^2(\omega L/c)}{4}} \quad (\text{C.13})$$

Because \cot is an odd function, this solution fulfills that

$$Z(0, \omega L/c) = \overline{Z(0, -\omega L/c)}$$

However, in order to get the right properties the positive solution must be chosen. This can be seen from the following rough analysis of the wave-equation in (C.4).

Assume that there is no reflected wave i.e. $p(x, t) = f(x - ct)$ then an explicit expression for the corresponding characteristic impedance can be found. Thus, the wave equation (C.4) gives

$$\begin{aligned} \frac{A_0}{\rho} \frac{\partial p(x, t)}{\partial x} &= \frac{\partial q(x, t)}{\partial t} \Leftrightarrow \\ -\frac{A_0}{\rho} f'(x - ct) &= \frac{\partial q(x, t)}{\partial t} \Leftrightarrow \\ q(x, t) &= \frac{A_0}{\rho c} p(x, t) \end{aligned}$$

This shows that $z(x, t) = p(x, t)/q(x, t) = \rho c/A_0$ is real and positive. Therefore, we assume that the real part of $Z(0, \omega)$ in the more general case discussed above should be positive too.

C.2 Case 2: Symmetric bifurcations, ($\alpha = \beta$)

Inserting $\alpha = \beta$ in (C.8) gives

$$Z(0, \omega) = \frac{ig^{-1} \sin(\omega L/c) + Z(0, \alpha\omega) \cos(\omega L/c)/(2\alpha^2)}{\cos(\omega L/c) + ig Z(0, \alpha\omega) \sin(\omega L/c)/(2\alpha^2)} \quad (\text{C.14})$$

Since the tree is symmetric the radius relation (6.1) gives

$$r_p^\xi = 2r_d^\xi = 2(\alpha r_p)^\xi \Leftrightarrow \alpha = \left(\frac{1}{2}\right)^{1/\xi}$$

This can also be seen from (6.4) and (6.4) because the geometry of the tree is self-similar.

It is now possible to determine $Z(0, \omega)$ using a recursive approach. This is done by predicting Z for smaller and smaller values of $\omega L/c$. When $\omega L/c$ becomes smaller than some given threshold some approximate value is assigned to Z . This approximation can be found by expanding Z in a series around $\omega = 0$. Let $Z(0, \omega) = h(\omega)$ then

$$Z(0, \omega) = h(\omega) = h(0) + h'(0)\omega + \mathcal{O}(\omega^2)$$

Assuming that $Z(0, \omega) = a\omega$ then

$$\begin{aligned} h(0) &= 0 \\ h'(0) &= \frac{iL}{cg} + \frac{Z'(0, \alpha\omega)}{2\alpha} \end{aligned}$$

Hence,

$$Z(0, \omega) = \frac{iL}{cg} \left(\frac{\omega}{1 - 1/(2\alpha)} \right) \quad (\text{C.15})$$

We have left out the computation for $h'(\omega)$ since it is rather messy. Since the algorithm for the asymmetric case is similar we refer to 3.

C.3 Case 3: Asymmetric bifurcations, ($\alpha \neq \beta$)

From (C.8) we had

$$Z(0, \omega) = \frac{ig^{-1} \sin(\omega L/c) + \cos(\omega L/c) / \left(\frac{\alpha^2}{Z(0, \alpha\omega)} + \frac{\beta^2}{Z(0, \beta\omega)} \right)}{\cos(\omega L/c) + ig \sin(\omega L/c) / \left(\frac{\alpha^2}{Z(0, \alpha\omega)} + \frac{\beta^2}{Z(0, \beta\omega)} \right)}$$

and from (6.1) we had

$$r_p^\xi = (\alpha r_p)^\xi + (\beta r_p)^\xi \Leftrightarrow 1 = \alpha^\xi + \beta^\xi$$

Using the asymmetry-relation (6.3) we get

$$(\alpha r_p)^2 = \gamma(\beta r_p)^2 \Leftrightarrow \alpha^2 = \gamma\beta^2$$

Hence,

$$(\gamma\beta^2)^{\xi/2} + \beta^\xi = 1 \quad \beta = (\gamma^{\xi/2} + 1)^{-1/\xi}$$

These correspond to the α and β found in Chapter 6. The algorithm follows the same approach as the symmetric case and in order to describe the recursive scheme we must again supply a stopping condition for small values of $\omega L/c$. In this case the expansion of $Z(0, \omega)$ in a series around $\omega = 0$ yields

$$Z(0, \omega) = h(\omega) = h(0) + h'(0)\omega + \mathcal{O}(\omega^2)$$

Hence,

$$Z(0, \omega) = \frac{iL}{cg} \left(\frac{\omega}{1 - \frac{1}{\alpha + \beta}} \right) \quad (\text{C.16})$$

As for the symmetric case the details are left out.

Algorithm 3: Determines $Z(0, \omega)$ for a self-similar asymmetric structured tree using a recursive scheme.

- For all allowed frequencies:
 - Determine α , β , and g .
 - If $\omega L/c < \epsilon$ set $Z(0, \omega)$ to the approximate value in (C.16).
 - Otherwise compute $Z(0, \alpha\omega)$ and $Z(0, \beta\omega)$ recursively.
 - Finally, determine $Z(0, \omega) = f(Z(0, \alpha\omega), Z(0, \beta\omega))$ using (C.8)

Appendix D

English summary

Several approaches can be used when modeling the arterial system. These range from simple Windkessel type models to advanced three-dimensional fluid dynamic models. This study is motivated by the need for a spatial and physiological, yet simple, model of the larger systemic arteries. The model should be used to evaluate and generate physiologically correct flow and pressure profiles for use in an anesthesia simulator. Thus, the aim of this dissertation was to develop a one-dimensional fluid dynamical model based on physiological principles for the larger systemic arteries showing that:

- The maximum pressure of the larger arteries increases away from the heart towards the periphery.
- The mean pressure of the smaller arteries drops according to the distribution of flow impedance of the vascular bed (Noordergraaf, 1978).
- The steepness of the incoming pressure profile increases towards the periphery.
- The reflected dicrotic wave separates from the incoming pressure wave and is more prominent at peripheral locations than at proximal locations.

We have constructed such a model by regarding the systemic arteries as a binary tree (the arterial tree) where each branch is represented by an elastic and tapering vessel. For each vessel flow and pressure are determined by solving Navier-Stokes equations for an incompressible Newtonian fluid (the blood) combined with a state equation relating pressure to cross-sectional area.

Arterial models for the larger arteries have been investigated earlier, see e.g. Anliker et al. (1971), Stettler et al. (1981), Lighthill (1989), or Pedley (1980). The basis for our approach follows the ideas outlined there. However, most of these models do not explicitly discuss how to derive a physiologically based boundary condition representing flow and pressure in the smaller arteries. Choosing an appropriate boundary condition is a central problem when modeling blood flow and pressure in the larger arteries. We have modeled the smaller arteries as asymmetric binary structured trees which are terminated when the radius of any vessel is less than some minimum radius modeling the peripheral resistance at the arteriolar level in a given organ. Then, the boundary condition for each terminal vessel of the larger arteries is determined by calculating the root impedance of the corresponding structured tree using a semi-analytical approach. In each vessel flow and pressure are found from an analytical

solution to a linearization of the viscous axisymmetric Navier-Stokes equations for an incompressible Newtonian fluid. This has provided a dynamical boundary condition reflecting the actual phase lag between flow and pressure as well as accommodated wave-propagation effects for the entire systemic arterial tree. The resulting model is physiologically adequate as well as computationally feasible.

The output from this model is pressure and flow profiles, averaged over the cross-sectional area of the vessels. These all exhibit the essential features characterizing the arterial pulse. This has been shown by comparisons to human as well as canine data. Furthermore, we have compared our model with two other models: a pure resistance model and Stergiopoulos' three element Windkessel model (Stergiopoulos et al., 1992). Our model essentially agrees with both the pure resistance model and the Windkessel model. In addition, it is able to predict observed high frequency oscillations for the impedance at the outflow boundaries. This is not possible with either of the simpler models. Based on these results, we have concluded that the structured tree is indeed a feasible boundary condition for determining flow and pressure in the larger arteries.

Appendix E

Resume på dansk

Blodstrømning og -tryk i de humane systemiske arterier kan modelleres ved brug af et bredt spektrum af forskellige principper varierende fra simple vindkeddelmodeller til avancerede tredimensionelle strømningsmodeller. Motivationen for denne afhandling er behovet for en model der kan beregne blodstrømning og -tryk for de store systemiske arterier. Den skal både have en rummelig udstrækning og være fysiologisk korrekt. Samtidigt skal den være tilstrækkelig simpel således at den i et realistisk tidsrum kan beregnes på en computer. Formålet med denne model er, at den skal kunne anvendes som reference model for tilsvarende men simplere modeller i en anæstesisimulator, idet den skal bruges til at evaluere og generere fysiologisk korrekte profiler for blodstrømning og -tryk i de store systemiske arterier. Formålet med denne afhandling har derfor været at udvikle en endimensional model for de store systemiske arterier baseret på fysiologiske principper. Den skal kunne vise at

- det maksimale blodtryk for de store arterier stiger distalt fra hjertet.
- middelblodtrykket for de systemiske arterier falder proksimalt fra hjertet.
- stigningen af den indkomne trykbølge øges distalt fra hjertet.
- den reflekterede bølge adskilles fra den indkomne bølge og bliver tydeligere distalt fra hjertet.

Vi har udviklet en model ved at betragte de systemiske arterier som et binært træ (det arterielle træ), hvori de enkelte grene er elastiske og snævres ind distalt fra hjertet. For hvert rør er blodstrømningen og -trykket bestemt fra løsninger til Navier-Stokes ligninger for en usammentrykkelig væske kombineret med en ligning, som relaterer blodtrykket til tværsnitsarealet af røret.

Sådanne modeller er blevet studeret tidligere, se f.eks. (Anliker et al., 1971; Lighthill, 1989; Pedley, 1980). Udgangspunktet for vores model hviler på disse arbejder. De fleste af disse tidligere modeller beskriver dog ikke, hvordan fysiologisk baserede randbetingelser, som udgør de små arterier, skal modelleres.

Dette er et centralt problem i forbindelse med modellering af blodstrømning og -tryk i de store arterier. Vi har antaget at de små arterier kan modelleres som asymmetriske binære strukturerede træer som bliver termineret når radius for alle rørene er mindre end en given minimum radius, som repræsenterer den perifere modstand i

arteriolerne i et givet organ. Randbetingelsen for hver terminal for de store arterier er modelleret ved at beregne impedancen i roden af de strukturerede træer. Rodimpedancen i de enkelte rør er så fundet ved at løse (analytisk) en lineariseret version af de viskøse Navier-Stokes ligninger for en usammentrykkelig Newtonsk væske. Dette har resulteret i en dynamisk randbetingelse som dels kan vise faseforskydningen mellem blodstrømningen og -trykket og dels tager højde for de fænomener, der er et resultat af bølgeudbredelse gennem det arterielle træ. På grund af vores behandling af de små arterier i et struktureret træ er det lykkedes os at udvikle en model, som er både fysiologisk korrekt men som også er mulig at bearbejde numerisk.

Resultatet fra vores beregninger er blodstrømnings og -tryk profiler som et gennemsnit over tværsnitsarealet af rørene. Disse viser alle de fænomener som karakteriserer pulsølgen. Vi har vist at vores model er korrekt; dels ved at sammenligne den med data fra både mennesker og hunde og dels ved at sammenligne den med en ren modstands model og med Stergiopulos et al. (1992) vindkeddemodel. Sammenligningerne viste at vores model kunne beskrive højfrekvente oscillationer for impedancen, hvilket ikke er muligt ved brug af de simple modeller. Derfor kan vi konkludere at vores randbetingelse, som modellerer de små arterier ved at se dem som et struktureret træ, er fysiologisk korrekt og kan bruges i praksis.

Bibliography

- Anliker, M., Rockwell, R. and Ogden, E. (1971). Nonlinear analysis of flow pulses and shock waves in arteries, *ZAMP* **22**: 217–246.
- Anliker, M., Stettler, J., Niederer, P. and Holenstein, R. (1978). Prediction of shape changes of propagating flow and pressure pulses in human arteries, in R. Bauer and R. Busse (eds), *Dynamics, Control Theory and Regulation*, Symposium in Erlangen, 28–30 October 1977, Springer Verlag, New York, USA, pp. 15–34.
- Atabek, H. (1968). Wave propagation through a viscous fluid contained in a tethered, initially stressed, orthotropic elastic tube, *Biophys J* **8**: 626–649.
- Atabek, H. and Lew, H. (1966). Wave propagation through a viscous incompressible fluid contained in an initially stressed elastic tube, *Biophys J* **6**: 481–503.
- Barnard, A., Hunt, W., Timlake, W. and Varley, E. (1966). A theory of fluid flow in compliant tubes, *Biophys J* **6**: 717–724.
- Bassingthwaighe, J., Liebovitch, L. and West, B. (1994). *Fractal Physiology*, The American Physiological Society Methods in Physiology Series, Oxford University Press, New York, USA.
- Batchelor, G. (1992). *Fluid Dynamics*, Cambridge University Press, Cambridge, G.B.
- Belardinelli, E. and Cavalcanti, S. (1992). Theoretical analysis of pressure pulse propagation in arterial vessels, *J Biomech* **25**(1): 1337–1349.
- Bergel, D. (1972). *Cardiovascular Fluid Dynamics*, Vol. 2, Academic Press, London, G.B.
- Berger, S. (1993). Flow in large blood vessels, *Contemp Math* **141**: 479–518.
- Boyer, C. (1989). *A History of Mathematics*, second edn, John Wiley & Sons, New York, USA.
- Caffisch, R., Majda, G., Peskin, C. and Strumolo, G. (1980). Distortion of the arterial pulse, *Math Biosci* **51**: 229–260.
- Caro, C., Pedley, T., Schroter, R. and Seed, W. (1978). *The Mechanics of the Circulation*, Oxford University Press, Oxford, G.B.
- Courant, R., Friedrichs, K. and Lewy, H. (1928). Über die partiellen differenzengleichungen der mathematischen physik, *Mathematische Annalen* **100**: 32–74.

- Crombie, A. (1961). *Augustine to Galileo, Volume 1*, Mercury Books, London, G.B.
- Dawber, T., Thomas, H. and McNamara, P. (1973). Characteristics of the dicrotic notch of the arterial pulse wave in coronary heart disease, *Angiology* **24**(4): 244–255.
- Fishman, A. and Richards, D. (1964). *Circulation of the Blood, Men and Ideas*, Oxford University Press, New York, USA.
- Forbes, L. (1981). On the evolution of shock-waves in mathematical models of the aorta, *Aust Math Soc (B)* **22**: 257–269.
- Fung, Y. (1996). *Biomechanics, Circulation*, second edn, Springer Verlag, New York, USA.
- Gaba, D. and DeAnda, A. (1988). A comprehensive anesthesia simulation environment: Re-creating the operating room for research and training, *Anesthesiology* **69**: 387–394.
- Gerrad, J. (1985). An experimental test of the theory of waves in fluid filled deformable tubes, *J Fluid Mech* **156**: 321–347.
- Gerrard, J. (1981). The effect of the skin friction on the solution of the one-dimensional equations of pulsatile flow in distensible tubes, *Med Biol Eng Comput* **19**: 79–82.
- Gizdulich, P. and Wesseling, K. (1988). Forearm arterial pressure-volume relationships in man, *Clin Phys Physiol Meas* **9**: 123–132.
- Gregg, D. (1966). Dynamics of blood and lymph flow, in C. Best and N. Taylor (eds), *The Physiological Basis of Medical Practice*, eighth edn, Williams and Wilkins, New York, USA.
- Griffith, T. and Edwards, D. (1990). Basal EDRF activity helps to keep the geometrical configuration of arterial bifurcations close to the murray optimum, *J Theor Biol* **146**: 545–573.
- Guyton, A. (1991). *Textbook of Medical Physiology*, eighth edn, W.B. Saunders Company, Philadelphia, USA.
- Holenstein, R., Nerem, R. and Niederer, P. (1984). On the propagation of a wave front in viscoelastic arteries, *J Biomech Eng* **106**: 115–122.
- Holenstein, R., Niederer, P. and Anliker, M. (1980). A viscoelastic model for use in predicting arterial pulse waves, *J Biomech Eng* **102**: 318–325.
- Horsfield, K. and Thurlbeck, A. (1981). Relation between diameter and flow in branches of the bronchial tree, *Bull Math Biol* **43**: 681–691.
- Horsfield, K. and Woldenberg, M. (1989). Diameters and cross-sectional areas of branches in the human pulmonary arterial tree, *Anat Rec* **223**: 245–251.
- Horsten, J., Steenhoven, A. V. and Dongen, M. V. (1989). Linear propagation of pulsatile waves in viscoelastic tubes, *J Biomech* **22**: 477–484.

- Iberall, A. (1967). Anatomy and steady flow characteristics of the arterial system with an introduction to its pulsatile characteristics, *Math Biosci* **1**: 375–385.
- Jensen, P. (1994–1998). Department of Anaesthesiology, Copenhagen University Hospital, Rigshospitalet, Denmark. Personal Communication.
- Jensen, P. (1997). *Development of a Methodology for Cognitive Analysis of Critical Incidents in Anaesthesia*, PhD thesis, Department of Anesthesia, Herlev University Hospital, University of Copenhagen, Denmark.
- Jones, E. (1973). A mathematical model for nonlinear analysis of flow pulses utilizing an integral technique, *ZAMP* **24**: 565–580.
- Kamiya, A., Ando, J., Shibata, M. and Masuda, H. (1988). Roles of fluid shear stress in physiological regulation of vascular structure and function, *Biorheology* **25**: 271–278.
- Kamiya, A. and Togawa, T. (1972). Optimal branching structure of the vascular tree, *Bull Math Biophys* **34**: 431–438.
- Karlson, M. (1995). Modelling and simulation of the human arterial tree – a combined lumped-parameter and transmission line element approach, in H. Power and R. Hart (eds), *Computer Simulations in Biomedicine*, Computational Mechanics Publications, Southampton, G.B., pp. 11–17.
- Kassab, G. and Fung, Y. (1995). The pattern of coronary arteriolar bifurcations and the uniform shear hypothesis, *Ann Biomech Eng* **23**: 13–20.
- Kassab, G., Rider, C., Tang, N. and Fung, Y. (1993). Morphometry of pig coronary arterial trees, *Am J Physiol* **265**: H350–H365.
- Ku, D. (1997). Blood flow in arteries, *Ann Rev Fluid Mech* **29**: 399–434.
- Lambert, J. (1958). On the nonlinearities of fluid flow in nonrigid tubes, *J Franklin Inst* **266**: 84–102.
- Landau, L. and Lifshitz, E. (1986). *Theory of Elasticity*, Vol. 7 of *Course of Theoretical Physics*, third edn, Pergamon Press, Oxford, G.B.
- Langewouters, G., Wesseling, K. and Goedhard, W. (1984). The static elastic properties of 45 human thoracic and 20 abdominal aortas in vitro and the parameters of a new model, *J Biomech* **17**(6): 425–435.
- Laurent, S., Hayoz, D., Trazzi, S., Boutouyrie, P., Waeber, B., Omboni, S., Brunner, H., Mancia, G. and Safar, M. (1993). Isobaric compliance of the radial artery is increased in patients with essential hypertension, *J Hypertens* **11**: 89–98.
- Lax, H. and Feinberg, A. (1959). Abnormalities of the arterial pulse wave in young diabetic subjects, *Circulation* **20**: 1106–1110.
- Lax, H., Feinberg, A. and Cohen, B. (1956). The normal pulse wave and its modification in the presence of human atherosclerosis, *J Chronic Dis* **3**: 618–631.

- Li, J.-J. (1987). *Arterial System Dynamics*, Biomedical Engineering Series, New York University Press, New York, USA.
- Lighthill, J. (1989). *Mathematical Biofluidynamics*, third printing edn, Society for Industrial and Applied Mathematics, Philadelphia, USA.
- Mazumdar, J. (1989). *An Introduction to Mathematical Physiology and Biology*, Cambridge University Press, Cambridge, G.b.
- McDonald, D. (1974). *Blood Flow in Arteries*, second edn, Edward Arnold, London, G.B.
- Milnor, W. (1982). *Hemodynamics*, Williams & Wilkins, New York, USA.
- Murray, C. (1926a). The physiological principle of minimum work. I. the vascular system and the cost of blood volume, *Proc Nat Acad Sci* **12**: 207–214.
- Murray, C. (1926b). The physiological principle of minimum work. II. oxygen exchange in capillaries, *Proc Nat Acad Sci* **12**: 299–304.
- Nichols, W. and O'Rourke, M. (1998). *McDonald's Blood Flow in Arteries*, fourth edn, Edward Arnold, London, G.B.
- Niederer, P. (1985). Damping mechanisms and shock-like transitions in the human arterial tree, *ZAMP* **36**: 204–220.
- Noordergraaf, A. (1978). *Circulatory System Dynamics*, Academic Press, San Diego, USA.
- Ockendon, H. and Ockendon, J. (1995). *Viscous Flow*, Cambridge texts in applied mathematics, Cambridge University Press, Cambridge, G.b.
- Oka, S. and Nakai, M. (1987). Optimality principle in vascular bifurcation, *Biorheology* **24**: 737–751.
- Olsen, J. and Shapiro, A. (1967). Large-amplitude unsteady flow in liquid-filled elastic tubes, *J Fluid Mech* **29**: 513–538.
- Olufsen, M. (1997a). A one-dimensional fluid dynamic model of the systemic arteries, in J. Ottesen and M. Danielsen (eds), *Proceedings from Mathematical Modelling in Medicine, September 1997, Roskilde University*, Roskilde University Press, Denmark. In press.
- Olufsen, M. (1997b). A structured tree outflow condition for arterial blood flow in the larger systemic arteries. Submitted to *Am J Physiol*.
- Olufsen, M. (1998). Numerical solutions to arterial blood flow in the larger systemic arteries with a structured tree boundary condition. Will be submitted to *Comp Biol Med*.
- Olufsen, M., Nielsen, F., Jensen, P. and Pedersen, S. (1994). The models underlying the simulator sophus, *Technical report*, IMFUFA, Roskilde University, Denmark. Text No. 278.

- Olufsen, M. and Ottesen, J. (1995a). Fluid-dynamical model of the aorta with bifurcations, *Technical report*, IMFUFA, Roskilde University, Denmark. Text No. 297.
- Olufsen, M. and Ottesen, J. (1995b). Outflow conditions in human arterial flow, in H. Power and R. Hart (eds), *Computer Simulations in Biomedicine*, Computational Mechanics Publications, Southampton, G.B., pp. 249–256.
- O'Rourke, M., Kelly, R. and Avolio, A. (1992). *The Arterial Pulse*, Lea & Febiger, Philadelphia, USA.
- Papageorgiou, G., Jones, B., Redding, V. and Hudson, N. (1990). The area ratio of normal arterial junctions and its implications in pulse wave reflections, *Cardiovasc Res* **24**: 478–484.
- Pedersen, E. (1993). *In Vitro and In Vivo Studies of blood flow in the Normal Abdominal Aorta and Aorta bifurcation (in Danish)*, PhD thesis, Department of Cardiothoracic and Vascular Surgery and Institute for Experimental Clinical Research, Århus University Hospital, Skejby, Denmark.
- Pedersen, E. (1997). Department of Thoracic Surgery, Skejby University Hospital, Denmark. Personal Communication.
- Pedley, T. (1980). *The Fluid Mechanics of Large Blood Vessels*, Cambridge University Press, Cambridge, G.B.
- Peskin, C. (1976). *Partial Differential Equations in Biology*, Courant Institute of Mathematical Sciences, New York University, USA.
- Pollanen, M. (1992). Dimensional optimization at different levels at the arterial hierarchy, *J Theor Biol* **159**: 267–270.
- Press, W., Teukolsky, S., Vetterling, W. and Flannery, B. (1989). *Numerical Recipes in Pascal – The Art of Scientific Computing*, Cambridge University Press.
- Raines, J., Jaffrin, M. and Shapiro, A. (1974). A computer simulation of arterial dynamics in the human leg, *J Biomech* **7**: 77–91.
- Reuderink, P., Hoogstraten, H., Sipkema, P., Hillen, B. and Westerhof, N. (1989). Linear and nonlinear one-dimensional models of pulse wave transmission at high womersley numbers, *J Biomech* **22**: 819–827.
- Rockwell, R., Anliker, M. and Elsner, J. (1974). Model studies of the pressure and flow pulses in a viscoelastic arterial conduit, *J Franklin Inst* **297**: 405–427.
- Rodkiewicz, C. (1983). *Arteries and Arterial Blood Flow, Biological and Physiological Aspects*, CIMS Courses and Lecture Notes no. 270, Springer Verlag, New York, USA.
- Rossitti, S. and Löfgren, J. (1993). Vascular dimensions of the cerebral arteries follow the principle of minimum work, *Stroke* **24**: 371–377.

- Roy, A. and Woldenberg, M. (1982). A generalization of the optimal models of arterial branching, *Bull Math Biol* **44**: 349–360.
- Schaaf, B. and Abbrecht, P. (1972). Digital computer simulation of human systemic arterial pulse wave transmission: A nonlinear model, *J Biomech* **5**: 345–364.
- Schreiner, W. (1993). Computer generation of complex arterial tree models, *J Biomech Eng* **15**: 148–150.
- Schreiner, W. and Buxbaum, P. (1993). Computer-optimization of vascular trees, *J Biomed Eng* **40**: 482–490.
- Schreiner, W., Neumann, F., Neumann, M., End, A., Roedler, S. and Aharinejad, S. (1995). The influence of optimization target selection on the structure of arterial tree models generated by constrained constructive optimization, *J Gen Physiol* **106**: 583–599.
- Schreiner, W., Neumann, M., Neumann, F., Roedler, S., End, A., Buxbaum, P., Muller, M. and Spieckermann, P. (1994). The branching angles in computer-generated optimized models of arterial trees, *J Gen Physiol* **103**: 976–989.
- Segers, P., Dubois, F., DeWachter, D. and Verdonck, P. (1997). Role and relevancy of a cardiovascular simulator, *To appear in J Cardiovasc Eng*.
- Shapiro, A. (1977). Steady flow in collapsible tubes, *J Biomech Eng* pp. 126–147.
- Solomon, E., Smidt, R. and Adragna, P. (1990). *Human Anatomy & Physiology*, second international edn, Saunders College Publishing, Philadelphia, USA.
- Steenhoven, A. V. and Dongen, M. V. (1986). Model studies of the aortic pressure rise just after valve closure, *J Fluid Mech* **166**: 93–113.
- Stergiopulos, N., Young, D. and Rogge, T. (1992). Computer simulation of arterial flow with applications to arterial and aortic stenosis, *J Biomech* **25**: 1477–1488.
- Stettler, J., Niederer, P. and Anliker, M. (1981). Theoretical analysis of arterial hemodynamics including the influence of bifurcations, part I: Mathematical model and prediction of normal pulse patterns, *Ann Biomech Eng* **9**: 145–164.
- Stoer, J. and Bulirsch, R. (1980). *Introduction to Numerical Analysis*, Springer-Verlag, New York, USA.
- Streeter, V., Keitzer, W. and Bohr, D. (1963). Pulsatile pressure and flow through distensible vessels, *Circ Res* **13**(3): 3–20.
- Tardy, Y., Meiseter, J., Perret, F., Brunner, H. and Arditi, M. (1991). Non-invasive estimate of the mechanical properties of peripheral arteries from ultrasonic and photoplethysmographic measurements, *Clin Phys Physiol Meas* **12**: 39–54.
- Taylor, L. and Gerrard, J. (1977). Pressure-radius relationships for elastic tubes and their application to arteries: Part 1 - theoretical relationships, *Med Biol Eng Comput* **15**: 11–17.

Liste over tidligere udkomne tekster
tilsendes gerne. Henvendelse herom kan
ske til IMFUFA's sekretariat
tlf. 46 75 77 11 lokal 2263

-
- 217/92 "Two papers on APPLICATIONS AND MODELLING
IN THE MATHEMATICS CURRICULUM"
by: Mogens Niss
- 218/92 "A Three-Square Theorem"
by: Lars Kadison
- 219/92 "RUPNOK - stationær strømning i elastiske rør"
af: Anja Boisen, Karen Birkelund, Mette Olufsen
Vejleder: Jesper Larsen
- 220/92 "Automatisk diagnosticering i digitale kredsløb"
af: Bjørn Christensen, Ole Møller Nielsen
Vejleder: Stig Andur Pedersen
- 221/92 "A BUNDLE VALUED RADON TRANSFORM, WITH
APPLICATIONS TO INVARIANT WAVE EQUATIONS"
by: Thomas P. Branson, Gestur Olafsson and
Henrik Schlichtkrull
- 222/92 On the Representations of some Infinite Dimensional
Groups and Algebras Related to Quantum Physics
by: Johnny T. Ottesen
- 223/92 THE FUNCTIONAL DETERMINANT
by: Thomas P. Branson
- 224/92 UNIVERSAL AC CONDUCTIVITY OF NON-METALLIC SOLIDS AT
LOW TEMPERATURES
by: Jeppe C. Dyre
- 225/92 "HATMODELLEN" Impedansspektroskopi i ultrarent
en-krystallinsk silicium
af: Anja Boisen, Anders Gorm Larsen, Jesper Varmer,
Johannes K. Nielsen, Kit R. Hansen, Peter Bøggild
og Thomas Hougaard
Vejleder: Petr Viscor
- 226/92 "METHODS AND MODELS FOR ESTIMATING THE GLOBAL
CIRCULATION OF SELECTED EMISSIONS FROM ENERGY
CONVERSION"
by: Bent Sørensen
- 227/92 "Computersimulering og fysik"
af: Per M.Hansen, Steffen Holm,
Peter Maibom, Mads K. Dall Petersen,
Pernille Postgaard, Thomas B.Schrøder,
Ivar P. Zeck
Vejleder: Peder Voetmann Christiansen
- 228/92 "Teknologi og historie"
Fire artikler af:
Mogens Niss, Jens Høyrup, Ib Thiersen,
Hans Hedal
- 229/92 "Masser af information uden betydning"
En diskussion af informationsteorien
i Tor Nørretranders' "Mærk Verden" og
en skitse til et alternativ baseret
på andenordens kybernetik og semiotik.
af: Søren Brier
- 230/92 "Vinklens tredeling - et klassisk
problem"
et matematisk projekt af
Karen Birkelund, Bjørn Christensen
Vejleder: Johnny Ottesen
- 231A/92 "Elektrondiffusion i silicium - en
matematisk model"
af: Jesper Voetmann, Karen Birkelund,
Mette Olufsen, Ole Møller Nielsen
Vejledere: Johnny Ottesen, H.B.Hansen
- 231B/92 "Elektrondiffusion i silicium - en
matematisk model" Kildetekster
af: Jesper Voetmann, Karen Birkelund,
Mette Olufsen, Ole Møller Nielsen
Vejledere: Johnny Ottesen, H.B.Hansen
- 232/92 "Undersøgelse om den simultane opdagelse
af energiens bevarelse og isærdeles om
de af Mayer, Colding, Joule og Helmholtz
udførte arbejder"
af: L.Arleth, G.I.Dybkjær, M.T.Østergård
Vejleder: Dorte Posselt
- 233/92 "The effect of age-dependent host
mortality on the dynamics of an endemic
disease and
Instability in an SIR-model with age-
dependent susceptibility
by: Viggo Andreasen
- 234/92 "THE FUNCTIONAL DETERMINANT OF A FOUR-DIMENSIONAL
BOUNDARY VALUE PROBLEM"
by: Thomas P. Branson and Peter B. Gilkey
- 235/92 OVERFLADESTRUKTUR OG POREUDVIKLING AF KOKS
- Modul 3 fysik projekt -
af: Thomas Jessen
-

- 236a/93 INTRODUKTION TIL KVANTE
HALL EFFEKTEN
af: Anja Boisen, Peter Bøggild
Vejleder: Peder Voetmann Christiansen
Erland Brun Hansen
- 236b/93 STRØMSSAMMENBRUD AF KVANTE
HALL EFFEKTEN
af: Anja Boisen, Peter Bøggild
Vejleder: Peder Voetmann Christiansen
Erland Brun Hansen
- 237/93 The Wedderburn principal theorem and
Shukla cohomology
af: Lars Kadison
- 238/93 SEMIOTIK OG SYSTEMEGENSKABER (2)
Vektorbånd og tensorer
af: Peder Voetmann Christiansen
- 239/93 Valgsystemer - Modelbygning og analyse
Matematik 2. modul
af: Charlotte Gjerrild, Jane Hansen,
Maria Hermannsson, Allan Jørgensen,
Ragna Clauson-Kaas, Poul Lützen
Vejleder: Mogens Niss
- 240/93 Patologiske eksempler.
Om sære matematiske fiske betydning for
den matematiske udvikling
af: Claus Dræby, Jørn Skov Hansen, Runa
Ulsøe Johansen, Peter Meibom, Johannes
Kristoffer Nielsen
Vejleder: Mogens Niss
- 241/93 FOTOVOLTAISK STATUSNOTAT 1
af: Bent Sørensen
- 242/93 Brovedligeholdelse - bevar mig vel
Analyse af Vejdirektoratets model for
optimering af broreparationer
af: Linda Kyndlev, Kare Fundal, Kamma
Tulinus, Ivar Zeck
Vejleder: Jesper Larsen
- 243/93 TANKEEKSPERIMENTER I FYSIKKEN
Et 1.modul fysikprojekt
af: Karen Birkelund, Stine Sofia Korremann
Vejleder: Dorte Posselt
- 244/93 RADONTRANSFORMATIONEN og dens anvendelse
i CT-scanning
Projektrapport
af: Trine Andreassen, Tine Guldager Christiansen,
Nina Skov Hansen og Christine Iversen
Vejledere: Gestur Olafsson og Jesper Larsen
- 245a+b
/93 Time-Of-Flight målinger på krystallinske
halvledere
Specialerapport
af: Linda Szkotak Jensen og Lise Odgaard Gade
Vejledere: Petr Viscor og Niels Boye Olsen
- 246/93 HVERDAGSVIDEN OG MATEMATIK
- LÆREPROCESSER I SKOLEN
af: Lena Lindenskov, Statens Humanistiske
Forskningsråd, RUC, IMFUFA
- 247/93 UNIVERSAL LOW TEMPERATURE AC CON-
DUCTIVITY OF MACROSCOPICALLY
DISORDERED NON-METALS
by: Jeppe C. Dyre
- 248/93 DIRAC OPERATORS AND MANIFOLDS WITH
BOUNDARY
by: B. Booss-Bavnbek, K.P.Wojciechowski
- 249/93 Perspectives on Teichmüller and the
Jahresbericht Addendum to Schappacher,
Scholz, et al.
by: B. Booss-Bavnbek
With comments by W.Abikoff, L.Ahlfors,
J.Cerf, P.J.Davis, W.Fuchs, F.P.Gardiner,
J.Jost, J.-P.Kahane, R.Lohan, L.Lorch,
J.Radkau and T.Söderqvist
- 250/93 EULER OG BOLZANO - MATEMATISK ANALYSE SET I ET
VIDENSKABSTEORETISK PERSPEKTIV
Projektrapport af: Anja Juul, Lone Michelsen,
Tomas Højgård Jensen
Vejleder: Stig Andur Pedersen
- 251/93 Genotypic Proportions in Hybrid Zones
by: Freddy Bugge Christiansen, Viggo Andreassen
and Ebbe Thue Poulsen
- 252/93 MODELLERING AF TILFÆLDIGE FÆNOMENER
Projektrapport af: Birthe Friis, Lisbeth Helmgård,
Kristina Charlotte Jakobsen, Marina Mosbæk
Johannessen, Lotte Ludvigsen, Mette Hass Nielsen
- 253/93 Kuglepakning
Teori og model
af: Lise Arleth, Kåre Fundal, Nils Kruse
Vejleder: Mogens Niss
- 254/93 Regressionsanalyse
Materiale til et statistikkursus
af: Jørgen Larsen
- 255/93 TID & BETINGET UAFHÆNGIGHED
af: Peter Harremoës
- 256/93 Determination of the Frequency Dependent
Bulk Modulus of Liquids Using a Piezo-
electric Spherical Shell (Preprint)
by: T. Christensen and N.B.Olsen
- 257/93 Modelling af dispersion i piezoelektriske
keramikker
af: Pernille Postgaard, Jannik Rasmussen,
Christina Specht, Mikko Østergård
Vejleder: Tage Christensen
- 258/93 Supplerende kursusmateriale til
"Lineære strukturer fra algebra og analyse"
af: Mogens Brun Heefelt
- 259/93 STUDIES OF AC HOPPING CONDUCTION AT LOW
TEMPERATURES
by: Jeppe C. Dyre
- 260/93 PARTITIONED MANIFOLDS AND INVARIANTS IN
DIMENSIONS 2, 3, AND 4
by: B. Booss-Bavnbek, K.P.Wojciechowski

- 261/93 OPGAVESAMLING
Bredde-kursus i Fysik
Eksamensopgaver fra 1976-93
- 262/93 Separability and the Jones Polynomial
by: Lars Kadison
- 263/93 Supplerende kursusmateriale til "Lineære strukturer fra algebra og analyse" II
af: Mogens Brun Heefelt
- 264/93 FOTOVOLTAISK STATUSNOTAT 2
af: Bent Sørensen
-
- 265/94 SPHERICAL FUNCTIONS ON ORDERED SYMMETRIC SPACES
To Sigurdur Helgason on his sixtyfifth birthday
by: Jacques Faraut, Joachim Hilgert and Gestur Olafsson
- 266/94 Kommensurabilitets-oscillationer i laterale supergitre
Fysikspeciale af: Anja Boisen, Peter Bøggild, Karen Birkelund
Vejledere: Rafael Taboryski, Poul Erik Lindelof, Peder Voetmann Christiansen
- 267/94 Kom til kort med matematik på Eksperimentarium - Et forslag til en opstilling
af: Charlotte Gjerrild, Jane Hansen
Vejleder: Bernhelm Booss-Bavnbek
- 268/94 Life is like a sewer ...
Et projekt om modellering af aorta via en model for strømning i kloakrør
af: Anders Marcussen, Anne C. Nilsson, Lone Michelsen, Per M. Hansen
Vejleder: Jesper Larsen
- 269/94 Dimensionsanalyse en introduktion metaprojekt, fysik
af: Tine Guldager Christiansen, Ken Andersen, Nikolaj Hermann, Jannik Rasmussen
Vejleder: Jens Højgaard Jensen
- 270/94 THE IMAGE OF THE ENVELOPING ALGEBRA AND IRREDUCIBILITY OF INDUCED REPRESENTATIONS OF EXPONENTIAL LIE GROUPS
by: Jacob Jacobsen
- 271/94 Matematikken i Fysikken.
Opdaget eller opfundet
NAT-BAS-projekt
vejleder: Jens Højgaard Jensen
- 272/94 Tradition og fornyelse
Det praktiske elevarbejde i gymnasiets fysikundervisning, 1907-1988
af: Kristian Hoppe og Jeppe Guldager
Vejledning: Karin Beyer og Nils Hybel
- 273/94 Model for kort- og mellemdistanceløb
Verifikation af model
af: Lise Fabricius Christensen, Helle Pilemann, Bettina Sørensen
Vejleder: Mette Olufsen
- 274/94 MODEL 10 - en matematisk model af intravenøse anæstetikas farmakokinetik
3. modul matematik, forår 1994
af: Trine Andreasen, Bjørn Christensen, Christine Green, Anja Skjoldborg Hansen, Lisbeth Helmgård
Vejledere: Viggo Andreasen & Jesper Larsen
- 275/94 Perspectives on Teichmüller and the Jahresbericht 2nd Edition
by: Bernhelm Booss-Bavnbek
- 276/94 Dispersionsmodellering
Projektrapport 1. modul
af: Gitte Andersen, Rehannah Borup, Lisbeth Friis, Per Gregersen, Kristina Vejre
Vejleder: Bernhelm Booss-Bavnbek
- 277/94 PROJEKTARBEJDSPÆDAGOGIK - Om tre tolkninger af problemorienteret projektarbejde
af: Claus Flensted Behrens, Frederik Voetmann Christiansen, Jørn Skov Hansen, Thomas Thingstrup
Vejleder: Jens Højgaard Jensen
- 278/94 The Models Underlying the Anaesthesia Simulator Sophus
by: Mette Olufsen(Math-Tech), Finn Nielsen (RISØ National Laboratory), Per Føge Jensen (Herlev University Hospital), Stig Andur Pedersen (Roskilde University)
- 279/94 Description of a method of measuring the shear modulus of supercooled liquids and a comparison of their thermal and mechanical response functions.
af: Tage Christensen
- 280/94 A Course in Projective Geometry
by Lars Kadison and Matthias T. Kromann
- 281/94 Modellering af Det Cardiovasculære System med Neural Puls kontrol
Projektrapport udarbejdet af:
Stefan Frello, Runa Ulsøe Johansen, Michael Poul Curt Hansen, Klaus Dahl Jensen
Vejleder: Viggo Andreasen
- 282/94 Parallelle algoritmer
af: Erwin Dan Nielsen, Jan Danielsen, Niels Bo Johansen

- 283/94 Grænser for tilfældighed
(en kaotisk talgenerator)
af: Erwin Dan Nielsen og Niels Bo Johansen
- 284/94 Det er ikke til at se det, hvis man ikke
lige ve' det!
Gymnasie matematikkens begrundelsesproblem
En specialerapport af Peter Hauge Jensen
og Linda Kyndlev
Vejleder: Mogens Niss
- 285/94 Slow coevolution of a viral pathogen and
its diploid host
by: Viggo Andreasen and
Freddy B. Christiansen
- 286/94 The energy master equation: A low-temperature
approximation to Bässler's random walk model
by: Jeppe C. Dyre
- 287/94 A Statistical Mechanical Approximation for the
Calculation of Time Auto-Correlation Functions
by: Jeppe C. Dyre
- 288/95 PROGRESS IN WIND ENERGY UTILIZATION
by: Bent Sørensen
- 289/95 Universal Time-Dependence of the Mean-Square
Displacement in Extremely Rugged Energy
Landscapes with Equal Minima
by: Jeppe C. Dyre and Jacob Jacobsen
- 290/95 Modellering af uregelmæssige bølger
Et 3.modul matematik projekt
af: Anders Marcussen, Anne Charlotte Nilsson,
Lone Michelsen, Per Mørkegaard Hansen
Vejleder: Jesper Larsen
- 291/95 1st Annual Report from the project
LIFE-CYCLE ANALYSIS OF THE TOTAL DANISH
ENERGY SYSTEM
an example of using methods developed for the
OECD/IEA and the US/EU fuel cycle externality study
by: Bent Sørensen
- 292/95 Fotovoltaisk Statusnotat 3
af: Bent Sørensen
- 293/95 Geometridiskussionen - hvor blev den af?
af: Lotte Ludvigsen & Jens Frandsen
Vejleder: Anders Madsen
- 294/95 Universets udvidelse -
et metaprojekt
Af: Jesper Duelund og Birthe Friis
Vejleder: Ib Lundgaard Rasmussen
- 295/95 A Review of Mathematical Modeling of the
Controlled Cardiovascular System
By: Johnny T. Ottesen
- 296/95 RETIKULER den klassiske mekanik
af: Peder Voetmann Christiansen
- 297/95 A fluid-dynamical model of the aorta with
bifurcations
by: Mette Olufsen and Johnny Ottesen
- 298/95 Mordet på Schrödingers kat - et metaprojekt om
to fortolkninger af kvantemekanikken
af: Maria Hermannsson, Sebastian Horst,
Christina Specht
Vejledere: Jeppe Dyre og Peder Voetmann Christiansen
- 299/95 ADAM under figenbladet - et kig på en samfunds-
videnskabelig matematisk model
Et matematisk modelprojekt
af: Claus Draby, Michael Hansen, Tomas Højgård Jensen
Vejleder: Jørgen Larsen
- 300/95 Scenarios for Greenhouse Warming Mitigation
by: Bent Sørensen
- 301/95 TOK Modellering af træers vækst under påvirkning
af ozon
af: Glenn Møller-Holst, Marina Johannessen, Birthe
Nielsen og Bettina Sørensen
Vejleder: Jesper Larsen
- 302/95 KOMPRESSORER - Analyse af en matematisk model for
aksialkompressorer
Projektrapport af: Stine Bøggild, Jakob Hilmer,
Pernille Postgaard
Vejleder: Viggo Andreasen
- 303/95 Masterlignings-modeller af Glasovergangen
Termisk-Mekanisk Relaksation
Specialerapport udarbejdet af:
Johannes K. Nielsen, Klaus Dahl Jensen
Vejledere: Jeppe C. Dyre, Jørgen Larsen
- 304a/95 STATISTIKNOTER Simple binomialfordelingsmodeller
af: Jørgen Larsen
- 304b/95 STATISTIKNOTER Simple normalfordelingsmodeller
af: Jørgen Larsen
- 304c/95 STATISTIKNOTER Simple Poissonfordelingsmodeller
af: Jørgen Larsen
- 304d/95 STATISTIKNOTER Simple multinomialfordelingsmodeller
af: Jørgen Larsen
- 304e/95 STATISTIKNOTER Mindre matematisk-statistisk opslagsværk
indeholdende bl.a. ordforklaringer, resuméer og
tabeller
af: Jørgen Larsen

- 305/95 The Maslov Index:
A Functional Analytical Definition
And The Spectral Flow Formula

By: B. Booss-Bavnbek, K. Furutani
- 306/95 Goals of mathematics teaching

Preprint of a chapter for the forthcoming International Handbook of Mathematics Education (Alan J. Bishop, ed)

By: Mogens Niss
- 307/95 Habit Formation and the Thirdness of Signs

Presented at the semiotic symposium

The Emergence of Codes and Intensions as a Basis of Sign Processes

By: Peder Voetmann Christiansen
- 308/95 Metaforer i Fysikken

af: Marianne Wilcken Bjerregaard, Frederik Voetmann Christiansen, Jørn Skov Hansen, Klaus Dahl Jensen, Ole Schmidt

Vejledere: Peder Voetmann Christiansen og Petr Viscor
- 309/95 Tiden og Tanken

En undersøgelse af begrebsverdenen Matematik udført ved hjælp af en analogi med tid

af: Anita Stark og Randi Petersen

Vejleder: Bernhelm Booss-Bavnbek
-
- 310/96 Kursusmateriale til "Lineære strukturer fra algebra og analyse" (E1)

af: Mogens Brun Heefelt
- 311/96 2nd Annual Report from the project
LIFE-CYCLE ANALYSIS OF THE TOTAL DANISH ENERGY SYSTEM

by: Hélène Connor-Lajambe, Bernd Kuemmel, Stefan Krüger Nielsen, Bent Sørensen
- 312/96 Grassmannian and Chiral Anomaly

by: B. Booss-Bavnbek, K.P. Wojciechowski
- 313/96 THE IRREDUCIBILITY OF CHANCE AND THE OPENNESS OF THE FUTURE

The Logical Function of Idealism in Peirce's Philosophy of Nature

By: Helmut Pape, University of Hannover
- 314/96 Feedback Regulation of Mammalian Cardiovascular System

By: Johnny T. Ottesen
- 315/96 "Rejsen til tidens indre" - Udarbejdelse af a + b et manuskript til en fjernsynsudsendelse + manuskript

af: Gunhild Hune og Karina Goyle

Vejledere: Peder Voetmann Christiansen og Bruno Ingemann
- 316/96 Plasmaoscillation i natriumklynger

Specialerapport af: Peter Meibom, Mikko Østergård

Vejledere: Jeppe Dyre & Jørn Borggreen
- 317/96 Poincaré og symplektiske algoritmer

af: Ulla Rasmussen

Vejleder: Anders Madsen
- 318/96 Modelling the Respiratory System

by: Tine Guldager Christiansen, Claus Dræby

Supervisors: Viggo Andreassen, Michael Danielsen
- 319/96 Externality Estimation of Greenhouse Warming Impacts

by: Bent Sørensen
- 320/96 Grassmannian and Boundary Contribution to the -Determinant

by: K.P. Wojciechowski et al.
- 321/96 Modelkompetencer - udvikling og afprøvning af et begrebsapparat

Specialerapport af: Nina Skov Hansen, Christine Iversen, Kristin Troels-Smith

Vejleder: Morten Blomhøj
- 322/96 OPGAVESAMLING

Bredde-Kursus i Fysik 1976 - 1996
- 323/96 Structure and Dynamics of Symmetric Diblock Copolymers

PhD Thesis

by: Christine Maria Papadakis
- 324/96 Non-linearity of Baroreceptor Nerves

by: Johnny T. Ottesen
- 325/96 Retorik eller realitet ?

Anvendelser af matematik i det danske Gymnasiums matematikundervisning i perioden 1903 - 88

Specialerapport af Helle Pilemann

Vejleder: Mogens Niss
- 326/96 Bevistæori

Eksemplificeret ved Gentzens bevis for konsistensen af teorien om de naturlige tal

af: Gitte Andersen, Lise Mariane Jeppesen, Klaus Provin Jørgensen, Ivar Peter Zeck

Vejledere: Bernhelm Booss-Bavnbek og Stig Andur Pedersen
- 327/96 NON-LINEAR MODELLING OF INTEGRATED ENERGY SUPPLY AND DEMAND MATCHING SYSTEMS

by: Bent Sørensen
- 328/96 Calculating Fuel Transport Emissions

by: Bernd Kuemmel

329/96 The dynamics of cocirculating influenza strains conferring partial cross-immunity and
A model of influenza A drift evolution
by: Viggo Andreassen, Juan Lin and Simon Levin

339/97 Defining Discipline
by: Wolfgang Coy

330/96 LONG-TERM INTEGRATION OF PHOTOVOLTAICS INTO THE GLOBAL ENERGY SYSTEM
by: Bent Sørensen

331/96 Viskøse fingre
Specialerapport af:
Vibeke Orlie og Christina Specht
Vejledere: Jacob M. Jacobsen og Jesper Larsen

332/97 ANOMAL SWELLING AF LIPIDE DOBBELTLAG
Specialerapport af:
Stine Sofia Korremann
Vejleder: Dorthe Posselt

333/97 Biodiversity Matters
an extension of methods found in the literature on monetisation of biodiversity
by: Bernd Kuemmel

334/97 LIFE-CYCLE ANALYSIS OF THE TOTAL DANISH ENERGY SYSTEM
by: Bernd Kuemmel and Bent Sørensen

335/97 Dynamics of Amorphous Solids and Viscous Liquids
by: Jeppe C. Dyre

336/97 PROBLEM-ORIENTATED GROUP PROJECT WORK AT ROSKILDE UNIVERSITY
by: Kathrine Legge

337/97 Verdensbankens globale befolkningsprognose - et projekt om matematisk modellering
af: Jørn Chr. Bendtsen, Kurt Jensen,
Per Pauli Petersen
Vejleder: Jørgen Larsen

338/97 Kvantisering af nanolederes elektriske ledningsevne
Første modul fysikprojekt
af: Søren Dam, Esben Danielsen, Martin Niss,
Esben Friis Pedersen, Frederik Resen Steenstrup
Vejleder: Tage Christensen